Impact of the morphology of soot aggregates on their radiative properties and the subsequent radiative heat transfer through sooty gaseous mixtures

Gizem Okyay

NNT : 2016SACLC031

THÈSE DE DOCTORAT
DE
L'UNIVERSITÉ PARIS-SACLAY
PRÉPARÉE À
CENTRALESUPÉLEC

ÉCOLE DOCTORALE N°579

Sciences mécaniques et énergétiques, matériaux et géosciences

Spécialité Énergétique

par

Mme. Gizem OKYAY

Impact of the morphology of soot aggregates on their radiative properties and the subsequent radiative heat transfer through sooty gaseous mixtures

Thèse présentée et soutenue à Châtenay-Malabry, le 19 Avril 2016.

Composition du jury:

M. BOULET, Pascal	Professeur, LEMTA Université de Lorraine	Président
M. VAILLON, Rodolphe	Directeur de Recherche CNRS, CETHIL	Rapporteur
M. VIGNOLES, Gérard	Professeur, LCTS Université de Bordeaux	Rapporteur
M. RIVIERE, Nicolas	Ingénieur de Recherche, DOTA ONERA	Examinateur
M. YON, Jérôme	Maître de Conférences, CORIA INSA Rouen	Examinateur
M. ENGUEHARD, Franck	Professeur, EM2C CentraleSupélec	Directeur de thèse
M. AMMOURI, Fouad	Ingénieur R&D, Air Liquide CRCD	Invité
M. AUGER, Thierry	Chargé de Recherche CNRS, MSSMat	Invité
M. JOUMANI, Youssef	Expert Thermicien, LNE	Invité

Laboratoire d'Énergétique Moléculaire et Macroscopique, Combustion
CNRS, CentraleSupélec.

Acknowledgements

This thesis is realized as a part of a collaborative project between academia and industry, supported by the Air Liquide, CentraleSupélec and CNRS Chair on oxycombustion and heat transfer for energy and environment and by the OXYTEC project, grant ANR-12-CHIN-0001. I would like to acknowledge the people who contributed and helped me to accomplish this interdisciplinary research, to reach my professional and personal goals, and transformed the doctoral thesis into a pleasant journey.

First of all, I would like to express my gratitude to my thesis supervisor Franck Enguehard, for his patience during three years and for allowing me to take decisions independently on the experimental applications of this study, which thought me considerably on conducting properly a research project. I also kindly acknowledge his scientific guidance, especially related to the core of my study on the radiative properties. His help during the preparation of the thesis defense was valuable as it was one of the hardest steps during my doctoral studies.

I would like to express my gratitude Youssef Joumani, who followed the thesis works from the industrial point of view, for his guidance and helps, his always-positive mood and motivation. And, of course, for his patience during the debugging of the heat transfer code!!! Special thanks for moving the computer mouse during my thesis defense to keep the Webex connection on :)

I would like to express my gratitude to Rodolphe Vaillon and Gérard Vignoles for having accepted to review the manuscript and for bringing constructive commentaries and perspectives to this work. I would like to extend this gratitude to all the jury members, Pascal Boulet, Nicolas Rivière, Jérôme Yon, who examined my work in detail and helped me to criticize my study and also to appreciate its added values and to improve my scientific approach. This acknowledgment is also extended to the invited members: Fouad Ammouri, Thierry Auger, Youssef Joumani.

I would like to thank Fouad Ammouri, whom I met during my master's studies, and since, I have learned a lot from him on the radiative transfer, which was very helpful for my integration into the subject at the beginning of my thesis

work, and for his participation to the jury. I would like to thank also further people from Air Liquide: Bernard Labegorre and Caroline Bertail with whom I exchanged multidisciplinary discussions and learned new techniques.

I gratefully acknowledge the members of MSSMat laboratory, who opened the doors for new horizons for me, and where I discovered new research opportunities on microscopy and my passion for tomography. I kindly acknowledge that the microscopy work was carried out within the MATMECA consortium supported by the ANR under contract number ANR-10-EQUIPEX-37 and has benefited from the facilities of the Laboratory MSSMat of CentraleSupélec. I express my deepest gratitude to Thierry Auger for his valuable time spent on the thinking about the sampling and the characterization issues and the microscopy studies, and for his always pleasant welcoming. I express also my deepest gratitude to Eva Héripré for her valuable time and support, helps and commentaries during the microscopy works. I would like to thank Thomas Reiss and Paul Haghi-Ashtiani for their time and help on my microscopy observation works in MSSMat, without forgetting Sokona Konate who guided me for the use of the facilities.

Of course, without the support of a team, and the financial support, goals would be harder to reach. Hence, I thank all the members of the OXYTEC chair and express my gratitude to Thierry Schuller for his support, and of course to our laboratory director Olivier Gicquel for ensuring that the thesis is accomplished in good conditions.

I kindly thank all the EM2C laboratory members, with special thanks to Nathalie Rodrigues, Brigitte Llobel, Noï Lavaud, Anne-Cécile Aiach for their valuable help on administrative procedures and to Sébastien Turgis, Mathieu Boileau for their patience and help on the computing and computer issues. I also kindly thank all the people involved in the physics research team, with whom I interacted very often during the axis meetings and conferences, for which I also express my gratitude to Sébastian Volz.

I think that one of the nicest parts of being a PhD candidate is to be on the both sides of the classroom: I was learning but also helping the teaching process. I am grateful to Franck Enguehard for his help during my small teaching mission of the heat transfer course, acknowledging my co-workers Antoine Renaud, Wafa Bendhaou, Marie Zarrouati, Mehdi Ayouz. For the students' energy projects and for the workshops, it was a pleasure to work with Fabien Bellet and Thomas Antoni. I would like to also acknowledge Philippe Scouflaire, Laurent Zimmer for their help on the supervision of the experimental activities of students, also acknowledging the help of Erika Jean-Bart, Alain Walton, Yannick Le Teno.

We did not only worked hard during these years, but also collected nice memories. Many thanks and good thoughts for people who never gave up on me

during the tough days. Without being exhaustive (unfortunately), I thank people who I did not mentioned yet but who helped me, either personally or professionally, on big or small matters, and shared nice chats: Macole Sabat, Ghada Asmar, Wassim Kassem, Pedro Volpiani, Jose Ordonez-Miranda, Adrien Chatelier, Sergei Gluchko, Carolyn Jacobs, my compatriot Oğuz Emre, Mihaela Cirisan, Jorge Brandle de Motta, Maria Castela, Nancy Kings, Mélody Cailler, Yunhui Wu, Erwan Pannier ("güle güle"), Maxime Philip, Marien Simeni Simeni. I specially thank Macole and Ghada for their support and valuable helps during the preparation of the "pot de thèse", and also thank "Bedro" and Adrien. Of course, I will not forget the office colleagues: Thanks to Layal Hakim, Alexis Cuquel for their nice welcoming and to Kyle Horne for his scientific helps when I first arrived; Haoxue Han, Umar Sheikh, Arthur Salmon, Gilles Bailet, Sergei Gluchko, Tan-Trung Nguyen, Cédric Mehl, Giampaolo Maio, David Mercier, for their patience during my stressful preparation stages for conferences, papers, manuscript and the defense.

Besides, I would never forget the support of the Turkish crew and the METU crew! I thank all of my dearest friends, who proved that distances does not matter: Gülen Sinem Tek, who always found a way to cheer me up; Tuğçe Yıldırım, Meriç Selamoğlu, Mehmet Yenişan, who never forgot to check on me if I was alive; without forgetting Ezgi Köker, Ürün Bakar, Aslıcan Yılmaz, Alper Onen. (Special thanks to Tuğçe: you know that you are the butterfly effect of all this adventure.)

Saving the best for the last: I could not make it until the end without the endless support and love of my family, my dear mother (sending homemade Turkish food via international postal service :)), father (who always trusts me in my choices) and sister (now that I am a PhD, I share the pain). Hence, once again, I dedicate my work to my beautiful family.

Abstract

Soot and its characterization are of interest to researchers from various domains such as combustion diagnostics, numerical combustion, atmospheric optics, environmental and health applications. In this study, the main interest is on the radiative properties of soot aggregates issued directly from combustion flames in order to determine the effect of the presence of soot on the radiative heat transfer in the simulation of high temperature industrial applications involving gas combustion. Current studies modeling the radiative heat transfer through sooty gaseous media consider only the absorption as the main phenomenon of material-radiation interaction. Generalized correlations are used to determine the radiative properties of soot: these radiative properties are either computed over numerically generated aggregate morphologies or simply as a function of the soot average size, the fractal dimension and the volume fraction. However, the material-radiation interaction is susceptible to be more complex and morphology dependent at the aggregate level because of multiple scattering when the size of the object reaches the order of magnitude of the incident radiation wavelengths.

In our work, we investigate the possibility to establish a computational methodology and workflow, starting from the definition of a realistic soot morphology up to the computation of the radiative heat transfer. To that end, observations of soot issued from propane/air, methane/air and methane/oxygen flames are performed using Scanning Electron Microscopy (SEM). SEM tomography is applied for the first time on soot issued from a propane/air flame, combined with Transmission Electron Microscopy (TEM) observations. 2D and 3D fractal analysis techniques are used to investigate the fractal properties of virtual (numerically generated) soot clusters and also of the tomography reconstructed objects. The radiative properties of soot are then computed using our in-house developed DDA (Discrete Dipole Approximation) code. Special attention is paid to the DDA modeling of soot because of the high complex extinction index of the material, and to the directional integration numerical methods because direction-averaged radiative properties are required for the subsequent radiative heat transfer simulations. The morphology and the radiative properties of the realistic morphology are compared to the ones of representative soot aggregates numerically generated by a DLCCA (Diffusion Limited Cluster-Cluster

Aggregation) algorithm. The similarities and discrepancies on the radiative properties are investigated, and the differences between representative virtual aggregates on the one hand and the tomography reconstructed object on the other hand in terms of radiative properties are highlighted. Finally the effect of the presence and of the morphology of soot on the radiative heat transfer within a sooty gaseous mixture in a 1D isothermal parallel plate configuration is investigated by the resolution of the radiative transfer equation using DOM (Discrete Ordinates Method).

Résumé

Les suies et leur caractérisation constituent des sujets de recherche très actuels dans divers domaines tels que le diagnostic de la combustion, la combustion numérique, l'optique atmosphérique, l'environnement et les applications de santé. Notre étude se concentre sur les propriétés radiatives des agrégats de suie issus de flammes de combustion; notre objectif est de déterminer l'effet de la présence de suies sur le transfert de chaleur par rayonnement pour la simulation d'applications industrielles à haute température impliquant la combustion de gaz. Les études actuelles de modélisation du transfert de chaleur par rayonnement à travers les mélanges gazeux chargés de suies ne considèrent que l'absorption comme phénomène d'interaction rayonnement-matière. Des corrélations généralisées sont utilisées pour déterminer les propriétés radiatives des suies, soit sur la base de morphologies générées numériquement, soit plus simplement à partir de la taille moyenne des suies, de leur dimension fractale et de leur fraction volumique. Cependant, lorsque la taille de l'objet atteint l'ordre de grandeur des longueurs d'onde du rayonnement incident, l'interaction matière-rayonnement est susceptible d'être plus complexe du fait du phénomène de diffusion au niveau de l'agrégation qui ne peut plus être ignoré.

Dans notre travail, nous établissons une méthodologie complète assortie d'une chaîne de calcul allant de la définition d'une morphologie de suie réaliste jusqu'au calcul du transfert de chaleur par rayonnement. A cette fin, des observations de suies émises par des flammes propane / air, méthane / air et méthane / oxygène sont effectuées par Microscopie Electronique à Balayage (MEB). La tomographie MEB est appliquée pour la première fois sur une suie issue d'une flamme propane / air, en combinaison avec la Microscopie Electronique en Transmission (MET) pour les observations. Des techniques d'analyse fractale 2D et 3D sont utilisées pour étudier les propriétés fractales d'agrégats de suie virtuels (générés numériquement) et de l'objet obtenu par la tomographie. Les propriétés radiatives des suies sont ensuite calculées en utilisant notre propre code d'Approximation Dipolaire Discrète (ADD - Discrete Dipole Approximation, ou DDA, en anglais). Une attention particulière est accordée à la modélisation ADD des suies en raison de l'indice optique complexe élevé de leur matériau constitutif, et aux méthodes numériques d'intégration directionnelle car les moyennes directionnelles des propriétés radiatives sont nécessaires pour

les simulations ultérieures de transfert radiatif. La morphologie et les propriétés radiatives de l'agrégat de suie réaliste (tomographié) sont comparées à celles d'agrégats de suie numériques représentatifs, générés par un algorithme d'agrégation amas-amas limitée par la diffusion (Diffusion Limited Cluster-Cluster Aggregation, ou DLCCA, en anglais). Les compatibilités et les écarts entre les propriétés radiatives sont examinés, et les différences entre agrégats numériques représentatifs d'une part et agrégat réaliste d'autre part en termes de propriétés radiatives sont soulignées. Enfin, l'effet de la présence et de la morphologie des suies sur le transfert de chaleur par rayonnement est étudié par la résolution de l'équation du transfert radiatif en utilisant la méthode des ordonnées discrètes (Discrete Ordinates Method, ou DOM, en anglais) dans un mélange gazeux chargé de suies et dans une configuration académique 1D de plaques paralléles isothermes.

Contents

List of Tables

List of Figures

Nomenclature

Latin Characters :

a_{dip}	Dipole size
a_{vox}	Voxel size
C	Cross-section
C_p	Penetration cofficient
D_f	Fractal dimension
d_p	Primary particle diameter
$\mathbf{E}$	Total electric field vector
f	Frequency
f_v	Volume fraction
g	Asymmetry parameter
k	Imaginary part of the complex optical index
k_f	Fractal prefactor
K	Wave number
Kn	Knudsen number
L	Distance
L_{agg}	Projected distance
m	Complex optical index
n	Real part of the complex optical index
$\mathbf{n}$	Unit vector
N_p	Primary particle number
P	Pressure
q	Radiative heat flux
Q	Efficiency
$\mathbf{r}$	Position vector
r_p	Primary particle radius
R_m	Mobility radius
R_g	Radius of gyration
R_{veq}	Radius of volume equivalent particle
T	Temperature
V	Volume
V_{eq}	Equivalent volume
x	Size parameter

Greek Characters :

α	Correction factor (fractals)
α_j	Polarizability
β	Extinction coefficient
δ	Dipole characteristic size
θ	Scattering angle
ε	Dielectric permittivity
κ	Absorption coefficient
λ	Wavelength
ν	Frequency
σ	Scattering coefficient
ϕ	Phase function
ϕ'	Normalized phase function
ω	Scattering albedo
$\mathbf{\Pi}$	Dipole moment vector

Abbreviations :

BSE	Backscattered Electron
CCA	Cluster-Cluster Aggregation
CM	Clausius-Mossotti
DDA	Discrete Dipole Approximation
DLA	Diffusion Limited Aggregation
DLCCA	Diffusion-Limited Cluster-Cluster Aggregation
DOM	Discrete Ordinates Method
EW	Equal Weights
HRTEM	High-Resolution Transmission Electron Microscopy
LDR	Lattice Dispersion Relation
LL	Lebedev Laikov
PAH	Polycyclic Aromatic Hydrocarbons
PCA	Particle-Cluster Aggregation
RDG	Rayleigh-Debye-Gans (-FA: for Fractal Aggregates)
RLA	Reaction Limited Aggregation
RR	Radiative Reaction
SE	Secondary Electron
SEM	Scanning Electron Microscopy
TEM	Transmission Electron Microscopy
TOMO	Tomography
VS	Virtual sphere

Subscripts & Superscripts :

abs	Absorption	p	Primary particle
agg	Aggregate	sca	Scattering
ext	Extinction	veq	Volume equivalent
NP	Non-polarized		

Introduction

Soot, produced by incomplete combustion processes, has its negative and positive impacts depending on the field of application. The resulting emissions have toxic effects (Lighty et al. (2000)) because the soot formation is accompanied by the formation of polycyclic aromatic hydrocarbons considered to have negative impact on the human respiratory system (Bockhorn (1994)). Emissions also have an impact on climate changes (Ramanathan and Carmichael (2008)) and are pollutants of the environment (Mansurov (2005)). Soot is nevertheless abundant in industrial processes (Calvo et al. (2013)) and favoured in some industrial applications where high temperatures are desired such as in glass and metal manufacturing, or where it is used as a raw material for chemical products such as toners, tires, additives (Bockhorn (1994)).

In combustion diagnostics, as well as in aerosol optics, researchers are interested in the chemical and physical nature of soot emissions (Vander Wal et al. (2010)) existing in different forms and processes such as soot issued from incomplete combustions of hydrocarbons (Khalizov et al. (2012)), ash depositions (Kamp et al. (2012)), elementary carbon combined with organic compounds forming aerosols (Calvo et al. (2013)) or flame soot and aggregates (Shaddix and Smyth (1996)). Regardless of the domain of application and the extensions of the methods, numerical and semi-empirical computational tools are developed for the determination of the radiative properties of soot and its aggregates.

Our study being part of the OXYTEC project (grant ANR-12-CHIN-0001) on oxycombustion and heat transfer, which is in close relation with industry, the main concern is on the high temperature industrial processes of gaseous hydrocarbon combustion. In industrial applications, the control of radiative heat transfer is crucial to determine potential hot spots inside the furnaces. For such processes, the contribution of soot becomes particularly important in fuel-rich combustion flames where the residence time of soot and the concentration of carbon atoms are much higher than in lean flames. In these conditions, the radiative properties of soot are presumed to become strongly dependent on its morphology and volume fraction because the soot particles collide to form complex shaped aggregates reaching the size of the thermal radiation wavelengths. Hence the microstructural characterization of soot is important

for a correct evaluation of its contribution to radiation heat transfer through the precise quantification of its radiative properties, i.e. absorption and scattering efficiencies in response to the thermal wavelengths.

An accurate characterization of soot radiation is only possible by correct definition of the material radiative properties and its morphology. Definition of radiative properties consists of the composition and optical properties of soot material. While for flame soot the composition is mostly black carbon, the optical index data is known to vary depending on flame and fuel conditions. Throughout this study, the material properties are fixed to one data base of soot complex optical index: we focus our study on the description of more realistic morphology and improvement of radiative properties. In literature, studies on soot morphology consist of analyses at different scales: macro, micro and nano (Liati and Eggenschwiler (2010)). At the macroscopic scale, the aggregation stage is important for the material-radiation interaction. The microscopic investigation of the small particles and the physico-chemical properties of emitted particles are important to interpret the combustion dynamics. The nanoscale investigation is used to retrieve information about the chemical and physical formation history (Vander Wal (2015)). The gas phase chemistry is important for the determination of the flame structure and numerical modeling (Frenklach (2002)).

In the very early researches, the effect of complex geometry in the solid phase (micron sized soot aggregates), is taken into account for soot radiation by using simplified assumptions on light scattering from groups of small particles (Lee and Tien (1983), Megaridis and Dobbins (1990), Farias et al. (1998)). The researches are still limited to a fractal description of soot simulated by numerical generation of aggregates, despite the uncertainties arising from experimental techniques for the determination of fractal descriptors reported to be highly dependent on the experimental extraction conditions (Lack et al. (2014)). Studies focusing solely on the effect of soot morphology on radiative properties are based on 2D analysis of soot aggregate images and subsequent numerical generation of the fractal geometry: some examples are the studies of Brasil et al. (1999), Liu and Mishchenko (2007), Chakrabarty et al. (2011), Skorupski and Mroczka (2014). The same is true for studies trying to extract morphological data from the in-situ experimental studies (López-Yglesias et al. (2014)).

Thanks to the advances in the numerical implementations of theoretical approximations, it is possible to integrate more rigorously the effect of complex geometry in the computation of the radiative properties and of the radiative transfer. In our study, we chose the electromagnetic theory based on the Discrete Dipole Approximation (DDA) for the modeling of the interaction between radiation and complex shaped objects in order to determine their radiative

properties. A complete series of coupled computational tools is developed in this study, starting from the 3D description of aggregates and going up to the evaluation of their radiative properties and the computation of the radiative heat transfer. Geometry of the aggregates, in between other variables such as the complex optical index of soot and the volume fraction, is one of the important input parameters for radiation simulation and diagnostic in combustion systems. The aim in this work is therefore to present a realistic 3D soot aggregate shape in order to feed the above mentioned series of computations. Hence, this manucsript is divided into three parts: "*morphology*", "*radiative properties*" and "*radiative heat transfer*".

Part I on morphology is composed of two studies: "*experimental*" (**Chapter 1**) and "*numerical*" (**Chapter 2**). In **Chapter 1**, we describe the ex-situ experimental procedures that we have applied on soot aggregates and particles extracted from a laboratory scale propane flame using the electron microscopy and tomography. Please note that Chapter 1 is partly adapted from our literature contribution entitled "Soot aggregate complex morphology: 3D geometry reconstruction by SEM tomography applied on soot issued from propane combustion" (Okyay et al. (2016)). Nevertheless, the necessary conditions and procedures are given more in detail here for the microscopy operations and 3D geometry reconstruction from tomography with the demonstration of the methods.

Chapter 2 will be focused on the numerical analysis of the morphology of soot aggregates issued from our combustion flames of propane and methane. First a brief review will be given on the formation of soot in order to reflect the morphology of soot and the orders of magnitude in question. Then the numerical methods will be explained for the generation of representative aggregates by computer simulations. This will be followed by the 2D fractal analysis of clusters of aggregates applied to SEM and TEM images. Different from literature studies on combustion soot, 3D fractal analysis of soot will be applied on the geometries otained from tomography. The fractal properties will be compared to the literature values and the discrepancies will be discussed.

Part II of the manuscript is dedicated to the radiative properties determined by the numerical solution of the material-light interaction (Chapter 3) and applications to our tomographied soot aggregates obtained (Chapter 4). In **Chapter 3**, the methods used in the computation of radiation-material interaction will be reviewed. Then, our in-house DDA algorithm will be explained with an emphasis on high complex optical index materials as soot. In **Chapter 4**, the radiative properties of soot will be investigated using the DDA tool developed in Chapter 3 and using the morphology informations obtained in Part I. First, the radiative properties of soot aggregates will be reviewed as a function of fractal parameters, particle number and size. Then, the radiative

properties will be derived for more realistic geometries of soot aggregates obtained from tomography: the numerically generated aggregates will be modified for particle overlapping, on the basis of our results obtained in Chapter 2, in order to increase the representativity of numerical aggregates. The radiative property results obtained using different methods (DDA, RDG-FA, Mie) will be compared for numerical aggregates and for tomography geometries.

Finally, in **Chapter 5** (**Part III**), the effect of soot morphology on radiative heat transfer will be investigated. The radiative transfer equation will be resolved using the Discrete Ordinates Method (DOM) for parallel plates configurations. First the effect of scattering will be quantified by simulating soot in a transparent medium at different temperatures. Then, radiation through sooty gaseous combustion products will be investigated for different volume fractions of soot, and for different gaseous mixtures. The discrepancies due to improved soot radiative properties (i.e. due to a better knowledge of soot morphology and its integration in radiation-matter interaction calculations) will be quantified for radiative heat flux and source rates.

Part I

Morphology

Chapter 1

Electron tomography on soot

The state-of-art of the work on soot from incomplete combustions comprises the characterization techniques based on in-situ and ex-situ techniques. Due to the limitations and uncertainties arising from in-situ measurements in a combustion flame for the definition of morphology for a dispersed group of aggregates, ex-situ observations under electron microscopy are often referred to in the literature for aggregate samples collected inside the flame. The latter ex-situ observations include the fractal analysis of 2D SEM/TEM images, the derivation of 3D geometry obtained by TEM tomography and the generation of numerical aggregates based on common fractal parameters. In our study, soot aggregates are extracted from a laboratory scale rich propane-air flame by thermophoretic sampling onto metal thin plates. Different than the previous researches, 3D geometry of soot is obtained here by SEM tomography: The geometry reconstruction techniques are successfully applied to a relatively small series of tilted SEM images of high resolution using the seeing through phenomenon occurring in nano-sized material samples with low atomic number. The observation of soot monomer size under TEM microscopy allows us to test the errors that may arise from the SEM imaging technique (like the pollution deposition on the substrate due to charging, the image artifacts due to the nature of secondary electron emissions) and from the simplified sampling procedure (not using the conventional holey carbon films but metal thin plates). The obtained 3D soot geometry is promising in terms of reducing the microscopy analysis time, simplifying the sampling procedure and expanding the 3D observation applicability by not limiting the material sampling to depositing soot and aerosols on TEM grids. Furthermore, the 3D geometry of soot enables a real 3D fractal analysis and gives information about the surface and volume of the object, not only important for the radiation but also useful for combustion simulations.

1.1 Scope of work: Defining 3D morphology of soot

The techniques used to define the soot morphology depend on its production source and type, i.e. soot extracted directly from combustion of various fuels, emitted in the air, aged to form aerosols. We are interested in the aggregates formed in our combustion flames where both in-situ and ex-situ characterization techniques are possible. In-situ techniques are not considered in this study because they provide information about groups of particles and do not yet provide information about the aggregate geometry as mentioned before. The aim of this work is to provide a realistic 3D complex morphology, hence to circumvent the link between the soot radiative properties and the fractal parameters where there are noticeable experimental uncertainties arising from in-situ techniques and protocols (Lack et al. (2014) and references therein).

Ex-situ characterization is more commonly used for the observation of emitted soot, like aerosols and particulate emissions from fires and engines than the flame soot because the representability of soot inside the flame by ex-situ observations can be a point of discussion. This question brings forward a future work on comparative study of ex-situ experiments with in-situ experiments; this problem is not tackled in this work.

Ex-situ techniques involve two steps such as sampling and microscopy observation. The commonly accepted sampling technique for flame soot is thermophoretic sampling explained by Dobbins and Megaridis (1987). The morphology of soot can be observed under TEM (Transmission Electron Microscopy) (Bescond et al. (2014), Tian et al. (2007)), SEM (Scanning Electron Microscopy) (China et al. (2013), Chakrabarty et al. (2014)), by AFM (Atomic Force Microscopy) (Lieb and Wang (2013)), by SEM-FIB (Focused Ion Beam Scanning Electron Microscopy) exhaust soot on filters (Kamp et al. (2012)), X-ray scattering (Bogan et al. (2010)) and very recently by HIM (Helium Ion Microscopy) (Schenk et al. (2015)).

While it is possible to characterize soot aggregate morphology by the classical techniques mentioned, relying on 2D image analysis or more recent works on TEM tomography, this study proposes SEM tomography for the 3D geometry reconstruction to describe actual soot aggregate morphologies. 3D SEM can seem unconventional for tomography applications, nevertheless it has already been successfully used for filament networks in medical applications in the works of Lück et al. (2010), Woodward and Wepf (2014). It is also mentioned as a promising technique by Walther et al. (2012). The contributions in this experimental study is not only to provide 3D geometry of soot but also to apply SEM tomography to combustion soot aggregates and therefore to propose a new method to define soot morphology. Utilization of SEM brings a great advantage over TEM with a relatively easy sampling and manipulation coupled to a rapid imaging procedure. The advantage of 3D imaging over 2D methods is to enable the complete visualization of the complex shape, which will allow for example

to quantify in 3D the effect of sintering on the fractal properties of soot and its radiative properties.

1.2 Ex-situ experimentation

1.2.1 Sampling material

Small metal plates are used as base material instead of TEM grids for the ease of manipulation while inserting into the flame and while observing under SEM. 5x5 mm plates are prepared from 1 mm thick inox sheets. The metal plates constitute electrically conductive support material required for SEM observation. Referring to the carbon patches used to fix samples on SEM holders and carbon covering made on biological samples for electron conductivity, it is presumed that the collected soot, composed mostly of carbon, will also allow the discharge of electrons. The thin metal plates are mirror polished, using mechanical polishing down to 1 micron diamond paste, to avoid any contrast problems that might occur in SEM images due to high surface roughness. The plates are also cleaned from any impurities by soaking with solvent in ultrasonic bath before introducing them into the flame for sampling.

1.2.2 Sampling conditions

Sampling of soot aggregates is performed by horizontally sweeping the thin metal plates trough the flame at different heights above the burner. This technique has been used by Lieb and Wang (2013) and Schenk et al. (2015) to deposit soot onto mica disks for observation under AFM. Thermophoretic forces allow particles to move from the high temperature flame and to stick to the sampler at ambient temperature. Immediate deposition of the soot on the support and direct insertion of the sampler into the flame is in good agreement compared to the most suitable sampling protocols proposed by Ouf et al. (2010). Soot is extracted at different heights in a propane/air flame. For all the extractions, the flame height is 36 cm and it is adjusted to fuel rich conditions to imitate high residence times.

In Chaper 2, observations will be presented for soot extracted in methane/air and methane/oxygen flames with different fuel concentrations in order to observe the aggregation pattern. However, as it will be shown in Section 2.1, the aggregates in methane flames are smaller and more compact. This is less favorable for tomography and fractal analyis. Also, the effect of the geometry on material-radiation interaction is more conventional in smaller aggregates compared to the radiation wavelength and sphere-like aggregates. Therefore the following sections in Chapter 1 reports only the results of by electron tomography on propane soot as an extreme case of aggregation and complex geometry.

1.2.3 Preparation for SEM

The charging of soot samples under the electron beam might be an issue on badly conducting samples. In this work we chose to not cover the samples with a conductive film, unlike other studies (Chakrabarty et al. (2014)), in order to preserve the original soot structure. We did not observe considerable charging on propane soot samples during SEM imaging after comparing the first and final images taken under the same microscopy conditions and during the recording of the tomograms presented in Section 1.3.

1.2.4 Preparation for TEM

For this study TEM is used to observe primary particle size and sintering morphology. TEM copper grids coated by holey carbon film (provided by Agar Scientific) is used. To our knowledge, soot solid material issued directly from incomplete combustion in flame is not soluble in any solvent (Moosmüller et al. (2009), Petzold et al. (2013), Bølling et al. (2009)). Therefore soot sample deposited on metal plate and then the TEM grid are soaked into an ethanol solution in the ultrasonic bath to allow the deposition of some soot material on the TEM grid. This soot dispersion method by ultrasonic agitation is also used by Alfè et al. (2010). Gaseous components trapped inside soot, if any, would be evacuated eventually in the SEM/TEM vacuum chamber (Gwaze et al. (2006)). This would not cause any considerable change in the sample structure, neither in TEM nor in SEM, because the soot is directly extracted directly from flame (Gwaze et al. (2006), Lobert et al. (1991)).

1.3 Microscopy conditions and imaging

In this section, the microscopy conditions are summarized for the observation, tomography and image recording of the samples in order to allow the reproducibility of the results. It should nevertheless be remembered that those conditions can be altered from one microscopy equipment to another, especially for the recent scanning electron microscopes equipped with several detectors and filtering mechanisms. Those equipments are sketched in Section 1.5 followed by the explanation of the interaction of the electron beam with our sample. The ultimate morphology results of the microscopy applications are given in Section 1.7.

1.3.1 SEM for observation

First, ex-situ observation is made to observe the aggregation pattern of the deposited soot in propane/air flame. Samples are collected at different heights above the burner: beginning of the flame, mid-height and top of the flame.

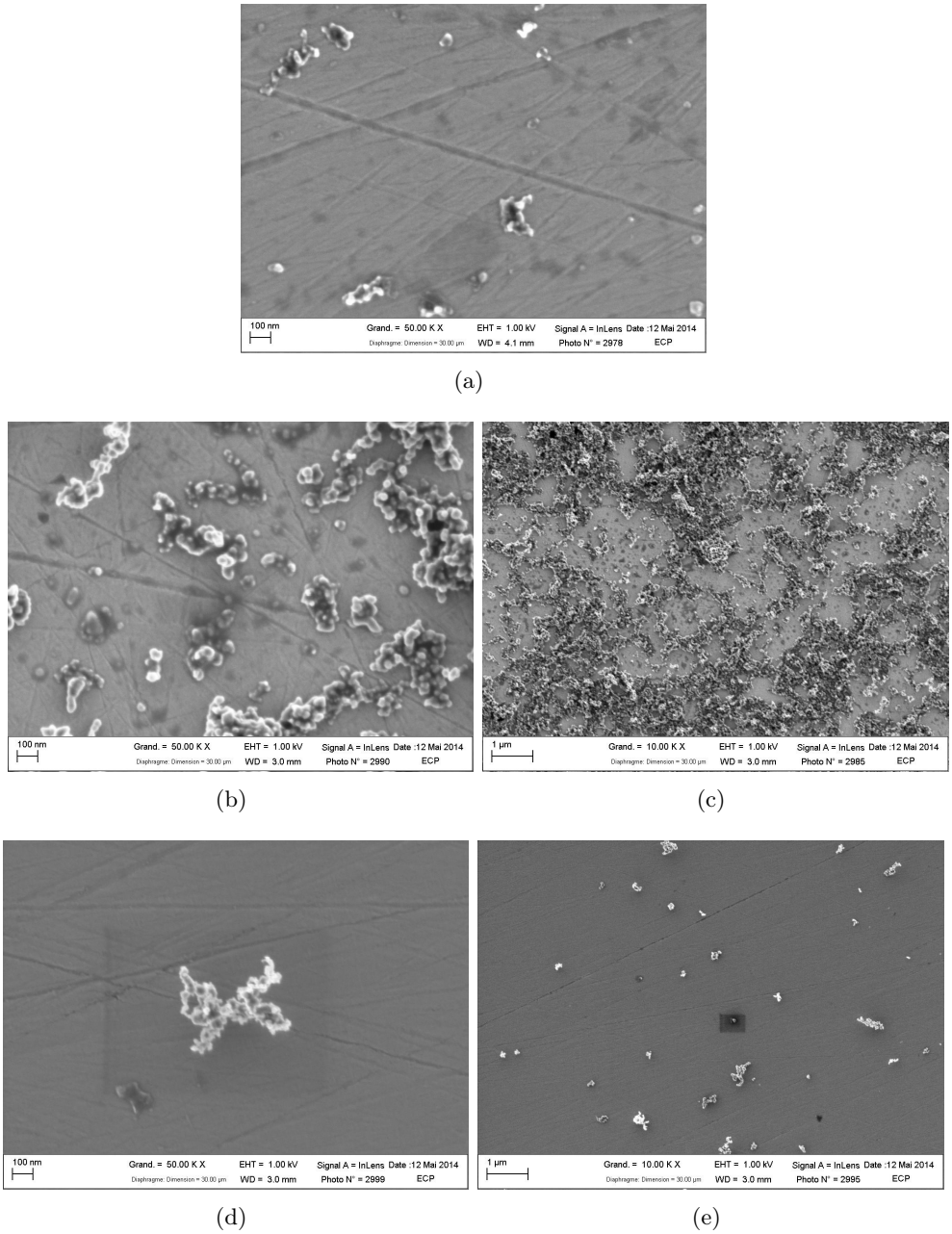

Figure 1.1: *SEM image of soot collected in a propane/air flame (a) at h=5 cm above the burner at magnification level 50.00 Kx; (b,c) at mid height of the flame at magnification level 50.00 Kx and 10.00 Kx; (d,e) at the top of the flame at magnification levels 50.00 Kx and 10.00 Kx.*

Images are recorded with Zeiss Leo Gemini 1530 under a beam accelerating voltage of 1kV and a working distance of 3 mm using the secondary electron

(SE) signal from InLens detector at magnification levels of 10000x up to 50000x. These images, presented in figures 1.1 are used for a preliminary 2D observation of the evolution of the soot shape, hence to verify if our sampling procedure can probe correctly the soot morphology information. As presented in Section 1.7.1, it is concluded that our sampling procedure is appropriate.

1.3.2 SEM for tomography

In order to apply the tomography 3D reconstruction, high resolution tomograms are needed. The tomogram is constituted from a series of tilted images of the object around the same rotation axis. The SEM images for tomography are recorded using a higher resolution SEM with the Elstar electronic column within the FEI Helios NanoLab 660. In order to construct the tomogram, the sample needs to be tilted around the same rotation axis. This rotation axis corresponds to the eucentric height of the tilt holder equipment of the microscope hence to the 4 mm working distance.

As it will be explained in Section 1.6, high enough voltage is necessary for tomography to retrieve the volume information from the scattered electrons but the substrate pollution is found to be considerable at voltages greater than 5 kV. The beam accelerating voltage is adjusted to 5 kV. Images are recorded using TLD (Through-the-Lens Detector) secondary electron signal.

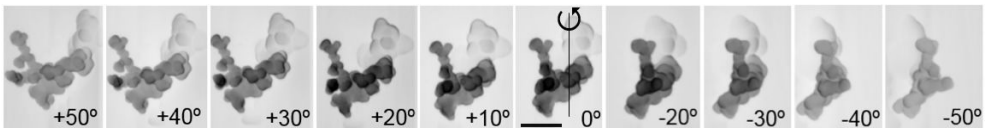

Figure 1.2: *Tomogram **S1a** obtained from contrast inverted SEM images, scale bar corresponds to 200 nm.*

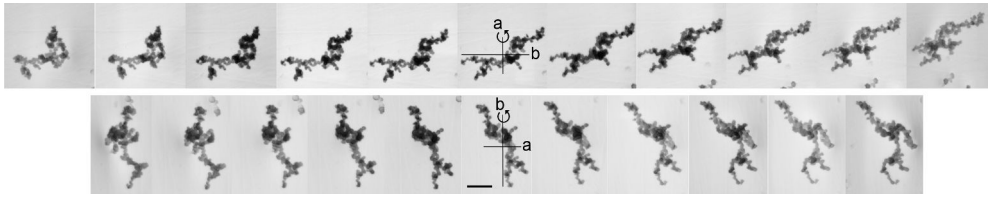

Figure 1.3: *Tomograms **S2a** (upper) and **S2b** (lower) obtained from contrast inverted SEM images, scale bar corresponds to 500 nm.*

Tomograms are recorded for two soot samples that we will name **S1** and **S2**. The first sample **S1** is collected in the midheight of the flame. One tomogram is obtained for **S1** by rotating it around one axis; we will name this tomogram of Figure 1.2 as **S1a**. The second soot sample **S2** is collected at the top of the

flame, i.e. near the afterflame zone. Two tomograms **S2a** and **S2b**, illustrated in Figure 1.3, are generated for **S2** by rotating it around dual axes **a** and **b** perpendicular to each other. The first tomogram **S1a** is taken with a magnification of 130520x and the following tomograms **S2a, S2b** with a magnification of 81575x. We did not observe any background contrast problems thanks to the low surface roughness of the base metal plate and there is not considerable shadowing of the object due to the small size of our soot samples.

Tilted images are taken between +50° and -50° to build up the tomograms. Knowing that the carbon deposition on the substrate under the electron beam can be an issue in the SEM chamber, observation time under the microscope is kept at its minimum by taking a small number of images therefore by making large angular steps between tilted images. SEM series are recorded at every 10°. Our SEM stage allows a maximum tilt angle of 60° in eucentric position but practically we were limited to 50°, it was not possible to swap beyond this stage with our soot sample mounted on the tilt holder because of the small working distance. We therefore took the SEM image series from +50° to 0° and then remounted the sample after rotating it by 180° to complete the rest of the tomogram from 0° to -50°, basically following the methodology explained in the work of Lück et al. (2010). To construct the dual axis tomogram for **S2**, the second image around b-axis is recorded using the same methodology after rotating the sample by 90°.

1.3.3 TEM for observation

Soot monomers are imaged by FEI Titan TEM. The recordings presented in Figure 1.4 are taken in BF (Bright Field) mode, at an electron beam voltage of 300 kV and the magnification levels are 115000x and 230000x. Images obtained by TEM are used for observation, checking the monomer size within aggregates and checking the tomography post-processing threshold values as will be explained in Section 1.6.2.

1.4 Methods to process electron microscopy recordings

Below are given the main highlights of the tools and methods used for tomography. Evaluation of the mathematical algorithms on the 3D geometry reconstruction techniques being out of the scope of this study, information is given on the used methods, options and parameters with justification based on literature survey. Nonetheless the test cases and discussions of the options is given in Section 1.6. The consequent application and analysis on soot are presented in Section 1.7.

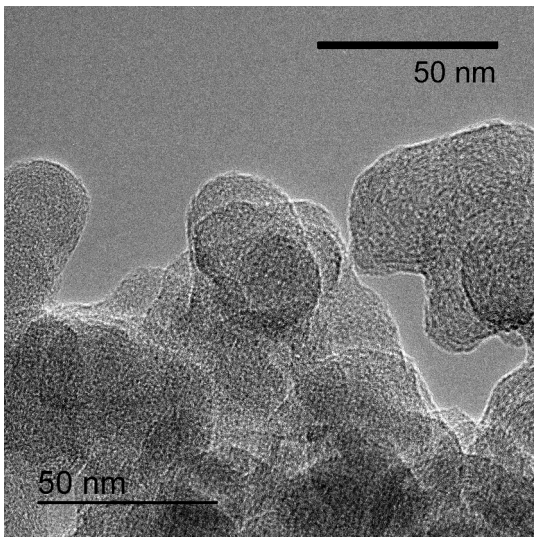

(a)

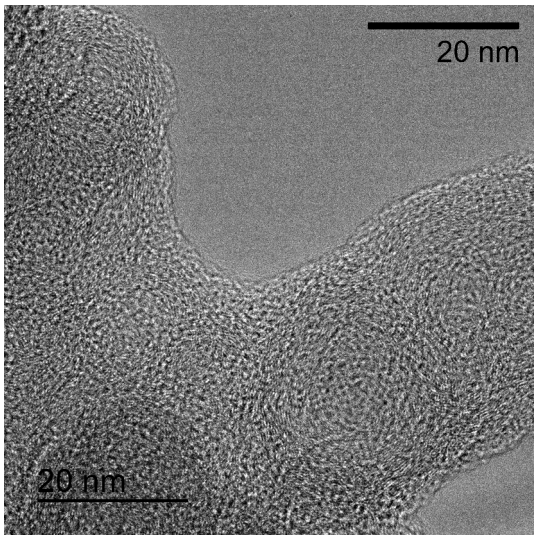

(b)

Figure 1.4: *TEM images of monomers of soot collected at midflame at magnification levels of (a) 115000x and (b) 230000x.*

1.4.1 Pre-processing and image treatment

High contrast and high resolution SEM images similar to the one of Figure 1.8(a) are contrast inverted to obtain the tomograms as presented in Figures 1.2 and 1.3. Before applying the tomography reconstruction, the tomograms obtained are pre-processed for noise reduction and grey scale adjustment. Those image treatments are accomplished using ImageJ which is a commonly used

software to process microscopy images (Abramoff et al. (2004), Collins et al. (2007)).

1.4.2 Tomography reconstruction

TomoJ, an extension of ImageJ, is used for the reconstruction of the 3D geometry using SEM tomograms. The reconstruction algorithms in TomoJ are equivalent to those in IMOD (Messaoudi et al. (2007)) noting that IMOD has been used for SEM tomography in the work of Lück et al. (2010). In order to locate the correct rotational axis in every image, automatic translational alignment of the tilt series is performed in TomoJ. The tomograms are reconstructed by SIRT (simultaneous iterative reconstruction technique) and ART (algebraic reconstruction techniques) algorithms due to their greater accuracy as cited by Messaoudi et al. (2007). The reconstructed 3D geometry is exported as MRC data to post-process the volume data.

1.4.3 Post-processing

UCSF Chimera, originally developed for molecular graphics, is used for the visualization of reconstructed 3D geometry. The Volume Viewer extension of UCSF Chimera enables the visualization of 3D data in MRC data format (Pettersen et al. (2004)) obtained from the tomography by electron microscopy. The interactive interface enables different treatments of 3D volume data such as signal thresholding and refinement of surface meshing. It also enables the exportation of the surface data for further analysis such as volume discretization, which will be performed in our follow-up work on fractal analysis in Chapter 2 and on soot-radiation interaction in Chapter 4.

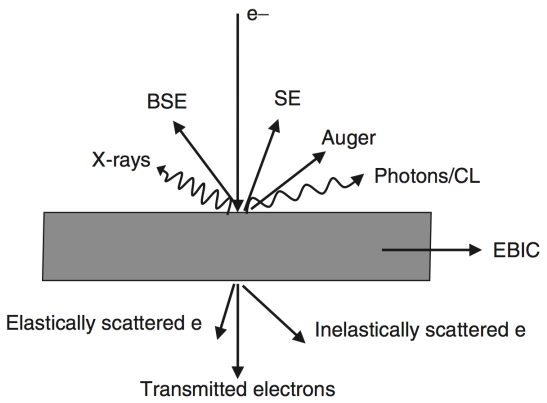

Figure 1.5: *Specimen interaction under the electron beam. EBIC stands for the electron beam interaction current, illustration from Bell and Erdman (2012).*

1.5 SEM tomography

1.5.1 Imaging in electron microscopy

Various signals are produced from the interaction of a specimen with the incident electron beam in the electron microscope, including the SE (Secondary Electrons), BSE (Backscattered Electrons) and transmitted electrons as illustrated in Figure 1.5. Imaging is realized using a combination of the detected electrons and the current produced on the sample by the electron beam.

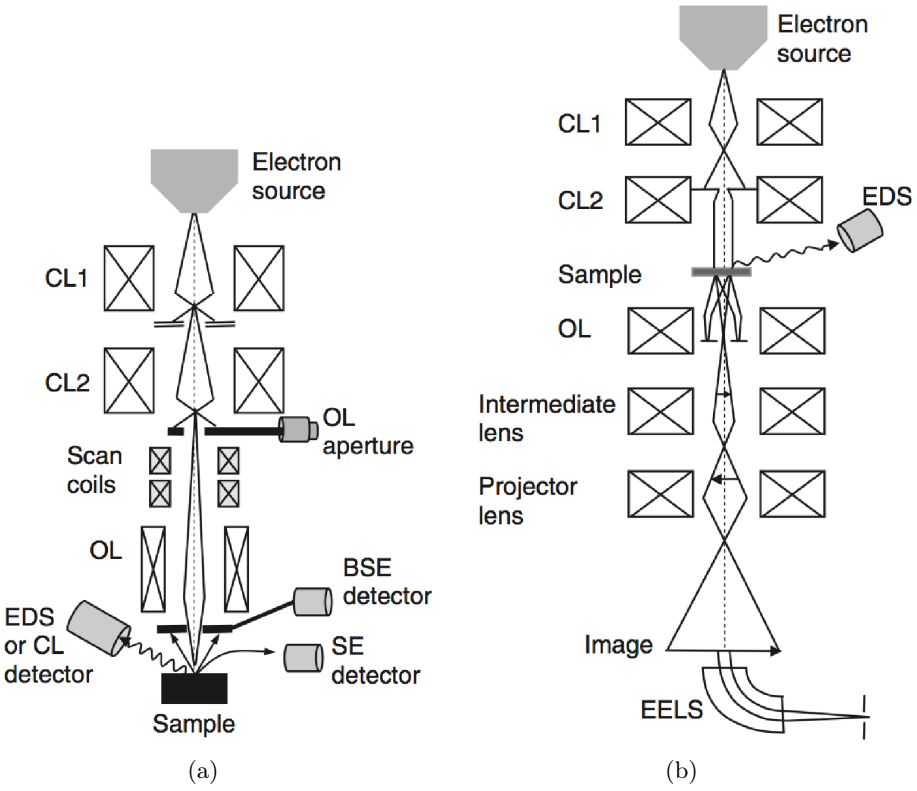

Figure 1.6: *Illustration of (a) SEM and (b) TEM cross sections, from Bell and Erdman (2012).*

If the specimen is thin enough, i.e. around hundred nanometers, it is possible to obtain projection images under TEM microscope basically using the signals of the transmitted electrons. In SEM, there are various detectors equipped to receive different combination of signals as can be seen in Figure 1.6. Conventional SEM detectors, except with STEM (Scanning Transmission) detector, do not provide real projections of the object as would be given by a transmitted signal because they use a secondary electron signal that depends on topography details.

In recent SEM equipments, the in-lens TLD detector is located inside the electron column of the microscope and is arranged rotationally symmetric around the optical axis. The SE electrons are collected with high efficiency and at the very top of the sample. Therefore the electron collection is symmetrical and the object details are equally visible with minimum distortion and minimum shadowing. Images with high contrast can be obtained at low voltages and at small working distances. Resulting recordings can be treated as projection images.

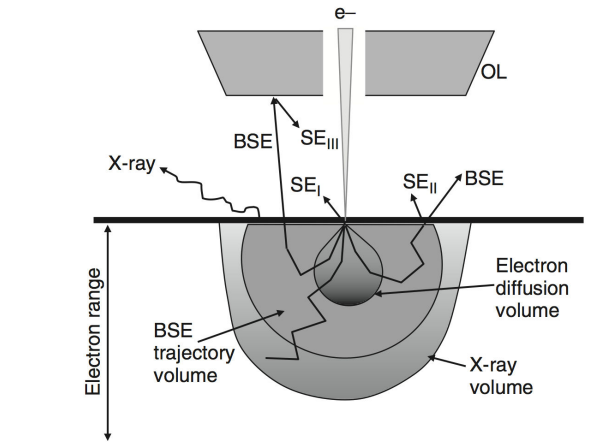

(a)

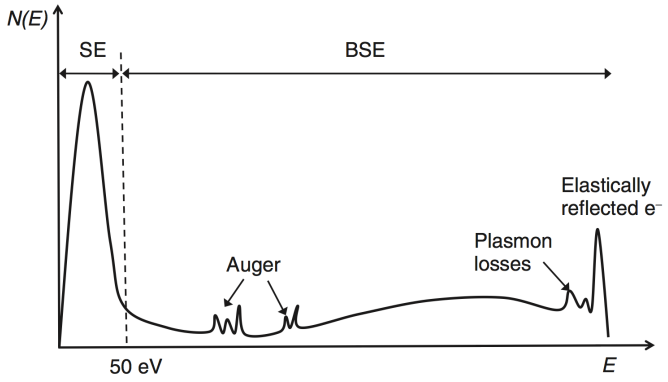

(b)

Figure 1.7: *(a) Electron beam excitation volume (d) Number of electrons escaped from the interaction volume versus their energy and type. Images are from Bell and Erdman (2012).*

As illustrated in Figure 1.7(a), a portion of SE signals are generated from BSE interaction inside the material volume. Also, even though a magnetic field filtering in TLD is applied to detect only SE, a portion of the BSE is collected at the transition energy range between SE and BSE as depicted in Figure 1.7(b).

Hence our SEM images can include two types informations: surface (SE I) and volume (SE II, SE III and BSE).

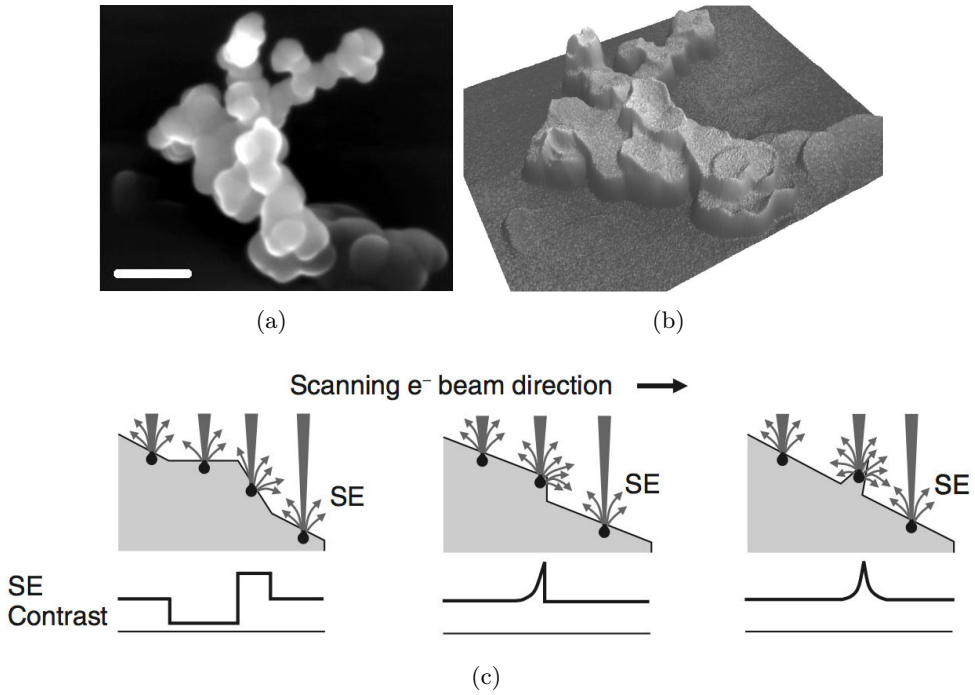

Figure 1.8: *(a) SE (Secondary Electron) image of propane soot aggregate **S1** obtained from TLD (Through-the-Lens Detector) in SEM. Scale bar corresponds to* 100 *nm. (b) Topography with artifacts, reconstructed from grayscale signal levels of 2D SEM image. (c) Illustration of the electron beam interaction volume in SEM with samples having a convex surface and a sharp edge, from Bell and Erdman (2012).*

A conventional way to obtain 3D information from SEM images is to interpret gray scale signals, in combination with SE (secondary electron) stereo pairs or four quadrant BSE (back scattered electron) images to reconstruct the surface topography. One preliminary attempt is made to obtain a morphology based on the interpretation of the gray scale levels as presented in image in Figure 1.8(a). When a stereo pair is constructed, it gives information about the profile edges seen from different view angles. Artifacts show up when the surface topography is built as presented in Figure 1.8(b). The edges of the object seem to be bright because there are more secondary electrons escaped on the edges as illustrated in Figure 1.8(c). However there are different ways of interpretation of this information: Hollows can be detected instead of bumps depending on the scanning order of the electron beam as shown in Figure 1.8(c) as the contrast level remains the same. Concave surfaces are obtained in the reconstruction instead of convex surfaces.

The morphology is not correctly detected by surface gray scale interpretation

of images, due to the collection of volume information mentioned before, hence this conventional SEM method to obtain the morphology is eliminated. The source of the volume information is explained in the following section.

1.5.2 Electron beam interaction with specimen

It is indeed difficult to observe perfectly the surface profile of thin samples composed of material with small atomic number. For nano-sized samples, one can see through the material when looking at high resolution 5kV SEM recordings in Figures 1.2 and 1.3 contrary to 1kV SEM images in Figure 1.1. Similar observations are made with SEM images in the literature covering boron nitride (BN) sheets and whiskers. The BN sheets with a total sample thickness of a few hundreds of nanometers are translucid under the SEM beam accelerating voltage between 3 kV and 10 kV, as observed in the SEM images presented in the works of Liu et al. (2014), Miele et al. (2014), Xue et al. (2013).

In fact, for carbon and BN samples, one needs a very low accelerating voltage to obtain good surface image contrast under SEM. The size of the electron beam interaction volume inside the material, illustrated in Figure 1.7(a), increases with increased accelerating voltage and decreases with higher material density and higher atomic number. This is shown for the depth of electron penetration z (μm) in Equation 1.1 and for the width of the excited volume y (μm) in Equation 1.2 given by Severin (2004) (originally by Potts (1987)), where ρ (g/cm^3) is the material density and E_0 (kV) is the incident energy of the electron beam.

$$z \approx 0.1 \left(\frac{E_0^{1.5}}{\rho} \right) \tag{1.1}$$

$$y \approx 0.077 \left(\frac{E_0^{1.5}}{\rho} \right) \tag{1.2}$$

In thin and low-density samples, the electron beam interaction volume becomes comparable to the sample size. As a result, small samples tend to show transparency at some range of accelerating voltage (5 kV to 10 kV in our case). Noting that soot material properties are close to density and atomic number of elements composing BN and that the electrical conductivity is similar (because BN is isoelectronic to carbon), it is concluded that the transparency in SEM images of both materials are due to the same phenomenon. Soot has a density of around 1.5 g/cm^3 as an average soot material density value presented in the work of Slowik et al. (2004) studying the propane combustion soot mass and fractal properties, the same average value is given by Horvath (1993). This value is lower than the average density of BN. Therefore a higher penetration depth and a higher transparency are expected for electrons incident on

our propane soot samples, compared to BN sheet images, which explains the transmission-like effect obtained in SEM images of Figures 1.2 and 1.3.

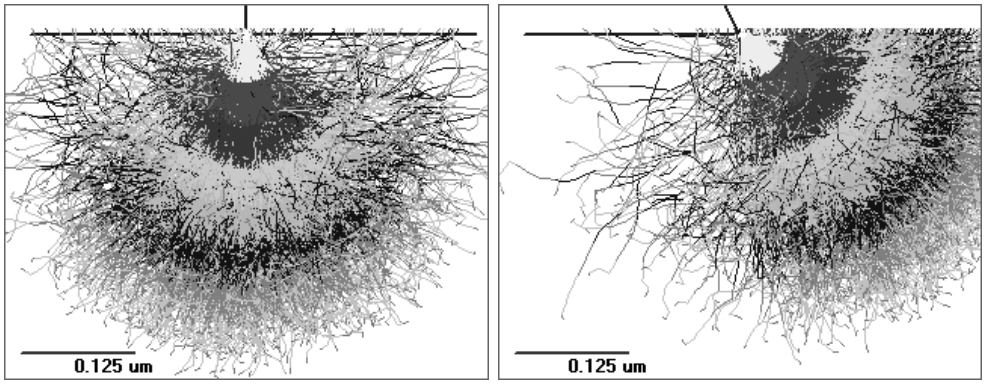

(a) (b)

Figure 1.9: *Monte Carlo simulation results for electron interaction volume in black carbon material (a) for normal incidence and (b) for* 50° *inclined incidence at 5 kV beam accelerating voltage for a bulk carbon sample with 500 nm thickness. Scale bars correspond to 0.125 microns.*

The depth and the width of the interaction volume of the electron beam inside the material can be estimated by empirical correlations of Equations 1.1 and 1.2, or by Monte Carlo (MC) simulations. In our study the beam acceleration voltage is chosen as 5 kV because at higher voltages samples were either charged and polluted very rapidly, exploded or not visible. The empirical law given by Potts (1987) estimate the electron penetration depth at around 560 nm and the width of the interaction area at around 430 nm based on an accelerating voltage of 5 kV and on a density of 2.0 g/cm^3 referring to the value given by Slowik et al. (2004) for the density of black carbon.

The empirical results given above are consistent with the MC simulations for the computation of the electron interaction volume inside a carbon bulk sample. According to the MC tool proposed by Joy (1995), the interaction volume between a carbon bulk sample and the incident electron beam of 5 kV is around 400 nm, as shown in Figure 1.9 both at non-tilted and at maximum tilt angle 50° of the sample. We indeed do not see beyond this depth of around 500 nm if looked in the images presented in Figures 1.2 and 1.8. It is therefore concluded that the whole volume of a soot aggregate interacts with the high energy part of the scattered 5 kV beam and consequently that the SEM images have a transparency artifact that will be used as an advantage for tomography reconstruction. Also, as mentioned in the previous section, the TLD detector captures the information issued from the volume and not only from the surface, by detecting a noise due to a tail of BS electrons yielding volume and chemical

information at an accelerating voltage of 5 kV. As a result, the detected signals forming SEM images contain not only surface and contour information but also material thickness data. Finally, we use these artifacts mentioned above in SEM images to treat as projection images and to build up tomograms in order to mimic transmission signals. In the next section, test cases are presented to validate the tomography procedure using SEM images.

1.6 Test cases for tomography

To test the tomography tools, virtual spheres are generated by the reconstruction of virtual projection images. A spherical object is chosen as a test case because our soot aggregates are composed of nearly spherical monomers hence show spherical convex surfaces.

The method for testing the tomography procedure via a virtual object is mentioned in the study of Alpers et al. (2013) on the reconstruction of nanowire geometries. Alpers et al. (2013) tested their reconstruction on phantoms, i.e. simulated objects, by comparing the reconstructed sectional images to test different tomography algorithms.

In our work the comparison is made between the theoretical surface and volume data and the reconstructed 3D data of the virtual object as we are interested in that type of information for future fractal aggregate analysis. The SIRT algorithm is chosen as reconstruction option, and 100 iterations are performed as recommended when using TomoJ and as more than 50 are proposed in SIRT for noisy data of small number of images in the work of Alpers et al. (2013).

1.6.1 Test case for the number of images in the tomogram

A virtual sphere object **VS1** is artificially generated as in Figure 1.10(a) in binary mode. The aim is to compare the theoretical sphere volume and surface to the ones obtained after tomography reconstruction. The length to pixel ratio, l/δ $(nm/pixels)$, is equal to 1.0 which is equivalent to our high resolution SEM images of Figures 1.2 and 1.3. The sphere diameter pixels correspond to 100 nm because the actual soot sample material thickness reaches a hundred of nanometers at its maximum. A small number of projection images is used in each tomogram in order to test noise level produced due to possible lack of information and also due to the usage of SEM images.

The tomography reconstruction **VS1t1** (Figure 1.10(b)) is obtained by using an image stack from -80° to 80° with 10° increments. The tomography reconstruction **VS1t2** (Figure 1.10(c)) is obtained by using an image stack from -50° to 50° with 10° increments. As can be seen in Figure 1.10(b), perfect spherical geometry is obtained for **VS1t1**. The reconstructed surface becomes

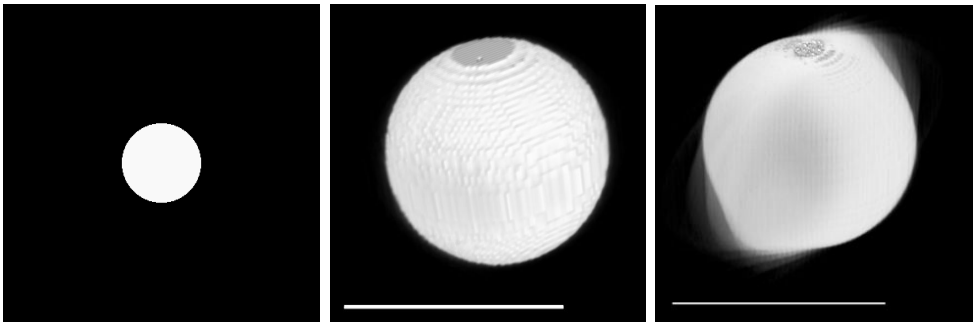

(a) **VS1** (b) **VS1t1** (c) **VS1t2**

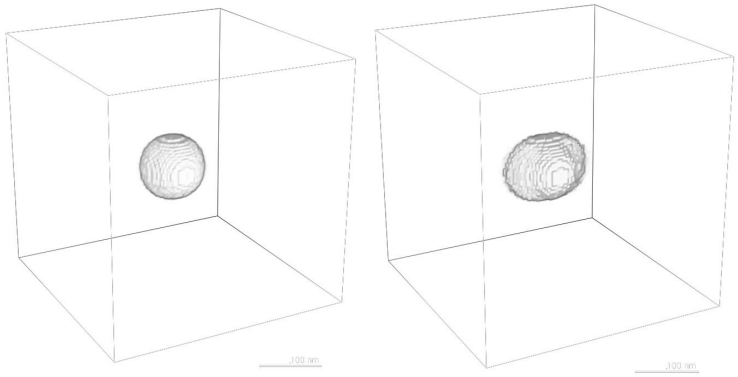

(d) **VS1t1** (e) **VS1t2**

Figure 1.10: *(a)* ***VS1****: 2D image of the virtual sphere (d = 100 nm) used as projection image for test tomograms; (b)* ***VS1t1****: Tomography reconstruction with 17 images for ±80°; (c)* ***VS1t2*** *Tomography reconstruction with 11 images for ±50°. The reconstruction volumes are presented in (d) and (e). Scale bars correspond to 100 nm.*

noisy when the span angle is decreased from 160° to 100° for **VS1t1** in Figure 1.10(c).

1.6.2 Test case for the effect of secondary electrons on the edges

Another test case is established on a second virtual sphere in order to simulate imaging conditions closer to our SEM recordings. To test the effect of the secondary electron (SE) signal intensified on the geometry edges as seen in Figure 1.8, the second virtual sphere **VS2** with edge defects (Figure 1.11(a)) is artificially generated with brighter edges in gray scale mode. The resolution is again $l/\delta = 1.0$. As we are limited to a span of 100° in our SEM recordings, **VS2** is tested with a stack ranging from -50° to 50° with 10° increments.

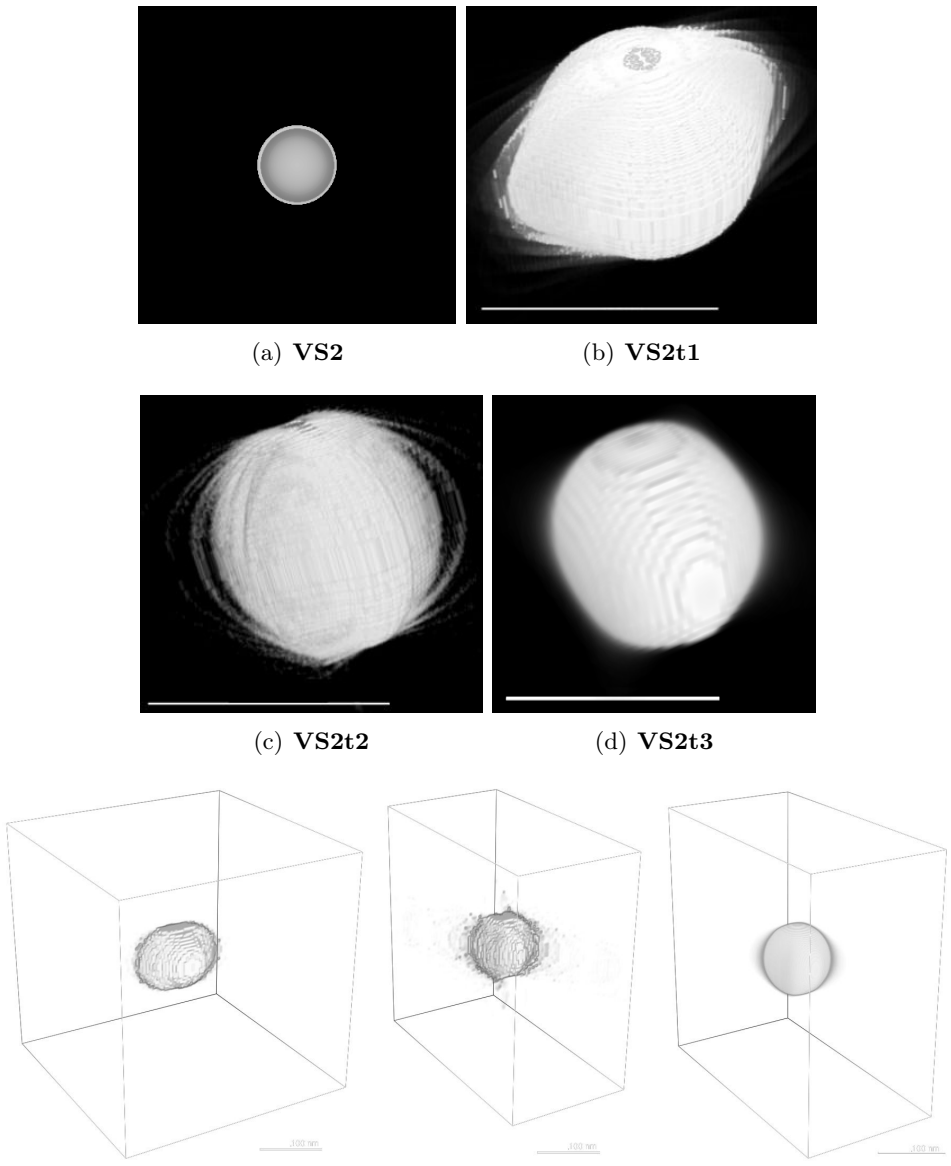

(a) **VS2** (b) **VS2t1**

(c) **VS2t2** (d) **VS2t3**

(e) **VS2t1** (f) **VS2t2** (g) **VS2t3**

Figure 1.11: *(a)* ***VS2****: 2D image of the virtual sphere (d =* 100*nm) with edge artifact; (b)* ***VS2t1****: Tomography reconstruction with 11 images for* $\pm 50°$*; (c)* ***VS2t2****: Elongation correction applied on the reconstruction VS2t1; (d)* ***VS2t3****: Filtering the tomography signals of VS2t2. The reconstruction volumes are presented in (e), (f) and (g). Scale bars correspond to* 100 *nm.*

It is observed that the tomography reconstruction **VS2t1** provides more noisy surface information due to the edge artifact (Figure 1.11(b)). As demonstrated in the previous test case **VS1t2** and as known from the literature, reconstruc-

tion with missing projection images produces an elongated geometry in the direction perpendicular to the reconstruction axis (Alpers et al. (2013), and references therein). Therefore an elongation correction is applied on **VS2t1** using TomoJ. The resulting geometry **VS2t2** is illustrated in Figure 1.11(c).

After the 3D reconstruction, the tomography signals obtained are as plotted in Figure 1.12. Here $i = 1$ is the ultimately chosen threshold value. Surface and volume graphs are brought to the same scale for a better observation of their variations as a function of threshold i. The values are normalized, i.e. divided by the volume and surface data of the selected threshold level $i = 1$. If V_0 and S_0 are the original volume and surface data then the normalized values are respectively $V = V_0/V_{0(i=1)}$ and $S = S_0/S_{0(i=1)}$.

The interactive visualization of the 3D geometry suggested that the acceptable range of the thresholding is between $0.95 < i < 1.03$ presented in Fig. 9. In this range, the minimum variation point in V and S indicates the optimum signal level for tomography object (Adachi et al. (2007)). As can be seen in Figure 1.12 the points corresponding to $i = 1$ present the minima compared to their neighboring data. After this thresholding process of **VS2t2**, the volume information is correctly obtained with 0.6% error while the surface information has 7% error due to the reconstruction noise. Values are presented in Table 1.1.

The 3D information is still noisy after the correction due to the bright edge artifact. We can decrease this noise by filtering the tomography signals in Chimera Volume Viewer. A Gaussian filter is applied on the reconstruction signals and **VS2t3** is obtained with a smooth geometry as illustrated in Figure 1.11(d). As listed in Table 1.1, the volume and the surface area of **VS2t3** is found with 0.5 % and 1.2 % errors respectively compared to the theoretical values. This proves the suitability methodology used during the 3D reconstruction.

Object	V (nm^3)	S (nm^2)	$Error_V$	$Error_S$
Theoretical	$5.236\ 10^5$	$3.142\ 10^4$	–	–
VS2t2	$5.201\ 10^5$	$3.373\ 10^4$	0.6 %	7.3 %
VS2t3	$5.216\ 10^5$	$3.102\ 10^4$	0.4 %	1.3 %

Table 1.1: *Theoretical volume and surface data compared to the reconstructed tomograhy objects (**VS2t2**) and after (**VS2t3**) noise filtering.*

We can reach high accuracy on a theoretical virtual object with signal corrections and filtering. Though we do not know a priori the noise level that can occur in the reconstruction of 3D soot. Hence we consider that the test case closest to our tomogram conditions is **VS2t2**. This includes small number of images, the bright edge artifacts and no signal filtering. In the following application, it is assumed that one has the same degree of error on the volume and

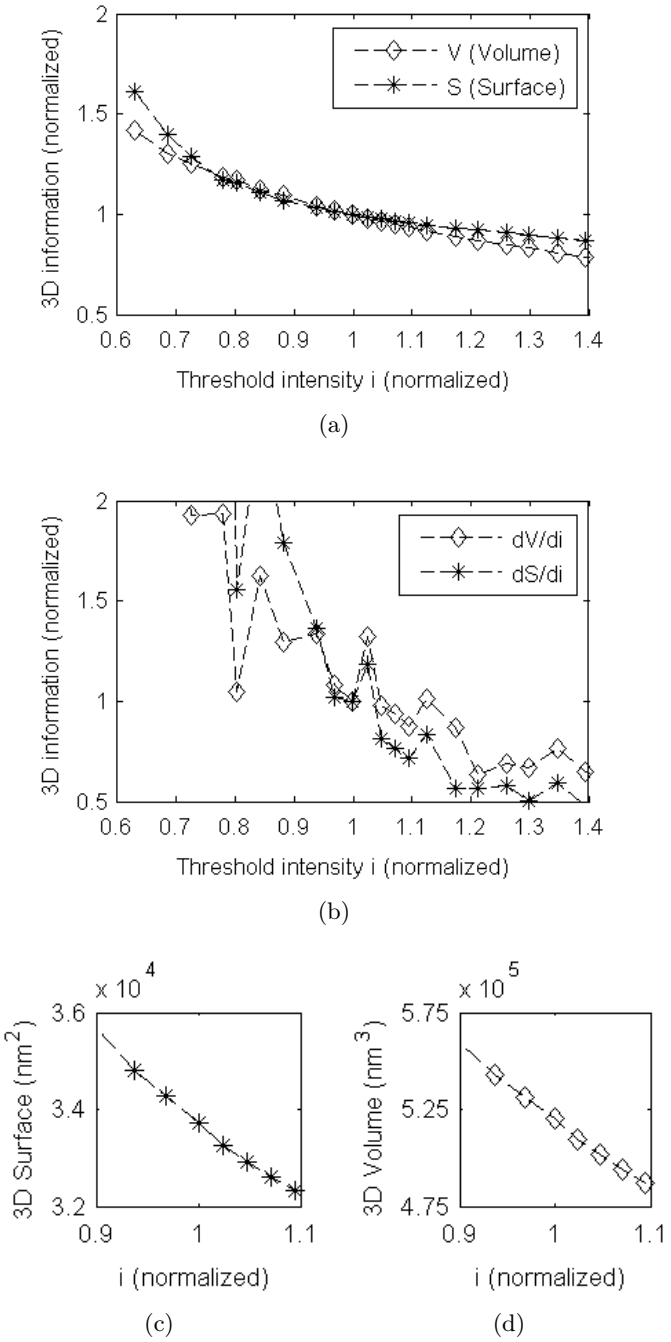

Figure 1.12: *Thresholding of 3D volume data: Surface area and volume data versus signal threshold for* ***VS2t2*** *reconstruction.*

surface data obtained from 3D reconstructions of soot, knowing that the same techniques are used as in **VS2t2**.

1.7 Soot in 2D and 3D

1.7.1 2D observations of soot aggregates and monomers

A visual study is made on the SEM images of Figure 1.1. This allowed us to verify two aspects of our study: the sampling procedure and the benchmarking of the reconstructed geometry in terms of thresholding.

First, a visual comparison is made with the work of Onischuk et al. (2003) which is also on soot issued from propane/air combustion. As expected, the sample collected at midheight of the flame (Figure 1.1(b)) is more compact than the one collected at the root of the flame (Figure 1.1(a)). The sample collected at the top in the afterflame zone is more chain-like and composed of smaller monomers (Figure 1.1(d)). Again as expected, the concentration at midheight of the flame is greater than at the afterflame zone as shown in Figures 1.1(c) and 1.1(e). This geometry and size of the aggregates and the evolution of the aggregation through the height of flame matches the tendency shown in the TEM micrographs of propane/air soot given by Onischuk et al. (2003). This similarity indicates the suitability of the simplified sampling procedure used in this study. The samples collected are representative of the flame combustion soot.

Second, an observation is made under TEM to see more precisely the monomer size and the shape of the aggregates. Soot deposited on TEM grid by the methods explained in the previous section is presented in Figure 1.4. According to the TEM recordings the mean monomer size is around 27 nm. This is in agreement with the recordings of soot deposited on TEM immediately after propane/air combustion (Brugière et al. (2014)). The monomer information obtained is important during the tomography reconstruction: SEM tomograms are created from a combination of secondary and backscattered electrons information and not from real projection images. SEM images are therefore validated with the mean monomer size observed in TEM recordings against the artifacts possibly generated by secondary electron signal. Monomer size is also used for the thresholding of the tomography signal after 3D reconstruction.

1.7.2 Soot in 3D

The tomograms of samples **S1** and **S2**, presented in Figures 1.2 and 1.3, are pre-processed in ImageJ to reduce background noise due to the surface rugosity of the support and to blur the borders to reduce the artifact of bright edges. Different tilt angles provide different amount of escaped electrons on the specimen surface, hence affecting the image contrast. Therefore the images in a tomogram are equalized to the same mean contrast level. Finally, the processed images are reconstructed with the methodology explained in the previous section, using SIRT algorithm with up to 100 iterations in TomoJ.

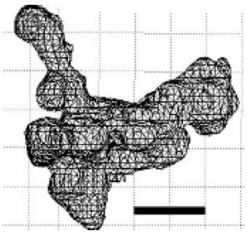

Figure 1.13: *Post-processing: Surface meshing and of the 3D reconstruction of the **S1a** tomogram. Scale bar corresponds to 100 nm.*

Reconstruction of the first tomogram **S1a** of Figure 1.2 allowed us to examine the applicability of the algorithm on small number of recordings with large angular steps to obtain 3D geometry. The complex geometry obtained is presented in Figure 1.13.

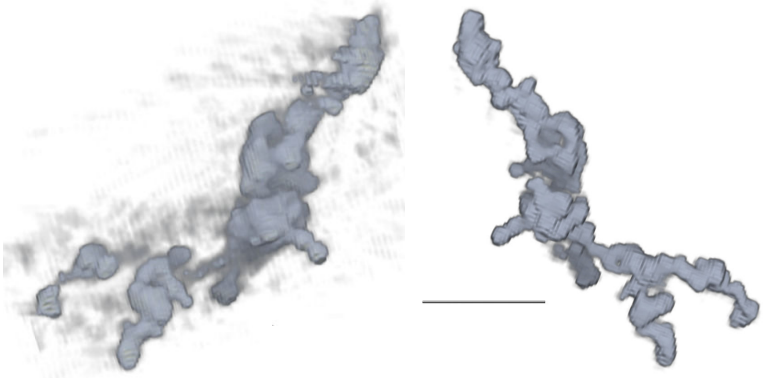

(a) (b)

Figure 1.14: *Reconstructions of the same aggregate rotated around 2 perpendicular axes: (a) a-axis (tomogram **S2a** of Figure 1.3); (b) b-axis (tomogram **S2b** of Figure 1.3). Scale bar correspond to 500 nm.*

The bigger sample **S2** is recorded in dual axis tomograms as previously shown in Figure 1.3. As presented in Figure 1.14, the dual axis tomograms are in good agreement when compared qualitatively for the shape and the size of the aggregate, therefore they verify the reconstruction methodology. The reconstruction obtained from **S2a** (a-axis tomogram) is however very noisy due to the elongated shape of the aggregate. This noise is expected because the apparent thickness of the material is higher when rotated around a-axis. Therefore the second tomogram **S2b** is to be used for further analysis for the determination of the volume and surface thresholding.

The reconstruction obtained from b-axis is presented in Figure 1.15(b). In Figure 1.15(c), it is observed that a high threshold level can underestimate the

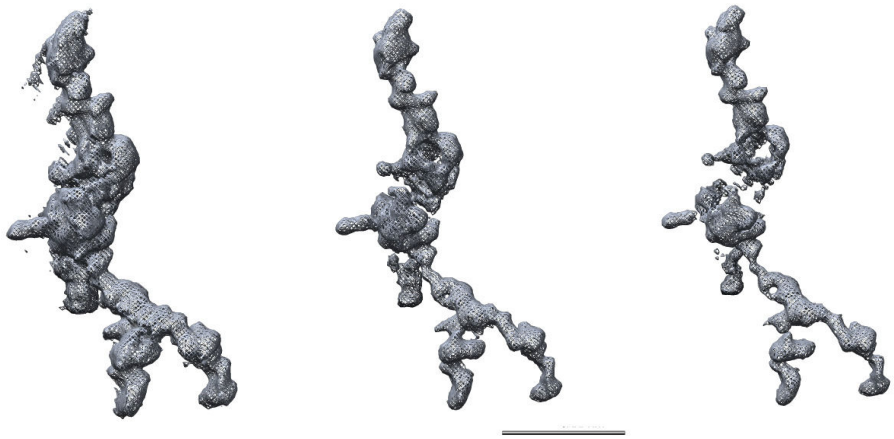

(a) (b) (c)

Figure 1.15: *Visualisation of the impact of the threshold level on the reconstructed geometry of **S2b**: (a) low level; (b) selected value; (c) high level. Scale bar corresponds to 500 nm.*

material volume. In Figure 1.15(a), the reconstruction volume is overestimated because the low signal threshold brings noise to the reconstructed volume. To overcome this problem the method proposed by Adachi et al. (2007) is used in combination with dual axis comparison.

Adachi et al. (2007) propose the visual inspection of noise combined with the plotting of the surface versus signal threshold value graphs. The valid range of the signal threshold value is chosen by visual detection of the reconstructed geometry. Then this threshold value is fine tuned by choosing the minimum value of the change in surface area.

For our tomogram **S2b** the changes in the volume and the surface are plotted against the threshold value in Figure 1.16. The **R(i)** range corresponds to the visually inspected valid threshold values giving a visually acceptable reconstruction as in Figure 1.15(b). This valid range excludes the reconstructions with too much noises (as in Figure 1.15(a)) or with abnormal gaps (as in Figure 1.15(c)). The selected threshold value ($i = 1$) corresponds to the minimum of dS/di and dV/di graphs in the **R(i)** range, noting that the same trend is observed for the virtual sphere in the previous test case presented in Figure 1.12.

Finally, the surface to volume ratio (S/V) of the 3D soot of Figure 1.17(b) is compared to the ones in the literature to check the validity of the physical properties obtained from our tomography reconstruction. Our preliminary results indicate a S/V ratio of $(13.2 \pm 0.8)\ 10^7\ m^{-1}$ for the 3D aggregate; the uncertainty is due to noise in the tomography signal. According to observations done

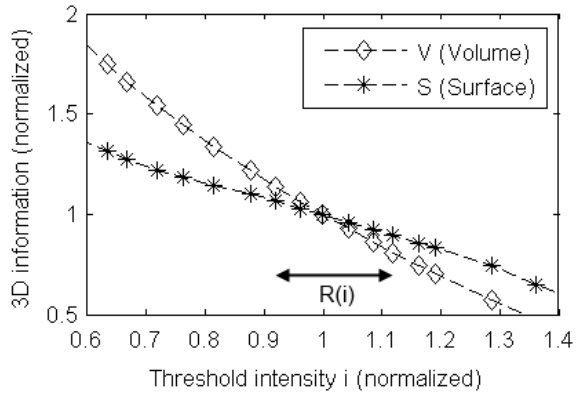

(a)

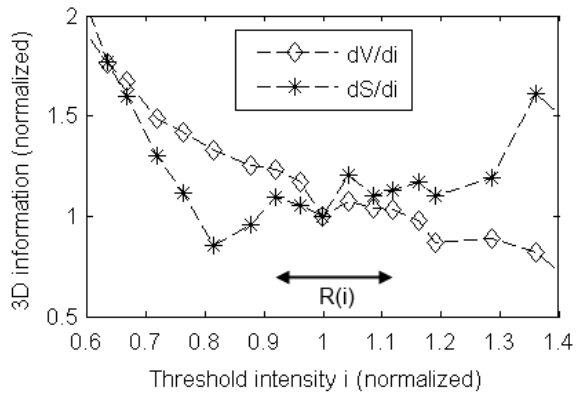

(b)

Figure 1.16: *Thresholding of 3D volume and surface data of **S2b**: (a) surface area and volume versus signal threshold; (b) change in surface area and in volume versus signal threshold.*

by Adachi et al. (2007) and Van Poppel et al. (2005) on Asian dust, diesel and biomass soot, the S/V ratio for such 3D aggregates ranges between 6 10^7 m^{-1} and 29 10^7 m^{-1}. As expected, the S/V ratio of our propane soot aggregate of the same order of magnitude of emitted diesel soot at 13.7 10^7 m^{-1} and 10.8 10^7 m^{-1}.

In the SEM tomography reconstructions on soot above, the aggregate shape is complex but the primary particles have spherical surface therefore the tomography sharp edges are avoided in the images. This limits the image artifacts coming from secondary electron (SE) detection. The absence of sharp edges is also another advantage for reconstruction: a small number of rotated images is sufficient for tomography.

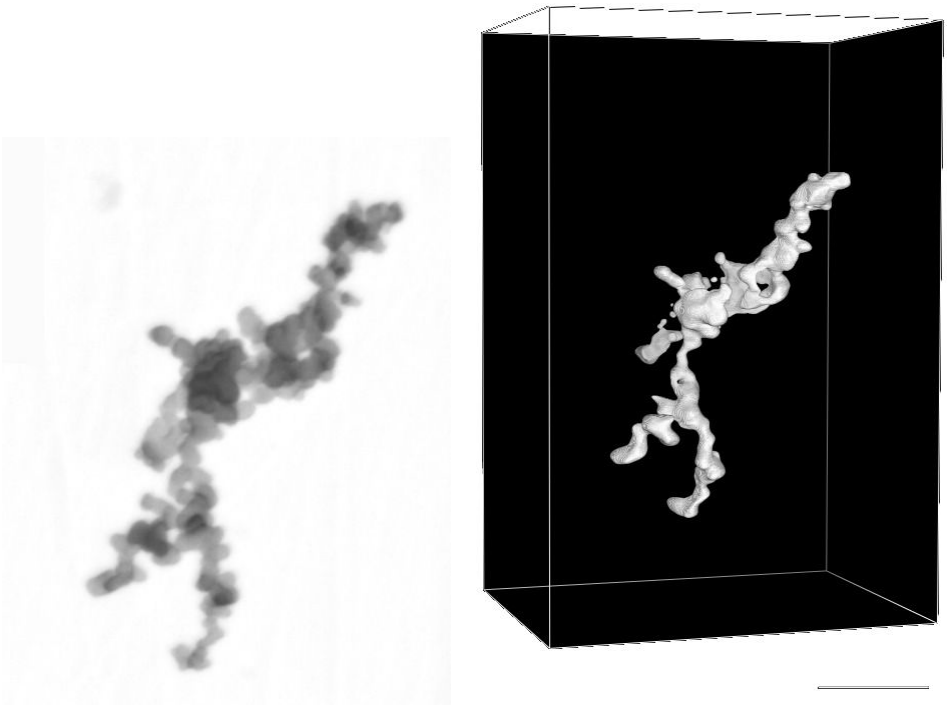

(a) (b)

Figure 1.17: *(a) A SEM recording of propane soot used in 3D reconstruction; the inverted image is processed for contrast adjustment and edge correction to reduce the effect of the SE signal. (b) Reconstructed 3D geometry of the soot aggregate after tomography signal thresholding and filtering.*

1.8 Conclusion and perspectives on microscopy studies

To conclude, it is believed that this technique works for our soot samples because of different reasons mentioned in the test cases of SEM tomography. Soot is mainly composed of carbon, a low-density material with small atomic number. Also the aggregates are not dense and are highly fragmented, therefore the sample is thin as tens of nanometers even though the aggregate length can reach micron size. This is an advantage for the electron penetration depth because the complete volume of the aggregate interacts under the high energy part of electron beam and thus provides transmission-like images.

In this chapter we proposed a simplified methodology to obtain complex soot aggregate shape in 3D by applying SEM tomography, a technique applied for the first time on soot issued directly from a combustion flame. The validity of tomography reconstruction of SEM recordings is justified by usage of vir-

tual objects. The tested methodology is then applied to the tomography of a propane combustion issued soot aggregate. The geometries obtained from dual axis tomograms comply with each other. The material volume information is obtained correctly. The precision of the surface area information is around 7 % due to the noise in the tomography reconstruction.

The technique proposed is less time consuming for microscopy and easier to handle with SEM equipment compared to TEM. The sampling procedure is easy and less expensive in terms of support material. The imaging procedure can be applied not only to flame soot but also to the deposited soot on walls unless the soot morphology is highly porous.

For further benchmarking of the microscopy techniques, TEM and SEM tomograms could be compared if soot is collected on TEM grids and if there is no charging issue on TEM grid samples under SEM. This technique could be applied to soot aggregates issued from the flames of different fuel types for subsequent comparison of fractal parameters and fractal analysis techniques. In the future, a chemical composition mapping can be done under TEM for a better definition of the optical properties of aggregates.

If the samples are badly conducting then a conductive thin film would be needed. This will lead to a revision of the thresholding methodology of the tomography signal.

One drawback can be the loss of information on surface details if the tomogram signals are too noisy. If one wants to decrease the uncertainty/error level on the surface area of 3D data, the reconstruction should be improved by constructing a microscopy support setup that would allow to cover a larger tilt angle range up to 120° or more. A simultaneous dual-axis reconstruction can also be considered in order to improve the quality of the 3D tomography information.

Further investigations, like the impact of the cooling rate caused by the usage of metal plates, or the ageing due to storage in ambient air between sampling and observation, restructuring of the sample under high voltage beam, can be studied in future works on sampling and storage protocols.

2D and 3D soot information obtained from microsopy studies are analysed in the next chapter to derive fractal properties and compare them with the literature information on soot and its morphology. Those results will be further used in Chapter 4 where the radiative properties of tomography soot are compared to the ones of virtual numerically generated aggregates.

Chapter 2

Fractal analysis and numerical generation

Soot aggregates are referred to in literature as fractal objects. A complete 3D definition of soot was not possible with high precision until recent developments in measurement equipment and imaging devices. Hence various in-situ and ex-situ techniques are established using the fractal definition combined with empirical formulations relating the morphology, mass, mobility to the fractal parameters. The aim of the work presented in this chapter is to propose a fractal analysis methodology not only relying on empirical formulae but using 3D geometry of soot obtained from tomography. First, soot formation is summarized with an overview of the soot structure at different observation scales. Here, the common fractal parameters are cited from researchers working on soot aggregates from different sources in order to understand the weaknesses and the uncertainties arising from empirical relations and numerical aggregate generations. Second, the fractal theory is reviewed with numerical aggregate generation algorithms. Finally 2D and 3D analyses are done on soot observations. For the validation of 3D methods, the numerically generated aggregates are analyzed for their fractal properties by 3D cube counting method. After this validation, the fractal analysis methodology is implemented to 3D soot obtained from tomography. Regarding the 3D analysis, it is concluded that the soot can be indeed considered as a fractal object at micron level even though the appearance of this fractal behavior is less clear at smaller scales. Nonetheless, the relationship between 2D and 3D fractal parameters will remain uncertain until an extensive 2D-3D comparative study is applied on numerous real 3D aggregate samples. Furthermore, as a perspective, soot morphology at nano scale can be studied to see its effect on the optical properties coupled to micro scale morphology.

2.1 Soot as mass fractals

Soot formation is a complex phenomenon combining chemical reactions dependent on physical conditions. There are many parameters affecting the process such as the temperature, fuel, stoichiometry, velocity. Researchers focus on different aspects of the unknowns. On one hand, efforts are given to explain the chemistry behind the formation which determines the flame structure. On the other hand, the physical parameters of particulate media, such as the mobility and the optical properties, are examined for radiation analysis and material characterization.

Soot structure and size can vary depending on the flame conditions and the reaction time. The formation starts from molecular level forming spherical particles with a diameter of few tens of nanometer. If the flame is highly sooty, those particles can stick together to form aggregates reaching micron size. Those formation steps are reviewed in the following sub-sections.

As far as the radiative heat transfer is concerned, the main parameter affecting the radiative properties of soot is its micro scale properties, i.e. its aggregation pattern and the size of the particles forming the aggregate. Only at that size level the complex material-light interaction becomes important, as will be detailed in the Part II on radiative properties. Soot precursors and primary particles are considered to be too small for such consideration.

Nonetheless, the nano scale structuring of soot affects conceivably the radiative properties through the modification of the atomistic structuring hence the optical properties. At present, researchers try to explain soot history by observing its nano structure as will be mentioned in Section 2.1.2.

The final aim of our work is to observe the complex material-light interaction on soot issued from the combustion of hydrocarbons. Here, the emphasis is given on fractal-like soot. Hence, throughout this Section 2.1, soot morphology and its fractal descriptors are explained with a brief reminder on soot formation and on the fractal theory.

2.1.1 Soot formation

In ideal conditions of gaseous hydrocarbon combustion with enough oxidant, the final output of the chemical reactions is supposed to give only carbon dioxide and water with maximum heat release. However in realistic conditions and flame dynamics, the excess fuel or the lack of oxydant leads to incomplete combustion products such as carbon monoxide, hydrocarbon products as PAH (polycyclic aromatic hydrocarbons) and soot (Bockhorn (1994)). Soot is

mainly composed of black carbon and can contain some gaseous components and condensed matter on its surface.

The formation of soot can be considered in four general processes (Bockhorn (1994) and Frenklach (2002)), related to the creation of both gaseous and of solid phases as illustrated in Figure 2.1(a):

- formation of precursors, the molecular and gaseous phase,
- nucleation, transition to solid phase (inception),
- surface reactions leading to growth (and to oxidation),
- coagulation and agglomeration

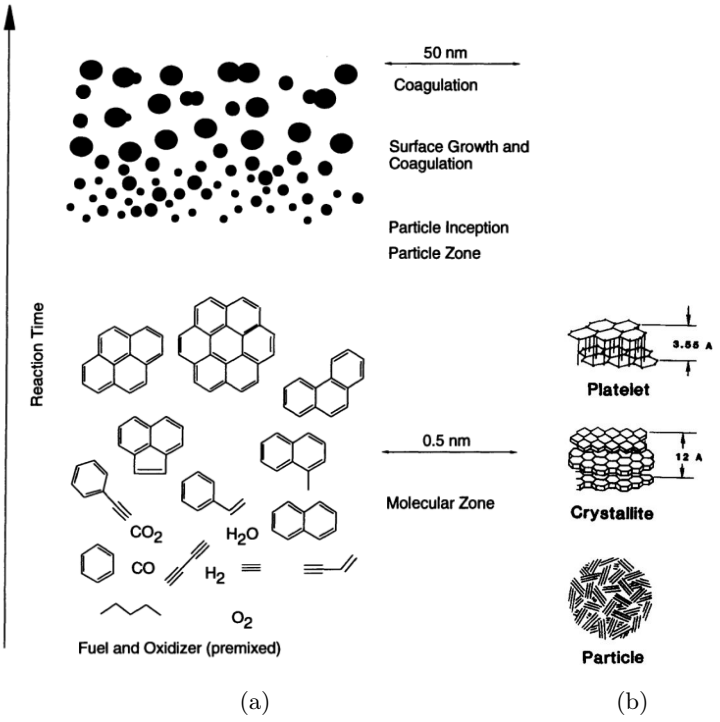

Figure 2.1: *(a) Soot formation in premixed flames, illustration from Bockhorn (1994). (b) The nanostructure of soot illustrated by Smith (1981).*

Soot formation at gaseous phase is related to the detailed chemical reactions which determines the flame structure. The gaseous phase molecules are formed from the dissociation of the input fuel molecules in the form of C_3H_3, C_2H_2, etc. At the molecular level, PAH (Polycyclic Aromatic Hydrocarbons) are known as soot formation precursors. The most widely accepted and used method for PAH formation and soot inception is HACA (Hydrogen abstraction-C_2H_2 acetylene addition (Frenklach et al. (1985), Frenklach and Wang (1991)). The chemical

path is illustrated in Figures 2.2 and 2.3. This is the most commonly accepted route to soot inception, even though other schemes are proposed in the works of Castaldi et al. (1996), Melius et al. (1996), claiming that that this HACA mechanism cannot yield the very high PAH concentrations observed in flames. The molecular phase is further reviewed in the works of Richter and Howard (2000), Frenklach (2002), Miller et al. (2005), McEnally et al. (2006).

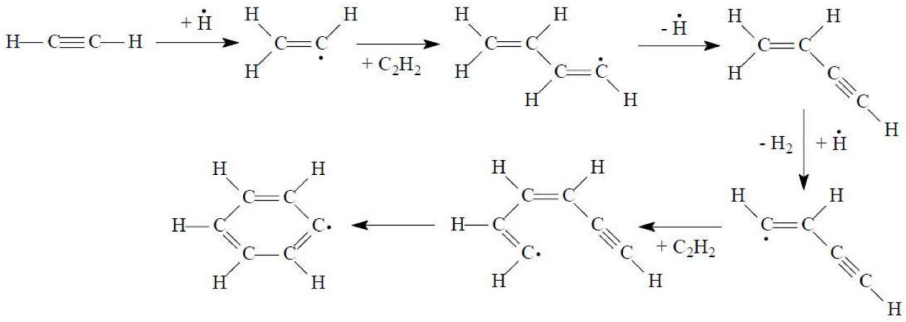

Figure 2.2: *HACA mechanism for the formation of phenyl as a first aromatic ring, illustration retrieved from Caumont-Prim (2013), originally based on the works of Frenklach et al. (1985).*

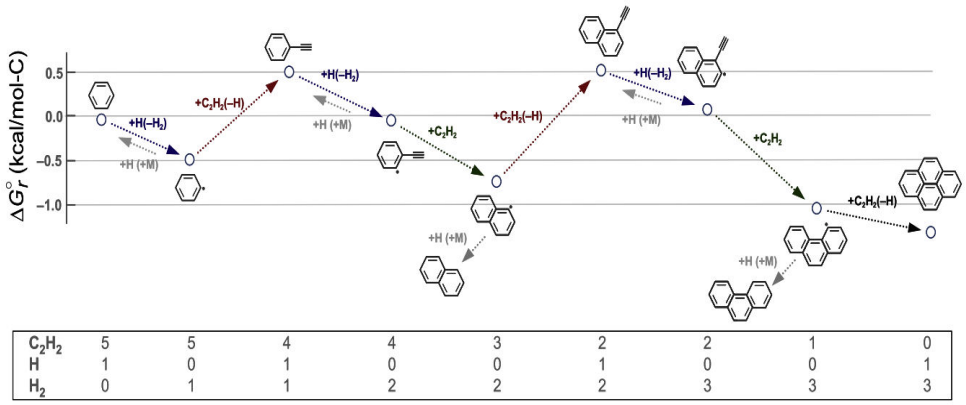

Figure 2.3: *HACA mechanism as an example of formation of larger aromatic rings from phenyl for benzene at 1800K according to the illustration from Wang (2011).*

The resulting aromatic rings in the gaseous phase grow up to form the solid phase particles. The soot inception is also called particle nucleation. This stage leads to solid nano particles of size small down to 1.5 nm (Frenklach et al. (1985)). Discussions about different nucleation mechanisms can be found in the work of Wang (2011) .

The small solid soot particles grow by consuming combustion product molecules such as PAH, acetylene, benzene, in the form of surface chemical reactions and physical coagulations. This surface growth is the main phenomenon determining the mass of soot (Haynes and Wagner (1982), Bockhorn (1994)).

In addition to the surface reactions, the solid particles resulting from inception coagulate and coalesce to form new larger spherical particles. When the soot is aged, i.e. particles reaching a certain size, those particles collide and stick with each other to form more complex shapes. And they agglomerate to form soot as fractal-like aggregates.

In the solid phase, soot constitute a particulate media suspended in the surrounding gas and follow a stochastic motion following the gas movement. The flow regime of the gas around the particle is determined by its Knudsen number Kn given in Equation 2.1 (DeCarlo et al. (2004), Baron and Willeke (2001)).

$$Kn = \left(\frac{\lambda_g}{r_p}\right) = \left(\frac{\lambda_0}{r_p}\right)\left(\frac{101.3}{P}\right)\left(\frac{T}{293.15}\right)\left(\frac{1+110/293.15}{1+110/T}\right) \tag{2.1}$$

In the above equation, λ_g [nm] is the mean free path of the gas molecules, r_p [nm] is the radius of the particle (or the mobility radius R_m of the aggregate), T [K] is the temperature, P [kPa] is the pressure, λ_0 [nm] is the mean free path of air at room temperature and 1 atm pressure conditions which is around 68 nm according to Jennings (1988).

The limit $Kn \ll 1$ corresponds to the continuum regime where the gas surrounding the particle is considered as a continous fluid. The limit $Kn \gg 1$ corresponds to the free molecular regime. For an intermediate range of $0.1 < Kn < 10$, the particles are at the transition regime of the flow (Sorensen (2011)): soot particles and aggregates are mostly formed in this range considering the mobility radius R_m of aggregates in the range of few hundreds of nanometers replacing r_p in equation 2.1 (Sorensen (2011)).

In the regime governing the formation of soot, the motion of particles is affected by multiple collisions with gas molecules following a stochastic behavior. This random motion of particles is presumed to be of Brownian type. This Brownian motion can be of ballistic or diffusive type, depending at which limit of Kn the soot particle and soot aggregate are placed. As the particle (or aggregate) radius r_p is generally greater than tens of nanometers, and less than few hundreds of nanometers, the particles (or aggregates) are supposed to follow a diffusive Brownian motion, representative of the lower limit of the transition regime.

In parallel to the processes above, there is the structural rearrangement of the material from amorphous state to the formation of graphitic layers. As illustrated in Figure 2.1(b), the graphitic layers are separated by a certain distance inside the particle. This rearrangement induces a change in the material properties of soot throughout its journey. A glance to those properties is given in Table 2.1, according to the review by Dobbins (2007).

	Precursor nanoparticles	Carbonaceous soot
Morphology	Singlet spherules	Chained fractal aggregates
C/H ratio	1.8 to 2.2	5 to 10
Composition	PAHs, Aliphatics	C Crystallites, Residual H
Mobility diameter	2 to 10 nm	0.1 to 10 microns
Material density (g/ml)	around 1.2	around 1.8
Refractive index (visible light)	around $1.6 + 0.05i$	variable around $1.9 + 0.5i$

Table 2.1: *General view on the physical properties of soot from hydrocarbon fuels, table from Dobbins (2007), based on the works of Blevins et al. (2002), D'Alessio et al. (1992), Park et al. (2004), Oktem et al. (2005), Sorensen and Feke (1996) and Sorensen (2001).*

The soot formation processes can be distinctly observed for example in laminar flame conditions whereas they can occur simultaneously in turbulent conditions. The shape of the carbon structure (graphitic layers or amorphous) and the chemical composition of soot can vary therefore depending on the conditions such as temperature, pressure, type of fuel and oxydizer, homogeneous (premixed) mixtures or diffusion flames, etc. Not only the gaseous phase products differ accordingly but also the solid phase is affected: different particle size implies different surface reactivity and growth, varied mobility of particle, hence different aggregate morphology.

Oxidation process listed above is not a separate step of the soot formation but can occur at any time of the combustion process. During oxidation, all the carbon products react to produce CO and they are no more effective in the formation of soot. In rich flames, OH radicals are causing the oxidation. In stoichiometric conditions and below, O_2 and OH are both effective (Bartok and Sarofim (1991)).

In the next paragraphs, observations of soot morphology are presented corresponding to different formation levels at different scales in Section 2.1.2 and

Section 2.1.3. As the morphology of soot aggregate is commonly presented as a fractal object in the literature, the fractal theory is briefly reviewed in Section 2.1.4. The morphology descriptors of fractal-like soot in literature are then listed in Section 2.1.5.

2.1.2 Soot at nanoscale

It is stated that the material refractive index, hence the absorption and scattering properties of soot, are modified by the molecular arrangement and the restructuring of carbon at nano scale (Bond and Bergstrom (2006) and references therein). This argument can be examined by a comparative study between in-situ and ex-situ experiments, for example on optical properties measurements, coupled to microscopy observations of the soot molecular structure. This type of study on soot nanostructure is performed to investigate the effect of the temperature and aging on the soot properties in the study of Alfè et al. (2010).

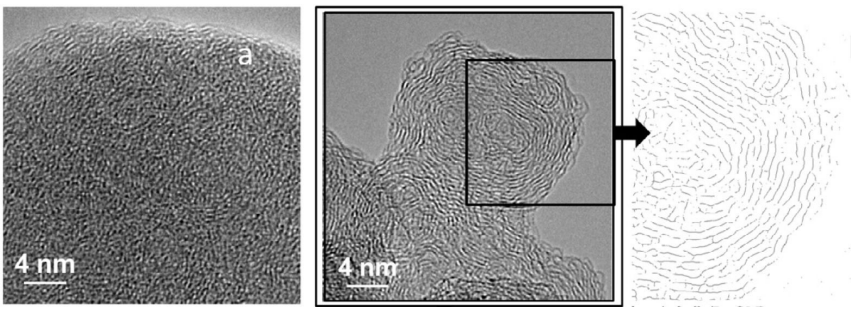

(a) (b)

Figure 2.4: *HRTEM (High-Resolution TEM) analysis example from the studies of Apicella et al. (2015): (a) nascent soot HRTEM image ; (b) mature soot HRTEM image and their resulting morphology for fringe analysis. (Reprinted with permission from Elsevier.)*

On the other hand, high resolution TEM (HRTEM) analyses are performed on soot nano-structure by Botero et al. (2016), Fernandez-Alos et al. (2011) to extract further information about soot formation history. For example in the studies of Apicella et al. (2015), Raman spectroscopy is coupled to fringe analysis on HRTEM images of soot as depicted in Figure 2.4, allowing the observation of its aromatization, carbonization history. A similar study is performed by Vander Wal and Tomasek (2003) on the oxidation history. The information on soot formation history is extracted depending on the size, orientation and

organization of the crystallite structure. It is also possible to obtain information about the molecular structure of aromatics from fringe simulations coupled to HRTEM image analysis, as depicted in Figure 2.5.

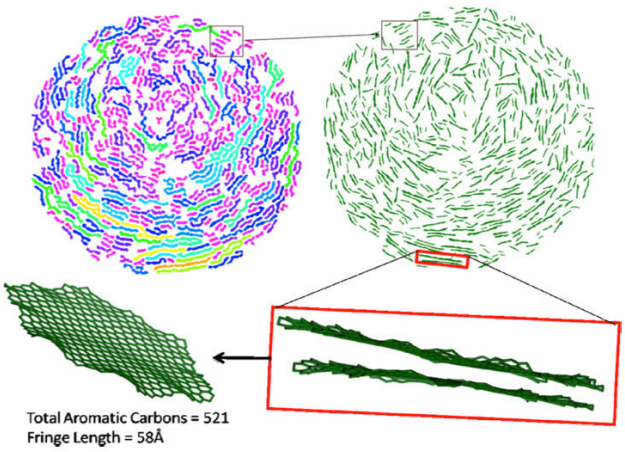

Figure 2.5: *Example of soot lattice fringe image from HRTEM (right) and the molecular slice model (left) as studied and illustrated by Fernandez-Alos et al. (2011), reprinted with permission from Elsevier.*

The nanostructure of soot can be used as an input variable for the radiation simulation only if an atomistic model can be used on soot aggregates to simulate their optical properties. There are tools being developed to simulate the optical properties of soot from an atomistic approach in the studies of García Fernández et al. (2015). As a perspective, a similiar HRTEM study can be performed to study the nanostructure and the subsequent effects on radiation, numerically and experimentally.

In our study, the simulation of the radiative properties will be performed at microscopic and macroscopic level by conventional simulation methods (mainly by discrete dipole approximation), as will be explained in Chapters 3 and 4. In those simulations, bulk material properties are to be used. Hence, such an atomistic morphology characterization is not applicable and not considered in our study.

2.1.3 Soot at micro scale: monomers and aggregation

In the earlier literature on soot mechanism, there are mainly two approaches for the formation of soot aggregates in terms of transition from the coalescent growth to fractal objects:

- Approach based on the coalescence of viscous droplets: Prado et al. (1981), Prado and Lahaye (1981) presume that liquid droplets coalesce all along their journey during the combustion according to their observations on pyrolysis of fuels. The very small droplets coalesce completely to form a new spherical particle whereas larger droplets don't have time to coalesce completely and the particle shape is sphere-like but irregular, hence forming the aggregates.

- Approach based on the simultaneous coagulation and surface growth of solid particles: Wersborg et al. (1973), Haynes and Wagner (1982), Smith (1983) propose that the nano sized solid particles coagulate and the simultaneous surface growth allows a more or less spherical shape of the particles. When the surface growth rate is low or the particle size is large (at the level of large monomers), the soot shape becomes more complex. At this level, the coagulated shape is no more smoothened by surface reactions hence the fractal-like geometry is formed.

In both approaches, it is accepted that the coagulation follows immediately the inception. Later numerical simulations by Mitchell and Frenklach (1998), Frenklach (2002) lead to the conclusion that the aggregation starts as early as particle nucleation stage. As the particles collide and coalesce, they also collide with PAH and other molecules. Sticked particles are burried under the spheroidal cover formed by the surface reactions so that the particle surface appears smooth. When the colliding particles become very large, at larger residence times, either the surface reactions are not fast enough to bury the sticked particles in a spheroidal cover, or there are not enough gaseous molecules to react, depending on the location in the flame. This produces complex shaped soot, which will be considered to be fractal-like. This brings us to the definition of fractal object in the next paragraph.

2.1.4 Fractal definition

Fractal theory is first introduced by Mandelbrot (1977). It is presented under different mathematical formulations to describe numerically the irregular patterns encountered in nature including the shapes of coastlines, mountains, clouds, snowflakes, colloids, but also Brownian fractals (Mandelbrot (1982)) .

By definition, a fractal object is an irregular geometry composed of the repetition of the same pattern at different size scales. This pattern and the whole geometry can be expressed in terms of length, volume, area (Mandelbrot (1982)). Theoretically, this repetition follows a specific correlation regardless of the size of the object ("scale-invariance") and the observation scale ("self-similarity").

For fractal clusters (and Brownian fractals), the correlation is formulated by a self-similarity rule presented in Equation 2.2 (equation from Bushell et al. (2002), originally formulated by Mandelbrot (1977)):

$$M \propto R^D \tag{2.2}$$

Here R is the linear measure for the size of the object, M is the mass of the object (it can also be replaced by the number of elements or volumes depending on the context), and D is the dimension defining the degree of rugosity of the object (which will be later transformed to the so-called fractal dimension D_f).

The dimension D is smaller or equal to the dimension of the space in which the object is placed. Hence, if a 2D image is in question, the maximum value of D is 2. For a 3D object the maximum computed value of D is 3.

In real life, the validity of the correlation is bounded by the maximum size of the object and the size of the smallest constituents. This will be demonstrated on soot during our fractal analysis in Sections 2.5 and 2.6.

Note that in Equation 2.2, the total quantity M of the object is proportional to the characteristic length R. Later, to ensure an equality for soot, a proportionality constant will be introduced as the fractal prefactor when the fractal theory above is formulated in terms of dimensionless fractal parameters. Hence, each fractal parameter will be specific of one type of geometrical pattern and one type of aggregation mechanism. This is explained for soot material in the next section.

2.1.5 Descriptors for soot morphology

In the previous section on the fractal theory, it is mentioned that the object is composed of the repetition of the same pattern. In the literature, soot aggregate morphology is described by mass fractal definition by assuming that it is the repetition of identical geometry: collection of identical spherical primary particles.

In reality the primary particles composing an aggregate are not exacly of same size and they are spheroidal. The distribution of primary particle size forming the aggregates is known to follow the normal or log-normal distribution rules, as stated in the works of Köylü and Faeth (1992) on acetylene and ethylene soot, of Wentzel et al. (2003) on diesel and palas soot, and in many other studies.

In premixed flames, the aggregates are composed of few tens of primary particles whereas in the turbulent flames the primary particle number composing an aggregate can go up to thousands of particles. In both cases, the deviation around the mean particle diameter is generally small (few nanometers) whereas the primary particle diameter is generally in the range $20nm \lesssim d_p \lesssim 50nm$, according to the litterature review presented later in this section. Hence, efforts are given to determine the mean primary particle size in the morphology analysis in the next sections, considering that primary particles are spheroidal.

The suitability of the normal distribution function and the choice of mean diameter will presented and discussed in Section 2.3 in our experimental observations on soot morphology, more specifically in Section 2.3.1 on soot monomers. Here we return back to the fractal descriptors for soot.

Soot aggregates are defined as fractal-like objects by Jullien and Botet (1987) in the form of a density autocorrelation function (nevertheless the same notation was mentioned for other aggregate types in the works of Forrest and Witten (1979)). This density autocorrelation function can be represented in the following form (equation taken from Bushell et al. (2002)):

$$g(r) = g(|\mathbf{r}_j - \mathbf{r}_i|) = \frac{1}{4\pi} \sum_{i=1}^{N} \sum_{j=1}^{N} \frac{\phi(\mathbf{r}_i)\phi(\mathbf{r}_j)}{|\mathbf{r}_j - \mathbf{r}_i|} \tag{2.3}$$

An earlier representation of the above formula for aggregates can be found in Witten and Sander (1981). In equation 2.3, $g(r)$ is the probability of having material at a distance r from the reference point i. $\phi = 1$ if there is material at the point of interest, $\phi = 0$ otherwise. Note that function in Equation 2.3 behaves differently at different scales for fractal aggregates:

- When $r > R_{agg}$, the observed distance is larger than the aggregate size hence the probability of finding material drops to zero:

  $$g(r) \to 0 \tag{2.4}$$

  In the above equation, R_{agg} is the radius of the sphere or circle encompassing the aggregate.
- When $r_p < r < R_{agg}$, the density autocorrelation function follows an autosimilarity (fractal) rule, which is demonstrated by Forrest and Witten (1979):

  $$g(r) \propto r^{(D_f - d)} \tag{2.5}$$

  In the above equation, d is the spatial dimension, r_p is the primary particle radius.

To force the convergence condition given in Equation 2.4 on the determination of fractal dimension from Equation 2.5, a cut-off function $h(x)$ is used (Cai et al. (1995)) :

$$g(r) \propto r^{(D_f - d)} h(x) \tag{2.6}$$

In the above Equation 2.6, $x = r/\xi$ where r is the observation distance to the reference point and ξ is the characteristic length of the fractal cluster. The function $h(x)$ should be selected so that the material density should be zero at the outer radius R_{agg} of the aggregate. Further exploitation of this function is not needed for our fractal analyses which will be given in the following sections. One can refer to the studies of Mountain and Mulholland (1988), Cai et al. (1995), Sorensen et al. (1995) for different formulations of the cut-off function.

Integrating the Equation 2.5 for distances $r < R_{agg}$ (in 2D or 3D) will account for all the material inside the region of interest. This leads to the following proportionality relation for the number of particles:

$$N \propto (R)^{D_f} \tag{2.7}$$

Later Samson et al. (1987) demonstrated that the self-similarity rule of equation 2.5 is applicable to individual soot aggregates generated by their cluster-cluster aggregation. (Such numerical aggregate generation methods will be presented in the Section 2.2.) On the other hand, Kolb et al. (1983) demonstrated the applicability of the density autocorrelation function on the similar diffusion-limited-like simulated fractals. This leads to the conclusion that soot aggregates are fractal-like: they follow the fractal law expressed in equation 2.7 in a specific range (Colbeck (2008)), $r_p < r < R_{agg}$.

Samson et al. (1987) introduced the fractal prefactor in the previously presented similarity law where R is the dimensionless size of the cluster and k_f is the prefactor defining the proportionality constant. The characteristic length is defined by $R = R_g/r_p$ to obtain a dimensionless property. In some literature studies, the cluster size R_g is normalized by particle diameter $R = R_g/d_p$ (Samson et al. (1987), Köylü et al. (1995)). When soot aggregates are considered monodisperse, this expression is transformed to the Equation 2.8 and the mass fractal dimension is equal to the number fractal dimension. As a result, the mass in the original similarity rule can be replaced by the number of identical primary particles N_p composing the aggregate:

$$N_p = k_f \left(\frac{R_g}{r_p} \right)^{D_f} \tag{2.8}$$

Thus, for the upcoming numerical simulations and fractal analyses, the parameters defining a soot aggregate are the number of primary particles N_p, the radius of gyration R_g, the radius of the primary particles r_p, the fractal dimension D_f and the prefactor k_f, each one leading to a different soot structure, as illustrated in figure 2.6 for D_f.

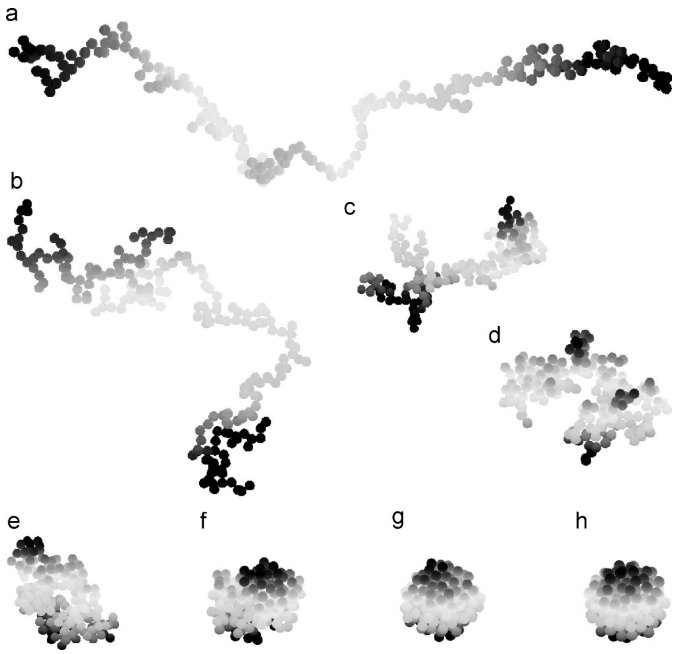

Figure 2.6: *Examples of fractal aggregates with N_p=200 and different D_f and k. (a)-(g) Df=1.25, 1.5, 1.75, 2, 2.25, 2.5, 2.75 and k=1.6. (h) D_f=3 and k=1.2. Reprinted from Liu et al. (2008) with permission from Elsevier.*

As in the above equations a definition is needed for the size R of the aggregate, a brief reminder is given on different diameter computations:

- Aggregate diameter D_{agg}: Diameter of the smallest sphere encompassing the aggregate (Rogak and Flagan (1990)), known also as the collision diameter.
- Diameter of gyration D_g: It will be defined in Equation 2.10.
- Mobility diameter D_m: Diameter of a sphere with the same migration velocity in a constant electric field as the aggregate of interest (Flagan (2001)).
- Volume equivalent diameter D_{veq}: Diameter of a spherical particle of the same volume as the aggregate under consideration (Baron and Willeke (2001)).

- Mass equivalent diameter D_{meq}: It is similar to D_{veq} but D_{meq} does not include internal voids isolated from surrounding air, resulting in $D_{meq} \leq D_{veq}$ (Baron and Willeke (2001)).
- Aerodynamic diameter D_{ae}: Diameter of a sphere with standard density that settles at the same terminal velocity as the aggregate of interest, dependent on the fluid flow regime (DeCarlo et al. (2004)).

In this study, only image and tomography analysis techniques are used. The radiative properties are then computed based on 3D geometry. Therefore, among the diameter definitions, the volume equivalent diameter D_{veq} and the diameter of gyration D_g are the most important ones for our work. D_{veq} will be used to compare the radiative properties of soot of identical volumes with different geometry configurations. D_g will be used for the fractal analysis of the 3D individual aggregates and of the 2D images of clusters of aggregates.

To find the radius of gyration for the above equation, 3D information is needed, as presented in the Equation 2.9 which gives the position of the center of mass of the aggregate $\mathbf{r}_c$ computed from the positions $\mathbf{r}_i$ of the centers of primary particles composing the aggregate.

$$\mathbf{r}_c = \frac{1}{N_p} \sum_{i=1}^{N_p} (\mathbf{r}_i) \tag{2.9}$$

$$R_g^2 = \frac{1}{N_p} \sum_{i=1}^{N_p} (\mathbf{r}_i - \mathbf{r}_c)^2 \tag{2.10}$$

Attention should be paid to the definition of the dimensionless parameters. For example the density function of the fractal object can be expressed in terms of different definitions of the aggregate radius (equation taken from Bushell et al. (2002)):

$$(1 - \epsilon) = k_x \left(R_x / r_p\right)^{D_f} \tag{2.11}$$

In the above Equation 2.11, ϵ is the porosity. The subscript x accounts for the definition of R. The values of k_x and R_x should be consistent: k_m and R_m for mobility measurements, k_g and R_g for image analysis, etc. Sorensen draws attention to this distinction in his reviews (Sorensen (2011), Sorensen (2001)) stating that there is some confusion with the correction and conversion factors during the computation of R_m, R_g, R_{agg}, and k_f parameters in literature. Therefore we clarify that throughout our study the prefactor k_f values are

obtained from the radius of gyration R_g from 2D/3D geometry analysis, and any mobility study is not performed.

When it is not possible to obtain an exact 3D geometry of soot, researchers often refer to numerically generated fractal soot aggregates as a first good approximation. Hence, fractal parameters and the size of the aggregates are investigated by either light scattering, mobility, settling or image analysis. An extensive but not exhaustive list of those fractal parameters, particle sizes and numbers are given in Tables 2.2 and 2.3.

According to the values in Table 2.2 for soot issued from hydrocarbon flames, most of the D_f values range between 1.6-1.9 while k_f ranges between 1.2-3.5. The very high values of k_f are probably due to a different definition of the similarity rule where the particle radius is sometimes replaced by particle diameter. It is known that the measurement of D_f is more precise and the values are universal to fuel type and process. The agreement on the prefactor k_f is less clear. In the study of Filippov et al. (2000), the discrepencies in k_f values are related to the difficulty of obtaining k_f from experimental measurements because one has to compute first D_f and than k_f. Also, D_f value is universal to measurement method: The values of D_f obtained from image analysis or light scattering are theoretically the same. This latter is not valid for k_f. Similarly, according to our fractal analysis in this Chapter, it will be also concluded that the k_f is dependent on the experimental and observational conditions and that it can be a result of particle overlapping as stated by Brasil et al. (2001).

As shown in Table 2.3, the mean particle diameter ranges between 10 to 50 nm. The number of particles composing the aggregate is highly variable, probably due to extraction conditions and flame conditions changing the residence time of soot.

The collisional behaviour is different in the aggregation process depending on the physical and chemical conditions under which the particles are clustering. Again, depending on the fluid conditions, particles and aggregates can collide in a more or less monodisperse or polydisperse behaviour. The final aggregate formed has a fractal factor and a fractal prefactor which indeed reflect this formation history. In order to mimick those different behaviours, there exist different numerical methods of generating the fractal aggregates. This leads us to the next section where the fractal generation algorithms are summarized.

2.2 Numerical generation

The basic and the most commonly used fractal generation algorithms are of two types: the particle-cluster aggregation (PCA) and the cluster-cluster aggregation (CCA) (Filippov et al. (2000)). In PCA method the aggregation occurs

Reference	Method	Type	D_f	k_f
Brasil et al (2000)	CS	-	1.82	1.27
Cai et al (1995)	3D TEM	Methane	1.74	1.23
Cai et al (1995)	2D TEM	Methane	1.74	2.45
Colbeck (1997)	TEM	Diesel	2.04	-
Colbeck (1997)	TEM	Butane	1.97	-
Gangopadhyay et al. (1990)	TEM	Methane/O2 flame (premixed)	1.6 ± 0.15	2.18
Hu and Köylü (2004)	TEM	Acetylene flame	1.77 to 1.88	1.6 to 2.2
Hu et al. (2003)	TEM	Ethylene flame	1.74 ± 0.11	2.2 ± 0.4
Jullien and Botet (1987)	CS	-	1.78 ± 0.04	-
Kim and Choi (2003)	ALS/TEM	Methane/air	1.8 to 1.95	-
Köylü and Faeth (1992)		Propane flame	1.74	
Köylü et al (1995)	ALS	Acethylene flame	1.86	2.25
Köylü et al (1995)	ALS	Ethylene flame	1.75	2.78
Köylü et al (1995)	3D TEM	Methane	1.65	2.71
Köylü et al (1995)	2D TEM	Acethylene flame	1.67	2.39
Köylü et al (1995)	2D TEM	Ethylene flame	1.66	2.35
Köylü et al (1995)	2D TEM	Acethylene flame at 1/4 Patm	1.73	2.17
Lee et al (2000)	3D TEM	Methane/air flame	1.93	7.91
Lee et al (2000)	3D TEM	Methane/50% O2 flame	1.75	6.46
Meakin (1984)	CS	-	1.82	1.37
Megaridis and Dobbins (1990)	2D TEM	Ethylene flame	1.62 ± 0.04	1.80
Megaridis and Dobbins (1990)	2D TEM	Ethylene flame	1.74 ± 0.06	2.18
Mountain and Mulholland (1988)	CS	-	1.69	1.59
Mountain and Mulholland (1988)	CS	-	1.74	1.05
Mountain et al (1986)	CS	-	1.7 to 1.9	-
Mulholland et al. (1988)	CS	-	1.89 to 2.07	-
Onischuk et al (2003)	TEM	Propane	1.7 ± 0.1	-
Puri et al (1993)	ALS	-	1.4	3.50
Samson et al (1987)	3D TEM	Acethylene flame	1.4	3.49
Samson et al (1987)	2D TEM	Acethylene flame	1.47	2.67
Samson et al. (1987)	TEM	Acetylene flame	1.5 to 1.6	-
Sorensen and Feke (1996)	2D TEM	Acetylene	1.8	1.7
Sorensen et al (1992)	LS	Butane	1.96	
Sorensen et al (1992)	LS	Methane/O2 flame (premixed)	1.73	-
Tian et al (2006)	TEM ROD	Ethylene coflow diffusion	1.77 ± 0.01	2.4 ± 0.4
Tian et al (2007)	CS ROD	-	1.78	2.3 to 2.7
Wu and Friedlander (1993)	CS	-	1.84	1.30
Zhang et al. (1988)	TEM	Methane flame	1.72 ± 0.10	-
Zhang et al. (1988)	TEM	Methane flame	1.62 ± 0.06	-

Table 2.2: *Literature values for the measured and computed D_f and k_f of soot from gaseous hydrocarbon combustion flames, or from computer simulations of the corresponding aggregation methods. Most of the values are retrieved from the reviews of Köylü et al. (1995), Brasil et al. (2001), Maugendre (2009) while some corrections and additions are performed. CS=Computer Simulations, ALS=Angular Light Scattering, LS=Light Scattering, TEM=Transmission Electron Microscopy, ROD=Relative Optical Density.*

Reference	Type	d_p (nm)	N_p
Evans et al. (1986)	Crude-oil pool fire	45	5 - 200
Harris et Weiner (1984)	Toluene/ethylene (premixed)	20-25	5 - 200
Hu and Koylu (2004)	Acetylene flame	17-34	
Hu et al. (2003)	Ethylene flame	19 to 35	
Koylu et al. (1997)	Etylene/air	18-32	
Koylu et Faeth (1991)	Ethylene	32	
Koylu et Faeth (1991)	Propane	30	364
Krishnan (1999)	Acethylene turbulent	47	417
Krishnan (1999)	Ethylene turbulent	32	467
Krishnan (1999)	Propylene turbulent	41	460
Krishnan (1999)	Butadiene turbulent	42	-
Krishnan (1999)	Benzene turbulent	50	552
Krishnan (1999)	Cyclohexane turbulent	37	-
Krishnan (1999)	Toluene turbulent flame	51	526
Krishnan (1999)	n-Heptane turbulent flame	35	260
Lee et al. (1962)	Gaseous HC flame	20 to 40	5 - 200
Lee et al . (2000)	Methane/air flame	19.8	10-180
Lee et al . (2000)	Methane/50% O2 flame	10.8 to 21.7	10-600
Lee et al . (2000)	Methane/O2 flame	10.9	-
Megaridis and Dobbins (1989)	C2H4 diffusion flame	up to 40	5 - 200
Megaridis et Dobbins (1989)	Ethylene	30-37	
Megaridis (1990)	Ethene flame	11.8-22.1	4-130
Prado et al. (1977)	Turbulent kerosene flame	19 to 30	5 - 200
Prado et al. (1977)	Premixed C3H8/O2 flame	15 to 26	5 - 200
Prado et al. (1981)	Propane/O2 (premixed)	15-26	
Roessler (1982)	Diesel engine	30	5 - 200
Samson et al. (1987)	Acetylene smoking flame	20 to 30	5 - 200
Sorensen (1996)	Acethylene/air	23	10-2000
Tian (2004)	Ethylene coflow diffusion	29	1-1610
Wey et al. (1984)	C3H8 diffusion flame	14 to 20	5 - 200
Williams et al. (2006)	Ethylene	36	
Wood et al. (1984)	Swirl-stabilised combustor	50	5 - 200
Zhang et al. (1988)	Methane/O2 premixed	20	5 - 200
Zhang et al. (1988)	Methane/O2	20	
Zhao et al. (2006)	Ethylene/air	20	
Zhu et al. (2002)	Acetylene	51	

Table 2.3: *Literature values of mean primary particle diameter and number of particles composing soot aggregate, mainly from hydrocarbon combustion. Most of the values are retrieved from the reviews of Maugendre (2009) and of Van-Hulle (2002), while some corrections and additions are performed.*

between isolated particles and clusters whereas in CCA method the aggregation between clusters is allowed.

For the generation of aggregates in 3D, the aggregation algorithm consists of displacing randomly the primary particles in a cubical network, following the aggregation algorithm. Depending on the fractal dimension desired, the algorithm converges (or not) to the presumed values of the fractal dimension and the prefactor, until they form the desired size of the aggregate. A preliminary illustration is given in Figure 2.7.

The original versions of the algorithms involve identical primary particles, and this displacement of the particles can follow a ballistic motion or a diffusive behaviour depending on the phenomenon to be represented. Note that the ballistic type codes generate more compact aggregates even if it is of the same type (PCA or CCA).

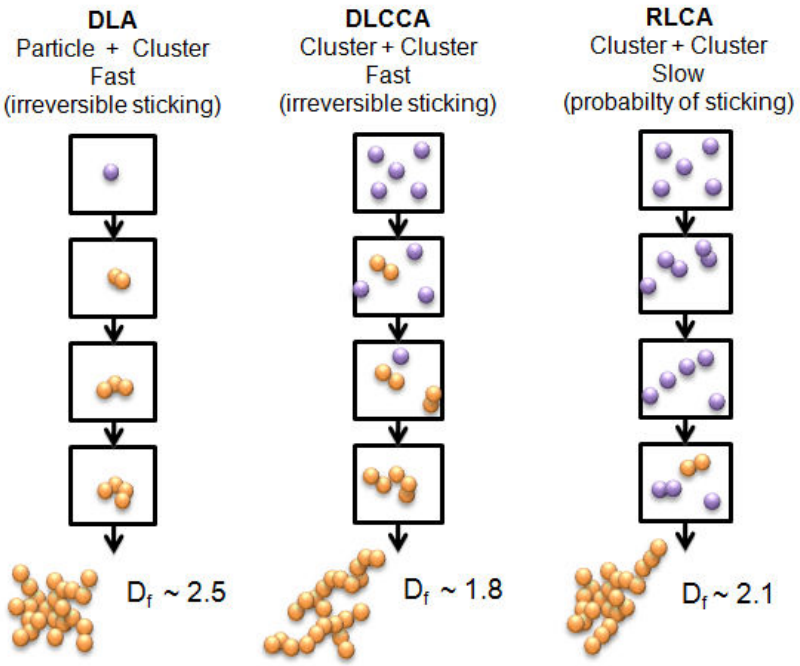

Figure 2.7: *Illustration of the evolution during PCA and CCA methods.*

2.2.1 DLCCA

In Diffusion-Limited Cluster-Cluster Aggregation (DLCCA), the primary particles are introduced all at once in a network space. Particles move according

to diffusion hence they follow a random motion. The sticking probability is 1, which means a bond is formed each time there is a collision between clusters or between particles. This property comes from the consideration of Brownian motion where the collision causes the sticking due to the strong Van der Waals interactions at very short distances comparable to the particle diameter. At greater distances, particles are considered free from forces (neglecting any electrostatic forces). This property makes DLCCA a fast aggregation algorithm. Both single particles and clusters of adhered particles are allowed to move throughout the network. This random motion continues until the size of the desired aggregate is reached.

This CCA type method, developed originally by Kolb et al. (1983) and Meakin (1983b), produces aggregates with a fractal dimension $1.6 \lessapprox D_f \lessapprox 1.9$ (Kulkarni et al. (2011) and references therein). It is known to be suitable for the virtual generation of soot aggregates (Sorensen et al. (1998)), different types of aerosol aggregates, iron aggregates (Forrest and Witten (1979)), silica aggregates (Rojanski et al. (1986)) , colloids and gold (Weitz and Oliveria (1984)).

In 2D space, DLCCA gives a fractal dimension around $D_f \simeq 1.5$, and the relationship between the 2D and 3D fractal properties is not clear. For soot aggregates, some empirical correction/conversion factors are given in studies using TEM/SEM analysis of morphology (Sorensen (2011) and references therein). This will be discussed later in this chapter, during our fractal analysis of 3D soot from electron tomography compared to the fractal analysis of 2D images in the tomograms.

2.2.2 RLCA

The Reaction Limited Cluster Aggregation (RLCA) is also a CCA type algorithm. Different from DLCCA, particles adhere to each other after several collisions following a given sticking probability. This probability is due to the chemical conditions of the aggregation process (Jullien and Kolb (1984)).

RLCA generates aggregates with a fractal dimension of $1.9 \lessapprox D_f \lessapprox 2.2$ (Fry et al. (2004), Kulkarni et al. (2011) and references therein). RLCA aggregates are more compact than the ones generated with DLCCA. They are applicable to simulate colloids or aggregates produced from chemical reactions and low temperature applications (Nyeki and Colbeck (1995)).

2.2.3 DLA

Diffusion Limited Aggregation (DLA) is a PCA type method. As DLCCA, DLA is of fast aggregation type mimicking Brownian motion. In DLA method,

different from DLCCA, primary particles are introduced one by one into the given space. The position of the first particle is fixed. The second particle is introduced to move randomly until colliding with the first particle. At each collision, the sticking is irreversible meaning that the probability of sticking is equal to 1. Further particles are introduced following the same methodology, with the position of the cluster being fixed.

This method, initially introduced by Witten and Sander (1981), produces aggregates with a fractal dimension of $D_f \simeq 2.5$ (Meakin (1983a)).

More detailed illustrations and mathematical formulations behind the numerical aggregation methods, not limited to soot, can be found in studies by Meakin (1999) or very recently by (Teichmann and van den Boogaart (2015)).

2.2.4 Representative soot aggregates

The above aggregation models are purely based on the scaling law of the fractal theory. In some soot studies, the aggregation between identical objects is extended to polydisperse clusters in order to take into account the realistic combustion dynamics such as the size distribution of primary particles (Yon et al. (2015), Wu et al. (2015)), or the simultaneous coagulation and surface growth for the simulation of primary particles (Mitchell and Frenklach (2003), Morgan et al. (2007)).

The range of interest of fractal dimension D_f for our study is betweeen 1.6 and 1.9, corresponding to hydrocarbon generated soot aggregate fractal parameters listed in Table 2.2. The studies of Brasil et al. (2000) try to propose a unique prefactor value for aggregates independent of their size, by using a combination of numerical generations and light scattering theory: they found a value of $k_f = 1.27$. Colbeck (2008) and Brasil et al. (2001) relates the discrepancy on k_f between studies to the sintering (coalescence of primary particles by overlapping and neck formation) of primary particles. The same effect is mentioned by Oh and Sorensen (1997b) on the effect of sintering on the prefactor.

The range for fractal parameters in question is covered by DLCCA, hence in this work the aggregation algorithm of Mackowski (2006) is used to generate representative numerical soot aggregates. They are composed of identical unit spheres and the input variables are D_f, k_f and N_p, following self similarity rule presented in Equation 2.8. We remind that during the analysis of radiative properties of numerical aggregates in Chapter 4, several aggregate generations will be made with given D_f and k_f, to account for the random nature of this aggregation process. An example for the mean values of D_f and k_f of interest is illustrated in Figure 2.8.

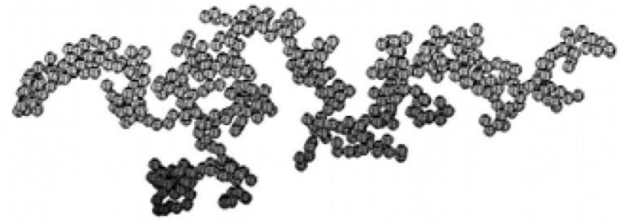

Figure 2.8: *Example of hydrocarbon emitted soot, generated using DLCCA,* $D_f = 1.7$*,* $k_f = 2.0$*,* $N_p = 500$

In the next two sections, the fractal analysis will be performed both on numerical aggregates and the real tomography aggregate. It will be shown in the 3D fractal analysis that the tomography object exhibits a fractal behaviour and that DLCCA generated fractals constitute a good first approximation to determine the geometry. Nevertheless, as will be seen later, the radiative properties of the DLCCA generated aggregates and the tomography aggregate exhibit slight discrepancies. Those discrepancies will be discussed later in Chapter 4 and are most likely due to the lack of information in the DLCCA aggregates on the combustion history of the soot:

- different interactions between particles and clusters, variation of the mean particle size distribution,
- change in the chemical reactions due to increase in cluster surface area,
- variation of the cluster mass, speed and orientation during the aggregation process, etc.

2.3 Experimental observations, image analysis on groups of clusters

As it was explained in Chapter 1, extractions were made from propane and methane flames. Below in Figure 2.9 is given an example of propane soot agglomerate observed under SEM. As we will see later, at large scales the agglomeration follows more or less the fractal behavior following the universal D_f and k_f values, if compared to the numerical fractal aggregate of Figure 2.8.

In Figure 2.10, we show SEM recordings of soot collected from different conditions, but with the same collection time $t = 3s$. It is seen that the combustion of propane and methane with air represents similiar agglomeration patterns for rich flames regardless of fuel type.

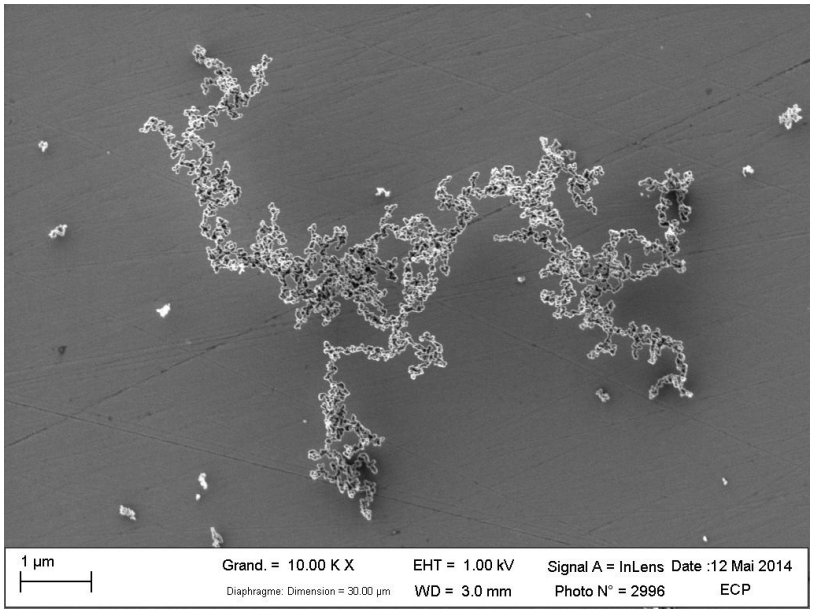

Figure 2.9: *Soot sample collected from propane/air flame at top HAB (Height Above Burner).*

2.3.1 Monomer size

The mean diameter of the primary particles is important for the fractal analysis, the numerical aggregate generation and the simulation of the radiative properties.

As will be stated later, the fractal analysis is only meaningful between the maximum linear size of the aggregate and the mean monomer diameter. Beyond those limits the analysis is not able to capture the irregularity pattern. Numerical fractal aggregates are therefore to be generated based on the mean monomer diameter.

TEM and high resolution SEM images are analysed for the particle size. Analysis is performed mainly on propane soot for tomography object, but also on methane soot to compare their primary particle mean diameter. The analysis is performed using ImageJ software (Abramoff et al. (2004), Collins et al. (2007)) by the particle analysis plugin where the size and number of particles are semi-automatically detected using the circle diameter as the variable parameter. Note that during SEM tomography, recordings of tilted positions have elongation distortion on the image. (This distortion is corrected during the tomography reconstruction but not directly on 2D images). Only non-tilted images are analyzed for tomography object to prevent the effect of elongation on the mean diameter.

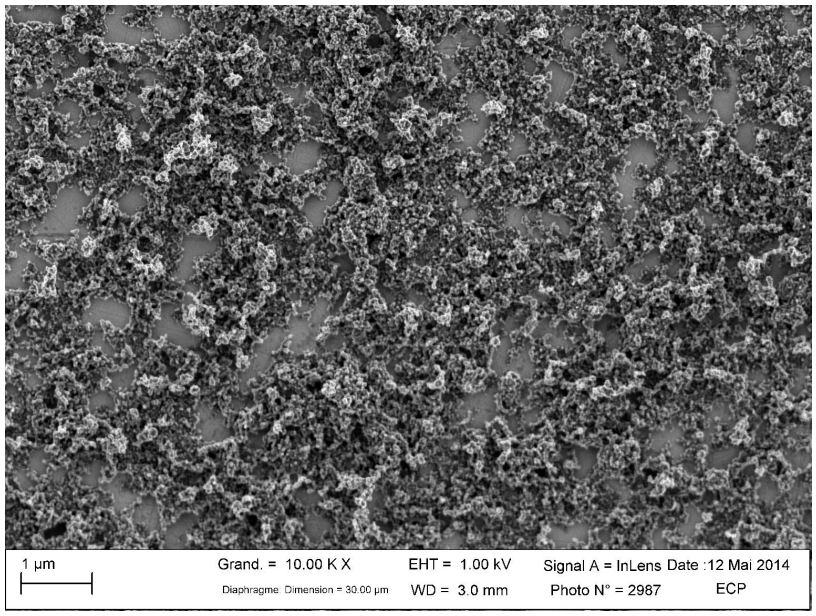

(a)

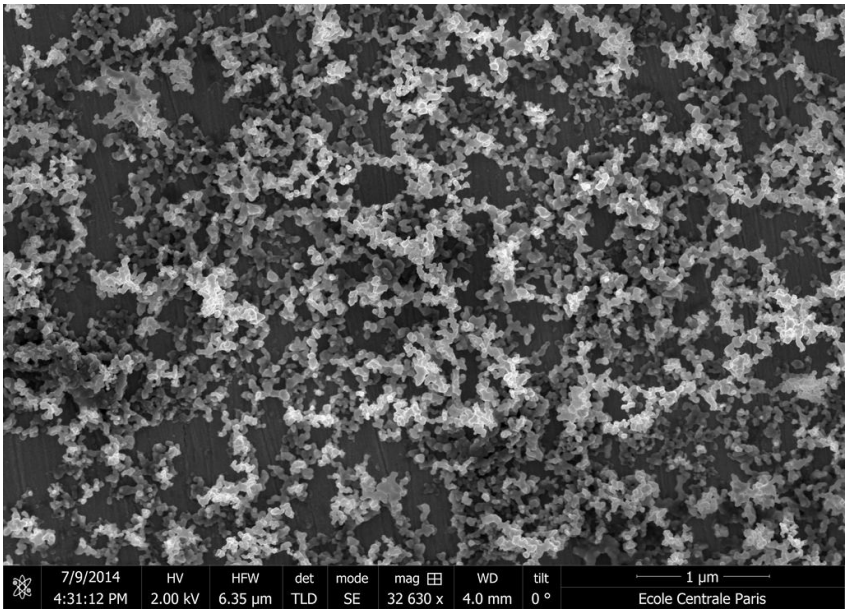

(b)

Figure 2.10: *Comparison on soot collected from (a) propane/air fuel rich (recorded with Zeiss Leo Gemini 1530); (b) methane/air fuel rich flames (recorded with FEI Helios NanoLab 660); at top HAB, t=3s. Note the high resolution of image (b) equipment, which enabled us to perform tomography in SEM.*

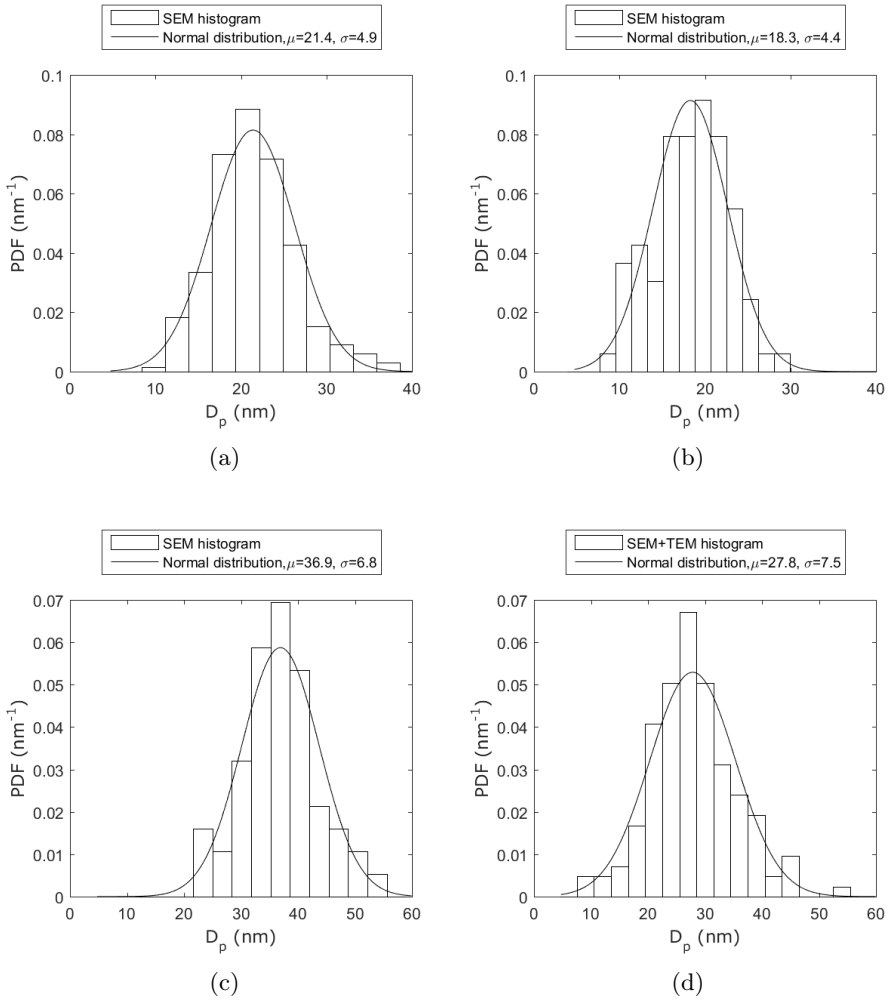

Figure 2.11: *Determination of mean monomer diameter for (a) rich methane/oxygen at top of flame; (b) methane/oxygen stochio at top of flame; (c) rich propane/air at mid-HAB (tomography object); (d) rich propane/air at top of flame (tomography object).*

The monomer size distributions are illustrated in Figure 2.11 for propane and methane. A normal distribution is chosen for the particle size distribution. A log-normal distribution can also be accurately used for flame soot, as stated by Köylü and Faeth (1992). In Figure 2.11, it is observed that the normal distribution is slightly biased towards large particles (Köylü and Faeth (1992)). The mean diameter for the tomography propane soot is around 30 nm depending on the measurement location, whereas the mean diameter for methane soot is around 20 nm. The results are in agreement with the literature values, previously presented in Table 2.3. The size of the primary particles tend to decrease

after mid HAB and this is related to the oxidation of soot (Köylü et al. (1997), Megaridis and Dobbins (1989)) and its carbonization (Reilly et al. (2000)).

In the very recent studies by Liu et al. (2015), the effect of polydispersity is stated to be small for total extinction and absorption but considerable for scattering. Here, we are not particularly interested in the particle size distribution function but in the mean particle diameter, knowing that the polydispersity is not taken into account in our determination of the radiative properties. This will be discussed later in Chapter 4 on soot radiative properties.

Regarding studies on soot particle size, further research exists in literature focusing on the combustion simulations (Balthasar and Kraft (2003)), the automatic determination of particle size and distribution (Bescond et al. (2014)) and the effect of the distribution (Liu et al. (2006)). Again, with the concern of radiative properties, we focus on the aggregation pattern leading to micron sized objects, as presented in the following analyses.

2.3.2 Cluster analysis

It is possible to determine the fractal dimensions of groups of aggregate clusters by image analysis. The self similarity rule of Equation 2.8 can be used by defining N_p, R_g and r_p. The mean particle radius is evaluated using the method in the previous section. The number of particles N_p and the radius of gyration R_g are 3D parameters and not readily available from 2D images. Empirical relations are derived by researchers for N_p and R_g. They simulated 2D projections of numerically generated 3D fractals and did reverse calculations on D_f and k_f.

For the computation of R_g, the following equation is proposed, relating the R_g and the primary particle mean radius r_p to the maximum projected distance L_{agg} of the aggregate (equation taken from Yon et al. (2011)):

$$\frac{R_g}{r_p} = \frac{L_{agg}}{\beta d_p} \tag{2.12}$$

The value for β ranges between 1.45 and 1.5 (Samson et al. (1987), Wentzel et al. (2003), Brasil et al. (1999), Oh and Sorensen (1997b)). Here we used $\beta = 1.48$ in our study as proposed by Yon et al. (2011) and as it constitutes an average value to the literature data.

Similarly, an empirical relation is derived to determine the number of primary particles on a 2D image of a fractal cluster (A_p is the projected area of the primary particle with mean diameter, A_{agg} is the projected area of the aggregate):

$$N_p = k_a \left(\frac{A_{agg}}{A_p} \right)^{\alpha} \tag{2.13}$$

The value of k_a in literature ranges between 0.97 and 1.44 (Brasil et al. (1997)). The value of α ranges between 1.07 (Oh and Sorensen (1997), Tian et al. (2004)) and 1.14 (Brasil et al. (1997)). In this study we used the values $k_a = 1.155$ and $\alpha = 1.095$ as average values.

In our study, we have the advantage to access those unknown variables by tomography of some soot particles and compare the 2D-3D conversion empirical data to a 3D application. Although this is not an exhaustive computation because the 3D tomography would be too much time consuming if applied to all the clusters examined in 2D.

Fractal dimensions can also be computed from $ln(N_p)$ versus L_{agg}/d_p plots. In this case, the geometrical fractal dimension is equal to the mass fractal dimension D_f. However the prefactor k_L obtained from this analysis should be converted to the mass fractal prefactor k_f according to the empirical relation as follows (Hu and Köylü (2004)):

$$k_f = k_L \left(\frac{D_f + 2}{D_f} \right)^{D_f/2} \tag{2.14}$$

In our analysis, we did not use the equation 2.14 in order to avoid any increase of errors due to the effect of uncertainty in k_f due to D_f. From the linear fits performed on the plots of Figure 2.12, we obtain the following parameters:

- From Figure 2.12(a), methane/O2 (stochio), we obtain $D_f = 1.87$ and $k_f = 1.30$.
- From Figure 2.12(b), methane/O2 (fuel rich), we obtain $D_f = 1.70$ and $k_f = 1.65$.
- From Figure 2.12(c), methane/air (fuel rich), we obtain $D_f = 1.65$ and $k_f = 1.50$.
- From Figure 2.12(d), propane/air (fuel rich), we obtain $D_f = 1.66$ and $k_f = 2.97$. Here the high prefactor value is related to the overlapping of particles. This overlapping is due to, first, the fuel rich condition: the aggregate is much larger than the previous cases indicating higher residence times where the surface reactions and the coalescence are more abundant. And second, the 2D projection analysis can overestimate the overlapping for larger aggregates.

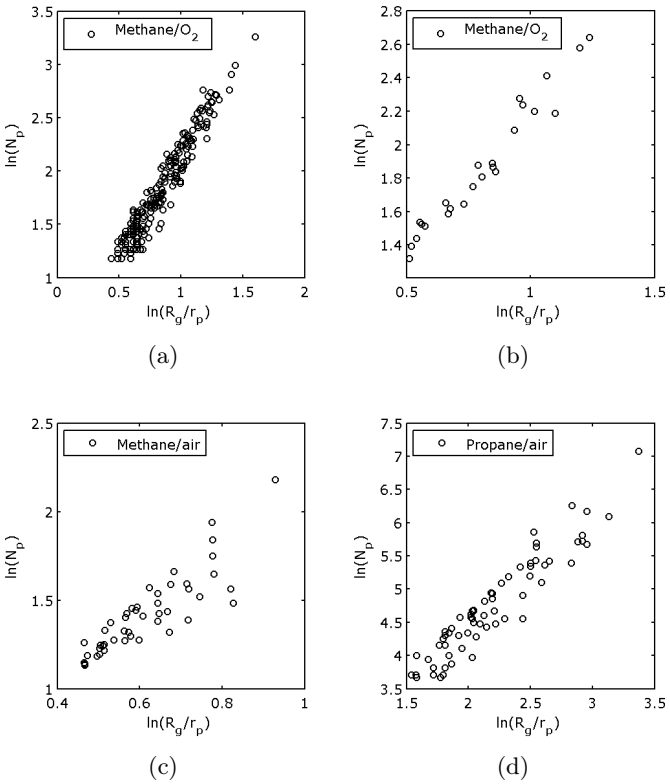

Figure 2.12: *2D image analysis on (a) methane/O2, stochio, top HAB; (b) methane/O2, rich, top HAB; (c) methane/air, rich, mid HAB ; (d) propane/air, rich, top HAB.*

2.4 Fractal analysis methods

Different methods are used in the literature to characterize aggregate morphology such as electron microscopy recordings, light scattering properties, mass-mobility relationships, settling analysis, or computer simulations, proposing different methods for the same interpretation of the D_f variable base on the autocorrelation function.

For the image analysis on soot, the most commonly known method is the usage of concentric shells placed at the center of gravity of the object. It consists of counting the material mass inside the corresponding shell with known radius. The technique is illustrated in Figure 2.13 retrieved from Xiong and Friedlander (2001). D_f can be determined from the log-log plot of the number of particles versus the radius distribution. It is stated that the image analysis works well on large particles (Köylü et al. (1995)) with low fractal dimension which results in less overlapping of fractal branches.

In the settling techniques, the particles are observed while suspended in a surrounding fluid. For highly aggregated structures, the technique needs some elaboration to determine accurately the particle dynamics, i.e. the drag, settling velocity and their relationship to the fractality. The advantage of this method is its ease of applicability to polydisperse aggregates, and the consideration of 3D complex shape of the object. But the difficulty arises from the conversion of hydrodynamic parameters to fractal properties.

In our study, the emphasis is given to individual aggregates and their 3D geometry which justifies our choice of image analysis techniques. Among those techniques, the usage of concentric spherical shells necessitates the computation over a 3D surface. This can lead to numerical errors due to surface mesh of the object which is eventually going to be discretized in cubic elements for the computation of the material volume. Hence, a relatively simple technique in 3D is chosen to be the "cube" (or "box") counting method. They are explained in the next following sections. These methods are equivalent to the analysis by concentric shells without any prior need to assume the distribution of primary particle size.

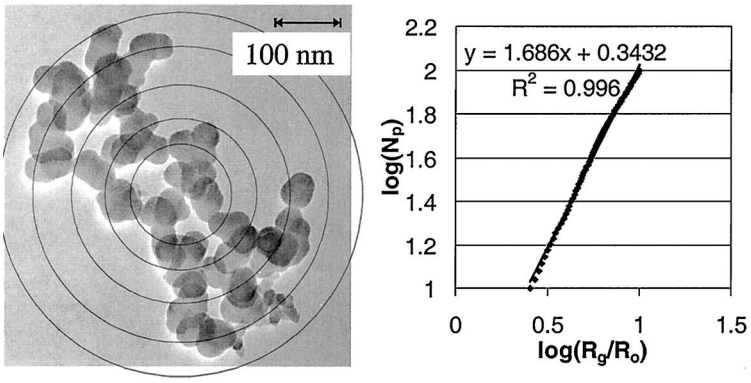

Figure 2.13: *Example for the fractal analysis method by concentric circles. (Here R_o is the normalizing radius.) Retrieved from Xiong and Friedlander (2001).*

2.4.1 Box counting

Box counting method proposed by Bushell et al. (2002) consists of covering the projection image of an object with boxes of a certain dimension a_{box}. The minimum number of boxes N_{box} encompassing the whole object is counted. The same procedure is repeated by gradually changing the box resolution a_{box}. The fractal dimension is expressed by the Equation 2.15, hence can be found from

a log-log plot of N_{box} vs a_{box}.

$$D_f = \lim_{a_{box} \to 0} \left(\frac{log(N_{box})}{log(1/a_{box})} \right) \tag{2.15}$$

At low resolution, i.e. at high a_{box} values, the box is so large that the object appears as a point hence N_{box} is equal to 1 and the slope of the line is zero. Similarly, this analysis can go beyond the fractal scaling at very high resolution with a_{box} smaller than the primary particle size.

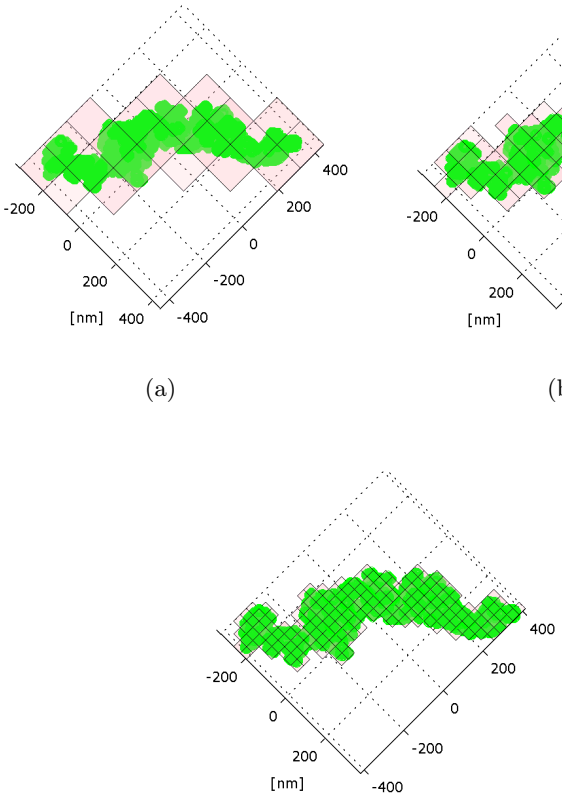

Figure 2.14: *Visualisation of the box counting on a fractal object with different resolutions; objects are completely enclosed by boxes; (a) $a = 128$ nm; (b) $a = 64$ nm; (c) $a = 32$ nm;*

This method is applied on the 2D microscopy images of soot and the results will be presented in Section 2.6.

2.4.2 Cube counting

The cube counting method is an extended version of the box counting and used also by Adachi et al. (2007) for soot and dust fractal analysis. This is basically a modified version of the method proposed by Xiong and Friedlander (2001). Instead of changing gradually the size of the circles, we change the size of the voxels englobing the aggregate. The gradual variation of the voxel size catches the surface details and gives information about the fractal behaviour.

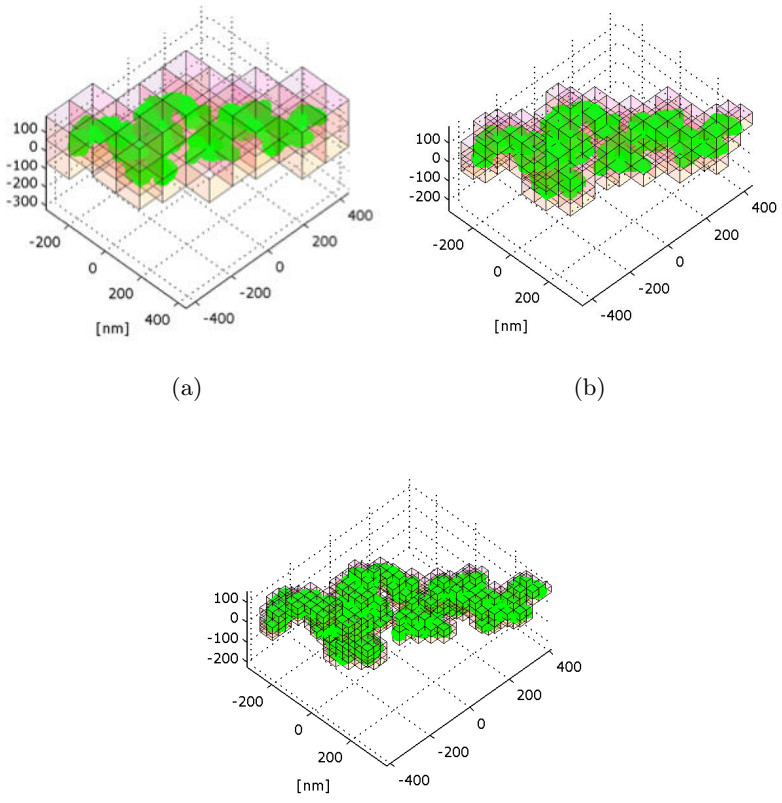

Figure 2.15: *Visualisation of the cube counting on a fractal object with different resolutions; objects are completely enclosed by cubes as clearly sen in the top view images; (a) $a = 128$ nm; (b) $a = 64$ nm; (c) $a = 32$ nm;*

Cube counting applied on the numerical object (DLCCA generated aggregate) to test the applicability and this test is presented in Section 2.5. Then it is applied to the tomography object to determine its fractal properties and the results will be presented in Section 2.6.

2.5 Analysis of the numerically generated soot

In order to test the applicability of the methods above, a reverse fractal analysis is made. Virtual aggregates are generated using DLCCA with known fractal dimensions. The cube counting method is applied in order to check whether the same values of D_f are obtained at the end.

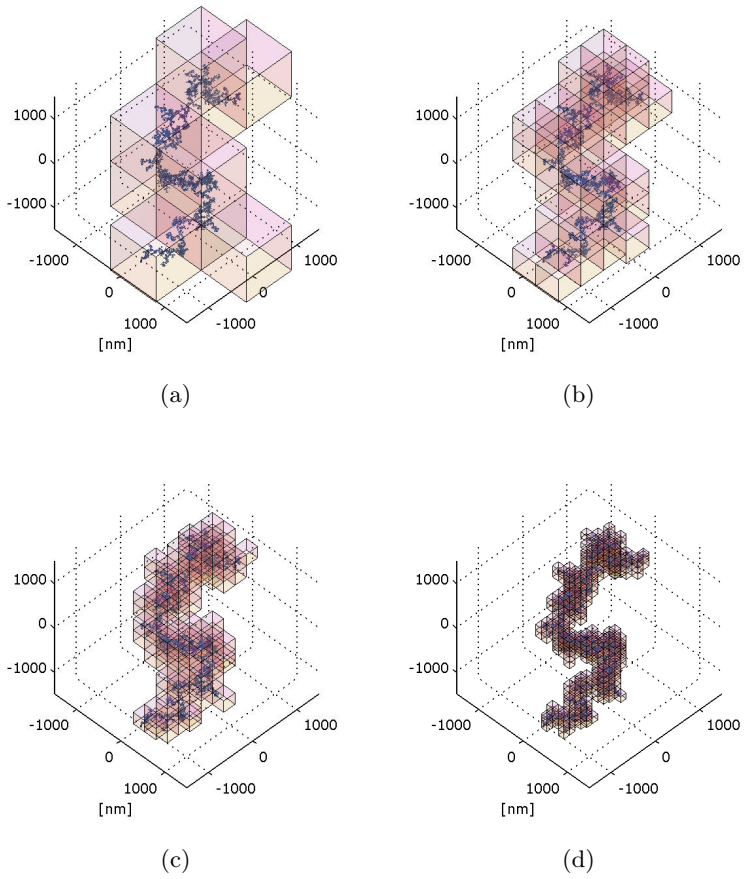

Figure 2.16: *Visualisation of the cube counting on the fractal object of* $N_p = 15000$ *with different cube resolutions; (a)* $a = 1024$ *nm; (b)* $a = 512$ *nm; (c)* $a = 256$ *nm; (d)* $a = 128$ *nm.*

For all the aggregates composed of spherical primary particles, surface mesh is generated in Matlab. An algorithm is written to voxelize this surface mesh into cubes encompassing the material as presented in Figure 2.16.

Even though it is mentioned that a fractal object follows a certain pattern correlation regardless of its size and its scale, the real life objects have a maximum

and minimum scale level beyond which the fractal definition becomes meaningless. In the cube or box counting method this is reflected by maximum voxel size, a_{max}, above which each voxel covers the object entirely therefore losing the irregularity patterns. The same is true below a minimum voxel size a_{min} : The object size is so large when $a < a_{min}$ that the voxels, again, lose the irregularity patterns as if they were in an infinite space, therefore converging to the value of the dimension of the space. ($D_{space} = 2$ for two dimensional space, $D_{space} = 3$ for three dimensional space, etc.) In between the two bounds a_{min} and a_{max} one observes the fractal behaviour.

In Figure 2.17, cube counting of different virtual aggregates is plotted. The transition regime, for $a_{min} < a < a_{max}$, is indeed linear. This proves the fractal nature of the spatial material arrangement within the aggregates. The slope of the linear transition regime gives the fractal dimension 1.7, as expected. The range a_{min}-a_{max} is largest for the biggest aggregate with $N_p = 15000$ in Figure 2.17(c) making the linear part more obvious. It should also be noted that the minimum bound corresponds to a resolution of $a_{min} = 16$ nm (maximum of $log(1/a)$) and is the same for all the aggregates regardless of their size. This is due to the limitation given by the size of the minimum autosimilar constituents: the fractal analysis is no more valid when the resolution goes below the mean diameter of the primary particles.

2.6 Analysis of the tomography soot

2.6.1 Segmentation of the 3D object

Adachi et al. (2007) state that the segmentation of a curved surface by cubes can yield errors especially for calculations of surface area A_s. Here, errors are reduced by maximizing the number of voxels used to represent the object, though we are limited by the resolution of the SEM images and by the computational effort (memory+time) for the tomography reconstruction. Therefore going below a resolution of few nanometers per voxel becomes cost effectless due to the limitations of the SEM imaging resolution and reconstruction noises, as it was illustrated in Figure 1.15. Keeping in mind this discretization limitation for the fractal analysis in the next section, also for the radiation simulations in Part II, we continue with the fractal analysis of the 3D tomography geometry.

2.6.2 3D fractal analysis

In this section, the emphasis is given on the fractal dimension D_f and the prefactor k_f. Obtaining the real 3D geometry from tomography and applying 3D

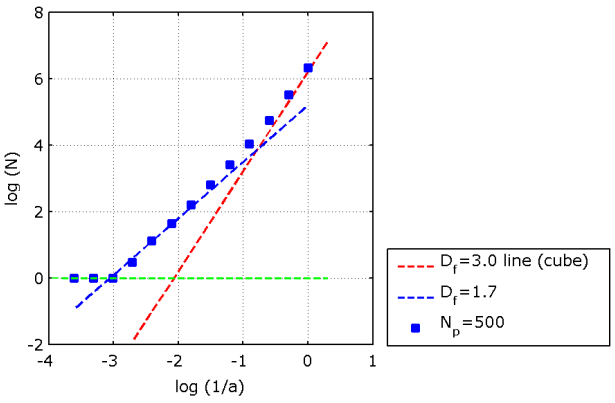

(a)

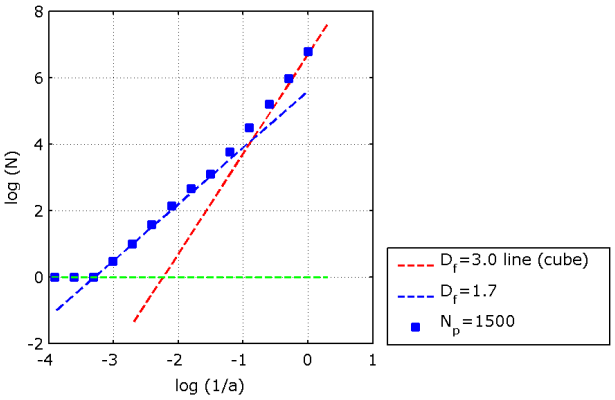

(b)

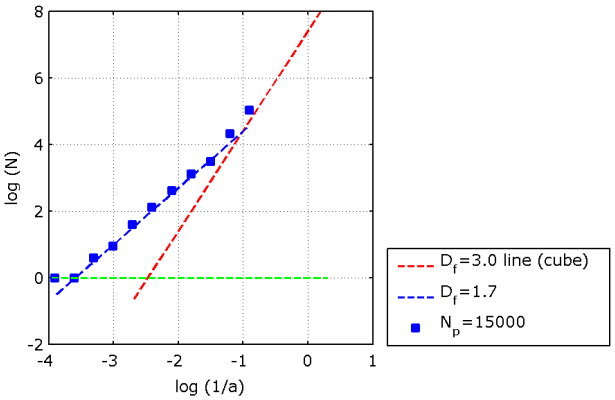

(c)

Figure 2.17: *Cube counting applied on virtual aggregates with the same fractal dimension D_f = 1.7 but different number of primary particles N_p; (a) N_p=500; (b) N_p=1500; (c) N_p=15000.*

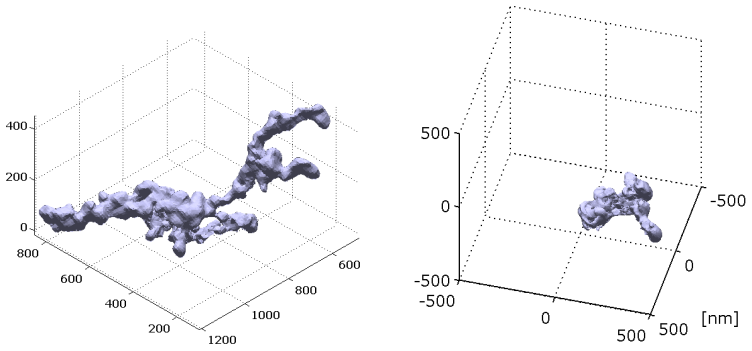

(a) Tomography of soot collected at the top of flame of propane/air.

(b) Tomography of soot collected at mid-HAB, in the flame of propane/air.

Figure 2.18: *Isosurfaces of the tomography reconstructed volumes exported to Matlab for discretization. Axis values are in nanometers.*

fractal analysis is very time costly. This limits the number of ex-situ experiments: we are limited to the 3D morphology parameters given by few number of particles in 3D. Here, we recall that the morphology is a result of physical and chemical phenomena. As previously explained in Section 2.2, D_f and k_f values reflect this history of the object. Also, Ouf et al. (2010) show that the morphology is not affected by this ex-situ process compared to other sampling methods and is representative of aggregate collected from flame. Therefore, we will consider that the sampled aggregates are representative enough for D_f and k_f of the population of soot that would have been collected under the same conditions.

The cube counting method explained in Section 2.4.2 is applied on tomography soot aggregates illustrated in Figure 2.18. As plotted in Figure 2.19, the 3D fractal analysis on the tomography object gives a value near $1.8 - 1.9$ for the fractal dimension of propane soot. This is in between the expected range of 1.6 to 1.9 for combustion soot and different from the tomography of diesel exhaust particles with D_f in the range of $2.2 - 3.0$ given by Adachi et al. (2007) and Van Poppel et al. (2005).

Note the upper and lower limits of the fractal behaviour in Figure 2.19. The lower limit (maximum voxel size) depends on the length scale of the aggregate, as stated by Oh and Sorensen (1998). The upper limit (minimum voxel size) is determined by the primary particle diameter d_p. Those limits are equivalent to the finite size effects on scattering studied by Oh and Sorensen (1999).

In 3D analysis, k_f can be computed directly from Equation 2.8 of the fractal theory for aggregates. R_g is computed in Matlab using the 3D surface infor-

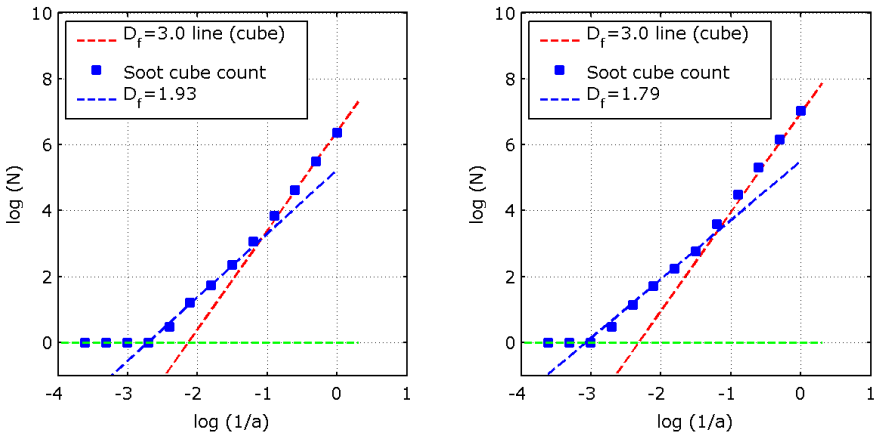

Figure 2.19: *3D fractal analysis on the tomography aggregates, (a) small aggregate (mid-height), (b) large aggregate (top of flame).*

mation given in Figure 2.18, without any need for empirical 2D-3D conversion such as given by Chakrabarty et al. (2006). For the Equation 2.8, N_p can be computed using the following relation:

$$V_{agg} = N_p \frac{4\pi}{3} \left(\frac{d_p}{2} \right)^3 \tag{2.16}$$

In equation 2.16, V_{agg} is the computed volume of the aggregate in Matlab, d_p is the mean diameter of the primary particles composing the aggregate. The primary particle determination was performed in Section 2.3.1. We remind that sufficiently large amount of clusters should normally be analysed to diminish the effect of selective sampling. The reason is that the analysis on particle (or cluster) size distribution of thermophoretically probed samples can be non representative as stated in the study of Caumont-Prim (2013) because the method can be selective on some types of aggregates affecting the range of size distribution. The following values are computed for tomography objects:

- Soot collected at the top of the flame: $D_f \approx 1.79$, $d_p \approx 27.8$nm, $N_p \approx 900$, $R_g \approx 284$nm, $k_f \approx 3.9$, $R_{veq} \approx 133$ nm.
- Soot collected at the mid-height of the flame: $D_f \approx 1.93$, $d_p \approx 36.9$nm, $N_p \approx 94$, $R_g \approx 100$nm, $k_f \approx 3.5$, $R_{veq} \approx 84$nm.

The above mentioned values show some discrepancy compared to the 2D cluster analysis given in Section 2.3.2. Note that in the determination of parameters, the fractal theory is used hence the particles are supposed to be in point contact.

The computed value of k_f drops rapidly (down to $k_f < 3$) if we consider slightly larger diameter d_p of primary particles in overlapping condition, or slightly larger number of primary particles. This difference is discussed in the following section, with comparison to the 2D fractal analysis on the same tomography objects.

2.6.3 Comparison with 2D values

The box counting method explained in Section 2.4.1 is applied on the projections of the tomography soot. As plotted in Figure 2.20, the identified 2D fractal dimensions are much lower than in 3D: $D_{f,2D} = 1.55 < D_{f,3D} = 1.79$ for the big aggregate (Figure 2.18(a)) and $D_{f,2D} = 1.58 < D_{f,3D} = 1.93$ for the small aggregate (Figure 2.18(b)).

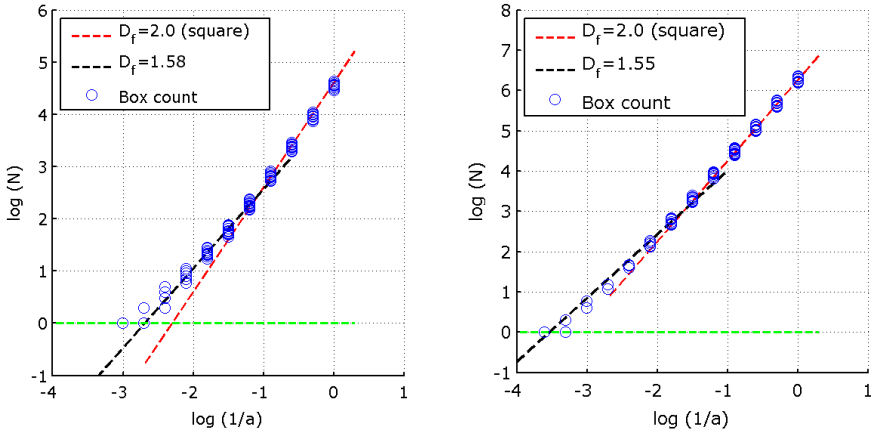

Figure 2.20: *2D fractal analysis on images taken for the tomography of the aggregate at tilt angles, (a) small aggregate (mid-height), (b) large aggregate (top of flame).*

True fractal dimension can be underestimated in 2D as cited by Samson et al. (1987), Rogak and Flagan (1992), Tence et al. (1986). Rogak et al. (1993) and Samson et al. (1987) states that $D_{f,2D}$ computed from the projected surface area is lower by $10-15\%$ than $D_{f,3D}$ computed in 3D. For large aggregates, the underestimation by 2D analysis is more important due to the overlapping of fractal branches and undetected pores (Samson et al. (1987)), to the screening effects and cluster anisotropy (Oh and Sorensen (1999), Katrinak et al. (1993)). Researchers tried to analyse the 2D data by using the projected information of numerically generated 3D geometries with different conversion values (Köylü

et al. (1995), Oh and Sorensen (1997a), Lee and Kramer (2004)). Semi-emprical schemes are proposed by Brasil et al. (1999) on the analysis of 2D projections of numerically generated 3D aggregates. These schemes are successfully applied by Wentzel et al. (2003) on palas and diesel soot given that the density is small i.e. the overlapping is negligible between particles and aggregates. There is not one precise relationship between the actual D_f in 3D and the D_f derived from 2D images, especially for large aggregates.

We note the difference between the 2D and 3D fractal parameter values which were given in Table 2.2. For example Samson et al. (1987) reported $D_{f,2D} = 1.47$ and $D_{f,3D} = 1.4$ from TEM analysis on acetylene flame soot, smaller than propane soot, combined to stereo pair observation and 3D numerical generation. They also reported $k_{f,2D} = 2.67$ and $k_{f,3D} = 3.49$. This can explain the bigger discrepancy obtained in our study between the 3D and 2D fractal values of larger aggregates.

The fractal dimension of soot collected at mid-height of the propane/air flame is greater than the one observed at the top of the flame. This is expected from the observations of Onischuk et al. (2003), even though this behaviour is contradictory to a previous in-situ analysis of fractal dimensions by di Stasio (2001) on ethylene flame. In comparison with propane-oxygen flame of Slowik et al. (2004), the mean particle size and the aggregate size is larger as expected.

The computed fractal parameters, either 2D or 3D, indicate a decreasing D_f with increasing HAB. This finding is consistent with literature data (Hu and Köylü (2004), Onischuk et al. (2003)). We didn't study the variation as a function of the radial position in the flame, as given for example by Hu and Köylü (2004). First, because our sweeping method of the flame does not allow such precision and second, because the variation was found to be very small as stated by Hu and Köylü (2004) for ethylene and acethylene flames.

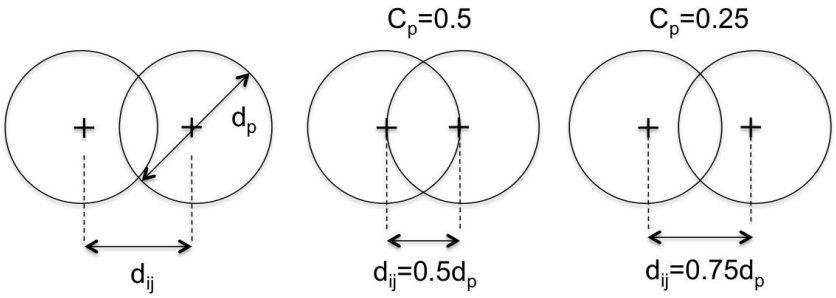

Figure 2.21: *Illustration of the overlapping (penetration) coefficient defined by Brasil et al. (2001).*

Brasil et al. (2001) state that the partial sintering (or overlapping) causes an

increase in the mass fractal prefactor for the same aggregate with the same D_f parameter. They proposed the following empirical relationship of Equation 2.17.

$$k_f = 1.3exp(2.2C_p) \tag{2.17}$$

In the above equation, C_p is the penetration coefficient defined by $C_p = (d_p - d_{ij})/d_p$, as illustrated in Figure 2.21. According to this semi-empirical relationship, the overlapping coefficients for our soot aggregates are $C_p = 0.50$ (Figure 2.18(a)) and $C_p = 0.45$ (Figure 2.18(b)). This information is important, and can explain the differences in the radiative properties between the tomography soot and representative numerical aggregates, presented in Chapter 4.

2.7 Conclusion and perspectives on morphology studies

Here we conlude Part I on the studies of morphology descriptions and 3D geometry generations of soot aggregates. To sum up, we applied tomography on soot aggregates in Chapter 1 to obtain complex soot geometry and applied microscopy observations to determine the sizes and fractal parameters of flame generated soot. In Chapter 2, we applied the conventional 2D fractal analysis, also a more reliable 3D fractal analysis, with comparison to tomography objects and representative numerical soot aggregates using fractal theory.

In this Chapter, we benefited from the advantage of tomography to obtain the real 3D parameters (N_p, k_f, D_f, volume V, surface area S, R_g) independently of each other, whereas the semi-empirical approaches in 2D are interdependent (Gwaze et al. (2006)).

Even though the relationship between the fractal parameters obtained in 2D and 3D analyses is not straightforward, Bushell et al. (2002) suggests the conditions given in equations 2.18 and 2.19. These relationships are valid from theoretical point of view but does not seem realistic for image analyses, because we know that fractal aggregates can have D_f values greater than 2 considering the real physics behind the aggregate formations. This is proved by the values given in literature for soot using 3D computations, such as for diesel soot (Colbeck et al. (1997)) and for TEM analysis (Samson et al. (1987)) and for numerically simulated aggregates (Mulholland et al. (1988)).

$$D_i = D_f, D_f < 2 \tag{2.18}$$

$$D_i = 2, D_f > 2 \tag{2.19}$$

Hu et al. (2003) proposed that D_f is independent of location within the flame. This seems to be more or less valid for the soot issued from methane according to the results given in Figure 2.12 for the 2D fractal analysis of clusters of aggregates. This behaviour is not clear for propane soot analysed in Section 2.3.2. We conclude that there are two reasons which can lead to this discrepancy:

- The first one can be the application of 3D analysis to an object which is not representative of the mean values. Note that we tried to select the largest aggregates for 3D analysis because they are the most susceptible to change the results of the simulations on the radiative properties and the radiative heat transfer.
- The second reason can be the variable accuracy depending on the size of the aggregates. The aggregates collected from methane flames reach barely micron sizes, independent of the location within the flame. Propane is more sooty with larger aggregates. Small aggregates are less favorable for 3D fractal analysis. If we observe the linear transition regions in Figures 2.19 (a) and (b), the applicable range of linear regression is bigger for larger aggregate, increasing the accuracy of the analysis.

We recall that Gwaze et al. (2006) indicated biased results of D_f depending on the image resolution. In the future, a sensitivity work can be carried out on the fractal analysis conditions (resolution of the images, numerical errors), the microscopy imaging conditions (recording time, contrast, electron energy), and the tomography reconstruction conditions (image resolution, reconstruction algorithms, etc.).

The 3D description of the complex shape by tomography can be used for the ex-situ analysis of emitted soot and of soot containing aerosols, for example to verify the definition of drag coefficients and permeability, porosity, specific surface area. 3D computed parameters can be used to validate/improve the empirical relations on the mass-mobility relationships. Our 3D results indicate also a specific surface area of around 88 m^2/g for the tomography aggregates, retrieved from 3D information $S/V = 13.2 \pm 0.8\ 10^7\ m^{-1}$ which was computed in Chapter 1, if we consider $\rho = 1500 kg/m^3$ (Horvath (1993),Slowik et al. (2004)). This value is higher, as expected, than the value 70 m^2/g computed from 2D SEM image analysis as a lower limit by Gwaze et al. (2006) for black carbon soot aggregates issued from wood combustion. This type of information can be used for the reactivity of soot.

Furthermore, the 3D information can be used to improve particle size distribution functions (PSDF) (Frencklach (2002), to correct the light absorption, light

scattering properties hence to determine more accurate in-situ results such as flame emissivity, soot volume fraction etc. For such corrective applications, the 3D analysis should be repeated to sufficiently large samples and for different fuel conditions. Here, we recall that in our study, the 3D analysis is intentionally performed on large aggregates to enhance the effect of the morphology on the radiative properties. The parametric information (fractal dimensions and prefactors) and 3D geometries will be used in Part II, for the determination of the radiative properties of soot aggregates.

Part II

Radiative properties

Chapter 3

Discrete Dipole Approximation

In this chapter, our computational methodology to determine the radiative properties of particles is explained. A brief review is given on the different existing tools. These tools are either applicable to perfect geometrical shapes (as spheres or groups of spheres) or to random geometries. Considering the complex shape of soot reaching micron sizes as obtained in the previous chapters, and the average temperature rates for industrial combustion applications, there is need for a tool applicable to complex geometries. Here, the thermal radiation is succeptible to probe significantly the complex geometry at visible and near infrared (IR) regions of the radiation spectrum. The Discrete Dipole Approximation (DDA) method offers the best compromise between its applicability to complex random geometries and its relatively less computational effort in between other methods such as Generalized Multi-particle Mie, T-matrix, etc. Besides, there are commonly used approximations such as Mie solution for volume equivalent sphere and Rayleigh-Debye-Gans solution for fractal aggregates. In this section, a brief reminder is given on the electromagnetic theory for radiation. Then, a review is made on the methods used in literature for the determination of the radiative properties of particles, with emphasis on soot aggregates. As we have complex shaped aggregates with high material refractive index, the utilisation of DDA can be cumbersome. In order to optimize the computational effort for soot material and to generate a comprehensive coupled workflow of "morphology analysis - radiative properties - radiation transfer", we developed our in-house DDA tool. Our methodology is explained with some clarifications on the important input/output parameters and numerical methods. Finally, to understand the limitations of the DDA method, test cases are presented for spherical particles and fractal aggregates, for different refractive indices and size parameters. For soot aggregates, the methods developed are further exploited in Chapter 4.

3.1 Complex material-radiation interaction

To implement the radiative properties of soot into the simulation of the radiative heat transfer, the spectra of the extinction coefficient β_λ, the scattering albedo ω_λ and the scattering phase function Φ_λ of the particulate media are needed. Different electromagnetic theories give the solution for isolated particles or isolated aggregates. Therefore those properties are to be generalized to an ensemble of particles (or an ensemble of aggregates). The derivation of those properties for groups of particles depends on their density in the flame, i.e. their volume fraction.

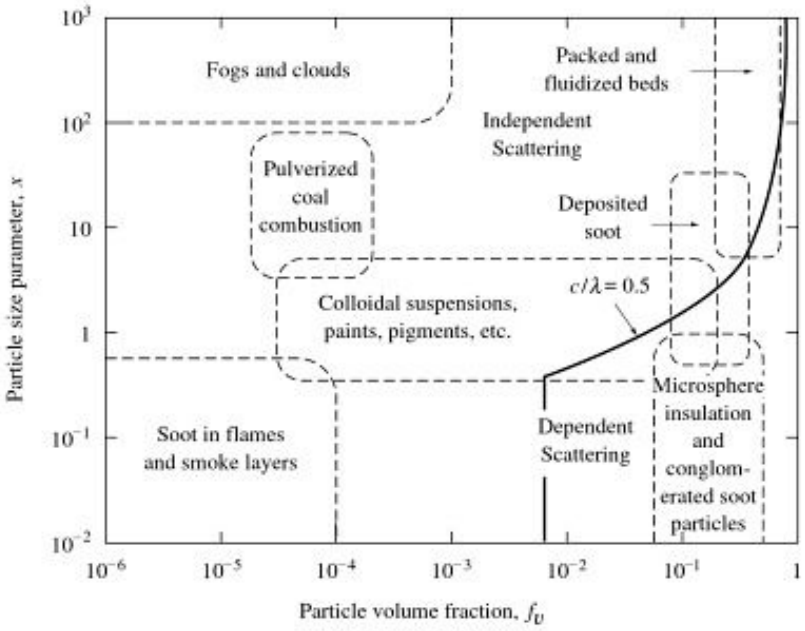

Figure 3.1: *Dependent and independent scattering regimes as a function of size paramater and volume fraction of particles, reprinted from Modest (2013) with permission from Elsevier, originally based on the works of Tien and Drolen (1987).*

At macroscopic level, we consider a cloud of soot particles with a specified volume fraction in the range of $f_v \sim 10^{-5}$ for a combustion flame, hence the distance between clusters is very large compared to the wavelength. The domains of dependent and independent scattering are illustrated in Figure 3.1, which shows that the volume fractions of flame soot are too low to consider dependent scattering between individual clusters. For such configuration, the simulation of the radiative properties for a group of clusters falls within the range of independent scattering. Therefore, the radiative properties of a cloud

of particles can be directly computed from the radiative properties of individual clusters.

In our work, the difficulty arises when the individual clusters have complex shapes. At microscopic scale, we observe micron size fractal-like aggregates with the spheroidal primary particles sticked and coalesced. This leads to a complex material-light interaction. Studies in literature try to consider this complex interaction by using various computational methods. Those methods are briefly reviewed in the following Section 3.2, with the explanation of our choice on DDA model.

3.2 Review of methods

When a particle is subject to radiation, as illustrated in Figure 3.2, the incident wave interacts with the particle as a function of the geometry of the particle and of the material properties of the host and the particle. The rate and the pattern of this interaction are determined by the solution of the Maxwell's equations with their boundary conditions.

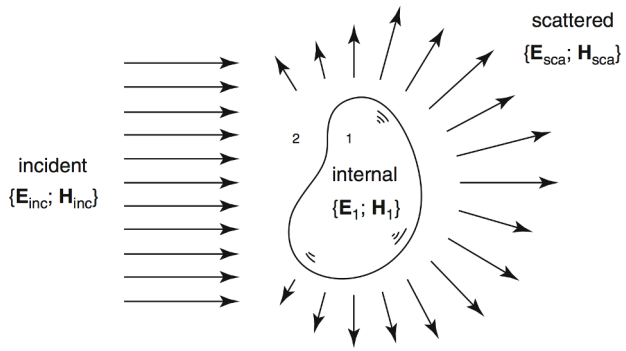

Figure 3.2: *Illustration of the incident and scattered electromagnetic fields around a random shaped particle, from Bohren and Huffman (1983).*

In literature, there are different analytical and computational methods used for the calculation of this light scattering problem. Here, we start with the simplest method, Mie theory for a spherical particle. It is followed by surface based and volume based computational methods applicable to complex geometries.

3.2.1 Mie solution

Mie theory proposes originally the solution of the radiative properties for an isolated sphere placed in vacuum (van de Hulst (1957)) and subject to an incident plane electromagnetic wave with the wavelength λ. The size of the sphere is defined relative to the incident wavelength, by its size parameter x computed as follows, where $D_p = 2R_p$ is the spherical particle diameter:

$$x = \frac{\pi D_p}{\lambda} \tag{3.1}$$

The Mie solution for the extinction and scattering efficiencies is computed as:

$$Q_{ext} = \frac{2}{x^2} \sum_{n=1}^{+\infty} (2n+1) \Re e(a_n + b_n) \tag{3.2}$$

$$Q_{sca} = \frac{2}{x^2} \sum_{n=1}^{+\infty} (2n+1)(|a_n|^2 + |b_n|^2) \tag{3.3}$$

The variables Q_{ext}, Q_{abs} and Q_{sca} are defined respectively as the extinction, absorption and scattering efficiencies of the particle. They are dimensionless parameters that indicate the particle capacity to extinguish, absorb and scatter the incident radiative power per surface area. Noting that the projected surface of a spherical particle remains the same for each incident direction, the dimensionless efficiencies can also be expressed in terms of cross-sections C with surface dimensions (m^2, nm^2 etc.) such as $Q_{ext} = C_{ext}/(\pi R_p^2)$, $Q_{abs} = C_{abs}/(\pi R_p^2)$ and $Q_{sca} = C_{sca}/(\pi R_p^2)$. It is worth recalling here that for the fractal-like aggregate properties obtained by DDA, we will compute the cross-sections C because the projected surface area of the aggregate depends on the projection directions.

By definition, the total extinction is the sum of the absorption and scattering. Hence, $Q_{ext} = Q_{abs} + Q_{sca}$ and the computation of the cross-sections are interdependent because Mie solution gives originally Q_{ext} and Q_{sca} variables. In the above Equations 3.2 and 3.3, the Mie series coefficients a_n and b_n are obtained from Riccati-Bessel functions $\psi_n(z)$ and $\zeta_n(z)$:

$$a_n = \frac{\psi_n{}'(mx)\psi_n(x) - m\psi_n(mx)\psi_n{}'(x)}{\psi_n{}'(mx)\zeta_n(x) - m\psi_n(mx)\zeta_n{}'(x)} \tag{3.4}$$

$$b_n = \frac{m\psi_n{}'(mx)\psi_n(x) - \psi_n(mx)\psi_n{}'(x)}{m\psi_n{}'(mx)\zeta_n(x) - \psi_n(mx)\zeta_n{}'(x)} \tag{3.5}$$

Further physical description of the model can be found in literature (Bohren and Huffman (1983)) with the solution of partial derivaties and the number of computed terms in the expansion series (Deirmendjian et al. (1961), Wiscombe (1980)). Note that in the following sections, the coefficient a_1 will be defined as the dipole polarizability of one spherical monomer in between other polarizability models. The complex optical index m of the material is expressed as in equation 3.6 (Born and Wolf (1999)), where n is the refractive index and k is the extinction index:

$$m = n + ik \tag{3.6}$$

In some studies, the volume equivalent material approach is used for soot computations. Therefore we will use the Mie solution for two cases. First, for the test cases of DDA with the analytical (numerically computed but exact) solution of Mie. Second, for the comparison of soot spectra computed by DDA and by Mie in the following Chapter 4. In this study, we consider homogeneous soot material hence the computational algorithms by Mätzler (2002) (computational tool scited by Wriedt (2012) on the review of existing and powerful Mie solution options). It is also possible to find other extensions of Mie solution for further considerations of spherical object such as coated spheres, magnetic properties, etc. This method being limited to spherical or spheroidal objects, the methods applicable to random geometries are reviewed in the next sections.

3.2.2 Surface Based Methods

T-matrix is a surface based method for the computation of light scattering problem and is first introduced by Waterman (1971) for metallic scatterers, technique known also as EBCM (extended boundary condition method). The technique is then extended to dielectric scatterers with random shapes, for example to aggegates of spheres (Peterson and Ström (1973), Xu (1995), Mackowski and Mishchenko (1996)). A recent and optimized version of the code applicable to random scatterers is proposed by Waterman et al. (2015).

In T-matrix method, the scatterer is replaced by a set of surface currents over the surface of the scatterer, so that the sources and fields are the same as the original scattering problem in the exterior region (Wriedt and Comberg (1998)). This method is said to be numerically exact because the "T-matrix" includes

the full solution of the scattering problem by relating the expansion coefficients of the incident field to the expansion coefficients of the scattered field. (In fact, EBCM is a method used to compute the "T-matrix" as stated by Nieminen et al. (2003)). The difficulty arises from the stability and the accuracy of numerical modeling for irregular grains (Wriedt and Comberg (1998)), high aspect ratios (Mishchenko et al. (2002)) and large scatterers with hundreds of spheres, due to the computation of expansion coefficients while trying to minimize the truncation errors.

GMT (Generalized Multipole Technique) is another surface based technique used to compute scattering from arbitrary geometries, nevertheless the studies indicate computational difficulties for small distances between particles (Comberg and Wriedt (1999)). This technique is also called MMT (Multiple Multipole Technique) (Ludwig (1989)).

3.2.3 Volume Based Methods

The volume based methods try to express the interaction of the scatterer volume with the incident field via the Volume Integral Equation (VIE) formulation. The VIE formulation is known to be the basic formula for DDA (Discrete Dipole Approximation) in its integral form and is expressed as follows (equation taken from Wriedt and Comberg (1998)):

$$\mathbf{E}(\mathbf{r}) = \mathbf{E_{inc}}(\mathbf{r}) + K \int_V (\varepsilon_{\mathbf{r}'} - 1)\mathbf{G}(\mathbf{r}, \mathbf{r}')\mathbf{E}(\mathbf{r}')\mathrm{d}^3\mathbf{r}' \tag{3.7}$$

In the above Equation 3.7, $\mathbf{E}$ is the total field, $\mathbf{r}$ is the position vector of an arbitrary point, $\mathbf{r}'$ is any point inside the scatterer with volume V, $\varepsilon_{\mathbf{r}'}$ is the dielectric permittivity of the scatterer, $K = 2\pi/\lambda$ is the wave number, and $\mathbf{G}(\mathbf{r}, \mathbf{r}')$ is the Green's dyadic for unbounded free space. The solution using VIE method is also called IEFS (Integral Equation Formulation for Scattering).

DDA (Discrete Dipole Approximation) is a special form of VIE where the volume integral in Equation 3.7 is approximated by discretizing the object into dipole elements and summing their radiative effects. This is purely a numerical method and the accuracy of the results should theoretically increase with finer discretization, hence with increasing number of dipoles. This method approximates the scatterer geometry by dipole elements, hence any complex geometry can be studied as long as the positions of the dipoles are known with their dielectric properties. DDA method is also called Coupled Dipole Method (CDM) because the dipoles (or the volume elements) are interacting with each other. We will see later, in Section 3.3 devoted to the description of DDA, that the volume integral of Equation 3.7 is replaced by an interaction matrix $\widetilde{\mathbf{A}}$ and that the field $\mathbf{E}$ is defined as $\mathbf{E_{ext}}$ in the DDA.

3.2.4 Other techniques

There are other rigorous solutions for the treatment of light scattering problems by random geometries such as FEM (Finite Element Method) (Volakis et al. (1994)), GMM (Generalized Multiparticle Mie solution) (Xu and Gustafson (2001)) and FDTD (Finite Difference Time Domain).

The FEM method is not a well known and not widely applied method for light scattering problem, hence the applicability limits are not clear. Therefore its usage to our aggregated shapes is not considered. GMM is an extension of the analytical Mie solution to aggregates composed of identical hard spheres hence not on random geometries.

The FDTD method is applicable to random scatterers. Here, the temporal and spatial derivatives of Maxwell's equations are reformulated by their finite-difference equivalents. This method is applicable to random geometries and not limited to dieletric materials. For example, FDTD is successfully used on Gaussian spheres by Sun et al. (2012). Nevertheless, the computational effort is significant, first due to discretization of the host medium with the scatterer and second due to a much severe discretization criterion than DDA modeling.

3.2.5 RDG-FA

This theory is based on Rayleigh scattering by small particles which is a special case of Mie scattering for particles small compared to the incident wavelength (Bohren and Huffman (1983)).

While the RDG (Rayleigh-Debye-Gans) theory considers the summation of the properties of individual particles, thus neglecting the interactions between them, RDG-FA (RDG for Fractal Aggregates) is adapted by Dobbins and Megaridis (1991) for an application to fractal aggregates.

The RDG-FA method is computationally easy and extensively used for the soot radiation and its experimental measurement, as cited in many studies of Dobbins, Köylü, Sorensen. Hence, the method is coupled to rigourous solution techniques as DDA and GMM, either to test the accuracy limits of RDF-FA (Farias et al. (1996) using IEFS) or to bring improvements to the RDG-FA method for the computation of thermal radiative properties of soot (Yon et al. (2014)). Even though the technique does not take into account explicitely the random scatterer geometry (making it therefore not applicable to our tomography soot) we will include the results obtained by RDG-FA in Chapter 4 for numerically generated aggregates due to its common usage for soot.

In the following equations, the model is reviewed for the cross-sections C_{abs}, C_{sca} and the scattering phase function Φ of the aggregate. The model proposed by Dobbins and Megaridis (1991) is described. The subscripts "agg" and "p" account for the "aggregate" and the "primary particle", respectively:

$$C_{abs,agg} = N_p C_{abs,p} \tag{3.8}$$

$$C_{sca,agg} = N_p^2 C_{sca,p}\, g(K, R_g, D_f) \tag{3.9}$$

$$\Phi_{agg}(\theta) = \frac{4\pi}{C_{sca,agg}} \frac{C_{vv,agg}(\theta) + C_{hh,agg}(\theta)}{2} \tag{3.10}$$

The notation $C_{vv,agg}(\theta)$ and $C_{hh,agg}(\theta)$ accounts for the differential scattering cross-sections which satisfy the following condition (equation taken from Eymet et al. (2002)):

$$C_{vv,agg}(\theta) = C_{hh,agg}(\theta) = N^2 C_{vv,p}(\theta) f(qR_g) \tag{3.11}$$

In the above equations 3.10 and 3.11, θ is angle between the incident direction and the scattering direction, the subscripts "vv" (vertical-vertical) and "hh" (horizontal-horizontal) define the directions of polarization of the incident and scattered lights. R_g is radius of gyration of the aggregate, D_f is the fractal dimension of the aggregate, x_p is the size parameter of the primary particles, $K = 2\pi/\lambda$ is the wave number. The particle properties are computed from the Rayleigh scattering solution for small particles as follows:

$$C_{abs,p} = \frac{4\pi x_p^3}{K^2} \mathrm{Im}\left(\frac{m^2 - 1}{m^2 + 2}\right) \tag{3.12}$$

$$C_{sca,p} = \frac{8\pi x_p^6}{3K^2} \left|\frac{m^2 - 1}{m^2 + 2}\right|^2 \tag{3.13}$$

The function g in Equation 3.9 is defined as follows:

$$g(K, R_g, D_f) = \left(1 + \frac{4}{3D_f} K^2 R_g^2\right)^{(-D_f/2)} \tag{3.14}$$

The structure factor f is a function of the aggregate size and morphology:

$$f(qR_g) = \exp\left(\frac{-(qR_g)^2}{3}\right) \text{ for } (qR_g)^2 \leqslant 1.5D_f \text{ (Guinier regime)} \quad (3.15)$$

$$f(qR_g) = \left(\frac{e(qR_g)^2}{1.5D_f}\right)^{(-D_f/2)} \text{ for } (qR_g)^2 > 1.5D_f \text{ (Power-law regime)} \quad (3.16)$$

Finally, the magnitude q of the scattering wave vector is defined as:

$$q(\theta) = \frac{4\pi}{\lambda}\sin\left(\frac{\theta}{2}\right) \quad (3.17)$$

This theory allows a relatively easy approximation of the radiative properties of soot aggregates as a function of the wavelength λ. Note that in those semi-empirical relationships, the morphology of the aggregate is described by limited parameters, such as N_p, R_g and D_f. As we need a more general applicability on complex shapes, a more rigorous solution is looked for as will be explained in the next paragraph.

3.2.6 Choice of model for radiative properties

Many researchers who investigated the effect of the aggregate morphology on the radiative properties of combustion soot (and on the radiative heat transfer) studied numerical and analytical techniques like DDA (Yon et al. (2014)), IEFS (Eymet et al. (2002)), T-matrix (Mishchenko et al. (2013)), GMM (Liu and Snelling (2008)), RDG-FA or simply the Mie theory using the equivalent volume approach for the computation of the radiative properties (Sorensen (2011) and references therein).

Although the methods like DDA allow the simulation on arbitrary geometries not limited to clusters of spheres, many recent works (Liu and Mishchenko (2007), Liu, Mishchenko, and Arnott (2008), Mishchenko, Liu, and Mackowski (2013)) try to find these properties based on numerically exact methods for numerically generated aggregates where the monomers are point-contact spheres, therefore avoiding the problem of complex sintered geometry of soot in the determination of radiative properties.

The morphology studies in Part I have shown that soot issued from combustion flames has a complex geometry. For such arbitrary shapes, the interaction of

the incident radiation with the object is complex. The analytical solution of this interaction is not straigthforward: either the exact solution alorithms need to be numerically modeled and solved, or semi-empirical models are used. As the properties of representative numerical aggregates will be compared to the ones of tomography object with random geometry, we wish to do the comparison on the basis of the same simulation tool. In this case, DDA offers the best option, applicable to random geometries with relatively easy handling for aggregated shapes.

There exist publicly available DDA codes, such as DDSCAT (Draine and Flatau (2013)) and ADDA (Yurkin and Hoekstra (2011)) as the most commonly used and actively updated codes (Wriedt (2009)). Those codes are optimized for the computation of large systems, hence the accelerating methods such as parallelization and FFT are implemented into the code. This latter imposes a cubic lattice of dipoles. While this constraint is not problematic for tomography soot, it prevents the usage of 1 dipole per monomer for the numerically generated aggregates, which convinced us to develop our own simulation tool. Another advantage to have an in-house code is to have the complete control on the implemented models for the polarizability, the computation of the scattering properties and the direction-averaged radiative properties.

In the next sections, the DDA solution is detailed with emphasis given on the models selected for the simulation of the soot material and of the aggregate shapes. The model description is followed by the code development to find the thermal radiative properties. Test cases are presented that compare DDA results to the Mie solution for spheres of different complex refractive indices. Finally, preliminary applications are presented on representative numerical aggregates.

3.3 Discrete Dipole Approximation

In this section, the modeling principle of DDA technique for the determination of thermal radiative properties in the far field is briefly presented. This technique was originally proposed by Purcell and Pennypacker (1973) and further developed in the studies of Draine (1988), Draine and Goodman (1993). In our study, the equations are adapted from Enguehard (2009) and Lallich (2009). An extensive review and demonstration of the model can be found in the works of Enguehard (2009). The study of Lallich (2009) presents DDA modeling towards an application on nanoporous silica aggregates. In our work, the focus is on soot aggregates hence any choice of model is to be tested and validated for soot material.

In Chapter 5, it is considered the radiative properties of the particulate soot are independent the host gaseous medium. The absorption and scattering spectra

are then assumed to be the summation of the gaseous and particulate media properties. This assumption will be explained in Chapter 5, Section 5.1.2. Therefore the DDA simulations of the radiative properties of soot will be performed under the assumption that the soot aggregate is surrounded by vacuum.

3.3.1 Linear system of unknown dipole moments

The Discrete Dipole Approximation (DDA) allows the computation of the electromagnetic field around an object, without any need of a regular geometry as in the case of Mie solution for spheres.

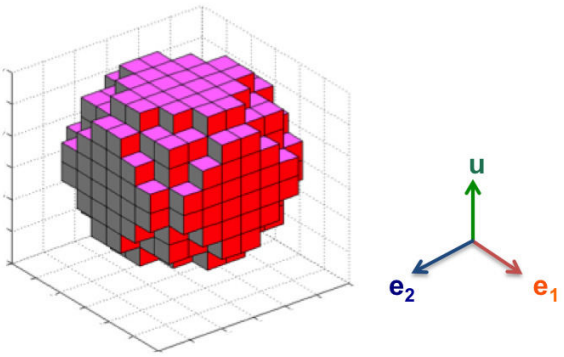

Figure 3.3: *Illustration of the discretization of an object into volume elements for DDA; the computations of the radiative properties are to be performed for an incident plane wave direction* $\mathbf{u}$ *with two different linear polarizations* $\mathbf{e}_1$ *and* $\mathbf{e}_2$*, noting that* $\mathbf{u}$, $\mathbf{e}_1$, $\mathbf{e}_2$ *is an orthogonal set of unit vectors.*

The methodology consists of discretizing the object, subject to an incident electromagnetic field, into N dipole elements as illustrated in Figure 3.3. The discretization should satisfy two conditions: path difference of the incident wave passing through the volume element should be negligible, and the size of the volume elements should be smaller compared to the attenuation length of the incident wave inside the material. Those conditions are expressed in terms of the following condition by Draine (1988):

$$|m|K\delta < 1 \tag{3.18}$$

In the above Equation 3.18, m is the complex optical index of the material, K is the wave number, δ is the characteristic size of the volume element i.e. of the dipole.

Each dipole is considered to be polarized under the effect of the external electromagnetic field. This polarization amount is expressed in terms of the dipole moment $\mathbf{\Pi}_j$:

$$\mathbf{\Pi}_j = \alpha_j \mathbf{E}_{\mathbf{ext},j} \tag{3.19}$$

The dipole moment $\mathbf{\Pi}_j$ is dependent on the material properties of the dipole element via its polarizability tensor α_j. In our study on soot, we consider isotropic material properties. Hence, the polarizability is reduced to a single scalar value of α_j from a diagonal tensor where the diagonal elements satisfy the relation $\alpha_{xx,j} = \alpha_{yy,j} = \alpha_{zz,j}$.

In the above Equation 3.19, the external (local) field at dipole j is the sum of the electromagnetic field incident on the object and of the field emitted by the $(N-1)$ neighbouring dipoles:

$$\mathbf{E}_{\mathbf{ext},j} = \mathbf{E}_{\mathbf{inc},j} + \sum_{k \neq j} \mathbf{E}_{k,j} \tag{3.20}$$

In Equation 3.20, $\mathbf{E}_{\mathbf{inc},j}$ is the incident electric field at dipole j and $\mathbf{E}_{k,j}$ is the electric field generated by the neighbouring oscillating dipole k on the dipole j. The self-radiation effect of the dipole j is accounted for in the polarizability term α_j and will be explained in Section 3.4.

The field $\mathbf{E}_{\mathbf{inc},j}$ at dipole j is generated by a plane wave incident on the object and is function of the dipole position as follows:

$$\mathbf{E}_{\mathbf{inc},j} = \mathbf{E_0} \exp(iK\mathbf{u} \cdot \mathbf{r}_j - i\omega t) \tag{3.21}$$

In the above Equation 3.21, $\mathbf{E_0}$ is the external field with the propagation direction $\mathbf{u}$ and magnitude E_0, $K = 2\pi/\lambda$ is the wave number, ω is the angular frequency of the incident plane wave. The position of the dipole j is defined by the vector $\mathbf{r}_j$. The field emitted by an oscillating dipole of dipole moment $\mathbf{\Pi}_k$ located at $\mathbf{r}_k$ at position $\mathbf{r}_j$ has the following expression (Jackson (1975)):

$$\mathbf{E}_{k,j} = \frac{1}{4\pi\varepsilon_0} \frac{\exp(iKr_{jk})}{r_{jk}} \left\{ K^2(\mathbf{n} \times \mathbf{\Pi}_k) \times \mathbf{n} + [3\mathbf{n}(\mathbf{n} \cdot \mathbf{\Pi}_k) - \mathbf{\Pi}_k] \left(\frac{1}{r_{jk}^2} - \frac{iK}{r_{jk}} \right) \right\} \tag{3.22}$$

$$r_{jk} = |\mathbf{r}_j - \mathbf{r}_k| \tag{3.23}$$

$$\mathbf{n} = \frac{(\mathbf{r}_j - \mathbf{r}_k)}{r_{jk}} \tag{3.24}$$

We note that the above Equation 3.22 is equivalent to the original formulation of Purcell and Pennypacker (1973) except the constant $1/4\pi\varepsilon_0$. The original formulation is expressed in terms of point dipoles hence this constant does not appear in their linear system representation.

In our model, α_j involves the dipole material volume, either a point dipole or a volume equivalent cubic dipole, as will be formulated in section 3.4.1. Very recently, Smunev et al. (2015) demonstrated the applicability of rectangular dipoles for DDA. According to their simulations with the ADDA code, the results obtained with cubic dipoles (either with classical DDA formulation or IGT-Integration of Green's Tensor) have good accuracy in the static limit. They concluded that this new dipole formulation, implemented in ADDA code, works well except for "high-contrast dielectric problems with $0 < \varepsilon < 0.1$ or $\varepsilon > 10$ ". Subsequently, the Equation 3.22 can be written in the matrix form:

$$\begin{aligned}\mathbf{E}_{k,j} = \frac{\exp(iKr_{jk})}{4\pi\varepsilon_0 r_{jk}^3} \Bigg[(K^2 r_{jk}^2 + iKr_{jk} - 1) \begin{pmatrix} 1 & 0 & 0 \\ 0 & 1 & 0 \\ 0 & 0 & 1 \end{pmatrix} \\ +(3 - 3iKr_{jk} - K^2 r_{jk}^2) \begin{pmatrix} n_x^2 & n_x n_y & n_x n_z \\ n_x n_y & n_y^2 & n_y n_z \\ n_x n_z & n_y n_z & n_z^2 \end{pmatrix} \Bigg] \begin{pmatrix} \Pi_{kx} \\ \Pi_{ky} \\ \Pi_{kz} \end{pmatrix}\end{aligned} \tag{3.25}$$

Finally the relation given in equation 3.25 can be expressed in terms of the dipole moment vector $\mathbf{\Pi}_k$ and the dipole-dipole (coupled dipole) interaction matrix:

$$\mathbf{E}_{k,j} = -\mathbf{A}_{k,j}\mathbf{\Pi}_k \tag{3.26}$$

When the Equation 3.26 is replaced into Equation 3.20 and then 3.19, the follwing linear system is obtained, where the only unknowns are the dipole moments $\mathbf{\Pi}_j$:

$$\widetilde{\mathbf{A}}\widetilde{\mathbf{\Pi}} = \widetilde{\mathbf{E}}_{inc} \tag{3.27}$$

In the linear system of Equation 3.27, $\widetilde{\mathbf{A}}$ is a 3Nx3N complex symmetrical matrix where the off-diagonal elements are computed from $\mathbf{A}_{k,j}$ in equation 3.25 and verifying the property of $\mathbf{A}_{k,j} = \mathbf{A}_{j,k}$. The diagonal tensors for $\mathbf{A}_{j,j}$ are simply $1/\alpha_j$ for isotropic material. The matrix illustration of this linear system of equations can be found in the works of Loke et al. (2011).

3.3.2 Solution of the system

For the numerical solution of the above complex linear system, the Bi-CGSTAB (bi-conjugate gradient stabilized) algorithm is used (Barrett et al. (1994)). This solution technique has relatively good convergence rates for symmetric DDA dipole interaction matrix, though is not limited to symmetry conditions as the QMR (quasi-minimal residual) algorithm having a faster convergence for higher refractive indices (Yurkin et al. (2007)). For faster convergence with Bi-CGSTAB, the formulation in terms of dipole moments $\mathbf{\Pi}_k$ is replaced by $\mathbf{\Pi}_k/\alpha_j E_0$ and the linear system of equations is established anew as an operation equivalent to a preconditioning. Some results on the convergence are presented in Section 3.4.4.

3.3.3 Thermal radiative properties

In this work, the radiative properties of objects are computed in order to be implemented into the radiative heat transfer equation. The thermal radiation is considered as non-polarized electromagnetic radiation (Modest (2013)). Hence, the extinction, absorption and scattering properties are to be computed accordingly.

The dipole moments are computed for two linearly polarized illuminations, with the incident direction $\mathbf{u}$ and orthogonal polarization directions $\mathbf{e_1}$ and $\mathbf{e_2}$ respectively. We note that we inserted two formulations in our code: radiative properties for a linearly polarized radiation and for non polarized radiation. In order to increase the performance of our code, we solve simultaneously the two linear systems corresponding to the polarizations $\mathbf{e_1}$ and $\mathbf{e_2}$ and the thermal radiative properties given by arithmetic means of the polarized properties. This translates into the following relations for C_{ext}^{NP}, C_{abs}^{NP}, C_{sca}^{NP}, the extinction, absorption and scattering cross sections of an ensemble of oscillating dipoles (Enguehard (2009)):

$$C_{ext}^{\mathrm{NP}}(\mathbf{u}) = \frac{K}{2\varepsilon_0 E_0}\mathrm{Im}\left\{\sum_{1\leq j\leq N}\left[\mathbf{e}_1\cdot\mathbf{\Pi}_j(\mathbf{u},\mathbf{e}_1)+\mathbf{e}_2\cdot\mathbf{\Pi}_j(\mathbf{u},\mathbf{e}_2)\right]\exp(-iK\mathbf{u}\cdot\mathbf{r}_j)\right\} \tag{3.28}$$

$$C_{abs}^{\mathrm{NP}} = \frac{K}{2\varepsilon_0 E_0^2}\sum_{1\leq j\leq N}\left[\|\mathbf{\Pi}_j(\mathbf{u},\mathbf{e}_1)\|^2+\|\mathbf{\Pi}_j(\mathbf{u},\mathbf{e}_2)\|^2\right]\left(\mathrm{Im}\frac{1}{\alpha_j^*}-\frac{K^3}{6\pi\varepsilon_0}\right) \tag{3.29}$$

$$C_{sca}^{\mathrm{NP}}(\mathbf{u}) = \frac{1}{2}\left(\frac{K^2}{4\pi\varepsilon_0 E_0}\right)^2 \int_{4\pi} \left\{ \left\| \mathbf{n} \times \left[\sum_{1\leqslant j\leq N} \mathbf{\Pi}_j(\mathbf{u},\mathbf{e}_1)\exp(-iK\mathbf{n}\cdot\mathbf{r}_j) \right] \right\|^2 + \left\| \mathbf{n} \times \left[\sum_{1\leqslant j\leq N} \mathbf{\Pi}_j(\mathbf{u},\mathbf{e}_2)\exp(-iK\mathbf{n}\cdot\mathbf{r}_j) \right] \right\|^2 \right\} \mathrm{d}\Omega \tag{3.30}$$

In DDA modeling, the cross-sections C_{ext}^{NP}, C_{abs}^{NP}, C_{sca}^{NP} are computed independently. This is advantegous because the quality of the computation can be checked upon whether the condition $C_{ext}^{\mathrm{NP}} = C_{abs}^{\mathrm{NP}} + C_{sca}^{\mathrm{NP}}$ is satisfied. In the above equations, the NP superscript accounts for non-polarized properties. Once the scattering cross-section is computed, it is also possible to compute the phase function Φ^{NP} and the corresponding asymmetry parameter g^{NP}:

$$\Phi^{\mathrm{NP}}(\mathbf{u},\mathbf{n}) = \frac{2\pi}{C_{sca}^{\mathrm{NP}}(\mathbf{u})}\left(\frac{K^2}{4\pi\varepsilon_0 E_0}\right)^2 \left\{ \left\| \mathbf{n} \times \left[\sum_{1\leqslant j\leq N} \mathbf{\Pi}_j(\mathbf{u},\mathbf{e}_1)\exp(-iK\mathbf{n}\cdot\mathbf{r}_j) \right] \right\|^2 + \left\| \mathbf{n} \times \left[\sum_{1\leqslant j\leq N} \mathbf{\Pi}_j(\mathbf{u},\mathbf{e}_2)\exp(-iK\mathbf{n}\cdot\mathbf{r}_j) \right] \right\|^2 \right\} \mathrm{d}\Omega \tag{3.31}$$

$$g^{\mathrm{NP}}(\mathbf{u}) = \frac{1}{4\pi}\int_{4\pi} \Phi^{\mathrm{NP}}(\mathbf{u},\mathbf{n}) cos(\mathbf{u},\mathbf{n})\, d\Omega \tag{3.32}$$

3.3.4 Note on the limitations of DDA

DDA has its own limitations as all approximate models trying to mimic the exact solutions of physical phenomena. Those limitations are either numerical or physical constraints.

The major physical constraint of DDA is the interpretation of the discretized volume elements as dipoles. This implies a sufficiently dense discretization, in order to consider each element as a point dipole. This condition is not solely a geometrical constraint but also depends on material properties. For a good enough precision of the DDA solution, the phase shift and the extinction should

be small enough in each discretization element. This is expressed in terms of the distance between dipoles (in our case the dipole size a_{dip}) and of the complex optical index m. As mentioned previously, our discretization should satisfy the following simulation condition (Draine and Flatau (1994)):

$$|m|\, K a_{dip} \leqslant \beta_{Draine} \tag{3.33}$$

In the above equation 3.33, β_{Draine} depends on the desired precision of the solution. While for cross-section values $\beta_{Draine} \leqslant 1$ is known to be good enough (Draine (1988)), a smaller constant gives a better precision for the computation of the phase function.

Regarding the accuracy of DDA, researchers compare the solution of the sphere properties with DDA. The comparison of Xu and Gustafson (1999) on aggregates of two identical spheres indicates a good performance of DDA for the complex refractive index and the size parameter in the range of $|m| \leq 2$ and $|m|\, \pi D_{veq}/\lambda \leq 10$, when compared to the rigourous solution for groups of spheres (Xu (1995), Xu (1997), lin Xu (1998)). Here D_{veq} is the diameter of the sphere with equivalent material volume to the cluster. For large clusters, the studies of Okamoto and Xu (1998) compare the results of DDA to the ones obtained from the rigourous solution (T-matrix) and conclude that DDA errors less than 2% for clusters composed of primary particles with $x \leq 0.2$. Good performance of DDA is also cited by Kimura (2001) for large aggregates composed of hundreds of primary particles with size parameter $x \sim 0.1$.

3.4 In-house DDA code

3.4.1 Dipole polarizability

DDA model is based on the discretizaton of the material into volume elements defined by their polarizability. In this paragraph, we briefly summarize the main models found in literature for the computation of dipole polarizability in DDA simulations. As will be explained later, one polarizability formulation is not capable of modeling accurately every type of material on the overall radiation spectrum.

3.4.1.1 CM

The basis of all polarizability prescriptions are issued from the Clausius-Mossotti (CM) formulation expressed as (Purcell and Pennypacker (1973)):

$$\alpha_j^{\mathrm{CM}} = 3\varepsilon_0 v_j \frac{\varepsilon_j - 1}{\varepsilon_j + 2} \tag{3.34}$$

This is the generalized version of the original dipole polarizability solution for a sphere. In equation 3.34, v_j is the volume of material corresponding to the j^{th} dipole, ε_j is the relative dielectric permittivity of the material of j^{th} dipole. Noting that this is the exact formulation of the dipole static polarizability, the usage of formulation in the non-static regime imposes the discretization condition $Ka_{dip} << 1$, where a_{dip} is the characteristic size of the dipole.

3.4.1.2 CMRR

Draine (1988) proposes a correction to the CM formulation of the polarizability as follows:

$$\alpha_j^{\mathrm{CMRR}} = \frac{\alpha_j^{\mathrm{CM}}}{1 - \dfrac{iK^3\alpha_j^{\mathrm{CM}}}{6\pi\varepsilon_0}} \tag{3.35}$$

This correction takes into account the contribution of the oscillating dipole itself on the external field $\mathbf{E_{ext}}$ at finite frequencies where the condition $Ka_{dip} << 1$ is not satisfied, noting that CM polarizability is recovered at the zero-frequency limit.

3.4.1.3 LDR

Draine and Goodman (1993) proposed a new formulation on the basis of the CM polarizability, called the Lattice Dispersion Relation (LDR):

$$\alpha_j^{\mathrm{LDR}} = \frac{\alpha_j^{\mathrm{CM}}}{1 + \dfrac{\alpha_j^{\mathrm{CM}}}{4\pi\varepsilon_0 a_{dip}^3}\left[b_1 + m^2 b_2 + m^2 b_3 S\right](Ka_{dip})^2 - \dfrac{2i(Ka_{dip})^3}{3}} \tag{3.36}$$

In the above Equation 3.36, the constant values are: $b_1 = -1.8915316$, $b_2 = 0.1648469$, $b_3 = -1.7700004$. The variable S is a function of the incident electromagnetic wave direction and the axes of the dipole lattice. In our case, the cartesian coordinates are used for the axes of the dipole lattice and for the description of the electromagnetic wave, thus S is as follows:

$$S = (\mathrm{u}_x e_x)^2 + (\mathrm{u}_y e_y)^2 + (\mathrm{u}_z e_z)^2 \tag{3.37}$$

In this formulation the radiative reaction correction is already taken into account Collinge and Draine (2004). The LDR polarizability model is known to be performant for low refractive indices but its accuracy is lower for highly absorbing materials with indices $\mathrm{Im}(m) \geqslant 2$ according to Collinge and Draine (2004).

3.4.1.4 DGF/VIEF

Another formulation for dipole polarizability is proposed by Goedecke and O'Brien (1988) and Hage and Greenberg (1990) for DGF/VIEF (Digitized Green's Function/ Volume Integral Equation Formulation) modeling, equivalent to DDA as mentioned previously in the volume integral methods for electromagnetic theory simulations. As LDR, it is a modified version of the CM formulation:

$$\alpha_j^{\mathrm{DGF}} = \frac{\alpha_j^{\mathrm{CM}}}{1 - \left(\frac{1}{12\pi}\right)^{(1/2)} \frac{\alpha_j^{\mathrm{CM}}}{\varepsilon_0 a_{dip}^3} (K a_{dip})^2} \tag{3.38}$$

To take into account the correction for the radiative reaction, α_j^{CM} in equation 3.35 can be replaced by α_j^{DGF}.

3.4.1.5 LFCSP

Given the decreasing accuracy of the polarizability models at finite frequencies, Rahmani et al. (2002) propose a correction of the external (local) field on a dipole as a function of the scatterer object geometry and dipole localisation. Here $\alpha_j^{\mathrm{LFCSP}}$ accounts for the Local Field Corrected Static Polarizability (Rahmani et al. (2004)). According to our modeling of DDA solution system, the original expression is:

$$\alpha_j^{\mathrm{LFCSP}} = \varepsilon_0(\varepsilon_j - 1)\Lambda_j^{-1} a_{dip}^3 \tag{3.39}$$

In the above Equation 3.39, Λ_j is the local field tensor and is a function of the depolarization tensor of the scatterer object (Rahmani et al. (2002)). In parallel to this work, Collinge and Draine (2004) used this expression α_j^{RCP} and applied the LDR modification to obtain a "Surface Corrected" version $\alpha_j^{\mathrm{SCLDR}}$.

3.4.1.6 $a_{1,Mie}$

Another description for polarizability is proposed by Doyle (1989):

$$\alpha_j^{a_1,Mie} = i\frac{6i\pi\varepsilon_0 a_{1,Mie}}{K^3} \tag{3.40}$$

This description is derived from the first term of Mie's expansion series for the radiative properties of spherical particles. Therefore, it gives the polarizability amount of an isolated sphere and successfully used for spherical particles of size parameters beyond 100 by Okamoto (1995). This model is successfully adopted in the studies of Lallich (2009) for silica aggregates composed of hundreds of primary spherical particles with diameter of ten nanometers.

3.4.1.7 Choice of model for dipole polarizability

In Table 3.1, several literature results on different polarizability formulations are listed. Only the simulation results with high refractive indices are given as our focus is on soot material. The results of Collinge and Draine (2004) and Rahmani et al. (2004) using LFCSP formulation indicate relatively accurate results for spherical scatterers with high permittivity values.

Variable	Model	x	$\lvert m\rvert Ka_{dip}$	m	% Error
$C_{sca,abs,ext}$	VIEF (Hoekstra et al. (1998))	5	0.51	$2.5+1.4i$	4
$C_{sca,abs}$	DGF (Draine and Goodman (1993))	≤ 3.2	–	$3+4i$	5, 35
$C_{sca,abs}$	LDR (Draine and Goodman (1993))	≤ 3.2	–	$3+4i$	15, 60
$C_{sca,abs,ext}$	LDR (Draine and Flatau (1994))	–	–	$2+i$	6
$C_{sca,abs,ext}$	SCLDR (Collinge and Draine (2004))	≤ 1.5	–	$5+4i$	5
$C_{sca,abs,ext}$	RCB (Collinge and Draine (2004))	≤ 1.5	–	$5+4i$	7
$C_{sca,abs,ext}$	CMRR (Rahmani et al. (2004))	–	≤ 0.7	$1.8+0.4i$	<2
$C_{sca,abs,ext}$	LFCSP (Rahmani et al. (2004))	–	≤ 0.7	$1.8+0.4i$	<1
$C_{sca,abs,ext}$	CMRR (Rahmani et al. (2004))	–	≤ 0.7	$2.5+1i$	<6
$C_{sca,abs,ext}$	LFCSP (Rahmani et al. (2004))	–	≤ 0.7	$2.5+1i$	<1
$C_{sca,abs,ext}$	CMRR (Rahmani et al. (2004))	–	≤ 0.7	$2.5+3.9i$	<5 (<30 for C_{abs})
$C_{sca,abs,ext}$	LFCSP (Rahmani et al. (2004))	–	≤ 0.7	$2.5+3.9i$	<5
$C_{sca,abs,ext}$	CMRR (Rahmani et al. (2004))	–	≤ 0.7	$7.4+9.4i$	<10 (<60 for C_{abs})
$C_{sca,abs,ext}$	LFCSP (Rahmani et al. (2004))	–	≤ 0.7	$7.4+9.4i$	<10

Table 3.1: *Errors of the literature results obtained by DDA compared to Mie solution for sphere using different polarizability models at high refractive indices. Some results are adapted from the review of Lallich (2009).*

Even though $a_{1,Mie}$ modeling for polarizability has a good performance for spheres, in our study this description is not considered because we want to do a comparative study between numerical aggregates and tomography aggregates, hence we try to keep the same simulation conditions as much as possible.

The $\alpha_j^{\mathrm{LFCSP}}$ formulation is promising but two difficulties arise with the solution of the system of DDA (Equation 3.27): the applicability on random geometries and the derivation of the solution system for random geometries. Rahmani et al. (2004) states that their formulation is only valid for uniformly polarized scatterer objects and the system of Equation 3.27 should be revised for non-uniformly polarized scatterers. The second problem is that the derivation of the depolarization tensor, thus the local field tensor Λ_j, is only straightforward for spheres but not trivial for random geometries. If one would like to investigate further this formulation, one can numerically compute the depolarization tensor (Yaghjian (1980)) or change the formulation of the solution system as presented by Chaumet, Sentenac, and Rahmani (2004). These two points increase the complexity level of our DDA modeling.

In our study, the numerical aggregates are simulated with 1 dipole/monomer due to the small size of the monomers compared to the radiation spectrum considered. The test case is presented in Section 3.5.1. This condition satisfies the condition given in equation 3.33 and the rule of thumb suggesting around 10 dipoles per wavelength (Yurkin and Hoekstra (2011)). Indeed, the clustering of touching spheres is a special case which should be treated carefully for light scattering problems. For a deeper physical insight of this special problem, one can refer to the works of Gérardy and Ausloos (1980),Claro (1982), Sansonetti and Furdyna (1980). In DDA simulations, in order to correctly represent a perfecly spherical object, the discretization of each sphere should be beyond N>1000. Yet, errors can arise in the IR region with very high refractive indices of soot and divergence problems arise for point contact spheres. For an aggregate of hundreds of monomers, this would drastically increase the computation time. Though from the experimental caracterization works, we already know that the soot monomers are not perfectly spherical thus such a computational effort becomes meaningless.

Second, Rahmani et al. (2004) states also that $\alpha_j^{\mathrm{LFCSP}}$ brings correction to the surface dipoles and is equivalent to CM formulation for the remaining dipoles. The model is actually prevents the shading effect of surface dipoles with high absorption. For the tomography soot with random complex geometry, we tried to avoid this problem by generating a small enough a_{dip} to satisfy the validity condition of DDA and relatively large a_{dip}, allowing the incident radiation to reach and interact with the internal volume of the object. Furhtermore, with this formulation, the effect of the geometry on the DDA results is reflected in a complex manner: not also the geometry affects the dipole-dipole interaction tensors $\mathbf{A}_{k,j}$ but also it affects the polarizability terms. With α_j variable for each dipole, the convergence of the system is much slower.

As can be seen in Table 3.1, CMRR and LDR polarizability models gives results with good accuracy (less than 2% error) for the typical soot complex refractive

index around $2.0 + 0.5i$ in the visible range, according to the literature review given in Chapter 2. It is noted that the errors in the absorption properties rise drastically beyond the values of complex refractive index $\sim 5 + 4i$.

As a result, the CMRR and LDR models are chosen for our DDA simulations on numerical soot aggregates and tomography soot objects. For these two models, test cases are presented in the next section to prove the applicability of our code on the soot material.

3.4.2 Directional integration

Numerical integration schemes in 3D space are needed for the computation of g^{NP} (equation 3.32) and of C_{sca}^{NP} (equation 3.30) given by the DDA model. Before computing the variables related to scattering of the real object, numerical integration scheme of the DDA code is tested with quadrature sets. Here, the phase function is simulated with Henyey-Greenstein (H-G) phase function (Henyey and Greenstein (1941)):

$$\Phi(\theta) = \frac{1 - g^2}{(1 + g^2 - 2gcos(\theta))^{3/2}} \tag{3.41}$$

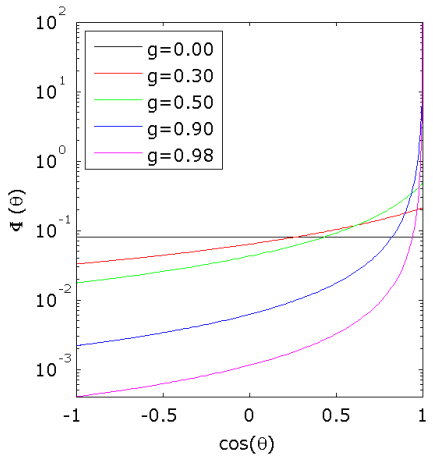

Figure 3.4: *Henyey-Greenstein function for different g factors.*

In Equation 3.41, g is the asymmetry factor and θ is the scattering angle. The phase function can be simulated either in backscattering or forward scattering configurations with the range of $(-1 < g < 1)$ as illustrated in figure 3.4. The

performance of the numerical integration scheme is verified for varying g values by checking the condition given in equation 3.42.

$$\int_0^{2\pi} \left\{ \int_0^{\pi} p(\theta) sin(\theta) d\theta \right\} d\varphi = 4\pi \tag{3.42}$$

Usage of quadratures is the easisest method for numerical directional integration, considering the scattering computation with the DDA model in 3D space. For angular discretization schemes, the sum of the weights corresponding to each direction is equal to the surface area of unit sphere (Coelho (2014)). However the directions vary according to the mathematical theory used in their derivation (Koch and Becker (2004)), therefore one set of quadrature is not sure to give the best result for the numerical computation of all physical problems.

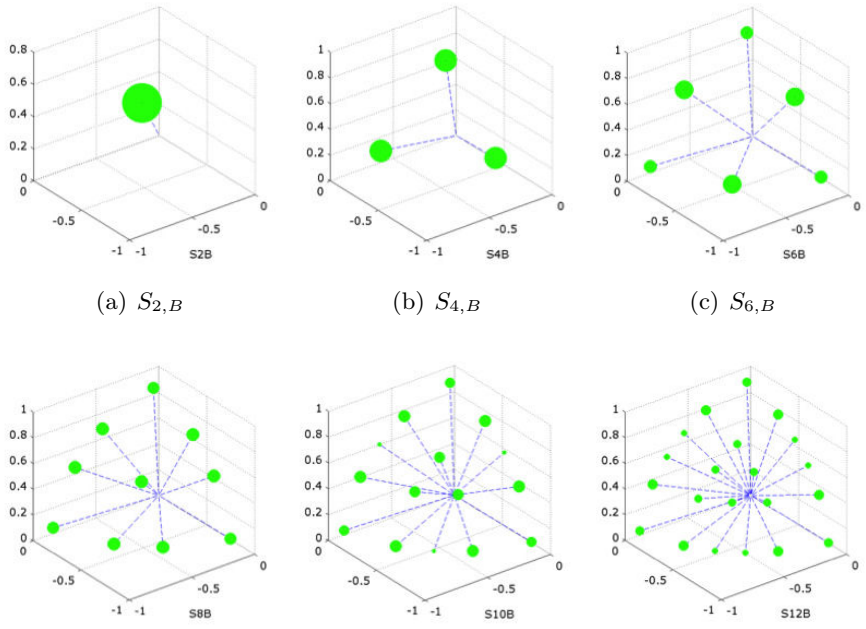

(a) $S_{2,B}$ (b) $S_{4,B}$ (c) $S_{6,B}$

(d) $S_{8,B}$ (e) $S_{10,B}$ (f) $S_{12,B}$

Figure 3.5: *Illustration of the discrete directions and their weigths, used for the H-G test and for the computation of scattering and configuration averaging in DDA, according to the S_N quadrature sets proposed by Balsara (2001). Size of the spheres is proportional to the weight of the corresponding direction cosines.*

Test cases are performed using level symmetric quadrature (S_N) sets, equal weight (EW) sets and Lebedev-Laikov type (LL), the three sets proposed by Koch and Becker (2004) for their study on DOM (Discrete Ordinates Method). As can be seen in Table 3.2, the S_N quadrature performance is good using S_6 and beyond for parameters around $g = 0.5$. The accuracy decays fast with higher values of the asymmetry parameter g.

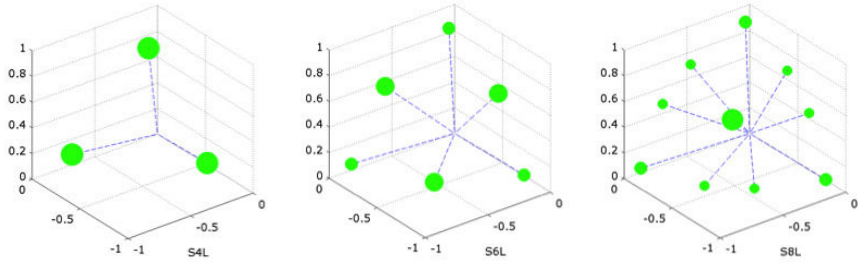

(a) S_4 (b) S_6 (c) S_8

Figure 3.6: *Illustration of the discrete directions and their weigths, used for the H-G test and for the computation of scattering and configuration averaging in DDA, according to the level symmetric quadrature sets proposed by Fiveland (1991), values are retreived from Lemonnier (2007). Size of the spheres is proportional to the weight of the corresponding direction cosines.*

Number of directions		**g**				
		0.50	**0.65**	**0.90**	**0.94**	**0.98**
24	(S_4)	1.0634	1.0938	0.4985	0.3009	-
48	($S_{6,B}$)	0.9983	1.0055	0.6477	0.4138	-
80	($S_{8,B}$)	1.0025	1.0186	0.7412	0.4865	0.1667
168	($S_{12,B}$)	1.0002	1.0037	0.8567	0.6045	0.2169

Table 3.2: *Some of the results obtained for H-G test using S_N to check the condition of equation 3.42 (normalized by 4π).*

To check the possibility of having higher accuracy with less number of directions, EW and LL sets are tested. EW sets are adapted from Leopardi (2006), study on the equal partitioning of the sphere surface. LL sets are obtained using an algorithm based on the work of Lebedev and Laikov (1999). Other types of quadratures (P_N, T_N, etc.) are not considered, as it is already known from the radiative heat transfer simulations that S_N sets give the best performance for low number of directions in anisotropic scattering (Hunter and Guo (2013)).

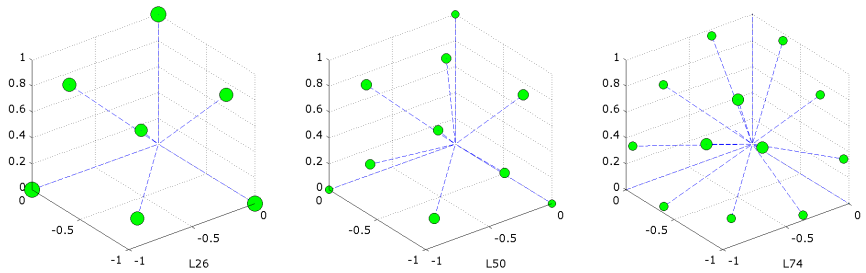

(a) LL_7 (b) LL_{11} (c) LL_{13}

Figure 3.7: *Illustration of the discrete directions and their weigths, used for the H-G test and for the computation of scattering and configuration averaging in DDA, according to the LL quadrature sets proposed by Lebedev and Laikov (1999). Size of the spheres is proportional to the weight of the corresponding direction cosines.*

Number of directions	g			
	0.50	**0.65**	**0.90**	**0.98**
26	1.0243	1.1328	-	-
38	1.0200	1.0691	-	-
50	1.0186	1.0473	-	-
74	1.0127	1.0285	2.8894	-
194	1.0059	1.0146	1.4946	-
434	1.0026	1.0070	1.1322	-
2030	1.0005	1.0015	1.0207	2.7958
5810	1.0002	1.0005	1.0084	1.4104

Table 3.3: *Some of the results obtained for H-G test using EW to check the condition of equation 3.42 (normalized by 4π).*

According to the results obtained in Table 3.3 and in Table 3.4, LL and S_N performances are much higher than equal weights for the same number of directions. Therefore, the selected quadratures are of S_N and LL type. The maximum g^{NP} value of soot aggregates is around 0.65, value given by Liu and Smallwood (2010a) for aggregates with $N_p = 600$, $d_p = 30$ nm, $m = 1.6 + 0.6i$ at $\lambda = 532$ nm. This is approximately the maximum g value in our considered range of λ. This will be tested on the scattering cross section and the phase function of soot type material, in Section 3.4.2. The same type of quadrature sets is used for the configuration averaging of the radiative properties, as explained in the next paragraph.

Number of directions	g			
	0.50	**0.65**	**0.90**	**0.98**
26 (LL_7)	1.0216	1.1932	-	-
38 (LL_9)	0.9976	0.9810	-	-
50 (LL_{11})	1.0000	1.0039	2.7279	-
74 (LL_{13})	0.9997	0.9888	0.6084	2.6444
194 (LL_{23})	1.0000	1.0000	1.0327	8.9889
434 (LL_{35})	1.0000	1.0000	0.9913	2.9004
2030 (LL_{77})	1.0000	1.0000	1.0000	0.9641
5810 (LL_{131})	1.0000	1.0000	1.0000	0.9961

Table 3.4: *Some of the results obtained for H-G test using LL to check the condition of equation 3.42 (normalized by 4π).*

3.4.3 Orientation averaging

When the particulate media is added to the heat transfer simulation, the orientation of the particles (in our case, of the soot aggregates) is random in a computational volume element. Therefore, an orientation (or configuration) averaging operation is needed to find the configuration averaged properties of an irregular shape object.

In this study, numerical averaging is performed by using fixed orientations with attributed weights. This technique is proposed by Okada et al. (2008) as numerical averaging using T-matrix, to reduce the computational cost of configuration averaging with a faster convergence. Moreover, the computations of different orientations are independent of each other, and can be executed in parallel without need of MPI, decreasing the computation time.

The integration by quadratures (or cubatures in multidimensions) can be considered for an orientation averaging, as cited by Penttilä and Lumme (2011). Various schemes are proposed in literature such as the optimal cubature on the sphere (Penttilä and Lumme (2011)), Lebedev-Laikov cubature (Penttilä and Lumme (2011)), Quasi-Monte Carlo method (Okada (2008)). Arithmetic mean averaging of equally spaced directions is another option but its computational convergence is less effective (Okada (2008)). Different from the cubatures proposed by Penttilä and Lumme (2011), we used the S_N and LL quadratures to compute the averaged properties of C_{ext}^{NP}, C_{abs}^{NP}, C_{sca}^{NP}, g and Φ^{NP}, as better performances are given by less computation directions.

For fractal-like aggregate objects, the number of directions needed for the configuration averaging decreases with higher extinction. Liu and Smallwood

(2010a) state that relatively small number of directions should be enough for convergence, even around 20 directions for aggregates with $N_p = 200$. They also claim that the orientation averaging is important for the total scattering cross-section and the asymmetry parameter. Therefore for soot, less than hundred directions should be enough to obtain a converged solution for the configuration averaged values. This corresponds to S_6, S_8, LL_{11} and LL_{13} which exhibit good performance for aggregated shapes as will be presented Section 3.5.

3.4.4 Convergence

The relative error in the iterative solution of the linear system in equation 3.27 is set to $\varepsilon_{DDA} = 10^{-5}$ for the variables $\mathbf{\Pi}_k/\alpha_j E_0$. The convergence of the conjugate gradient algorithm is relatively fast: the number of iterations N_{iter} is much lower than the number of dipoles $N_{iter} << N_{dip}$.

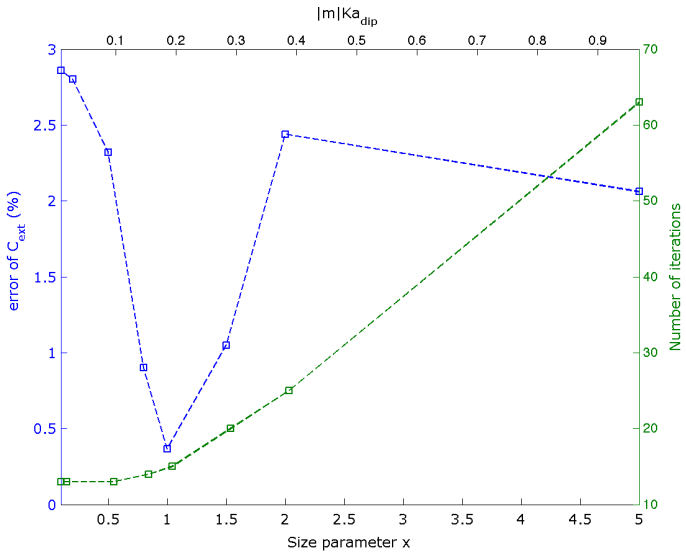

Figure 3.8: *Number of iterations ($\sim 17sec/iteration$) versus the size parameter and the relative error of cross-section compared to Mie solution, for a sphere ($m = 2.0 + 0.5i$) discretized into 5040 cubic volume elements with LDR polarizability formulation, with our in-house DDA code.*

An example of the computation time and the relative error with respect to size parameter is given in Figure 3.8 . The absolute error is $|C_{ext}^{NP} - C_{ext,Mie}|/C_{ext,Mie}$. Here, computation of dipole moments are considered to be independent and to be run independently on multiple processors for the configuration averaging. The maximum relative error is $\varepsilon_{DDA} = 10^{-5}$.

We consider homogeneous material with isotropic dipole polarizability α_j, the elements of the interaction matrix $\widetilde{\mathbf{A}}$ are not stored in the memory but recomputed during each iteration simultaneously for the two orthogonal polarizations of the corresponding incident field. This reduces the run time in small solution systems due to the memory ordering. Nevertheless the run times, especially for large size parameters ($x > 5$) remain longer compared to the DDA performance data given by Yurkin et al. (2007) for ADDA code. It should be remembered that in our case, first, the complex refractive index in question is quite large for DDA model and second, any acceleration algorithm is not implemented (such as FFT, etc.).

3.5 Applications

In this section, two applications will be presented. First, the test cases are performed as a comparison to the analytical Mie solution for a sphere. The limitations of the DDA model are set according to the size parameters and to the complex optical indices of our concern. Second, preliminary cases are treated for complex shapes. Fractal-like aggregates are numerically generated. Then the DDA solution is applied on those numerical aggregates, to test the performance of the configuration averaging and the numerical integration algorithms.

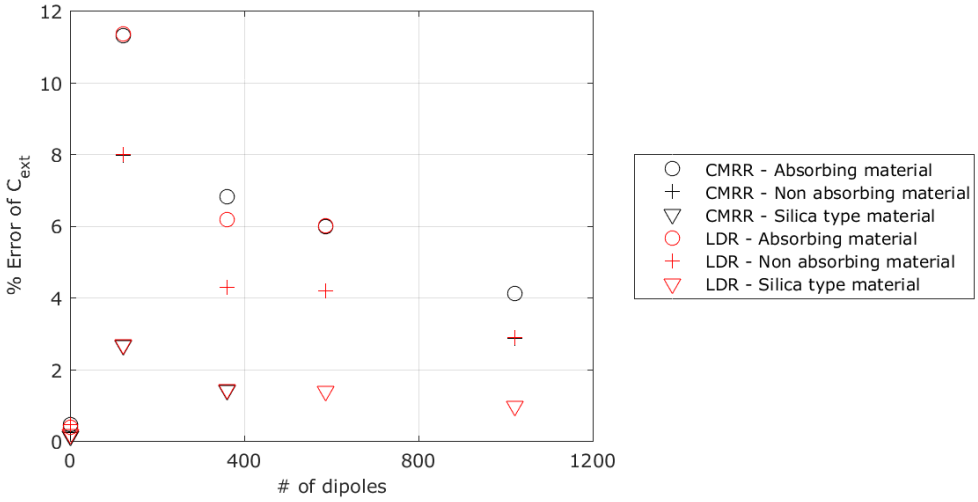

Figure 3.9: *Error on the extinction cross-section compared to Mie solution, as a function of the material discretization for different refractive indices: for a particle with $x = 0.06$: absorbing material ($m = 2.0 + 0.5i$, typical soot index), non absorbing material ($m = 2.0 + 5\text{e-}5i$), silica type material ($m = 1.45 + 5\text{e-}5i$).*

3.5.1 Test case with Mie solution

The mean particle diameter for soot issued from gaseous hydrocarbon combustion is noted as 20 nm, as presented in the literature review in Part I. First, this particle size is tested in DDA compared to Mie solution. Nevertheless, we observed larger particles in the soot issued from propane flame, reaching a mean diameter size of 36 nm. Therefore the DDA model is also tested for the largest size parameter of primary particles to be encountered in this study, around $x_{max} = 0.16$, considering the radiative transfer simulations through sooty mixtures presented in Chapter 5.

3.5.1.1 Effect of refractive index

In Figure 3.9, test case is presented for a monomer of 20 nm diameter and a wavelength $\lambda = 1$ micron. The chosen polarizability models are tested on different complex refractive indices.

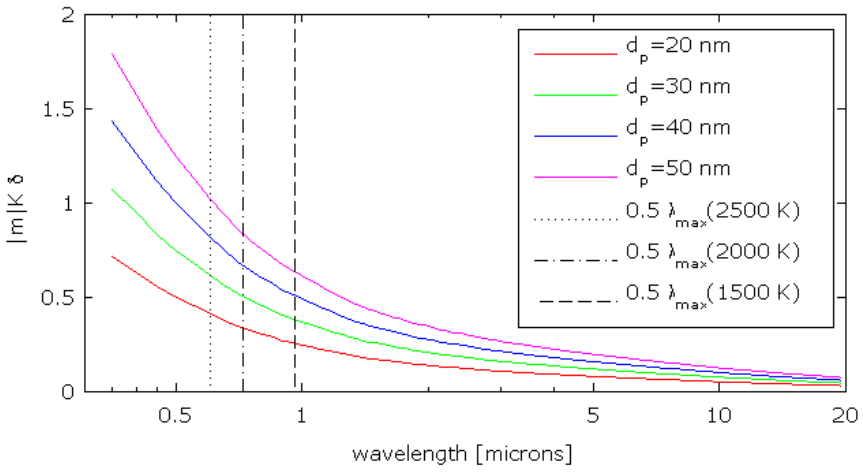

Figure 3.10: *Verification of the discretization condition proposed by Draine (Equation 3.33) for one dipole per monomer prescription for different monomer diameters d_p in the overall radiation spectrum of our interest with the complex optical index of soot at $T = 1600$ K according to Lee and Tien (1981) (which will be presented in Chapter 4).*

The results of Figure 3.9 show a very small difference of the properties obtained from the two polarizability definitions CMRR and LDR, as expected from the literature review of polarizability models in Section 3.4.1. Again, as expected, the % error increases with the increasing absolute value of the index m and not only dependent on the extinction index k. Furthermore, if we represent primary particles by 1 dipole, the Draine's condition (Equation 3.33) is perfectly satisfied

with $|m|Kd = 0.26$. This is also true for larger primary particle diameters, as illustrated in Figure 3.10. Discretization of the sphere introduces errors due to the surface roughness induced, as will be explained in the next section.

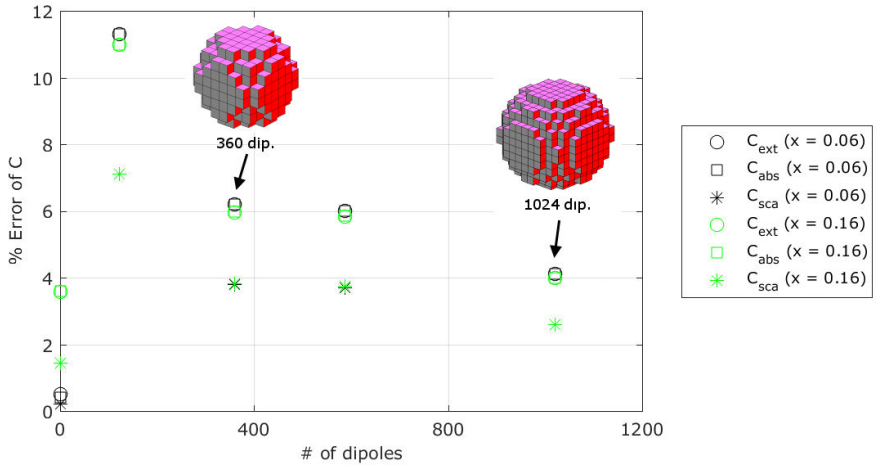

Figure 3.11: *Errors on the cross-sections compared to Mie solution, as a function of the material discretization for the mean size parameter ($x = 0.06$) and the maximum value ($x = 0.16$), $m = 2.0 + 0.5i$, using LDR polarizability prescription.*

3.5.1.2 Effect of size parameter

The same test case is repeated for a monomer of 36 nm diameter. This corresponds to the maximum mean size observed during the ex-situ observations of our tomography soot. Therefore $x = 0.16$ is taken as a maximum size parameter of soot monomer, corresponding to the smallest wavelength of interest in our radiative transfer simulations.

According to the results in figure 3.11, the increase in the size parameter does not change the error significantly. Especially, the dipole-dipole interaction behaviour is similar as the error levels are similar for two size parameters with the same discretization. In order to correctly represent a perfectly spherical surface, the discretization should be beyond thousand of dipoles. Once the sphere is discretized, the dipoles create a surface roughness displaces erronously the volume elements on the particle surface. It is possible to represent a primary particle correctly (with less than 3.5% error for all cross-sections) with one dipole using CMRR or LDR polarization terms. In this formulation, the equivalent volume of the dipole is adjusted to the dipole volume. The errors on the absorption and scattering are separately represented in Figure 3.12 for C_{abs} and C_{sca}. Therefore, in the next sections, one dipole per monomer will be used for

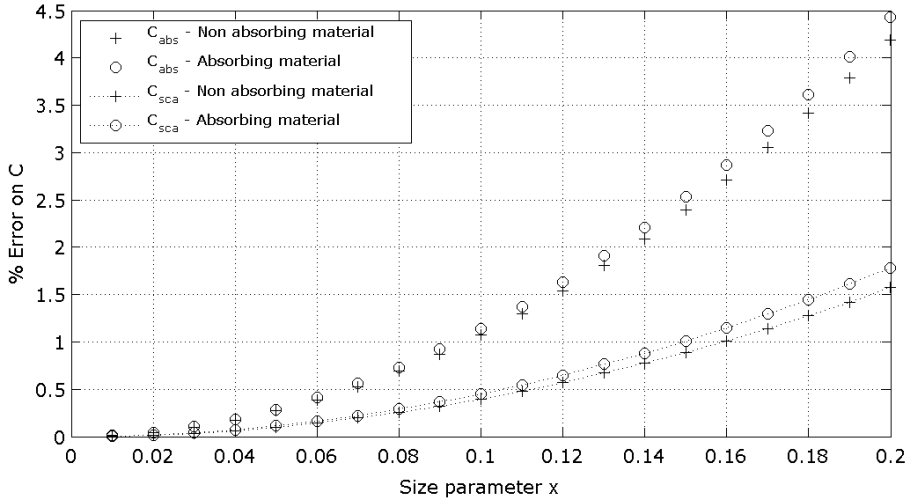

Figure 3.12: *Error as a function of size parameter for typical soot index and silica type material index for 1 dipole per monomer for absorbing ($m = 2.0 + 0.5i$) and non absorbing ($m = 2.0 + 5\text{e-}5i$) materials.*

aggregates formed of hard spheres, as it prevents discretization errors due to surface roughness, and also the divergence of the solution for touching spheres.

3.5.2 Application on aggregated materials

In this section, typical aggregates of combustion soot are generated numerically using the CCA methods explained in Chapter 2. Average values of $d_p = 20$ nm, $D_f = 1.7$ and $k_f = 2.0$ are selected from the literature. Meanwhile, the selected number of particles $N_p = 500$ is relatively large in order to better observe the effect of the multiple scattering between primary particles.

3.5.2.1 Effect of directional integration

The values of the DDA extinction, absorption and scattering cross-sections can be computed independently as explained in Section 3.3. This property can be used to check the convergence of the numerical solution, mainly of the directional integration for scattering parameters. Following the relation $C_{abs} + C_{sca} = C_{ext}$, another error term (in %) is defined for convergence as in equation 3.43:

$$\varepsilon_{DDA,sca} = \frac{|C_{ext}^{NP} - (C_{sca}^{NP} + C_{abs}^{NP})|}{C_{ext}^{NP}} * 100 \tag{3.43}$$

These errors are computed with DDA for soot type and silica type aggregate, using the cubature sets tested with the H-G function. The main results are summarized in Table 3.5. Here, we note again the very good performance of LL_{11} cubature with relatively low number of directions (50 directions over 4π steradians).

	Convergence Error (%)			
Numerical set	LL_7	S_6	LL_{11}	S_{12}
Silica type	0.03	0.63	3.4e-5	0.045
Soot type	0.002	0.03	1.6e-4	0.003

Table 3.5: *Error values $\varepsilon_{DDA,sca}$ to check the directional integration for scattering by DDA applied on the reference numerical aggregate ($d_p = 20nm$, $D_f = 1.7$, $k_f = 2.0$, $N_p = 500$) for soot type ($m = 2.0 + 0.5i$) and silica type ($m = 2.0 + 5\text{e-}5i$) materials.*

The results indicate that the solution for the dipole moments is converged and the numerical integration method can properly account for the multiple scattering inside the object. For larger aggregates and for objects with higher g parameter, the test should be repeated on the convergence of the numerical integration.

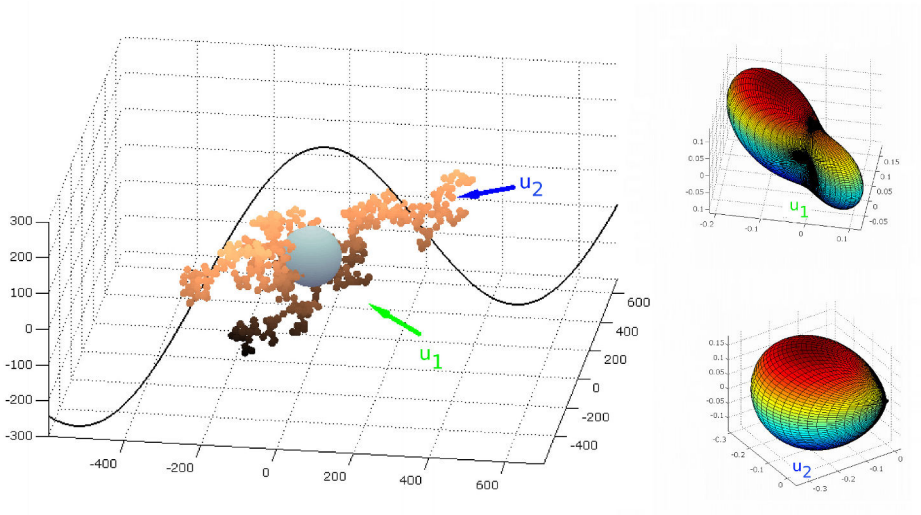

Figure 3.13: *Illustration of the phase function of the soot aggregate ($N_p = 500$, $d_p = 20nm$, $D_f = 1.7$ and $k_f = 2.0$) for different incidence directions $\mathbf{u_1}$ and $\mathbf{u_2}$ using $m = 2.0 + 0.5$ and $\lambda = 1\ \mu m$.*

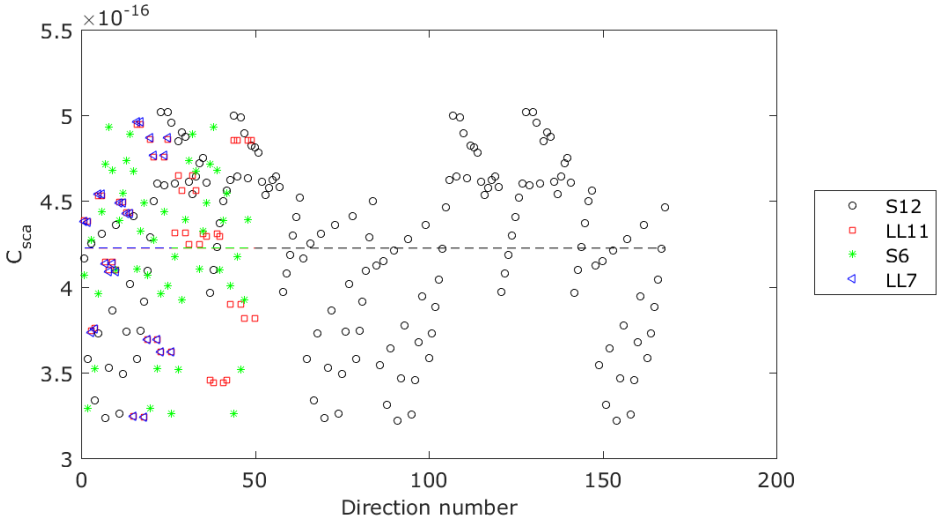

(a)

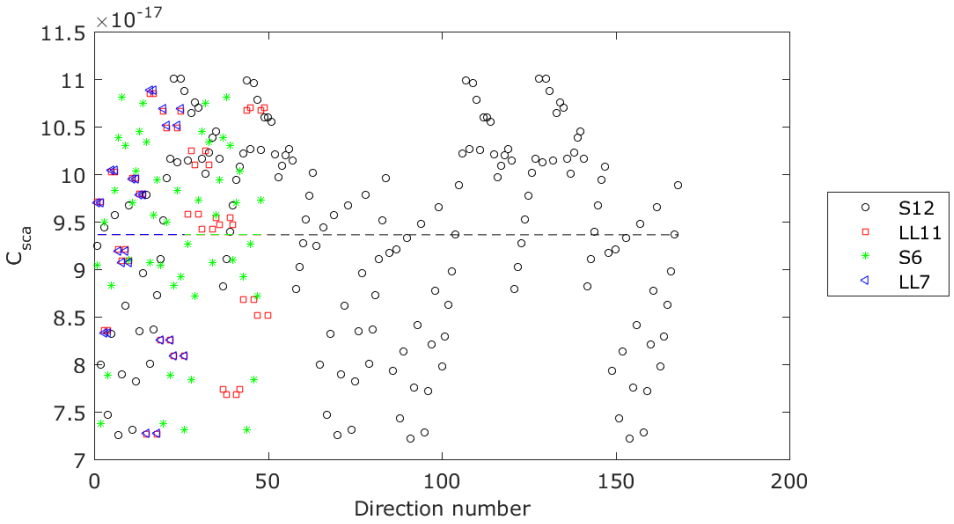

(b)

Figure 3.14: *Directional scattering cross sections for the aggregate illustrated in Figure 3.13, for (a) typical soot material, (b) silica type material, mentioned in Table 3.5.*

3.5.2.2 Effect of configuration averaging

As illustrated in Figure 3.13, the properties of the aggregated object are functions of the incident radiation direction (or the aggregate position configuration). Orientation averaging being treated as numerical integration, the most performant cubature sets are used as selected in Section 3.4.2.

The scattering is known to be the most sensitive to the configuration averaging. The scattering cross-sections are plotted for direction cosines imposed by the different cubatures in Figure 3.14. Results indicate that the computation over 4π steradians with less than 50 direction is enough to converge to averaged values of radiative properties of aggregates. This performance is also due to the computation of properties for the same object in different scattering planes for the same incident wave direction (Penttilä et al. (2007)), two planes in our case for thermal radiation. Note that the averaging seems to be unaffected by the complex index m for the same study object.

3.6 Conclusion on DDA model

In this chapter, we presented our DDA solution methodology, with an overview of the main tools used to determine the radiation-matter interaction properties of objects. As shown in Part I on morphology studies, numerical tools are needed to compute the radiative properties of random shaped objects. Numerically exact solutions are computationally expensive. As a numerical approximation, DDA is less demanding in terms of computational time and memory for the applications on random shapes.

In our DDA model and its applications, the emphasis was given on numerical modeling options, important for the derivation of the averaged radiative properties and for the convergence of the solution. Hence in this chapter, the applications were limited to comparison to analytical Mie solution and to tests on numerical aggregates, for the validation of our in-house code.

Our model will be further explored in the following Chapter 4 on soot radiative properties, with comparison to RDG-FA model. The radiative properties of soot will be investiged regarding the effect of the fractal parameters and the effect of the realistic geometry. An insight will also be given on the effect of the evolution inside the flame by application on the tomography objects.

Chapter 4

Radiative properties of soot

From literature studies, the usage of numerically generated aggregates seems to be a good starting point in the determination of the radiative properties of soot aggregates. We want to push the limit of the research further by computing the radiative properties of realistic 3D geometries of soot, obtained from tomography, and by comparing them to the properties of numerically generated aggregates. We investigate the adequacy of reducing the realistic geometry to a range of fractal parameters and to a specific aggregation algorithm. First, the DDA solutions of DLCCA generated aggregates are compared to T-matrix solutions in order to validate the fidelity of our DDA model on soot aggregates. In the second place, the radiative properties are observed as a function of the random generation around the fractal parameters of interest. The necessary number of numerical aggregate generations is determined to correctly represent the radiative properties of aggregates issued from hydrocarbon combustion. Once the representability is ensured, the properties of the numerical soot are compared to the tomography object, by conserving the parameters computed in Part I such as the fractal dimension, the aggregate material volume, the mean particle diameter, and the penetration coefficient. Finally, the radiative properties of small and large aggregates are compared, for tomography soot and for numerical aggregates, to mimic the evolution of the radiative properties of soot during aggregation within the combustion process. Discrepancies are observed in the radiative properties at small wavelengths due to complex geometry and, as expected, this is less significant for small aggregates. Nevertheless a second reason of discrepancy is the density of material contained in the bounding box of the aggregate, and is valid regardless of the size of aggregate. Care should be given to the results obtained because the observations are limited to one type of fuel and few ex-situ extractions due to the time costly application of tomography.

4.1 Inputs for the soot radiative properties

Here we briefly review the necessary input variables for the determination of the radiative properties of soot aggregates. There are three main inputs for our DDA simulations: 3D geometry, complex optical index, and polarizability model.

The common usage for soot aggregate geometry is the numerical generation using the CC (Cluster-Cluster) aggregation algorithms presented in Chapter 2. The numerical aggregates are generated with the original DLCCA algorithm which is known to be the most representative for combustion soot, using the algorithm of Mackowski (2006).

The originality of our approach arises from the tomography application because we have a real geometry to integrate into DDA simulations. Of course, the numerical generation of aggregates is important for practical purposes, especially for the generalization of the radiative properties for large data sets (such as a large range of fractal parameters and particles sizes), or for example in industrial applications where fast approximate computations are needed. Here, we will benefit from the real geometry to assess the accuracy limit of those properties computed from numerical generation.

Our range of interest being related to gaseous hydrocarbon combustion, we are interested in soot aggregates composed of few tens to hundreds of primary particles, with a particle diameter 10nm $\lessapprox d_p \lessapprox$ 50nm, a fractal dimension $1.6 \lessapprox D_f \lessapprox 1.9$ and a prefactor $1.5 \lessapprox k_f \lessapprox 2.5$. Those values were are issued from the morphology review of aggregates and the fractal analysis performed in Chapter 2. Note that we cannot give a larger range for the prefactor k_f using the original algorithms based on the fractal theory of touching spheres. Indeed, the prefactor is highly variable due to various conditions. These conditions include the observation size of the aggregate, the size distribution of particles and the particle ovelapping. The overlapping effect will be demonstrated in Section 4.5 as the radiative properties of tomography soot are compared to the ones of numerically generated particles with a penetration coefficient.

The second important input parameter of DDA is the complex optical index of soot in the spectral range of thermal radiation corresponding to high temperature applications around 1500 K to 2000 K, i.e. in the spectrum of $0.7\mu m \lessapprox \lambda \lessapprox 15\mu m$. There is not yet any in-house experimental data for soot radiation in the overall thermal radiation spectrum. To compensate the lack of experimental measurements over the complete spectral range, the dispersion model is used for the computation of the complex optical index of soot as a function of high temperatures. Of course, for a complete analysis of the radiative properties of soot, the optical indices for different conditions (flame conditions,

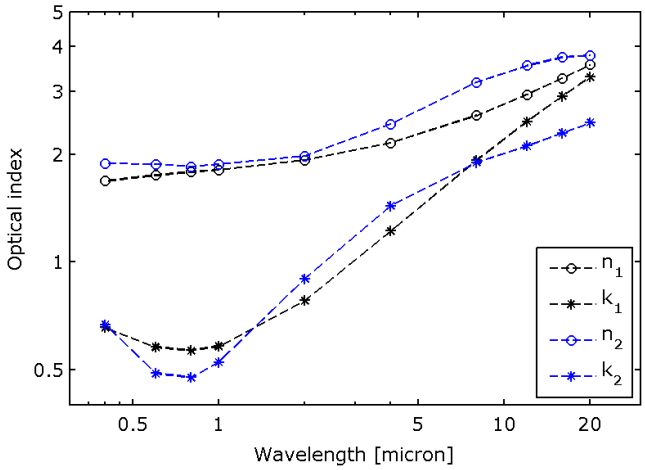

Figure 4.1: *Refractive index data of soot according to the studies of Chang and Charalampopoulos (1990) ($m_1 = n_1 + ik_1$) as a function of wavelength and according to the dispersion relation for $T = 1600$ K given by Lee and Tien (1981) ($m_2 = n_2 + ik_2$). Data is extracted from the studies of Mullins and Williams (1987).*

fuel type, stochiometry) are to be investigated experimentally because their dependency was reported in literature (Mullins and Williams (1987), Habib and Vervisch (1988), Charalampopoulos et al. (1989)) or the dispersion relation itself can be investigated for specific conditions (Yon et al. (2011)).

In our study, two data sets are used for the computation of soot radiative properties. The first one is computed from the dispersion relation presented in the semi-empirical findings of Dalzell and Sarofim (1969), Lee and Tien (1981), Mullins and Williams (1987), Habib and Vervisch (1988). The advantage of the dispersion theory is its dependency on temperature. We have retained the optical index data at a temperature of 1600 K, as it corresponds to the average temperature in our radiative heat transfer simulations involving $T_{min} = 300$ K and $T_{max} = 3000$ K. The second data set is obtained from the equations given by Chang and Charalampopoulos (1990) which are solely function of the wavelength. Both data sets are presented in Figure 4.1. Finally, to compensate the overestimation of the soot absorption in the mid-IR region by DDA, the dispersion relation ($m_2 = n_2 + ik_2$ in Figure 4.1)) is selected, because these data give slightly lower $|m|$ values in the mid-IR region.

Note that the radiation spectrum is discretized into a relatively small number of discrete wavelengths for the computation of radiative properties. This is allowed by the relatively smooth spectra of soot optical indices. The discrete number of wavelengths is kept small because the convergence rates, given in Chapter 3 (DDA modeling), become up to six times slower beyond 5 μm due to the high values of the optical index, and up to two times slower below 0.6

μm due to the increased multiple scattering effects.

Finally, the choice of polarizability model for radiation-soot interaction is an important input parameter, as presented in Chapter 3. Throughout this chapter, we will stick to the LDR (Lattice Dispersion Relation) polarizability definition because it has a very good performance and good enough accuracy with complex geometry, as long as the discretization is made on a cubic lattice. The suitability of LDR on irregular shaped aggregates was demonstrated by Flatau et al. (1993). We precise that the complex 3D geometries (obtained from tomography and from the overlapping of primary particles) are discretized into cubic volume elements to satisfy the LDR applicability condition. For aggregates of touching spheres, we use the "1 dipole/primary particle" principle to avoid discretization errors, as presented in Chapter 3. Note that for numerically generated aggregates, the centers of the primary particles are already located on a lattice due to the DLCCA generation algorithm. The performance of "1 dipole/monomer" is very good, compared to the T-matrix solutions, as will be presented in the next section.

4.2 Comparison to T-matrix solutions

The application of DDA on numerically generated soot aggregates can be cumbersome due to the high optical indices and due to the spheres in point contact. If we discretize each sphere into volume elements, the solution can diverge easily. The best compromise is given by the "1 dipole/monomer" representation, which is also used by Okamoto (1995), Okamoto and Xu (1998) for the simulation of soot aggregates. We note that they use the "a_1" term of Mie series expansion for the polarizability prescription. The difference between this formulation and LDR formulation for an equivalent volume of sphere is negligible for our primary particles for which the size parameter $x < 0.2$.

Case	m	λ (nm)	d_p (nm)	N_p	D_f	k_f	Presented in
1a	1.75+0.5i	870	30	200, 400, 600, 800	1.75	1.6	Figure 4.2
1b	1.75+0.5i	870	50	200, 400, 600, 800	1.75	1.6	Figure 4.2
2a	2+i	870	30	200, 400, 600, 800	1.75	1.6	Figure 4.3
2b	2+i	870	50	200, 400, 600, 800	1.75	1.6	Figure 4.3
3a	1.75+0.5i	870	30	200, 400, 600, 800	2.0	1.6	Figure 4.4
3b	1.75+0.5i	870	50	200, 400, 600, 800	2.0	1.6	Figure 4.4
4a	2+i	870	30	200, 400, 600, 800	2.0	1.6	Figure 4.5
4b	2+i	870	50	200, 400, 600, 800	2.0	1.6	Figure 4.5

Table 4.1: *Summary of the parameters used in our DDA calculations on numerical soot aggregates for the comparison with T-matrix.*

As a test case for numerical aggregates of touching spheres, we compared our DDA results to T-matrix ones. Note that T-matrix is a numerically exact solution, as explained in Chapter 3. Though, it is computationally expensive for large aggregates and truncation errors can arise for large clusters. Therefore we investigated the radiative properties of soot fractals proposed by Liu et al. (2008) and compared our DDA results with theirs obtained from T-matrix method. As summarized in Table 4.1, there are eight test cases, for aggregates composed of increasing number of primary particles.

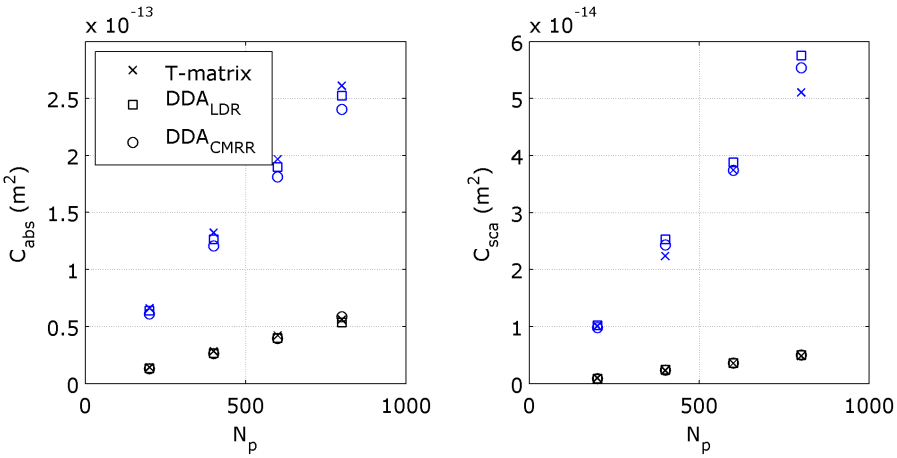

(a) Absorption cross-section

(b) Scattering cross-section

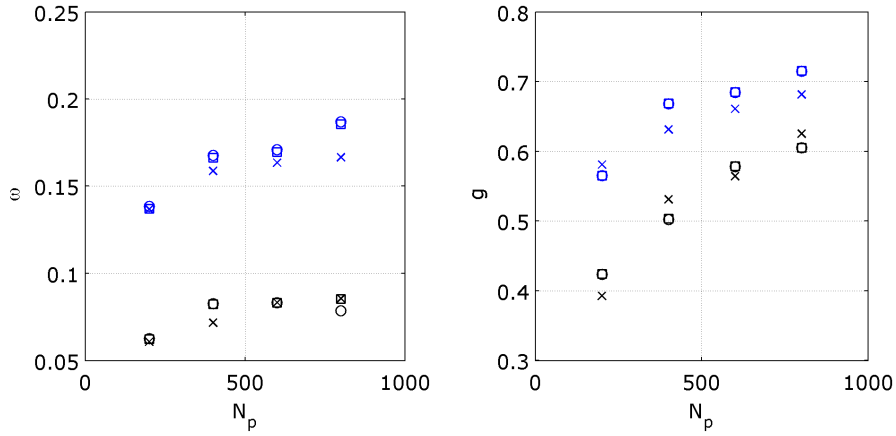

(c) Scattering albedo

(d) Asymmetry factor

Figure 4.2: *Test cases 1a and 1b of Table 4.1. Radiative properties of soot aggregates for fractal dimension $D_f = 1.75$ as a function of aggregate size N_p composed of $d_p = 30$ nm (black points) and $d_p = 50$ nm (blue points). Simulations are performed with optical index $m = 1.75 + 0.5i$ at $\lambda = 870$ nm. T-matrix solution values are retreived from Liu et al. (2008).*

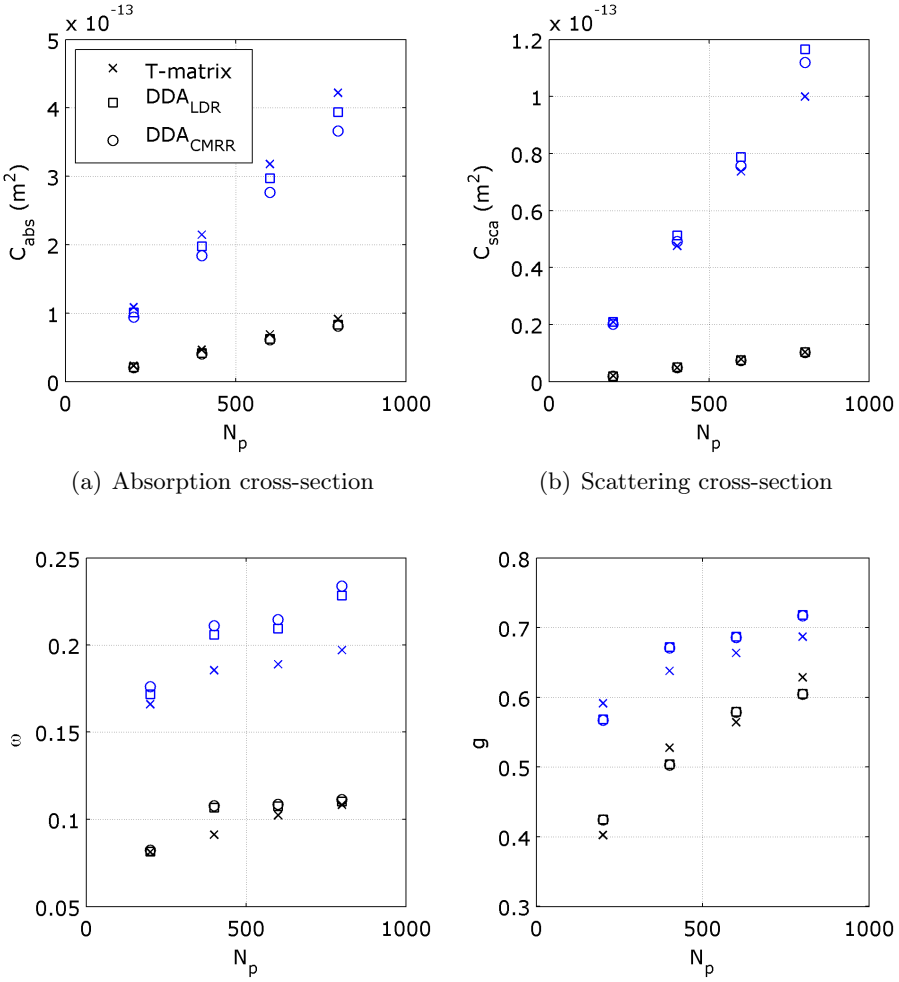

(a) Absorption cross-section

(b) Scattering cross-section

(c) Scattering albedo

(d) Asymmetry factor

Figure 4.3: *Test cases 2a and 2b of Table 4.1. Radiative properties of soot aggregates for fractal dimension $D_f = 1.75$ as a function of aggregate size N_p composed of $d_p = 30$ nm (black points) and $d_p = 50$ nm (blue points). Simulations are performed with optical index $m = 2.0 + 1i$ at $\lambda = 870$ nm. T-matrix solution values are retreived from Liu et al. (2008).*

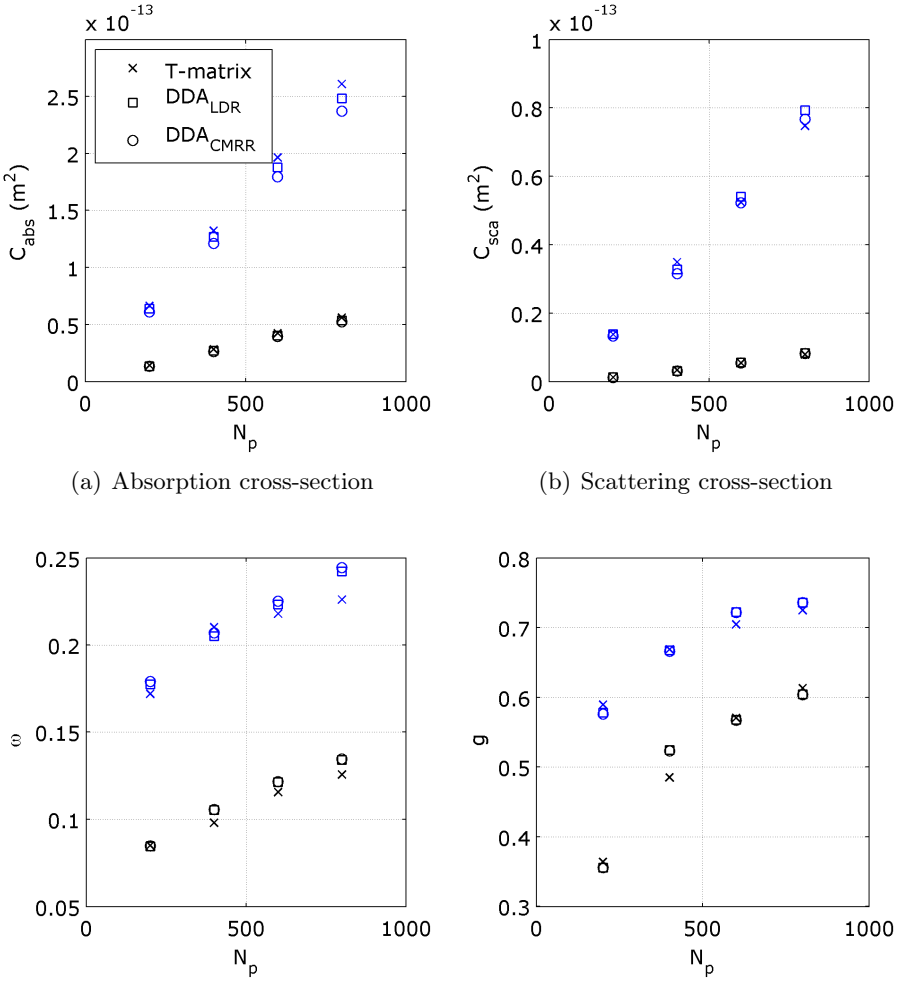

(a) Absorption cross-section

(b) Scattering cross-section

(c) Scattering albedo

(d) Asymmetry factor

Figure 4.4: *Test cases 3a and 3b of Table 4.1. Radiative properties of soot aggregates for fractal dimension $D_f = 2.0$ as a function of aggregate size N_p composed of $d_p = 30$ nm (black points) and $d_p = 50$ nm (blue points). Simulations are performed with optical index $m = 1.75 + 0.5i$ at $\lambda = 870$ nm. T-matrix solution values are retreived from Liu et al. (2008).*

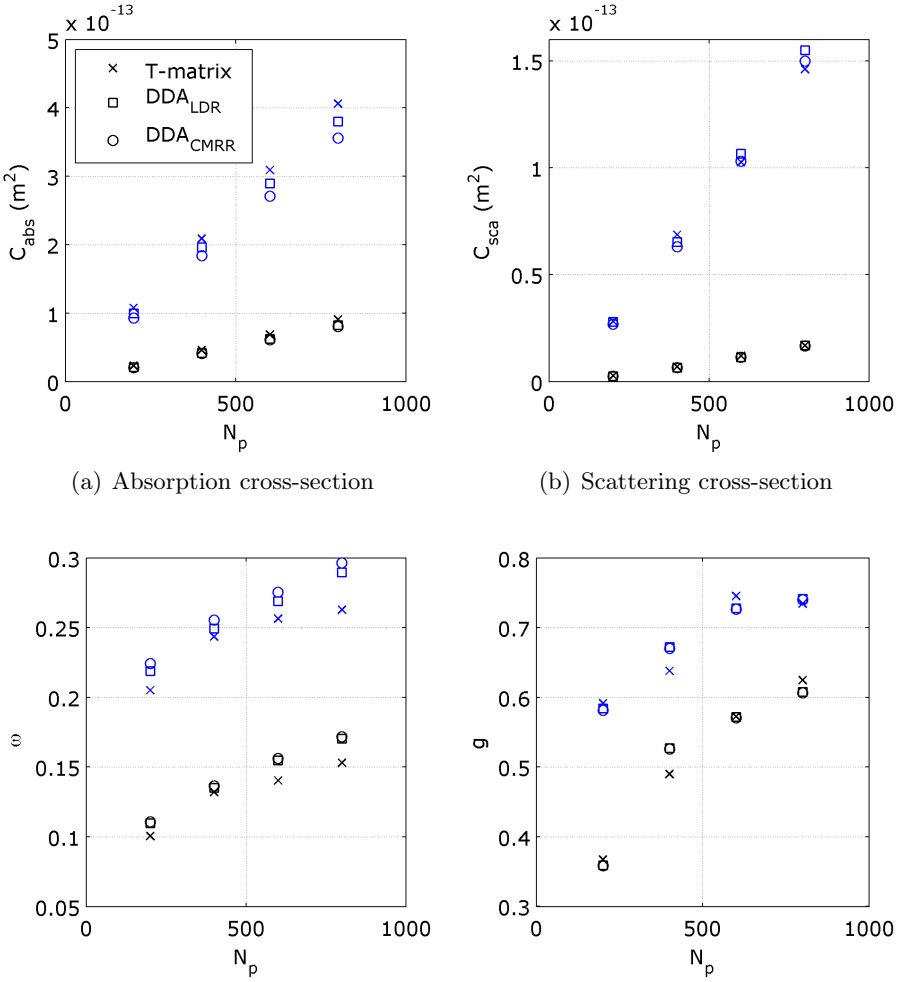

(a) Absorption cross-section

(b) Scattering cross-section

(c) Scattering albedo

(d) Asymmetry factor

Figure 4.5: *Test cases 4a and 4b of Table 4.1. Radiative properties of soot aggregates for fractal dimension $D_f = 2.0$ as a function of aggregate size N_p composed of $d_p = 30$ nm (black points) and $d_p = 50$ nm (blue points). Simulations are performed with optical index $m = 2.0 + 1i$ at $\lambda = 870$ nm. T-matrix solution values are retreived from Liu et al. (2008).*

For all the test cases, our results obtained using DDA comply well with the results of T-matrix. The maximum relative difference is around 8%, for the aggregates of $N_p = 800$ primary particles with diameter $d_p = 50$ nm and with the optical index value $m = 2+i$. This is somewhat expected because at $\lambda = 870$ nm, the discretization by "1 dipole/primary particle" can become too large to satisfy the DDA validity conditions that the phase change and attenuation should be negligible in each discretization volume element. According to the Draine's condition the discretization should satisfy $|m|2\pi d_p/\lambda < 1$ and we have $|m|2\pi d_p/\lambda = 0.81$. On the other hand, if the differences were solely due to DDA model, one would expect a systematic discrepancy with increasing size of the aggregate. This is not the case, especially when we compare the scattering albedo. Liu et al. (2008) state that one random generation is representative enough of one fractal dimension and prefactor. As will be presented in Section 4.3, the absorption can slightly vary from one aggregate generation to another even using the same fractal parameters and the same algorithm. This variation is more important for scattering. This brings us to the next paragraph, Section 4.3, on the effect of random generation and fractal parameters.

4.3 Effect of fractal parameters

In this section, we investigate the variation of the radiative properties of numerical aggregates as a function of random generation, around our mean reference parameters of $D_f = 1.7$, $k_f = 2.0$, $N_p = 500$. In fact, we had performed this analysis before the ex-situ experiments. This small sensitivity analysis brings information on the necessary level of precision on the fractal properties to be reached during the experimental characterization, and also to decide on the extent of soot morphological properties to be considered in heat transfer simulations.

Aggregate samples are generated first by varying D_f around its reference value with all other parameters fixed. The trends of the DDA results as a function of D_f are represented in Figure 4.6. As can be seen on these graphs, several numerical aggregates are generated for the same fractal parameter in order to account for the random nature of the aggregation process.

The same procedure is applied to study the sensitivity of the radiative properties to the prefactor k_f. The trends extracted for k_f in Figure 4.7 are globally similar to the ones presented in Figure 4.6. However, the sensitivities of the radiative properties to D_f and k_f are different, as summarized in Table 4.2.

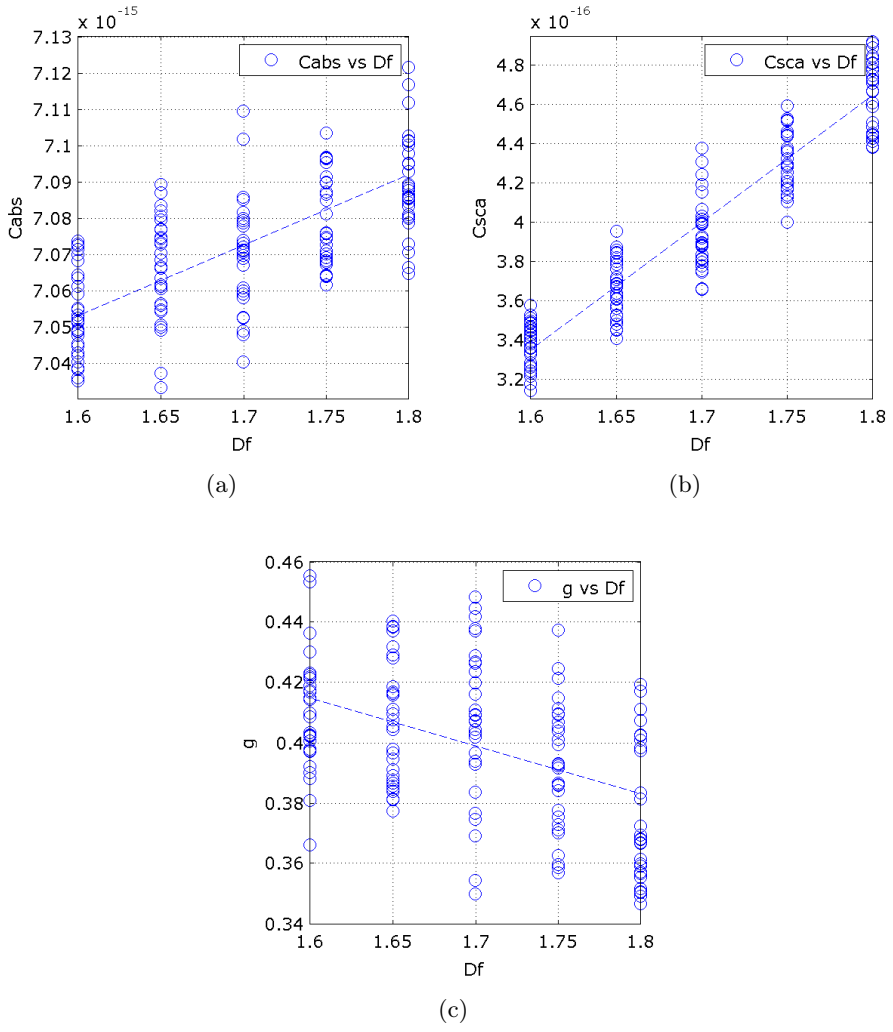

Figure 4.6: *Variation of the radiative properties of a set of randomly generated representative soot aggregates as a function of the fractal dimension D_f with all other parameters being fixed. $N_p = 500$, $d_p = 20$ nm, $k_f = 2.0$, $\lambda = 1\mu m$, $m = 2 + 0.5i$. (C_{ext} and C_{sca} are in m^2.)*

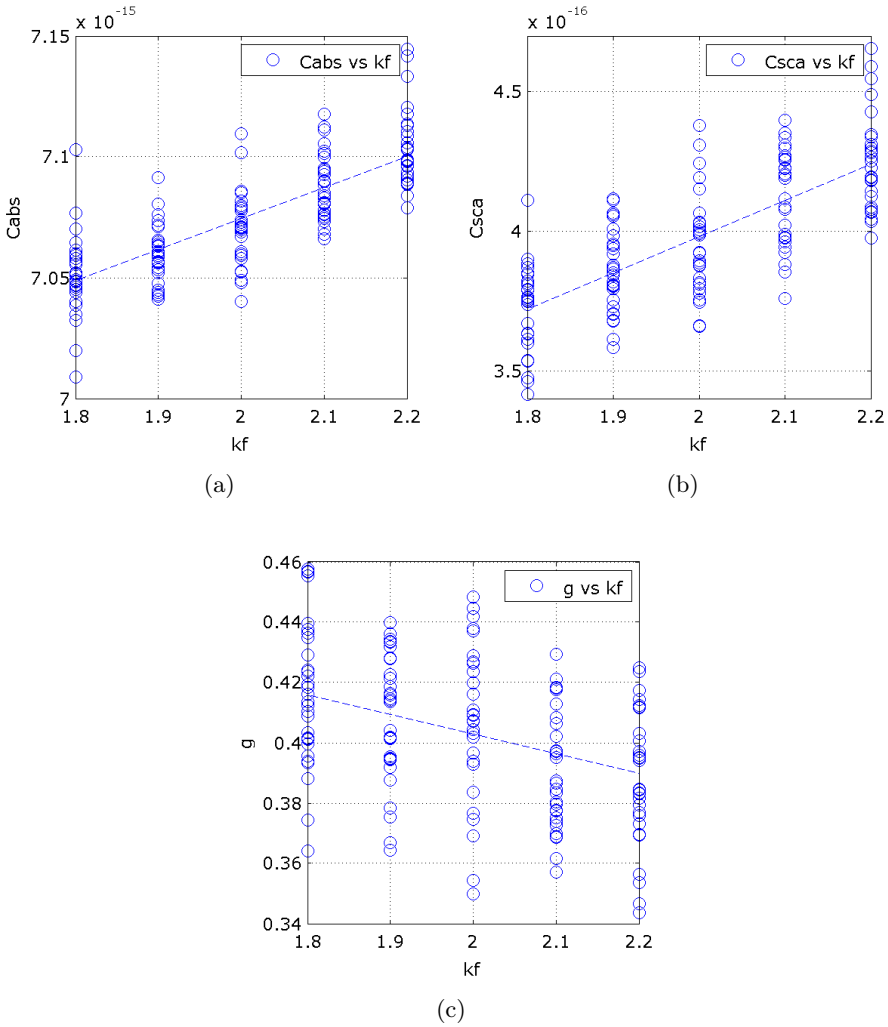

Figure 4.7: *Variation of the radiative properties of a set of randomly generated representative soot aggregates as a function of the fractal prefactor k_f with all other parameters being fixed. $N_p = 500$, $d_p = 20$ nm, $D_f = 1.7$, $\lambda = 1\mu m$, $m = 2 + 0.5i$. (C_{ext} and C_{sca} are in m^2.)*

The simulation results indicate that the interaction of soot with radiation is more affected by the value of the D_f parameter. This is logical, as D_f represents a sort of material density and elongation parameter. This was illustrated in Figure 2.6, in Chapter 2. In particular, varying D_f from 1.6 to 1.8 modifies the absorption by only 1.5% but the scattering by 46%. But as the absorption phenomenon dominates the scattering by soot, the sensitivity of soot radiative properties to the fractal parameters can be considered relatively small in the range of study if no particular variation is inspected due to scattering in the radiative heat transfer simulations. Therefore, the uncertainties on the fractal dimension and the prefactor does not seem to be critical for radiation of flame soot at this stage of the study.

	% change for 1 % modification of D_f	% change for 1 % modification of k_f
C_{abs}	0.12	0.04
C_{sca}	3.93	1.63
g	2.56	0.31

Table 4.2: *Sensitivity of the radiative properties to the fractal parameters for the reference soot aggregate.* $N_p = 500$, $d_p = 20$ *nm*, $D_f = 1.7$, $k_f = 2.0$, $\lambda = 1\mu m$, $m = 2 + 0.5i$.

Finally, the effect of the random generation seems to be more important for the radiative properties of soot than the precision on its fractal parameters. As presented in Figures 4.6 and 4.7, several tens of DLCCA generations are needed to obtain an acceptable ensemble average for the same fractal parameters. Therefore the properties of the numerical aggregates presented in the next sections are obtained from an ensemble average of 20 generations.

4.4 Effect of primary particle size and number

As the prefactor and the fractal dimension, the size of the aggregate and the number of primary particles are susceptible to affect the radiative properties of soot in a complex manner. Liu and Smallwood (2010b) studied the effect of aggregation on the absorption of flame soot, with a focus on LII (Laser-Induced Incandescence) measurements. They studied the primary particle size parameters $x_p = 0.088$, 0.177 and 0.354 (corresponding to the wavelengths $\lambda = 1064$, 532 and 266 nm) with the optical index of $m = 1.6 + 0.6i$. They generated aggregates with the fractal parameters $D_f = 1.78$ and $k_f = 2.3$, with numbers of primary particles $5 < N_p < 893$ and with the particle radius $r_p = 15$ nm. Their variables correspond perfectly to our range of study. Liu

and Smallwood (2010b) concluded that the real absorption of the aggregate is always greater than the sum of the absorptions of the individual particles, with a factor of 1.05 to 1.15 for size parameters $x_p < 0.2$. When the primary particles are larger, the separation distance between particles becomes very large and compensates for the effect of multiple scattering on the extinction of aggregates with $N_p > 100$.

Our study deals with aggregates always in the range of $x_p < 0.2$, therefore the absorption will always be increased by a factor of around 1.1 due to soot aggregation, which also complies with the results obtained by Yon et al. (2014). Besides, many studies propose simplified correlations and correction factors to take into account the effect of aggregation and geometry on the radiative properties. Some examples are on the effect of aggregation on absorption in the near and mid IR (Mackowski (2006)), on the effect of aggregation on absorption and scattering for LII measurements and improvements of RDG-FA theory (Yon et al. (2014)), on the parametrization of the effect of necking and overlapping (Yon et al. (2015)), on the relationship between the aggregate equivalent radius and the optical properties in the visible (Pandey et al. (2015)). Of course, this is not an exhaustive list in between numerous studies trying to elaborate parametric data and semi-empirical relationships on the radiative properties of either flame soot or aerosol black carbon.

It is concluded that most of the research is already performed on the parametrization of the aggregation effect (size of particles, size of aggregates and the variation of the fractal parameters) and on the correction of semi-empirical relationships (such as RDG-FA). Hence, we focus on the effect of realistic geometry in extreme cases of small and large aggregates, as will be presented in the next section.

4.5 Effect of real geometry

In this section, we will compare the radiative properties of realistic soot geometries obtained from tomography to the ones of their numerical equivalents generated by the DLCCA algorithm. To that end, we must build equivalent objects via the numerical generation. This latter is ensured by keeping the same fractal parameters and the same volume of material, as will be explained in the next paragraph.

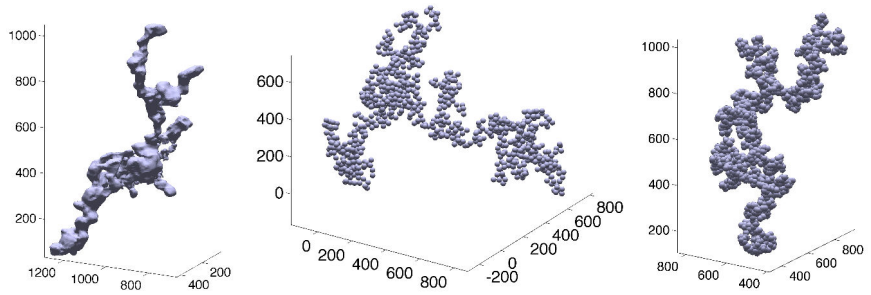

(a) **Tomography** (b) **DLCCA-original** (c) $\mathbf{C_p = 0.5}$

Figure 4.8: *Case 1: Large aggregate. a) Tomography soot; b) Volume equivalent generation with DLCCA hard spheres; c) Volume equivalent generation with DLCCA overlapping spheres.*

4.5.1 Numerical generation of equivalent objects

In the previous Section 4.2, it was concluded that the sensitivity of the radiative properties to the fractal parameters is low. Hence, even though we may have experimental errors in tomography data, the effect will be small on the radiative properties in the range of $1.55 < D_f < 1.95$ and $1.5 < k_f < 2.5$. This was demonstrated by Liu et al. (2008) for D_f. The variation around k_f is not considered anymore due to the high experimental uncertainties. As was explained in Section 2.6.3, and as presented in Table 4.3, the big interest of the k_f value is that it allows the determination of the penetration coefficient C_p between primary particles. The numerical aggregates of hard spheres are always generated with the fixed value of $k_f = 2.0$.

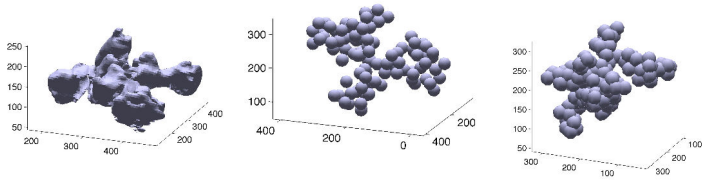

(a) **Tomography** (b) **DLCCA-original** (c) $\mathbf{C_p = 0.45}$

Figure 4.9: *Case 2: Small aggregate. a) Tomography soot; b) Volume equivalent generation with DLCCA hard spheres; c) Volume equivalent generation with DLCCA overlapping spheres.*

Throughout this chapter, we will focus on two extreme cases and do a com-

parative study between small aggregates ($N_p \approx 100$) and large aggregates ($N_p \approx 900$). Only in Section 4.6, we will compare the properties obtained from those extreme cases to the ones of spherical particles without aggregation, and to the ones obtained from the RDG-FA theory.

	Experimental Data					**Numerical Generation****								
	3D tomography				**Image analysis**	**DLCCA hard spheres**				**DLCCA overlapping spheres**				
	D_f	k_f	R_{veq} (nm)	C_p	d_p (nm)	D_f	k_f	N_p***	d_p (nm)	C_p	D_f	k_f**	N_p*	d_p (nm)
Case 1 (Big aggregate)	1.79	3.9	133	0.50	27.8	1.79	2.0	940	27.8	0.50	1.79	2.0	1250	27.8
Case 2 (Small aggregate)	1.93	3.5	84	0.45	36.9	1.93	2.0	100	36.9	0.45	1.93	2.0	150	36.9

* N_p: This is the original number of spheres when they were touching. When the particles overlap, the volume of material is approximately same as the original aggregate from tomography.
** k_f: The original aggregate is generated with $k_f = 2.0$. this value increases with after overlapping.
*** N_p is chosen such that the aggregate volume is approximately equal to the tomography aggregate.
**** One aggregate closest to the ensemble average values is selected in between 20 identical generations.

Table 4.3: *The parameters used in the numerical generations (DLCCA) to compare the properties of the tomography soot samples to the ones of numerical aggregates.*

Numerical aggregates are generated using DLCCA algorithm. To obtain the numerical aggregates with overlapping spheres, aggregates are generated with larger number of primary particles using the same DLCCA algorithm. Then the aggregate is squeezed to the diminish the distance between the centers of primary particles. This distance is derived from the overlapping coefficient C_p computed in Chapter 2. This operation of generation and overlapping is repated iteratively until the same volume is obtained for the tomography object and the numerical aggregate with overlapping spheres. The parameters are summarized in Table 4.3. As depicted in Figures 4.8 and 4.9, the size of the DLCCA aggregate with hard spheres is slightly longer in terms of maximum linear size, even though it has the same material volume, which will show up as a difference in the radiative properties. This brings us to the simulation of the radiative properties by DDA in the following sections.

4.5.2 Discretization of the tomography objects

Before presenting the final DDA results, the discretization conditions are briefly reviewed for complex geometries of the tomography objects and the sintered aggregates. It should be noted that the case with hard spheres is not concerned by this procedure. As it was explained in Chapter 3, the case of hard spheres is a special case where the "1 dipole/primary particle" discretization principle can be used for numerical aggregates of touching spheres; this was also demonstrated in Section 4.2. For the complex shapes obtained from the overlapping

spheres and from the tomography, the discretization is performed in order to keep the same material volume and the same radius of gyration of the object.

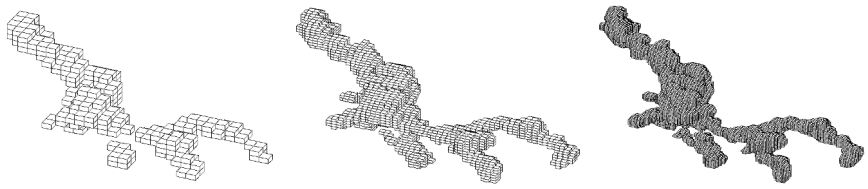

(a) $\mathbf{a_{dip} = 32nm}$ (b) $\mathbf{a_{dip} = 16nm}$ (c) $\mathbf{a_{dip} = 8nm}$

Figure 4.10: *Discretization of the tomography geometry of Figure 4.8(a) by the volume corrected voxelisation algorithm.*

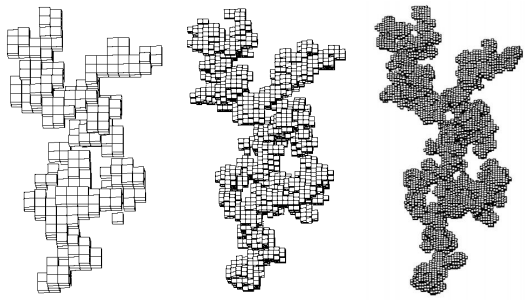

(a) $\mathbf{a_{dip} = 32nm}$ (b) $\mathbf{a_{dip} = 16nm}$ (c) $\mathbf{a_{dip} = 8nm}$

Figure 4.11: *Discretization of the numerically generated aggregate by DLCCA composed of hard spheres of Figure 4.8(c). A surface mesh is generated for the complex shape. It is then discretized by the volume corrected voxelisation algorithm.*

We stated in Chapter 3 that for soot with high optical index, the discretization into very small elements can result in overestimation of the absorption due to the shading effect by surface dipoles. Hence, we tried to keep the discretization coarse enough to prevent this effect (and also to reduce the DDA run times), and fine enough to obtain a converged solution. For the objects presented in Figures 4.10 and 4.11, the volume elements are conserved on a lattice grid where each cubic volume element is considered as a dipole. To obtain the discretization in those figures, the surface mesh is discretized into cubic elements using our voxelization algorithm written in Matlab and presented in Chapter 2 for fractal analysis. Of course, this type of voxelization preserves the complex geometry but overestimates the volume by encompassing the original surface

mesh of the soot aggregate. Therefore we have modified the voxelisation algorithm: the object is displaced slightly on the lattice grid and the surface dipoles are interchanged with neighbouring grid elements, until we obtain the best compromise between the numerical aggregates and the tomography object in terms of the material volume, the maximum linear size of aggregate, and the radius of gyration.

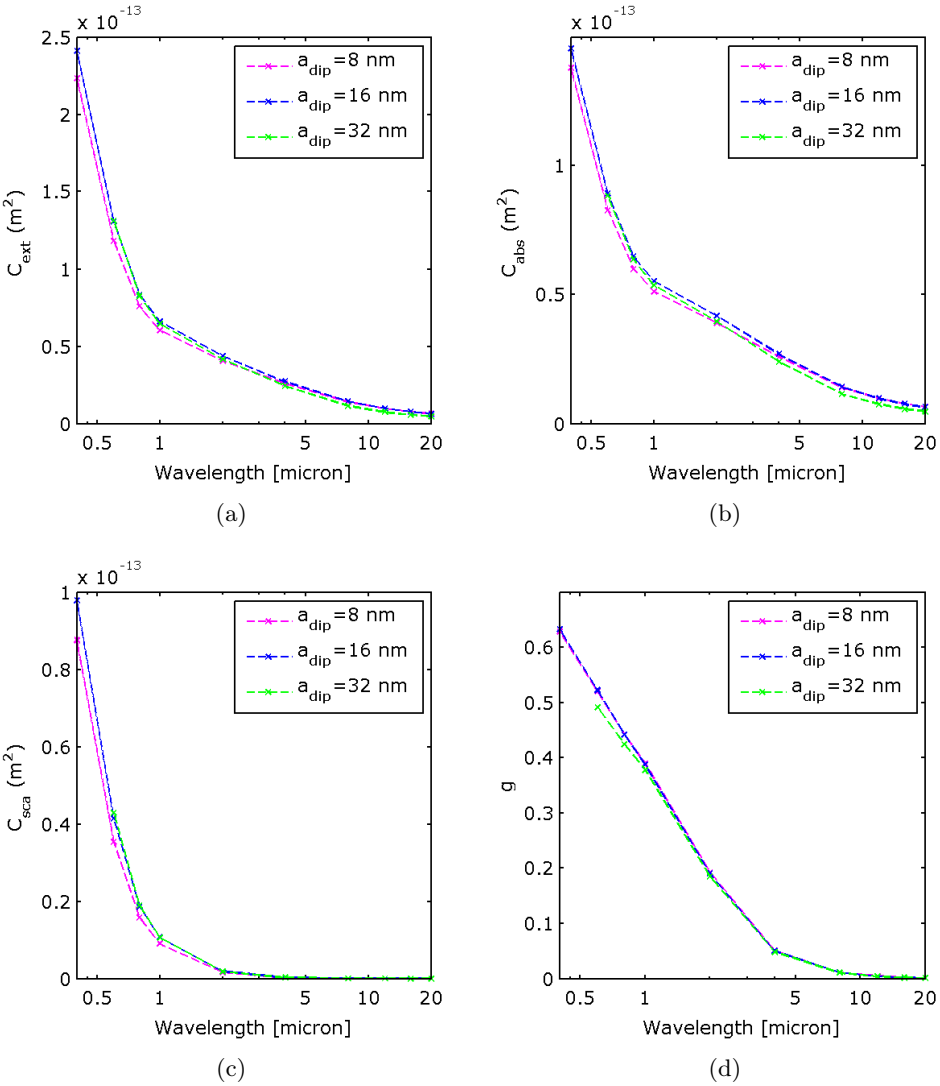

Figure 4.12: *Checking the convergence of the solution with the discretization of the tomography soot, (Case 1, large aggregate collected in afterflame zone). Note that the discretization volume can change slightly because we keep the dipoles on a lattice grid. The volume equivalent radius of the tomography soot is* $R_{veq} \approx 133$ *nm; it is* $R_{veq} \approx 136$ *nm for* $a_{dip} = 32$ *nm and* $a_{dip} = 16$ *nm, and* $R_{veq} \approx 132$ *for* $a_{dip} = 8$ *nm.*

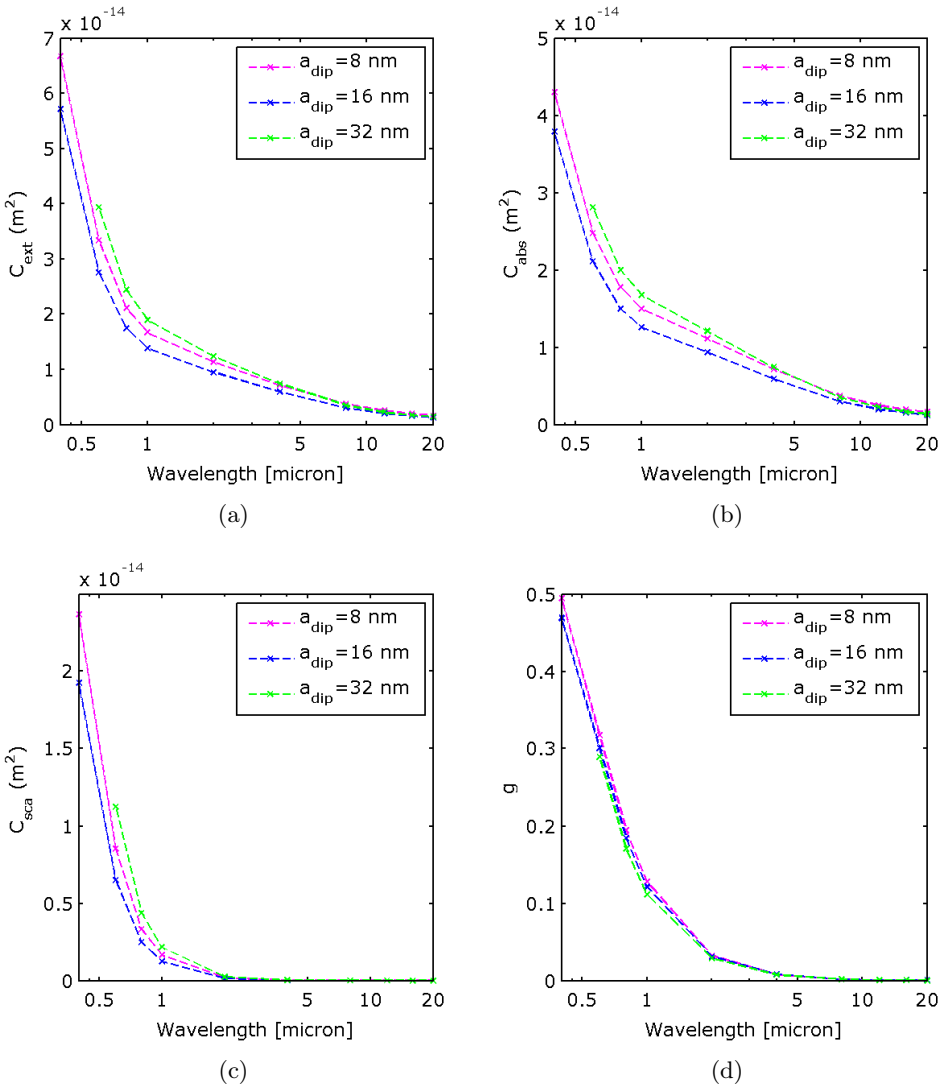

Figure 4.13: *Checking the convergence of the solution with the discretization of the tomograhpy soot (Case 2, small aggregate, collected at mid-flame). Note that the discretization volume can change slightly because we keep the dipoles on a lattice grid. The volume equivalent radius of the tomography soot is* $R_{veq} \approx 84$ *nm; it is* $R_{veq} \approx 91$ *nm for* $a_{dip} = 32$*,* $R_{veq} \approx 83$ *nm for* $a_{dip} = 16$ *nm, and* $R_{veq} \approx 86$ *nm for* $a_{dip} = 8$ *nm.*

As can be observed in Figures 4.10 and 4.11, a discretization with $a_{dip} = 16$ nm is able to depict reasonably well the geometry. The important point is to keep the dipole size smaller than the width of the overlapping neck between particles. We were able to keep similar geometrical properties at $a_{dip} = 16$ nm between tomography aggregate and DLCCA generated aggregate. As can be seen in Figure 4.12, for "Case 1 (large aggregate)", the differences between the 3 discretization levels are negligible above $\lambda = 0.8$ micron. For "Case 2 (small aggregate)", as presented in Figure 4.13, the differences are more pronounced but this can be due to the difference in the material volume. Again, we managed to conserve in acceptable limits the geometrical properties, volume and radius of gyration, between the numerical aggregate (overlapping spheres) and the tomography with $a_{dip} = 16$ nm. Therefore, we will keep this discretization throughout the analyses given in the next section.

4.5.3 Radiative properties of the tomography soot compared to the volume equivalent numerical aggregates

DDA simulations are performed on the equivalent morphology generations illustrated in Figures 4.8 and 4.9. The results obtained are presented in Figure 4.14 for the large aggregate and in Figure 4.15 for the small aggregates.

The behaviors observed from the DDA simulations indicate that the realistic soot aggregate can be perfeclty modeled as a fractal aggregate in the near and mid IR, if the overlapping is applied. This is true for absorption but also for scattering. Care should be given to scattering at smaller wavelengths. As can be seen in Figures 4.14 and 4.15, the absorption and scattering spectra, as well as the asymmetry parameter of the overlapping DLCCA aggregate diverge from the ones of the real object below 600 nm. Besides, there is a significant gap between the numerical aggregates with hard spheres and with overlapping spheres. High overlapping rate increases the overall extinction cross-sections of soot up to 20% for small aggregates, and up to 40% for large aggregates in the range of thermal radiation corresponding to combustion temperatures. It is noted that this increase in extinction of large aggregates is due to a significant increase in the scattering albedo due to the multiple scattering effects inside the aggregate. Nevertheless, the effect of scattering becomes negligible beyond 2 microns for the large aggregate and beyond 1 micron for the small aggregate. It is also observed that the g factor is smaller for the realistic shape of soot aggregate: the scattering phase function is more isotropic than predicted. This latter is illustrated for in the plots of phase functions of the large aggregate (Figure 4.16) and small aggregate (Figure 4.17).

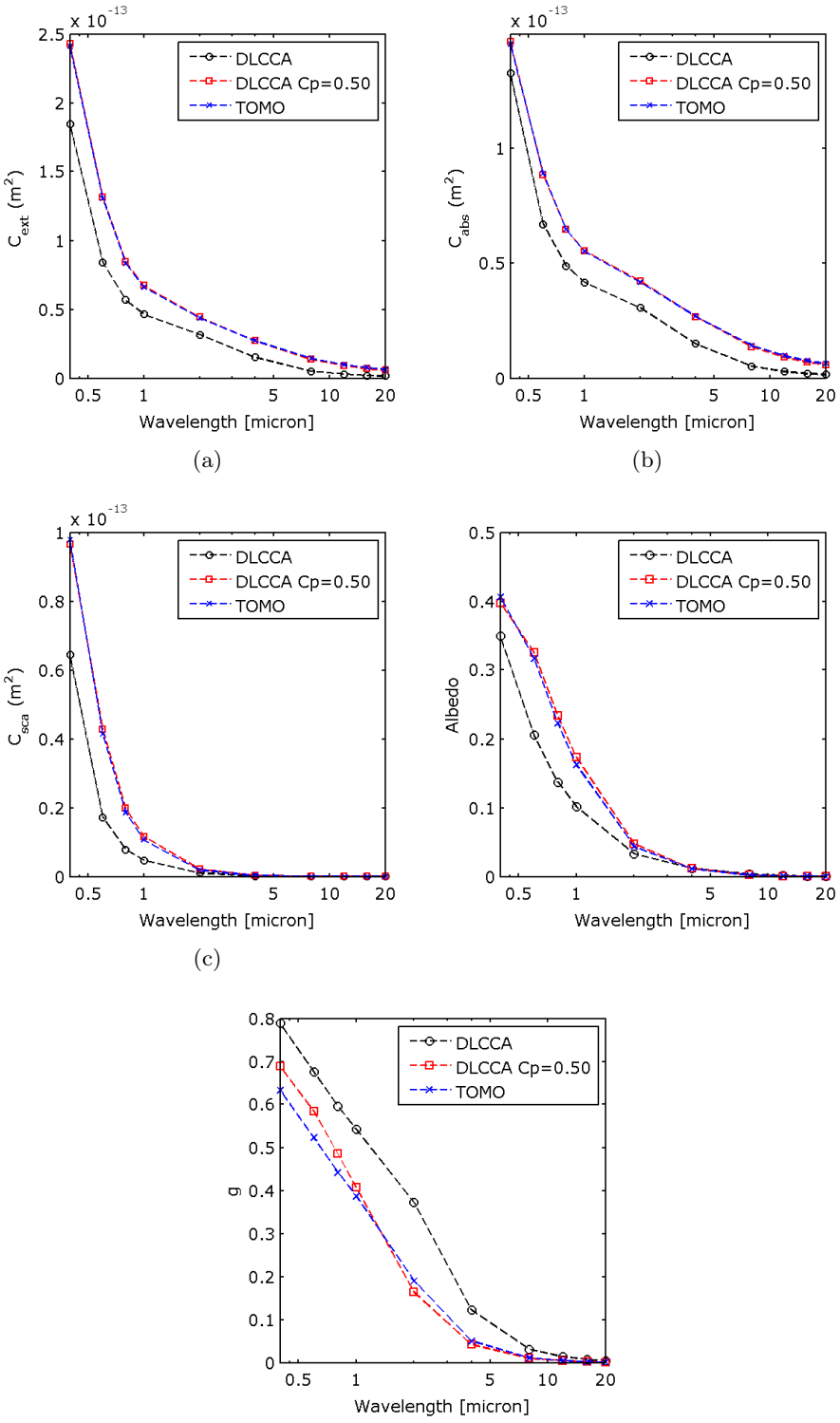

Figure 4.14: *Radiative properties (computed by DDA) of tomography soot (case 1 - large aggregate) and of the volume equivalent generations with and without particle overlapping.*

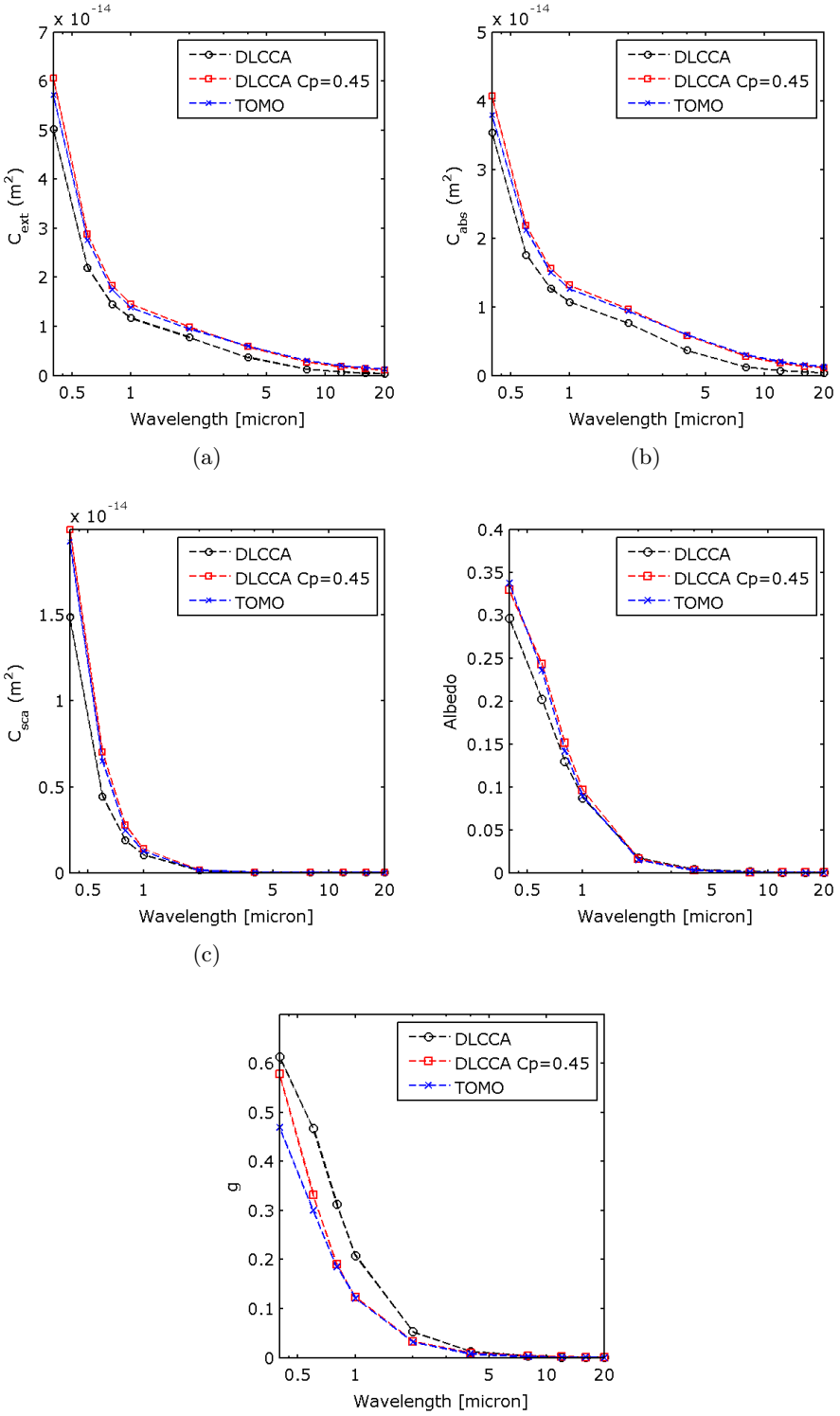

Figure 4.15: *Radiative properties (computed by DDA) of tomography soot (case 2 - small aggregate) and of the volume equivalent generations with and without particle overlapping.*

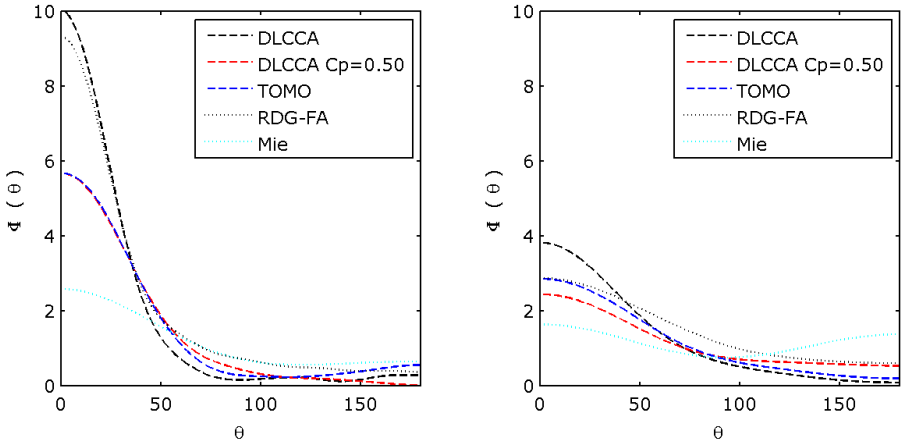

Figure 4.16: *Phase function of large aggregate at: (a) 800 nm; (b) 2 microns. Comparison of results obtained by DDA (for DLCCA and TOMO), by RDGFA and Mie theories.*

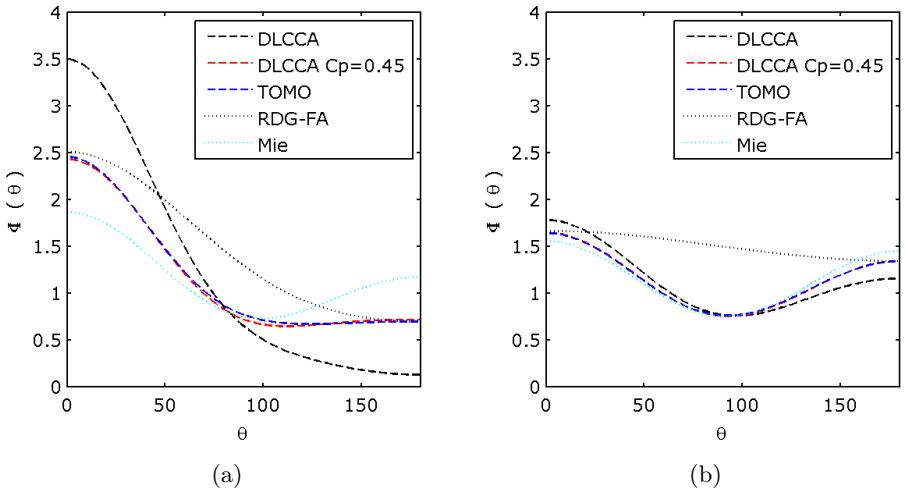

Figure 4.17: *Phase function of small aggregate at: (a) 800 nm; (b) 2 microns. Comparison of results obtained by DDA (for DLCCA and TOMO), by RDGFA and Mie theories.*

The comparison of the results of different radiation-matter interaction theories used (DDA, Mie, RDG-FA) will be discussed in Section 4.6. Here, we remind that the phase function $\Phi(\mathbf{u}, \mathbf{n})$ is computed by DDA for 50 directions of incident waves $\mathbf{u}$ in the emerging directions $\mathbf{n}$ over the 3D space. This complex information $\Phi(\mathbf{u}, \mathbf{n})$ is averaged over hundreds of scattering planes and reduced to the form of $\Phi(\theta)$ which will be integrated into the solution of the radiative transfer equation by the discrete ordinates method, as will be explained in Chapter 5.

The results obtained using the soot morphology from tomography comply with the literature results on the effect of overlapping mentioned by Yon et al. (2015) who focus also on the necking phenomena between particles. Note that in our spectral range of interest $\lambda \gtrsim 800$ nm, the radiation probes the geometry but can not capture the surface details therefore the effect of necking is ignored. Also our discretization is not fine down to a few nanometers to capture those reliefs, neither the resolution of our tomography. The application of DDA is nevertheless acceptable as long as we are not dealing with small wavelengths ($\lambda < 600$ nm) and as long as the true volume of the tomography aggregate is recovered in the discretized object.

4.6 Note on the usage of different models

As mentioned in Chapter 3, the RDG-FA theory is a simpler and faster approach to compute the radiative properties of soot aggregates. This theory is widely used, especially in in-situ experiments, due to its compromise on the rapidity of computations. Though the reported level of discrepancy reaches 20% between the rigorous solutions and RDG-FA (Sorensen (2001) and references therein). Furthermore, it is not aplicable to any complex geometry but limited to aggregates of hard spheres scattering in the Rayleigh limit. Therefore, in this section, we only take a glance at the results obtained by different computation methods of the radiative properties in order to assess their validity for our realistic soot geometries. The Mie solution is also introduced in order to demonstrate that the radiative properties in our spectral range of interest ($0.8 < \lambda < 20\ \mu m$) are not solely a function of the material volume.

In Figures 4.18 and 4.19, the results obtained by DDA in the previous section are compared to the ones obtained by RDG-FA and Mie theories. The Mie theory is applied to the aggregate in two different ways: by taking a volume equivalent sphere, and by summing the properties of N_p primary particles.

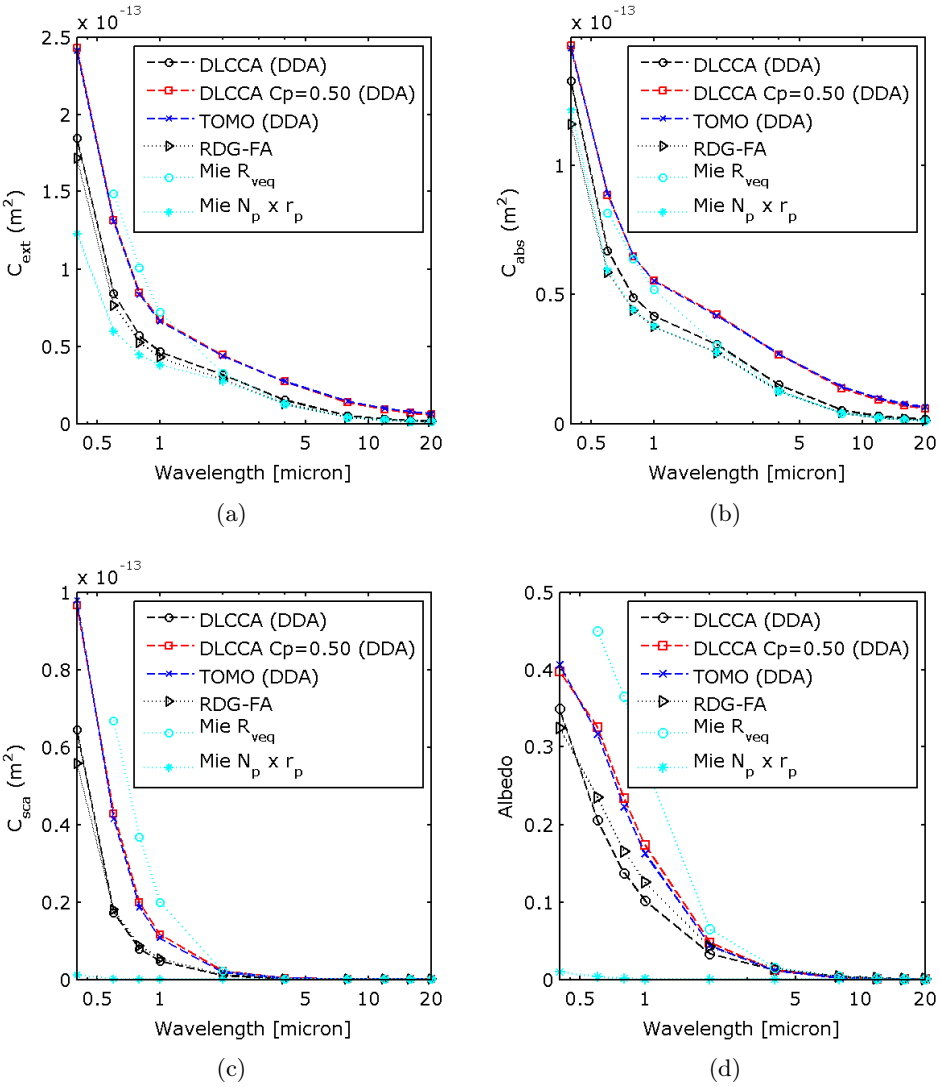

Figure 4.18: *Comparison between the DDA solutions and RDG-FA for large aggregate. The volume equivalent sphere radius is* $R_{veq} = 136$ *nm for all simulations.*

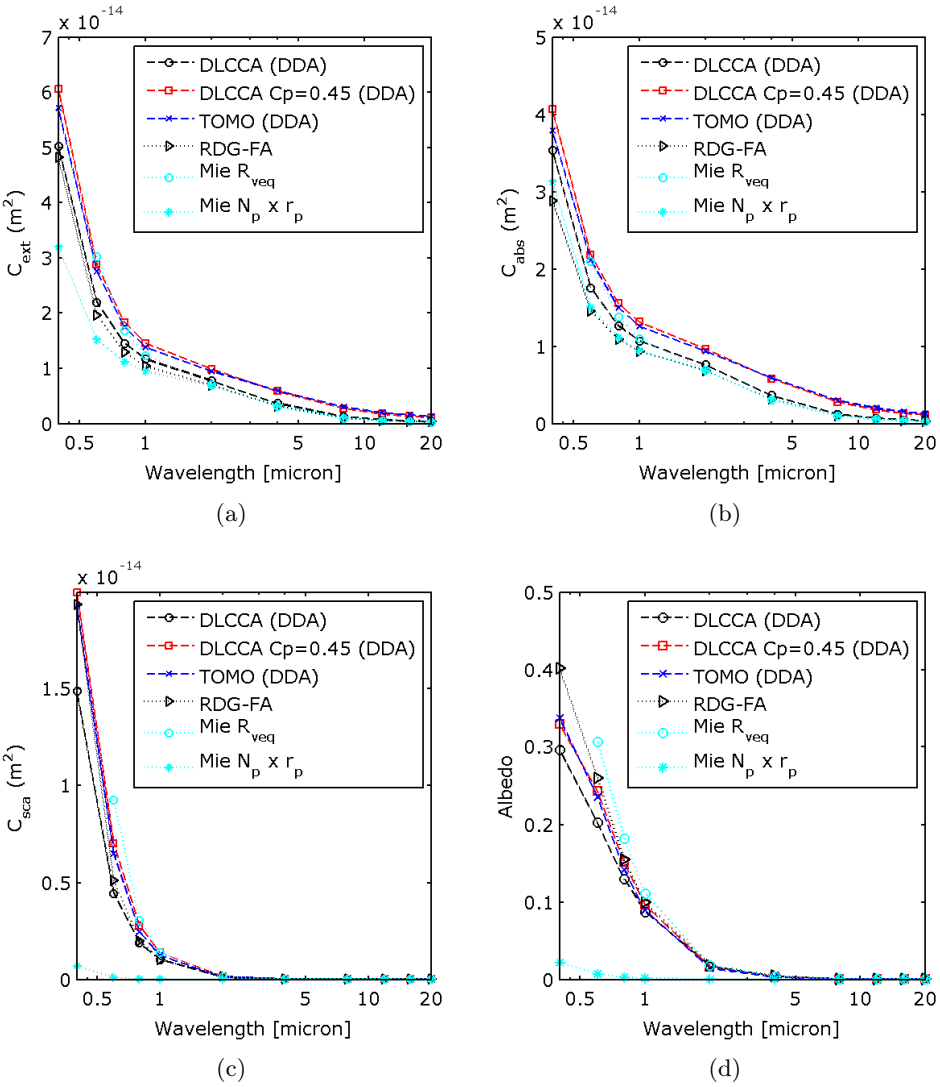

Figure 4.19: *Comparison between the DDA solutions and RDG-FA for small aggregate. The volume equivalent sphere radius is* $R_{veq} = 136$ *nm for all simulations.*

Concerning the absorption properties in Figures 4.18(b) and 4.19(b), the RDG-FA results are equal to the Mie solution for the sum of N_p primary particles. This is expected because RDG-FA considers that the primary particles are in the Rayleigh limit and the multiple scattering effect between primary particles is neglected. As a result, and again expected from literature studies, RDG-FA underestimates slightly the total extinction of soot aggregates.

On the other hand, the volume equivalent Mie particle approach is not realistic, especially in the near IR where the scattering properties diverge from the rigorous DDA solutions. This is illustrated in the cross-sections and scattering albedos of Figures 4.18 and 4.19, and in the scattering phase functions of Figures 4.16 and 4.17. It is worth recalling here that RDG-FA does not necessarily satisfy the energy conservation and the subsequent phase function should absolutely be corrected and renormalized before injecting in the radiation simulations. Hence we will stick to the rigorous solutions given by DDA in the next Chapter 5 for the numerical resolution of the radiative heat transfer.

4.7 Conclusion and perspectives on the soot radiative properties

In this chapter, we focused on the determination of the soot radiative properties as a function of the realistic complex shape. Our in-house rigorous DDA solution (which was developed in Chapter 3) was applied to the 3D geometry information obtained by tomography in Chapter 1 and to the numerical aggregates generated by the fractal information obtained in Chapter 2. The performed ex-situ applications (aggregate sampling, tomography reconstruction and radiative characterization by DDA) being costly, we investigated the possibility to represent soot by numerical aggregates in a more realistic way.

It was found out that the representativity of numerical aggregates composed of hard spheres is poor, especially for large aggregates of hundreds of primary particles. Therefore we generated numerical aggregates with equivalent volumes using the fractal dimension D_f and the overlapping coefficient C_p computed in the ex-situ fractal analysis. In this way, we obtained very similar radiative properties for the numerically generated aggregates with overlapping particles compared to the realistic soot. Finally, we found out that the representativity and the quality of the radiative properties of soot are notably enhanced by the generation of sintered primary particles. For the radiative properties in the near and mid IR, the cross-sections of aggregates can be enhanced by up to 20% for small aggregates (with $N_p \approx 100$) and by up to 40% for large aggregates (with $N_p \approx 900$) due to particle sintering, compared to aggregates of hard spheres.

Of course, the application range in this study is limited to few aggregates because we observed two extreme cases to give the maximum and minimum error bounds succeptible to be caused by the effect of realistic geometries. If the 3D fractal analysis results can be directly correlated to 2D image analyses, the radiative properties can be repeatedly computed by DDA for DLCCA generated aggregates with different overlapping coefficients C_p, particle numbers N_p and particle size parameters x_p, in order to obtain tabulated correction factors for soot aggregates issued from different processes. We note that the small differences between the aggregate with $N_p \approx 100$ from tomography and the corresponding DLCCA aggregate with overlapping particles can also be due to the polydispersity of primary particle size, which can also be studied in a future work.

In the next chapter, the radiative properties of soot will be integrated into the radiative heat transfer simulations. The effects of the aggregate size, of the particle overlapping and of the scattering on the radiative heat transfer will be examined. This will help us to quantify the level of errors which can be caused by the modeling of soot aggregates using conventional DLCCA methods, and by ignoring the scattering from soot for highly aggregated media.

Part III

Radiative heat transfer

Chapter 5

Radiation through sooty gaseous mixtures

In this chapter, the possible effects of soot and its aggregation on the radiative heat transfer are investigated. Literature data indicate that the scattering effect of soot can be neglected. Nevertheless, it has been shown in the previous section that the scattering and the total extinction of soot can be substantially enhanced in the near IR domain by the effect of multiple scattering due to the sintering of particles. Using those new findings, the radiative transfer will be investigated for participating media involving soot with and without gaseous combustion products. The radiative heat transfer equation is numerically solved using the Discrete Ordinates Method (DOM) in a 1D parallel walls configuration. The aim in this chapter is to investigate the difference between sooty and non-sooty cases, also between scattering and non-scattering cases. Detailed investigation of the radiative properties of gaseous mixtures, numerical investigation of the best implementation of DOM and comparison of the accuracy of the gas models are out of the scope of this study. Hence, an existing in-house radiation code is used, based on the local absorption coefficients in DOM through gaseous media with the SNB database. It was presumed during the electromagnetic radiation simulations in Chapter 4 that there is no interaction between the gaseous species and the soot particulate media, hence it is assumed that no correlation exists between soot and gas radiation spectra. Soot spectral extinction coefficients are extracted from the extinction cross-sections as a function of the volume fraction. The spectral scattering albedos and phase functions are introduced accordingly. Finally, the radiative heat flux and source terms are investigated as a function of the volume fraction and the aggregate size of soot, for different temperatures, with and without participating gases. The simulations with soot scattering are repeated for large distances between the walls in order to approach the industrial scales.

5.1 Solving the radiative heat transfer equation in participating media

When a monochromatic bundle of radiation crosses a semi-transparent participating medium, it interacts with the existing species. For our interest on combustion environments, those species are gases and soot particles. From the radiative heat transfer point of view, the interaction is expressed in terms of attenuation or amplification of the incident radiation. For a single radiation bundle, while the absorption and out-scattering by the medium attenuate its intensity, the in-scattering coming from the other radiation bundles and the emission of the species amplify it troughout its path. At an instant when we consider stationary conditions, all the interactions affecting the intensity field I_λ satisfy an energy conservation equation which is the radiative transfer equation (RTE) (Modest (2013)):

$$\mathbf{n}\cdot\nabla I_\nu(\mathbf{r},\mathbf{n}) = -\beta_\nu I_\nu(\mathbf{r},\mathbf{n}) + \kappa_\nu n_\nu^2 I_\nu^0(T(\mathbf{r})) + \frac{\sigma_\nu}{4\pi}\int_{4\pi}\phi_\nu(\mathbf{n}',\mathbf{n})I_\nu(\mathbf{r},\mathbf{n}')d\Omega' \quad (5.1)$$

In the above Equation 5.1, I_ν^0 is the blackbody radiation as a function of the temperature T at the position $\mathbf{r}$, $I_\nu(\mathbf{r},\mathbf{n})$ is the spectral intensity of the radiation at position $\mathbf{r}$ with unit vector $\mathbf{n}$ of propagation direction, $\phi_\nu(\mathbf{n}',\mathbf{n})$ is the scattering phase function of the medium with in-scattering direction $\mathbf{n}'$ and out-scattering direction $\mathbf{n}$, κ_ν is the absorption coefficient of the medium, σ_ν is the scattering coefficient (out-scattering) of the medium, and $\beta_\nu = \kappa_\nu + \sigma_\nu$ is the total extinction coefficient. The heat flux $\mathbf{q}$ (in W/m^2)is given by the following:

$$\mathbf{q}(\mathbf{r}) = \int_\nu\int_{4\pi} I_\nu(\mathbf{r},\mathbf{n})\mathbf{n}d\Omega d\nu \quad (5.2)$$

The source term (in W/m^3) is given by the following equation:

$$-\nabla\cdot\mathbf{q}(\mathbf{r}) = \int_\nu\int_{4\pi}\kappa_\nu\left[I_\nu(\mathbf{r},\mathbf{n}) - n_\nu^2 I_\nu^0(T(\mathbf{r}))\right]d\Omega d\nu \quad (5.3)$$

In all simulations, the walls are opaque, and they are assumed to behave either as blackbodies or as diffusely reflecting surfaces, for which the boundary condition writes (Modest (2013)):

$$I_\nu(\mathbf{r},\mathbf{n}) = \varepsilon_\nu I_\nu^0(\mathbf{r}) + \frac{\rho_\nu}{\pi}\int_{\mathbf{t}.\mathbf{n}'<0} I_\nu(\mathbf{r},\mathbf{n}')\left|\mathbf{t}.\mathbf{n}'\right|d\Omega' \quad (5.4)$$

In Equation 5.4, ε_ν and ρ_ν are the emissivity and reflectivity of the surface, $\mathbf{r}$ is the position of any point on the wall, $\mathbf{t}$ is the outward vector from the wall at point $\mathbf{r}$. Note that all the variables expressed with a subscript ν are spectral, and there is no straightforward analytical solution of the RTE when we introduce a non-uniform distribution of species involving anisotropic scattering. Consequently, numerical methods are necessary and we used the Discrete Ordinates Method (DOM) (Chandrasekhar (1960)), as it seemed the most straightforward technique with rapid simulations, to introduce scattering properties and spectral data, in between other solution techniques such as Monte Carlo, spherical harmonics, zonal methods (Modest (2013)). The methods used in DOM are briefly reviewed in the next paragraph.

5.1.1 Discrete Ordinates Method

On a spectral interval over which the radiative properties of the species are considered to be constant, the radiative transfer equation can be expressed in terms of the discrete ordinates approximations in the following form (equation adapted from Truelove (1988)):

$$\mu_i \frac{\partial I_i}{\partial x} + \xi_i \frac{\partial I_i}{\partial y} + \eta_i \frac{\partial I_i}{\partial z} = (1-\omega)\beta I^0 - \beta I_i + \frac{\omega\beta}{4\pi} \sum_{j=1}^{M} w_j I_j \Phi_{ij} \tag{5.5}$$

In the above Equation 5.5, i and j subscripts are the indices for ordinate directions, $I_i = I(x, y, z, \mu_i, \xi_i, \eta_i)$ is the radiative intensity at position (x, y, z) in the discrete direction i, Φ_{ij} is the scattering phase function between i and j discrete directions, μ_i, ξ_i, η_i are the direction cosines of direction i, and w_j is the angular weight associated to direction j. Here we introduce the scattering albedo of the medium defined by $\omega_\lambda = \sigma_\lambda / \beta_\lambda$. This formulation allows the numerical resolution of the RTE for rectangular control volumes in 3D (Raithby and Chu (1990)). Other formulations, such as axial symmetry, are not considered in the formuation of our DOM code because we limit our investigations to parallel plate configurations.

The radiative heat source term $\nabla \cdot \mathbf{q}$ (expressed in W/m^3) is the difference between the emitted power and the absorbed power per unit volume and expressed as follows (equation adapted from Truelove (1988)):

$$-\nabla \cdot \mathbf{q} = (1-\omega)\beta \left(\sum_j w_j I_j - 4\pi n^2 I^0 \right) \tag{5.6}$$

Again, I_j and w_j account for the contributions from in-scattering directions j. To determine those directions, the angular discretization is performed following the direction cosines given by the level symmetric S_8 quadrature of Fiveland (1984) with moderate number of angular discretizations, even though it can be insufficient for highly anisotropic scattering. Nevertheless, as demonstrated in Chapter 4, the anisotropy of phase function of the realistic soot aggregates is less than expected compared to aggregates of hard spheres, and the scattering albedo is always less than 0.5 which reduces the possible errors due to scattering. Also, for soot radiation, we will use symmetric boundary conditions where the anistropy effect is reported to be less important (Kim and Lee (1988)).

The gas absorption is formulated by local absorption coefficients (Ludwig et al. (1973)), formulation based on the statistical narrow band (SNB) model (Grosshandler (1980)). The spectrum of radiation is divided into more than 400 intervals for gaseous-only cases and soot-only cases, and more than 600 intervals for soot+gas simulations. Test cases are presented in Section 5.2 in order to verify the database of the code for gases only (Section 5.2.1), and also to validate our scattering algorithm (Section 5.2.2). The calculation box bounded by the six opaque walls is divided into more than 40^3 (20^3 for the test cases) rectangular control volume elements with optical thickness ($\tau_m = \beta l_m$) < 1 and an aspect ratio less than 1.5, using the step discretization scheme proposed by Raithby and Chu (1990). The parallel plates are simulated as black walls and the others are diffusely reflecting.

5.1.2 Implementation of soot radiative properties

The radiative properties of a cloud of particles can be considered as the summation of the individual effects of all particles if the scattering between those particles is independent (Modest (2013)). For the flame soot, the volume fraction ranges between $10^{-6} < f_v < 10^{-5}$. In theory, this falls in the independent scattering regime which was illustrated in Chapter 3 in Figure 3.1.

However, according to the observations, the primary particles stick, coalesce and form complex shaped aggregates. Those aggregates interact in a complex manner with the incident radiation. For this reason, the radiative properties of soot aggregates were computed in the previous chapter by the electromagnetic theory of DDA. Though, the volume fractions in question imply that the distance between neighbouring aggregates is so large that we can simply sum the effect of all aggregates in order to find the absorption and scattering properties of the cloud of soot.

When the medium is particulate with independent scattering between small particles in Rayleigh scattering regime, the summation of the effects of all

particles is given by the following relationship (Modest (2013)):

$$\kappa_{\lambda,soot} = \Im\left\{\frac{m_\lambda^2 - 1}{m_\lambda^2 + 2}\right\}\frac{6\pi f_v}{\lambda} \tag{5.7}$$

In the above equation 5.7, κ_{soot} is the absorption coefficient of soot, m is the complex optical index, f_v is the volume fraction and λ is the wavelength. A uniform distribution of particles is considered with size parameters in the Rayleigh limit, and recalling Equation 3.12 for the particle absorption cross-section $C_{abs,p}$ given by the Rayleigh theory, the equation for the absorption coefficient of a cloud of soot particles can be expressed as follows:

$$\kappa_{\lambda,soot} = \frac{C^p_{\lambda,abs}}{V_p} f_v \tag{5.8}$$

In equation 5.8, V_p is the volume of the primary particle. An accurate way to account for aggregation would be to introduce the aggregate size distribution function with the properties tabulated for each size of the aggregate. Nevertheless, we are looking for an upper limit of the effect of aggregation. Even though it is not realistic, a uniform distribution of aggregates will be considered for the seek of simplicity: the aggregates in one simulation have the same size and the same geometry. The orientation is random: the configuration averaging of radiative properties was performed in the previous Chapter 4. This allows us to compute the absorption coefficient of the soot cloud by replacing the particle properties by the aggregate properties, as the individual aggregates do not interact with their nearest neighbours:

$$\kappa_{\lambda,soot} = \frac{C^{agg}_{\lambda,abs}}{V_{agg}} f_v \tag{5.9}$$

In the above equation 5.9, we replaced the particle absorption cross-section C_p by the aggregate absorption cross-section C^{agg}, and the volume was replaced by the aggregate volume V^{agg}. With this formulation, we avoid the usage of the efficiency term $Q_{abs} = C_{abs}/A_{agg}$, where the projected area of the aggregate A_{agg} would change according to the incident wave direction.

In literature studies including the effect of soot coupled to gaseous media properties, the contribution of soot to radiation is found to affect notably the heat flux rates but the scattering from soot is nearly always neglected. One study investigating the scattering effect of soot is proposed by Eymet et al. (2002).

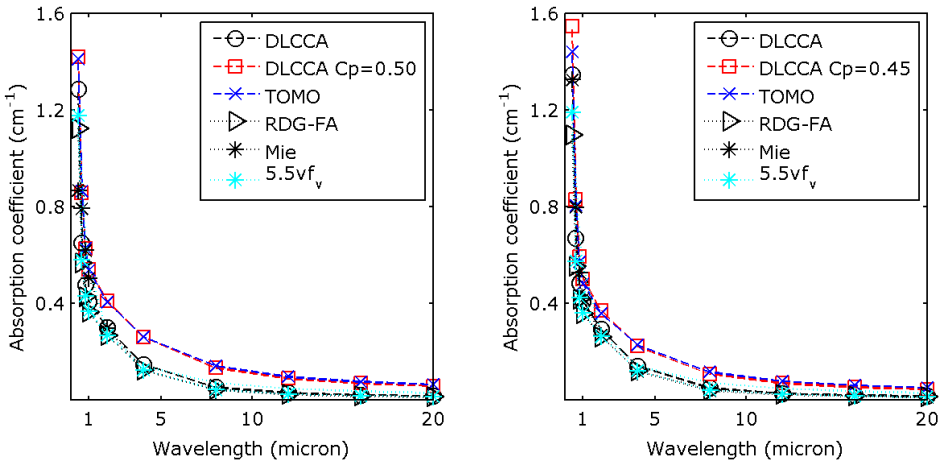

Figure 5.1: *Absorption coefficient spectra of (a) the big aggregate ($N_p \approx 940$), (b) the small aggregate ($N_p \approx 100$) computed using different methods for a volume fraction of $f_v = 10^{-5}$. Here the empirical formulation "$5.5\nu f_v$" is added as it constitutes a mean value for radiative transfer simulations in combustion sytems involving soot, as discussed in the study of Tessé (2001).*

They studied the effect of soot scattering on the radiative heat source and on the radiative heat flux in an isothermal medium at 2000 K bounded by two parallel infinite black walls, without participating gases. According to their findings, the scattering of soot is expected to have negligible effect on the radiative heat flux. We took the same simulation conditions as this work constitutes a good academic test case. On the other hand, our study differs in two ways: we used rigorous DDA, instead of RDG-FA, for the computation of the radiative properties and the scattering effect is highly enhanced by the sintering of particles as demonstrated in the previous chapter. Therefore we investigate the effect of this new contribution on soot radiative properties on the radiative heat flux rates.

In order to observe the contribution of the scattering, each case is simulated with and without scattering. We remind that the extinction coefficient is expressed by $\beta_\lambda = \kappa_\lambda + \sigma_\lambda$ where the scattering coefficient for soot is again computed in terms of the scattering cross-section of aggregates:

$$\sigma_{\lambda,soot} = \frac{C^{agg}_{\lambda,sca}}{V_{agg}} f_v \tag{5.10}$$

When the scattering is ignored, the extinction coefficient is reduced to $\beta_\lambda = \kappa_\lambda$. The absorption and scattering cross-sections are the spectral values computed

from DDA simulations, as illustrated in Figure 5.1. The phase function is parametrized also by the spectral g values in order to account for the effect of modified anisotropy as a function of wavelength. For $\lambda \leq 1\mu m$ the phase function is the one obtained from DDA because it is highly anisotropic. For $\lambda \geq 1\mu m$, the Henyey-Greenstein phase function is used with g parameter computed from DDA simulations. As we introduced scattering into DOM, special attention was given to its modeling. The scattering phase function should verify the following normalization condition:

$$\frac{1}{4\pi}\int_{4\pi}\Phi(n',n)\mathrm{d}\Omega' = 1 \tag{5.11}$$

Following the above relation in Equation 5.11, the values of the discretized phase function are renormalized as follows (Liu et al. (2002)) and replaced in Equation 5.5:

$$\Phi_{ij}{}' = \frac{\Phi_{ij}}{\frac{1}{4\pi}\sum_{j=1}^{M} w_j \Phi_{ij}} \tag{5.12}$$

For the simulations with scattering, we noted that the renormalization of the phase function does not change the result significantly. This is a result of our rigourous computation of the phase function using DDA where the energy is conserved as it was mentioned in Section 4.6.

5.2 Validation cases

5.2.1 Test cases with absorption only

In this section, we first validated the absorption of gases with grey-band approximation, with local absorption coefficient, using SNB. Comparison is made with simple cases from the literature. Configuration data is taken from the studies of Liu et al. (1998) for gases simulated between two parallel plates, as they also used the similar formulation of local absorption coefficient. They concluded that the heat flux and heat source terms are accurate enough with this model, compared to ray tracing results for correlated and non-correlated SNB models, even for a non-uniform distribution of gas fraction and temperature. The test cases are the following:

- **Case 1**: Pure water vapor at uniform temperature of $T = 1000$ K, at uniform pressure 1 bar, is simulated between parallel walls at a seperation distance of $L = 0.1$ m. Two parallel walls are black ($\varepsilon = 1$) and cold at $T = 0$ K, other walls being diffusely reflecting ($\varepsilon = 0$).
- **Case 2**: Same as Case 1, but the wall separation distance is $L = 1$ m.
- **Case 3**: Same as Case 2, with a parabolic concentration profile for $H_2O + N_2$ such that $f(H_2O) = 4(1 - x/L)x/L$. Here, f is the molar concentration of H_2O, x is the distance from the left wall, L is the separation distance of the walls.
- **Case 4**: Same as Case 1, but with a boundary layer temperature profile for H_2O (retrieved from Kim et al. (1991)) and a separation distance $L = 0.2$ m. The left wall is at $T = 1500$ K and the right wall is at $T = 300$ K.
- **Case 5**: Counterflow methane/air diffusion flame with given temperature and concentration profiles of H_2O and CO_2.

	Our results (kW/m^2)	**Values given by Liu et al. (1998)**
Case 1	17.60	17.6
Case 2	33.95	34.0
Case 3	31.10	31.1
Case 4	-267.7	-270.7
Case 5	36.0	34.8

Table 5.1: *Radiative heat flux values at the left wall, computed in the test cases for absorption, compared to results of Liu et al. (1998).*

As listed in Table 5.1 the results on the heat flux comply quite well with the literature values, as well as the heat source distributions in the cases with uniform temperature and homogeneous distibutions as plotted in Figures 5.2(a) and 5.2(b). Discrepancies are observed in the heat source term when a strongly non-uniform temperature or concentration profile is involved, as presented in Figures 5.2(c) and 5.2(d). Nevertheless, for data corresponding to counterflow methane/air diffusion flame, our data fits the literature values as presented in Figure 5.2(e), implying that our DOM algorithm is accurate in relatively symmetrical conditions, and is also fairly accurate in highy asymmetric distribution configurations.

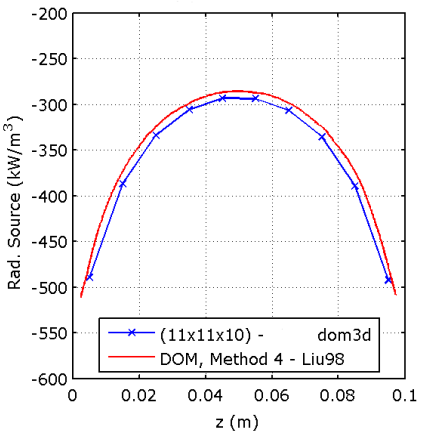

(a) CASE 1

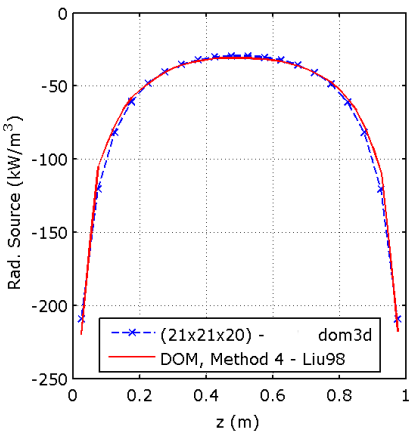

(b) CASE 2

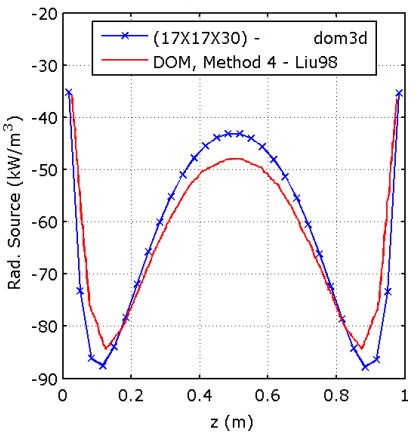

(c) CASE 3

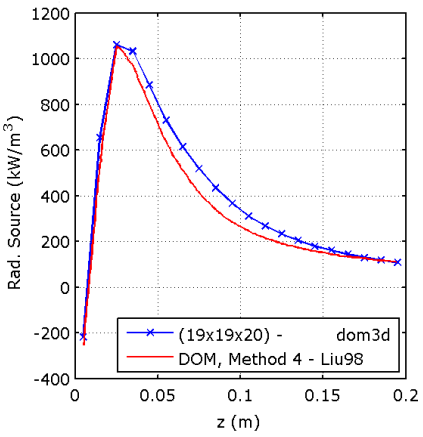

(d) CASE 4

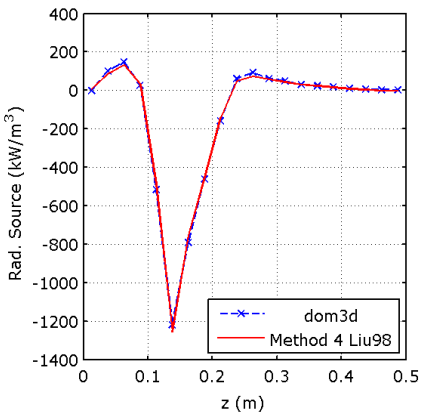

(e) CASE 5

Figure 5.2: *Comparison of the radiative heat source values obtained from our code and compared to the ones of Liu et al. (1998).*

5.2.2 Test case with scattering

To our knowledge, there is not any benchmarking solution of spectral simulations using DOM and involving anisotropic scattering. Therefore, the benchmarking of scattering in our code is performed by comparison to the results of Liu et al. (2002) where a gray medium is simulated for optical thickness of the slab with $\tau_L = 1, 3, 5, 7$ and for scattering albedos $\omega = 0.5, 0.8, 1.0$. The scattering phase function of the medium is given by Mie scattering for a size parameter of $x = 4$ and a complex optical index of $m = 2$. This corresponds to highly anisotropic and absorbing medium, which constitutes a good test cases before any application on soot aggregates. The values given in their study were dimensionless for a slab thickness L, hence a slab thickness of $L = 1$ m is chosen in our simulations.

As presented in Table 5.3, the simulations are repeated for uniform medium at 1500 K and 2500 K. For the heat flux, the difference due to aggregation is computed between the results obtained from Mie and DDA ("DLCCA and TOMO") spectral properties. The difference due to scattering is computed for the same model of radiative properties, for the radiation simulations performed with ("w sca") and without scattering ("w/o sca") of aggregates. The source term is given in the middle of the separation distance.

		Left wall			**Right wall**		
τ_L	ω	**Flux (kW/m^2) (Liu RDOM)**	**Flux (kW/m^2) (Our result)**	**% Difference**	**Flux (kW/m^2) (Liu RDOM)**	**Flux (kW/m^2) (Our result)**	**% Difference**
1	**0.5**	3095,1	3046,3	1.6	2040,6	1897,8	7.0
3	**0.5**	1985,7 2	2025,4	2.0	641,3	662,6	3.3
5	**0.5**	1464,9	1493,8	2.0	274,6	276,9	0.8
7	**0.5**	1157,8	1217,1	5.2	148,1	162,1	9.5

Table 5.2: *Comparison of validation cases for DOM using anisotropic scattering for a gray slab with thickness L=1m. The literature results are retrieved from Liu et al. (2002).*

The results are presented in Table 5.2 for $\omega = 0.5$ values, as the scattering albedos for the sooty mixtures will be always less than 0.5, as it was presented in the spectral properties of soot aggregates computed in Chapter 4. The differences between the fluxes are less than 10%. In our simulations, the slab is discretized into 40 elements. When control volume element is optically very thin, the errors due to anisotropic scattering increases as can be seen for $\tau_L = 1$, if the directional discretization over 4π steradians is not increased with the same rate.

It is concluded that the accuracy of our DOM algorithm is good enough for simulations with absorption and also with anistropic scattering. Therefore,

in the next sections, results will be presented first for a soot-only medium to investigate the effect of scattering, and then for sooty gaseous medium to examine the increase of heat fluxes due to soot and its aggregation combined with gasesous combustion products.

5.3 Applications with soot aggregates

In this section, the effect of morphology of soot on the radiative heat transfer will be investigated. To that end, all the cases will be solved using three different data sets for soot radiative properties: Mie solution of primary particles with scattering being ignored, DDA solution of DLCCA generated aggregates with hard spheres and DDA solution of realistic 3D aggregates obtained from tomography. The results of our DDA simulations of Chapter 4 indicate an overall increase of scattering but also of the absorption due to aggregation, and also due to overlapping. Therefore, we repeated the radiative transfer simulations for soot radiative properties computed by Mie solution for primary particles, by DDA for aggregates of hard spheres and again by DDA for aggregates with overlapping particles obtained from tomography. Mie solution is equivalent to RDG-FA when scattering is ignored. RDG-FA is not used in our computations because it does not necessarily satisfy the optical theorem and the energy conservation. DDA solution for aggregates of hard spheres is compared to the Mie solution in order to quantify the impact of aggregation on the radiative heat flux. Finally, the simulations are repeated using the spectral radiative properties of the tomography soot: This allows to see the effect of particle overlapping on the total radiative heat fluxes. Note that in Chapter 4, DLCCA generated aggregates with overlapping spheres were found to have very similar radiative properties compared to tomography soot, hence the simulations are not repeated for this latter.

5.3.1 Uniform soot volume fraction without gases

First, the total effect of scattering from soot is investigated by DOM simulations for uniform distributions of temperature and volume fraction. Gases, considered to be only absorbing, are not introduced to maximize the scattering rate.

The first simulation case is taken from Eymet et al. (2002): soot volume fractions of $f_v = 10^{-5}$ and $f_v = 10^{-6}$ at uniform temperature $T = 2000$ K are simulated between two parallel black walls at $T = 300$ K, at a separation distance of $L = 1$ m. The results are listed in Table 5.3, where q is the flux at the left wall and the radiative source is given at the half distance between the plates.

			q (kW/m^2)		% Δ due to	% Δ due to	Source (kW/m^3)		% Δ due to
			w/o sca	w sca	aggregation (w/o sca)	scattering	w/o sca	w sca	scattering
$f_v = 10^{-5}$	T = 1500 K	Np*Mie (small)	285,1				-38,3		
		DLCCA (small)	285,7	285,5	0,2	0,1	182,4	182,4	0,0
		TOMO (small)	286,2	286,1	0,4	0,1	591,9	592,1	0,0
		Np*Mie (big)	285,2				-37,2		
		DLCCA (big)	285,7	285,4	0,2	0,1	-341,4	-348,9	-2,1
		TOMO (big)	286,2	285,9	0,4	0,1	-236,2	-236,3	-0,1
	T = 2000 K	Np*Mie (small)	904,1				-65,0		
		DLCCA (small)	904,8	904,0	0,1	0,1	787,3	778,2	1,2
		TOMO (small)	905,7	904,8	0,2	0,1	2253,3	2254,9	0,1
		Np*Mie (big)	904,1				-62,9		
		DLCCA (big)	904,9	903,3	0,1	0,2	-1299,4	-1344,0	-3,3
		TOMO (big)	905,7	903,8	0,2	0,2	-838,5	-839,3	-0,1
	T = 2500 K	Np*Mie (small)	2209,6				-94,8		
		DLCCA (small)	2210,7	2205,2	0,0	0,2	2369,0	2369,9	0,0
		TOMO (small)	2211,7	2205,2	0,1	0,3	6465,3	6473,7	0,1
		Np*Mie (big)	2209,5				-91,5		
		DLCCA (big)	2210,5	2207,9	0,0	0,1	-3723,9	-3906,8	-4,7
		TOMO (big)	2211,7	2208,5	0,1	0,1	-2358,5	-2362,4	-0,2
$f_v = 10^{-6}$	T = 1500 K	Np*Mie (small)	245,2				-330,0		
		DLCCA (small)	252,6	252,0	3,0	0,2	-251,6	-254,0	-0,9
		TOMO (small)	272,0	271,4	10,9	0,2	-203,8	-205,6	-0,8
		Np*Mie (big)	246,2				-328,5		
		DLCCA (big)	254,7	253,6	3,5	0,4	-188,7	-193,5	-2,5
		TOMO (big)	276,2	275,2	12,2	0,4	-184,4	-190,0	-3,0
	T = 2000 K	Np*Mie (small)	822,8				-996,0		
		DLCCA (small)	839,8	837,0	2,1	0,3	-696,1	-710,4	-2,0
		TOMO (small)	877,3	874,2	6,6	0,4	-503,9	-514,5	-2,0
		Np*Mie (big)	825,2				-988,4		
		DLCCA (big)	844,4	840,0	2,3	0,5	-554,7	-579,2	-4,2
		TOMO (big)	886,5	881,3	7,4	0,6	-503,5	-531,1	-5,2
	T = 2500 K	Np*Mie (small)	2071,3				-2285,7		
		DLCCA (small)	2103,8	2093,7	1,6	0,5	-1460,8	-1514,3	-3,5
		TOMO (small)	2164,4	2152,1	4,5	0,6	-917,7	-956,5	-4,1
		Np*Mie (big)	2075,8				-2264,1		
		DLCCA (big)	2111,6	2098,2	1,7	0,6	-1278,1	-1361,5	-6,1
		TOMO (big)	2180,6	2162,7	5,0	0,8	-1093,5	-1181,3	-7,4

Table 5.3: *Simulation of a soot cloud of uniform volume fraction f_v and temperature T between parallel plates at a separation distance of $L = 1$ m using the radiative property spectra of the small ($N_p = 100$) and the big ($N_p = 940$) aggregates.*

			q (kW/m^2)		% Δ due to	% Δ due to	Source (kW/m^3)		% Δ due to
			w/o sca	w sca	aggregation	scattering	w/o sca	w sca	scattering
$f_v = 10^{-5}$	T = 1500 K	Np*Mie (small)	245,2				-3300,2		
		DLCCA (small)	252,6	252,0	3,0	0,2	-2516,5	-2539,6	-0,9
		TOMO (small)	272,0	271,4	10,9	0,2	-2038,5	-2055,7	-0,8
		Np*Mie (big)	246,2				-3285,0		
		DLCCA (big)	254,7	253,6	3,5	0,4	-1886,9	-1935,0	-2,5
		TOMO (big)	276,2	275,2	12,2	0,4	-1844,0	-1900,2	-3,0
	T = 2000 K	Np*Mie (small)	822,8				-9960,1		
		DLCCA (small)	839,8	837,0	2,1	0,3	-6960,9	-7104,3	-2,0
		TOMO (small)	877,3	874,2	6,6	0,4	-5039,4	-5144,7	-2,0
		Np*Mie (big)	825,2				-10480,1		
		DLCCA (big)	844,4	840,0	2,3	0,5	-5547,2	-5791,9	-4,2
		TOMO (big)	886,5	881,3	7,4	0,6	-5034,8	-5310,6	-5,2
	T = 2500 K	Np*Mie (small)	2071,3				-22857,2		
		DLCCA (small)	2103,8	2093,7	1,6	0,5	-14607,9	-15142,9	-3,5
		TOMO (small)	2164,4	2152,1	4,5	0,6	-9176,6	-9565,0	-4,1
		Np*Mie (big)	2075,8				-22640,8		
		DLCCA (big)	2111,6	2098,2	1,7	0,6	-12781,3	-13614,9	-6,1
		TOMO (big)	2180,6	2162,7	5,0	0,8	-10934,5	-11812,9	-7,4
$f_v = 10^{-6}$	T = 1500 K	Np*Mie (small)	109,9				-1562,7		
		DLCCA (small)	88,5	87,3	-19,4	1,4	-1628,2	-1610,5	-1,1
		TOMO (small)	111,1	109,9	1,1	1,1	-2031,8	-2014,9	-0,8
		Np*Mie (big)	80,7				-1584,8		
		DLCCA (big)	91,2	89,1	13,0	2,4	-1423,6	-1405,5	-1,3
		TOMO (big)	123,8	120,6	53,4	2,6	-1989,5	-1961,9	-1,4
	T = 2000 K	Np*Mie (small)	300,6				-5862,2		
		DLCCA (small)	335,4	327,8	11,6	2,3	-6042,5	-5938,6	-1,7
		TOMO (small)	398,4	390,7	32,5	2,0	-7147,9	-7045,3	-1,5
		Np*Mie (big)	304,7				-5935,9		
		DLCCA (big)	343,2	331,9	12,6	3,4	-5111,7	-5035,0	-1,5
		TOMO (big)	442,2	424,5	45,1	4,2	-6849,7	-6724,8	-1,9
	T = 2500 K	Np*Mie (small)	834,9				-15966,0		
		DLCCA (small)	942,7	902,3	12,9	4,5	-16363,0	-15984,5	-2,4
		TOMO (small)	1182,5	1118,0	41,6	5,8	-18783,2	-18401,3	-2,1
		Np*Mie (big)	825,1				-16142,8		
		DLCCA (big)	926,7	896,3	12,3	3,4	-13478,1	-13269,2	-1,6
		TOMO (big)	1069,0	1037,2	29,6	3,1	-17682,9	-17337,3	-2,0

Table 5.4: *Simulation of a soot cloud of uniform volume fraction f_v and temperature T between parallel plates at a separation distance of $L = 0.1$ m using the radiative property spectra of the small ($N_p = 100$) and the big ($N_p = 940$) aggregates.*

			q (kW/m^2)		% Δ due to	% Δ due to	Source (kW/m^3)		% Δ due to
			w/o sca	w sca	aggregation	scattering	w/o sca	w sca	scattering
$f_v = 10^{-5}$	T = 1500 K	Np*Mie (small)	286,2				0,0		
		DLCCA (small)	286,3	286,2	0,0	0,0	205,7	205,7	0,0
		TOMO (small)	286,3	286,3	0,0	0,0	597,1	597,3	0,0
		Np*Mie (big)	286,2				-0,0279		
		DLCCA (big)	286,3	286,0	0,0	0,1	-330,9	-338,2	-2,2
		TOMO (big)	286,3	286,1	0,0	0,1	-234,5	-234,7	-0,1
	T = 2000 K	Np*Mie (small)	905,6				-0,1		
		DLCCA (small)	905,7	905,6	0,0	0,0	825,4	825,6	0,0
		TOMO (small)	905,7	905,8	0,0	0,0	2261,7	2263,3	0,1
		Np*Mie (big)	905,6				-0,052		
		DLCCA (big)	905,7	904,7	0,0	0,1	-1282,4	-1326,8	-3,4
		TOMO (big)	905,7	904,9	0,0	0,1	-835,9	-837,0	-0,1
	T = 2500 K	Np*Mie (small)	2211,6				-0,1		
		DLCCA (small)	2211,7	2211,6	0,0	0,0	2423,4	2424,0	0,0
		TOMO (small)	2211,7	2212,3	0,0	0,0	6477,4	6485,0	0,1
		Np*Mie (big)	2211,6				-0,1		
		DLCCA (big)	2211,7	2208,2	0,0	0,2	-3699,9	-3883,3	-4,7
		TOMO (big)	2211,7	2209,1	0,0	0,1	-2354,8	-2360,8	-0,3
$f_v = 10^{-6}$	T = 1500 K	Np*Mie (small)	285,3				-2,9		
		DLCCA (small)	285,7	285,5	0,2	0,1	18,7	18,7	0,0
		TOMO (small)	286,2	286,0	0,3	0,1	59,4	59,5	0,0
		Np*Mie (big)	285,3				-2,8		
		DLCCA (big)	285,8	285,4	0,2	0,1	-34,0	-34,7	-2,1
		TOMO (big)	286,2	285,7	0,3	0,2	-23,5	-23,5	0,0
	T = 2000 K	Np*Mie (small)	904,2				-4,7		
		DLCCA (small)	904,9	903,7	0,1	0,1	79,6	79,7	0,0
		TOMO (small)	905,7	904,2	0,2	0,2	225,8	225,9	0,1
		Np*Mie (big)	904,3				-4,6		
		DLCCA (big)	905,1	903,1	0,1	0,2	-129,6	-134,0	-3,3
		TOMO (big)	905,7	903,0	0,2	0,3	-83,7	-83,8	-0,1
	T = 2500 K	Np*Mie (small)	2209,8				-6,7		
		DLCCA (small)	2210,7	2206,3	0,0	0,2	238,3	238,4	0,1
		TOMO (small)	2211,7	2206,0	0,1	0,3	647,2	648,1	0,1
		Np*Mie (big)	2209,9				-6,4		
		DLCCA (big)	2210,9	2204,2	0,0	0,3	-371,9	-390,1	-4,7
		TOMO (big)	2211,7	2202,4	0,1	0,4	-235,6	-236,0	-0,1

Table 5.5: *Simulation of a soot cloud of uniform volume fraction f_v and temperature T between parallel plates at a separation distance of $L = 10$ m using the radiative property spectra of the small ($N_p = 100$) and the big ($N_p = 940$) aggregates.*

The first case for $L = 1$ m is given in Table 5.3. If we compare the results obtained with aggregation but without scattering, to the results obtained with both phenomena, we observe that the aggregation is the main phenomenon affecting the the radiative heat flux rates and the effect of scattering seems to be negligible. Only at very high temperatures, the scattering albedo of soot aggregates is effective: the maximum difference in the radiative source term due to scattering is 7 %, for aggregates formed of overlapping particles. This was expected because the scattering albedo is enhanced for overlapping particles in the near IR domain. Nevertheless in combustion systems, the sooty regions are slightly shifted from the maximum temperature regions, hence relatively lower temperatures are more realistic for soot behavior. It is also noted that the effect of scattering is only observed for low volume fractions. When the volume fraction is above 10^{-6}, the absorption of soot becomes dominating, as expected from literature studies (Viskanta and Mengüç (1987)), and the effect of scattering becomes negligible even at high temperatures with enhanced scattering properties of realistic soot morphology.

The simulations are repeated for longer and shorter optical paths to see the change in the effect of scattering. For shorter optical path of $L = 0.1$ m, the results are presented in Table 5.4. Again, the overall effect of albedo is not drastically increased. Nevertheless, the effect of aggregation and of the realistic geometry on heat flux is more obvious, especially for volume fraction of $f_v = 10^{-6}$. For example for soot with volume fraction of 10^{-6} at a uniform temperature of $T = 2000$ K (Table 5.4), while the DLCCA aggregates (with hard spheres) increases the heat flux by 12 %, the realistic geometry increases it by up to 45 %, compared to the results obtained without aggregation.

For longer optical path, simulation is repeated for a separation distance of $L = 10$ m presented in Table 5.5. The trace of scattering, and also of aggregation, is lost through paths longer than a meter, as observed in the results of Table 5.5, due to the highly dominating absorption of the medium, hence to the decreased heat loss. Hence, it is concluded for the industrial scales, the effect of scattering can be ignored. Therefore, the scattering from soot is not included into simulations in the following section where soot is simulated with absorbing gases produced from gaseous combustion.

5.3.2 Soot with gaseous combustion products

In the previous section, it was demonstrated that soot scattering does not contribute significantly neither to the wall heat fluxes nor to the radiative source term of the radiative heat transfer, except for very high temperatures and relatively short optical paths. Therefore in this section, the effect of soot and

its morphology is investigated only by its absorption coefficient within gaseous mixtures containing H_2O, CO_2, N_2, as simulated previously in Section 5.2.1.

Results involving water vapour and soot are presented in Figures 5.3, 5.4 and 5.5 and also in Table 5.6. For all cases, the radiative source and heat flux rates are highly increased due to presence of soot, which is an expected result. At high volume fractions, the effect of aggregation and of the morphology subsides. This is directly related to the increased effect of absorption, as was explained previously in Section 5.3.1.

In the first case (Figure 5.3) where the separation distance is 0.1 m and volume fraction is 10^{-6}, the absorption coefficient of one species is not dominating the others. Therefore, the radiative properties of different aggregation patterns, hence different representations of the morphology of soot, affect the distribution of the radiative source term. This is also reflected on the radiative heat flux values at the wall, as presented in Table 5.6 for "Case 1" results. However, at low volume fractions, the increase in the heat flux rate is more related to morphology (overlapping of particles) than to the aggregation, as can be observed for all cases in Table 5.6.

The effect of morphology decreases with increasing volume fraction due to enhanced absorption. The same is true for increasing optical path as illustrated in Cases 2 (Figure 5.4) and Case 3 (Figure 5.5). Nevertheless, decreasing the volume fraction below $5 * 10^{-7}$ decreases the effect of aggregation and morphology because the gaseous absorption becomes dominant in this latter case, as can be observed in the results of Table 5.6.

As a final case, a gaseous mixture more representative of industrial applications of gaseous combustion is simulated between two parallel cold black walls. The mixture is composed of H_2, H_2O, CO, CO_2, N_2 with molar fractions of 0.42, 0.13, 0.39, 0.04, 0.02 respectively. The media is at uniform temperature $T =$ 1600 K. The results of the radiative source term are presented in Figure 5.6. The outcomes of the previous results of Cases 1 to 4 are also applicable Case 6: The morphology affects the radiative heat transfer when the absorption of one species is not very dominant, and at moderate volume fractions of soot ($f_v \approx 10^{-6}$); the effect of the realistic morphology (particle overlapping) on heat flux is higher than the effect of the aggregation.

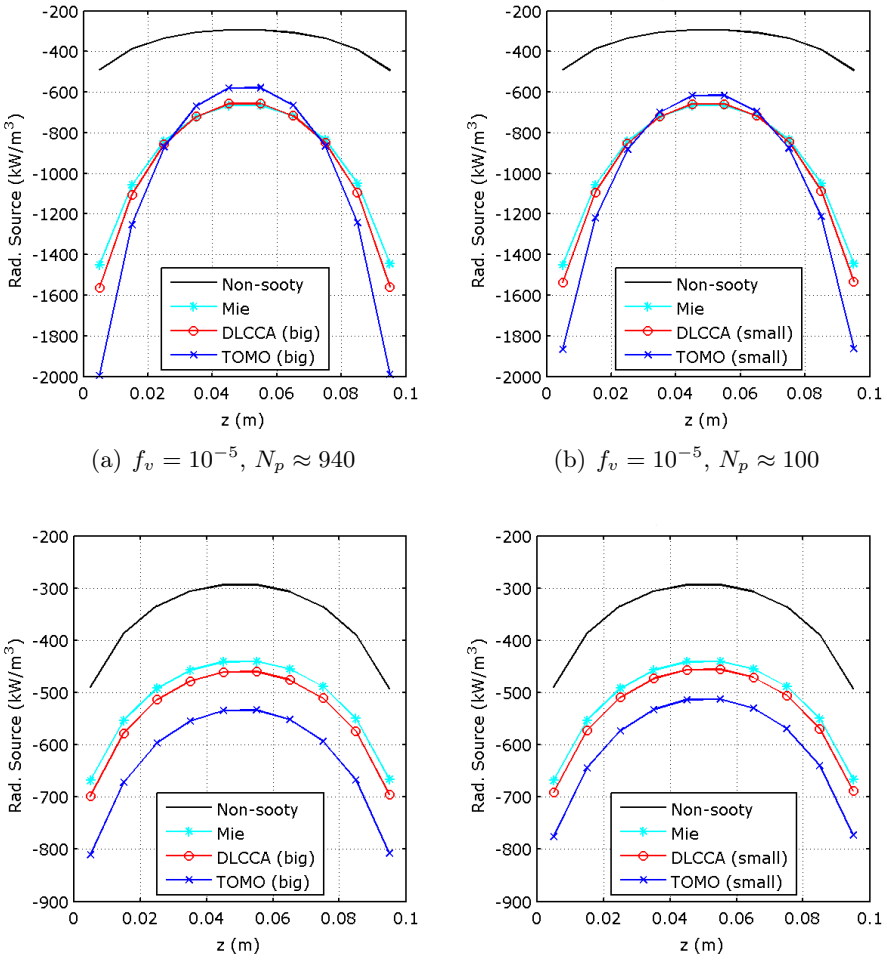

(a) $f_v = 10^{-5}$, $N_p \approx 940$ (b) $f_v = 10^{-5}$, $N_p \approx 100$

(c) $f_v = 10^{-6}$, $N_p \approx 940$ (d) $f_v = 10^{-6}$, $N_p \approx 100$

Figure 5.3: *Effect of soot on the radiative source term for a configuration of parallel cold walls at separation distance of* $L = 0.1$ *m, containing pure vapour at* $T = 1000$ *K and soot concentrations* $f_v = 10^{-5}$ *and* $f_v = 10^{-6}$.

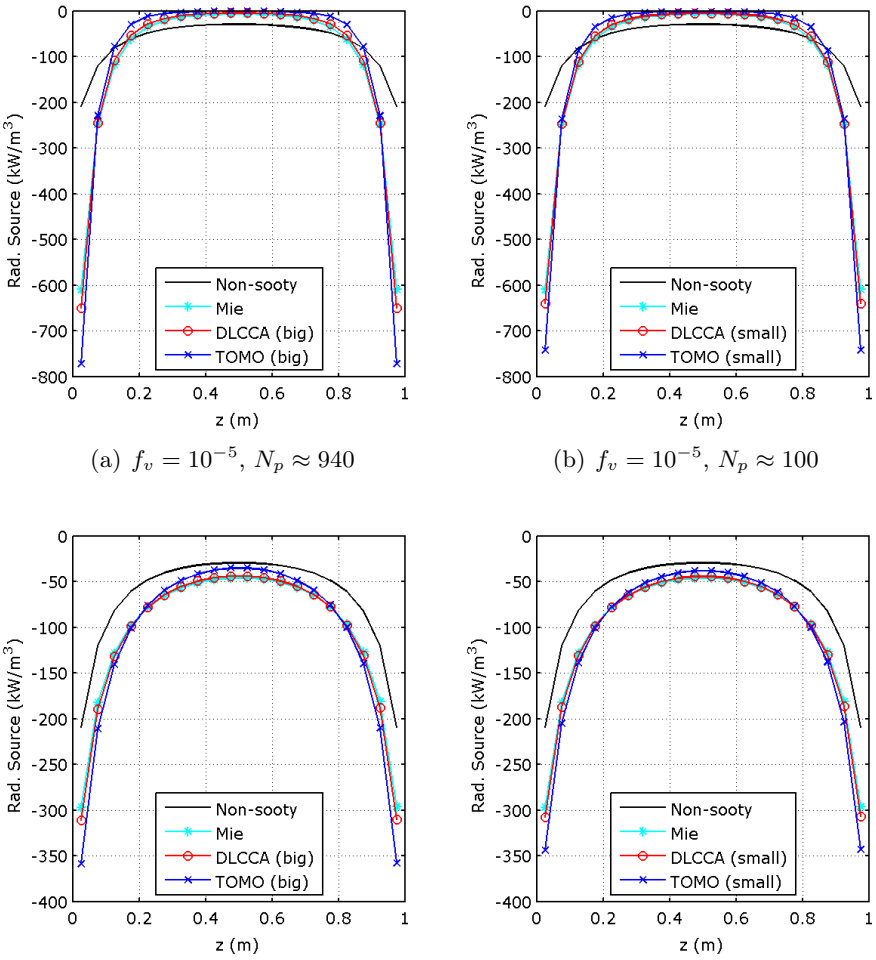

(a) $f_v = 10^{-5}$, $N_p \approx 940$ (b) $f_v = 10^{-5}$, $N_p \approx 100$

(c) $f_v = 10^{-6}$, $N_p \approx 940$ (d) $f_v = 10^{-6}$, $N_p \approx 100$

Figure 5.4: *Effect of soot on the radiative source term for a configuration of parallel cold walls at separation distance of* $L = 1$ *m, containing pure water vapour at* $T = 1000$ *K and soot concentrations of* $f_v = 10^{-5}$ *and* $f_v = 10^{-6}$.

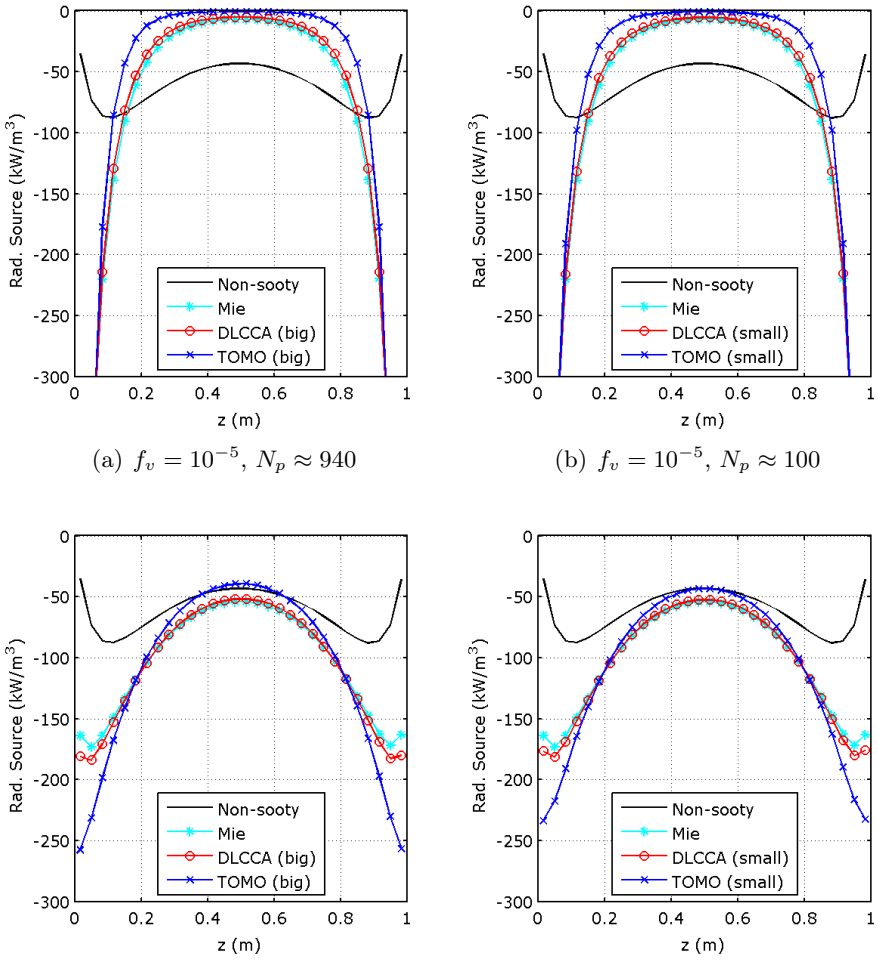

(a) $f_v = 10^{-5}$, $N_p \approx 940$ (b) $f_v = 10^{-5}$, $N_p \approx 100$

(c) $f_v = 10^{-6}$, $N_p \approx 940$ (d) $f_v = 10^{-6}$, $N_p \approx 100$

Figure 5.5: *Effect of soot on the radiative source term for a configuration of parallel cold walls at separation distance of $L = 1$ m, containing parabolic concentration profile of water vapour at $T = 1000$ K and soot concentrations of $f_v = 10^{-5}$ and $f_v = 10^{-6}$.*

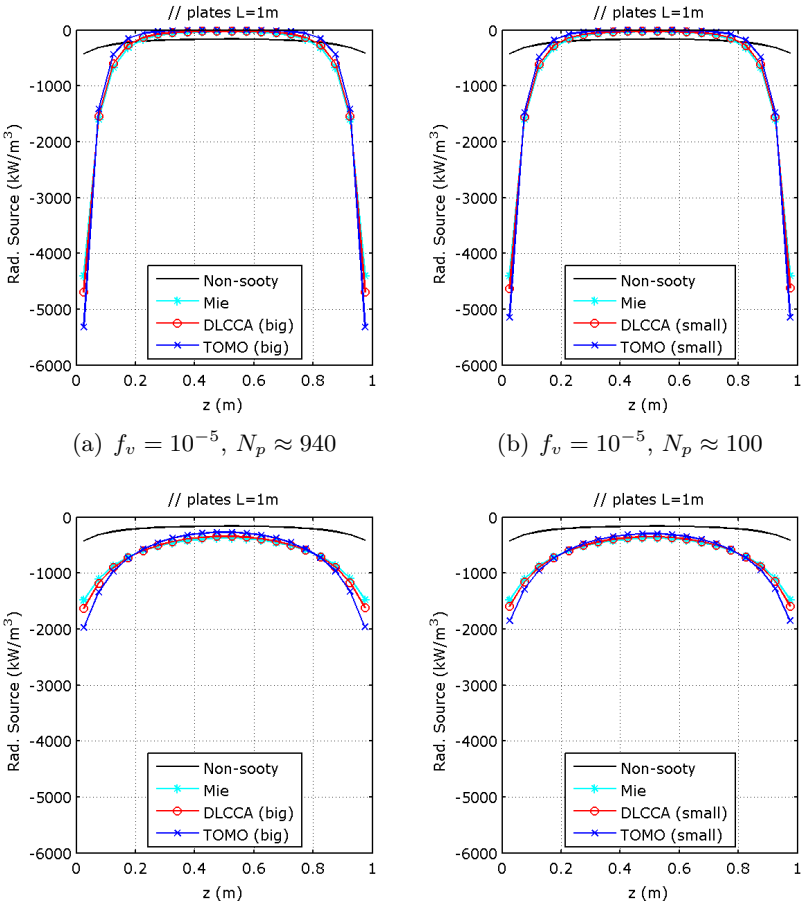

(a) $f_v = 10^{-5}$, $N_p \approx 940$ (b) $f_v = 10^{-5}$, $N_p \approx 100$

(c) $f_v = 10^{-6}$, $N_p \approx 940$ (d) $f_v = 10^{-6}$, $N_p \approx 100$

Figure 5.6: *Effect of soot on the radiative source term for a configuration of parallel cold walls at separation distance of $L = 1$ m, containing a mixture of gaseous combustion products (molar fractions of 0.42 H_2, 0.13 H_2O, 0.39 CO, 0.04 CO_2, 0.02 N_2) at 1600 K and soot concentrations of $f_v = 10^{-5}$ and $f_v = 10^{-6}$.*

		Heat flux at the left wall (kW/m^2)				
		Mie	**DLCCA (small)**	**TOMO (small)**	**DLCCA (big)**	**TOMO (big)**
$\mathbf{f_v = 10^-5}$	Case 1	46.8	48.1	52.6	48.5	53.4
	Case 2	56.5	56.6	56.6	56.6	56.6
	Case 3	56.5	56.5	56.6	56.6	56.6
	Case 4	-235.3	-232.7	-222.5	-231.9	-218.0
	Case 6	370.7	370.9	371.1	370.9	371.1
$\mathbf{f_v = 10^-6}$	Case 1	25.3	26.2	29.4	26.4	30.7
	Case 2	52.4	53.1	55.1	53.3	55.5
	Case 3	51.7	52.4	54.7	52.6	55.2
	Case 4	-248.2	-248.9	-250.5	-249.0	-251.0
	Case 6	345.7	350.8	361.7	352.2	364.2
$\mathbf{f_v = 2 * 10^-7}$	Case 1	19.5	19.7	20.7	19.8	21.1
	Case 2	42.6	43.4	46.0	43.7	46.9
	Case 3	40.7	41.5	44.4	41.7	45.6
	Case 4	-	-	-	-	-
	Case 6	-	-	-	-	-

Table 5.6: *Simulation of uniform soot distribution between parallel plates using radiative property spectra of small ($N_p = 100$) and big ($N_p = 940$) aggregates. Cases 1 to 4 correspond to the validation cases presented in Section 5.2.1, in which soot clouds have been added. Case 6 corresponds to the gaseous mixture presented in Figure 5.6.*

5.4 Conclusion and perspectives on the radiative heat transfer simulations

According to our results of radiative heat transfer simulations involving only soot (i.e. soot within transparent media), the scattering from soot seems to be negligible for radiation simulations, even though the scattering albedo is highly enhanced by morphology effects in the near IR region of radiation. The reason for this is the simultaneous increase in overall extinction and absorption of soot due to aggregation and sintering, and the resulting decrease of heat losses by soot clouds.

To sum up the results of the sooty gas radiation, for isothermal and homogeneous sooty media, if there is not one dominating species, the realistic morphology of soot can affect the heat flux up to 20% and modify the overall radiative source distribution, compared to the assumption where the aggregates are composed of hard spheres. For isothermal but non-homogenenous media, again if the absorption of soot do not overcome other gasous properties, the heat flux is affected by morphology up to 10% and the radiative source is locally affected. For long, optically very thick paths, the effect of soot morphology on the radiative flux is independent of scattering, of its anisotropy and homogeneity because

the *history effect* becomes less significant (Liu et al. (2002)) due to the high absorption rate of the medium.

Finally, it is concluded that the effect of a fine description of soot morphology is important for a precise evaluation of its radiative properties. However, its effect is found to be less crucial for radiative heat transfer. Nevertheless the outcomes can be important for combustion systems at laboratory scales, and for the subsequent in-situ diagnostics, where the optical paths are not very thick, and morphology parameters and aggregation can modifiy significantly the raditive heat fluxes and source terms.

Conclusion

In this study, the possible effects of soot morphology on its radiative properties and the subsequent radiative heat transfer have been investigated with a primary concern on high temperature combustion systems. A three step workflow was established: experimental determination of realistic morphology, numerical computation of radiative properties taking into account this morphology and finally numerical simulation of the radiative heat transfer.

To obtain realistic morphologies, ex-situ experiments were performed. Soot aggregate samples were collected thermophoretically. Samples were examined under electron microscopy. Electron tomography was performed to obtain 3D informations. While the tomography application was not the main objective of our study, it constituted a novelty in its domain by applying SEM tomography first time on soot aggregates. Finally, 3D geometries of soot aggregates were obtained.

In the second step, we analysed the information obtained from the ex-situ experiments and the tomographies. 2D fractal analysis was performed on clusters of aggregates by using semi-empirical analysis techiques. Also, informations were obtained on the size distribution of primary particles issued from methane and propane combustion, complying with literature values. 3D fractal analysis was applied on soot using tomography information, noting that the 3D information was much richer than the 2D images in terms of surface area and volume data, where we did not need any emprical relations to convert 2D data to 3D, such as the radius of gyration of aggregates, the number of particles, etc. This detailed 3D fractal analysis allowed us to compute easily the fractal dimension, the prefactor and also the overlapping of primary particles composing a soot aggregate. Using those experimental data, equivalent aggregates were generated numerically. Our results indicated that the fractal prefactor is indeed highly variable depending on the extraction conditions and the flame conditions whereas the fractal dimension is more universal to the material properties. Nevertheless, the relationship between 2D and 3D computed variables remains unclear and can be studied in a future work on a more detailed soot characterization coupled to in-situ experiments.

In the second part of the study, all the information obtained above was used for the analysis of the radiative properties of soot aggregates. After a short review of the effect of fractal parameters and of the size of the aggregate on the radiative properties, it was concluded that the radiative properties of soot aggregates are very little dependent on those parameters, in the range of interest of spectral wavelengths corresponding to high temperature applications. If the radiative properties change slightly according to the fractal dimension, it is actually due to a modification of the material density inside the bounding box encompassing the aggregate. This conclusion was obtained from the comparison of the radiative properties of realistic 3D geometries to the ones of equivalent numerical aggregates. In order to enhance the representativity of numerical aggregates, DLCCA generated aggregates were modified in order to allow particle overlapping, according to the values of the penetration coefficients obtained previously in the fractal analysis. It was realized that if the computed overlapping amount is applied to the numerical aggregates, the compatibility level is very high between the numerically generated aggregates and the tomography objects, in terms of the radiative properties spectra. Hence, it is concluded that the overlapping of particles plays an important role on the multiple scattering by modifying the radiative properties of soot aggregates by up to 40 percent in the near IR domain. This is true for large aggregates with particle numbers of ≈ 900 and also for smaller ones composed of ≈ 100 particles.

Finally, in the third part of the study, we investigated whether the improved radiative properties spectra of soot aggregates has an impact on scattering and on the total radiative heat transfer through sooty gaseous media. In terms of the radiative heat transfer, the outcomes of the morphology studies do not drastically affect the results of the radiative heat transfer for the long optical paths which can be encountered in industrial scales. The realistic morphology can nevertheless have an impact for applications where the soot volume fraction is moderate and absorption is not dominating. The findings with scattering can offer new perspectives in the determination of radiative properties, discovered to be more morphology dependent at the scales of optical diagnostics and of laboratory scale flames, and also at very high temperatures. We also emphasize that, an improved definition of soot morphology and radiative properties can also contribute to numerical combustion simulations, with the determination of accurate temperatures which affect subsequently the chemical kinetics involved. In that sense, it was demonstrated in Chapter 5 that besides morphology, an accurate determination of soot volume fraction is also important in order to correctly predict the heat source terms and the resulting temperatures.

To sum up, in the first part of this study, we elucidated the morphology of soot and its fractal descriptors. In the second part, we compared the radiative properties of realistic soot aggregates to the ones of numerical aggregates

which led us to demonstrate the excellent representativity in terms radiative properties of numerical aggregates with particle overlapping. The aggregates numerically generated by the fractal theory are indeed representative of flame soot and their subsequent radiative properties under the condition that the results of realistic combustion kinetics are considered which leads to the sintering and overlapping of primary particles. Our simple procedure consisted in the generation of enhanced representativity numerical aggregates by allowing particle overlapping. Of course, this procedure could be further improved: this representativity can be further increased by introducing particle size distributions into numerical generation, and also by improving the complex optical index data of soot issued from different processes and fuels. Also, we tried to propose a general solution for the most encountered soot aggregate geometry in hydrocarbon combustion. Nevertheless, some literature studies report that other geometries, such as carbon nanotube-like shapes combined with fractal aggregates, can be formed in methane flames even without catalyst. This can be the subject of future studies, as the workflow developed can be applied to a large spectrum of complex geometries and material properties.

References

Abramoff, M. D., P. J. Magelhaes, and S. J. Ram (2004). Image processing with imagej. *Biophotonics International 11*(7), 36–42. *(p. 15, 54)*

Adachi, K., S. Chung, H. Friedrich, and P. R. Buseck (2007). Fractal parameters of individual soot particles determined using electron tomography: implications for optical properties. *Journal of Geophysical Research: Atmospheres (1984–2012) 112*(D14). *(p. 25, 28, 61, 66)*

Alfè, M., B. Apicella, J.-N. Rouzaud, A. Tregrossi, and A. Ciajolo (2010). The effect of temperature on soot properties in premixed methane flames. *Combustion and Flame 157*(10), 1959 – 1965. *(p. 10, 39)*

Alpers, A., R. J. Gardner, S. König, R. S. Pennington, C. B. Boothroyd, L. Houben, R. E. Dunin-Borkowski, and K. J. Batenburg (2013). Geometric reconstruction methods for electron tomography. *Ultramicroscopy 128*(0), 42 – 54. *(p. 21, 23)*

Apicella, B., P. Pré, M. Alfè, A. Ciajolo, V. Gargiulo, C. Russo, A. Tregrossi, D. Deldique, and J. Rouzaud (2015). Soot nanostructure evolution in premixed flames by high resolution electron transmission microscopy HRTEM. *Proceedings of the Combustion Institute 35*(2), 1895 – 1902. *(p. xvi, 39)*

Balsara, D. (2001). Fast and accurate discrete ordinates methods for multidimensional radiative transfer. part i, basic methods. *Journal of Quantitative Spectroscopy and Radiative Transfer 69*(6), 671 – 707. *(p. xviii, 96)*

Balthasar, M. and M. Kraft (2003). A stochastic approach to calculate the particle size distribution function of soot particles in laminar premixed flames. *Combustion and Flame 133*(3), 289 – 298. *(p. 56)*

Baron, P. and K. Willeke (2001). *Gas and particle motion*, Volume 2, pp. 61–82. Wiley. New York. *(p. 37, 45)*

Barrett, R., M. Berry, T. Chan, J. Demmel, J. Donato, J. Dongarra, V. Eijkhout, R. Pozo, C. Romine, and H. van der Vorst (1994). *Templates for the Solution of Linear Systems: Building Blocks for Iterative Methods*. Society for Industrial and Applied Mathematics. *(p. 88)*

Bartok, W. and A. Sarofim (1991, Dec). *Fossil fuel combustion: A source book*. John Wiley & Sons, New York, NY (United States). *(p. 38)*

Bell, D. and N. Erdman (2012). Low voltage electron microscopy: principles

and applications. John Wiley & Sons. *(p. xv, 15, 16, 17, 18)*

Bescond, A., J. Yon, F. X. Ouf, D. Ferry, D. Delhaye, D. GaffiÃ©, A. Coppalle, and C. Rozé (2014). Automated determination of aggregate primary particle size distribution by tem image analysis: Application to soot. *Aerosol Science and Technology 48*(8), 831–841. *(p. 8, 56)*

Blevins, L. G., R. A. Fletcher, B. A. B. Jr., E. B. Steel, and G. W. Mulholland (2002). The existence of young soot in the exhaust of inverse diffusion flames. *Proceedings of the Combustion Institute 29*(2), 2325 – 2333. *(p. xiii, 38)*

Bockhorn, H. (1994). Springer-Verlag, Berlin. *(p. xvi, 1, 34, 35, 37)*

Bogan, M. J., D. Starodub, C. Y. Hampton, and R. G. Sierra (2010). Single-particle coherent diffractive imaging with a soft x-ray free electron laser: towards soot aerosol morphology. *Journal of Physics B: Atomic, Molecular and Optical Physics 43*(19), 194013. *(p. 8)*

Bohren, C. and D. Huffman (1983). *Absorption and Scattering of Light by Small Particles*. Wiley-VCH, Weinheim. *(p. xviii, 77, 79, 81)*

Bølling, A. K., J. Pagels, K. E. Yttri, L. Barregard, G. Sallsten, P. E. Schwarze, and C. Boman (2009). Health effects of residential wood smoke particles: the importance of combustion conditions and physicochemical particle properties. *Particle and fibre toxicology 6*(29), 20. *(p. 10)*

Bond, T. and R. Bergstrom (2006). Light absorption by carbonaceous particles: An investigative review. *Aerosol Science and Technology 40*(1), 27–67. *(p. 39)*

Born, M. and W. Wolf (1999). *Principles of Optics*. Cambridge University Press. *(p. 79)*

Botero, M., D. Chen, S. González-Calera, D. Jefferson, and M. Kraft (2016). HRTEM evaluation of soot particles produced by the non-premixed combustion of liquid fuels. *Carbon 96*, 459 – 473. *(p. 39)*

Brasil, A., T. Farias, and M. Carvalho (1999). A recipe for image characterization of fractal-like aggregates. *Journal of Aerosol Science 30*(10), 1379 – 1389. *(p. 2, 57, 68)*

Brasil, A., T. Farias, and M. Carvalho (2000). Evaluation of the fractal properties of cluster-cluster aggregates. *Aerosol Science and Technology 33*(5), 440–454. *(p. 52)*

Brasil, A., T. Farias, M. Carvalho, and U. Koylu (2001). Numerical characterization of the morphology of aggregated particles. *Journal of Aerosol Science 32*(4), 489 – 508. *(p. xiii, xviii, 47, 49, 52, 69)*

Brugière, E., F. Gensdarmes, F. Ouf, J. Yon, and A. Coppalle (2014). Increase in thermophoretic velocity of carbon aggregates as a function of particle size. *Journal of Aerosol Science 76*(0), 87 – 97. *(p. 26)*

Bushell, G. et al. (2002). On techniques for the measurement of the mass fractal dimension of aggregates. *Advances in Colloid and Interface Science 95*(1), 1 – 50. *(p. 41, 43, 46, 60, 70)*

Cai, J., N. Lu, and C. Sorensen (1995). Analysis of fractal cluster morphology

parameters: Structural coefficient and density autocorrelation function cutoff. *Journal of Colloid and Interface Science 171*(2), 470 – 473. *(p. 43, 44)*

Calvo, A., C. Alves, A. Castro, V. Pont, A. Vicente, and R. Fraile (2013). Research on aerosol sources and chemical composition: Past, current and emerging issues. *Atmospheric Research*, 1–28. *(p. 1)*

Castaldi, M. J., N. M. Marinov, C. F. Melius, J. Huang, S. M. Senkan, W. J. Pit, and C. K. Westbrook (1996). Experimental and modeling investigation of aromatic and polycyclic aromatic hydrocarbon formation in a premixed ethylene flame. *Symposium (International) on Combustion 26*(1), 693 – 702. *(p. 36)*

Caumont-Prim, C. (2013). *Détermination de la distribution de taille des nanoparticules de suie par analyse du spectre d'extinction et de diffusion angulaire de la lumière*. Ph. D. thesis, Thèse de doctorat, INSA, Rouen. *(p. xvi, 36, 67)*

Chakrabarty, R. K., N. D. Beres, H. Moosmüller, S. China, C. Mazzoleni, M. K. Dubey, L. Liu, and M. I. Mishchenko (2014). Soot superaggregates from flaming wildfires and their direct radiative forcing. *Sci. Rep. 4*. *(p. 8, 10)*

Chakrabarty, R. K., M. A. Garro, B. A. Garro, S. Chancellor, H. Moosmüller, and C. M. Herald (2011). Simulation of aggregates with point-contacting monomers in the cluster–dilute regime. part 2: Comparison of two-and three-dimensional structural properties as a function of fractal dimension. *Aerosol Science and Technology 45*(8), 903–908. *(p. 2)*

Chakrabarty, R. K., H. Moosmüller, M. A. Garro, W. P. Arnott, J. Walker, R. A. Susott, R. E. Babbitt, C. E. Wold, E. N. Lincoln, and W. M. Hao (2006). Emissions from the laboratory combustion of wildland fuels: Particle morphology and size. *Journal of Geophysical Research: Atmospheres 111*(D7), n/a–n/a. D07204. *(p. 67)*

Chandrasekhar, S. (1960). *Radiative transfer*. New York: Dover,. *(p. 141)*

Chang, H. and T. Charalampopoulos (1990). Determination of the wavelength dependence of refractive indices of flame soot. *Proceedings of the Royal Society of London A: Mathematical, Physical and Engineering Sciences 430*(1880), 577–591. *(p. xix, 111)*

Charalampopoulos, T., H. Chang, and B. Stagg (1989). The effects of temperature and composition on the complex refractive index of flame soot. *Fuel 68*(9), 1173 – 1179. *(p. 111)*

Chaumet, P., A. Sentenac, and A. Rahmani (2004, Sep). Coupled dipole method for scatterers with large permittivity. *Phys. Rev. E 70*, 036606. *(p. 94)*

China, S., C. Mazzoleni, K. Gorkowski, A. C. Aiken, and M. K. Dubey (2013). Morphology and mixing state of individual freshly emitted wildfire carbonaceous particles. *Nature communications 4*. *(p. 8)*

Claro, F. (1982, Jun). Absorption spectrum of neighboring dielectric grains.

Phys. Rev. B 25, 7875–7876. *(p. 94)*

Coelho, P. J. (2014). Advances in the discrete ordinates and finite volume methods for the solution of radiative heat transfer problems in participating media. *Journal of Quantitative Spectroscopy and Radiative Transfer 145*, 121 – 146. *(p. 96)*

Colbeck, I. (2008). *Fractal Geometry of Aerosol Particles*, pp. 273–315. John Wiley & Sons. *(p. 44, 52)*

Colbeck, I., B. Atkinson, and Y. Johar (1997). The morphology and optical properties of soot produced by different fuels. *Journal of aerosol science 28*(5), 715–723. *(p. 70)*

Collinge, M. and B. Draine (2004, Oct). Discrete-dipole approximation with polarizabilities that account for both finite wavelength and target geometry. *J. Opt. Soc. Am. A 21*(10), 2023–2028. *(p. 92, 93)*

Collins, T. J. et al. (2007). Imagej for microscopy. *Biotechniques 43*(1 Suppl), 25–30. *(p. 15, 54)*

Comberg, U. and T. Wriedt (1999). Comparison of scattering calculations for aggregated particles based on different models. *Journal of Quantitative Spectroscopy and Radiative Transfer 63*(2-6), 149 – 162. *(p. 80)*

D'Alessio, A., A. D'Anna, A. D'Orsi, P. Minutolo, R. Barbella, and A. Ciajolo (1992). Precursor formation and soot inception in premixed ethylene flames. *Symposium (International) on Combustion 24*(1), 973–980. Twenty-Fourth Symposium on Combustion. *(p. xiii, 38)*

Dalzell, W. and A. Sarofim (1969). Optical constants of soot and their application to heat-flux calculations. *ASME. J. Heat Transfer. 91*(1), 100–104. *(p. 111)*

DeCarlo, P., J. Slowik, D. Worsnop, P. Davidovits, and J. Jimenez (2004). Particle morphology and density characterization by combined mobility and aerodynamic diameter measurements. part 1: Theory. *Aerosol Science and Technology 38*(12), 1185–1205. *(p. 37, 45)*

Deirmendjian, D., R. Clasen, and W. Viezee (1961, Jun). Mie scattering with complex index of refraction. *J. Opt. Soc. Am. 51*(6), 620–633. *(p. 79)*

di Stasio, S. (2001). Observation of restructuring of nanoparticle soot aggregates in a diffusion flame by static light scattering. *Journal of Aerosol Science 32*(4), 509 – 524. *(p. 69)*

Dobbins, R. (2007). Hydrocarbon nanoparticles formed in flames and diesel engines. *Aerosol Science and Technology 41*(5), 485–496. *(p. xiii, 38)*

Dobbins, R. and C. Megaridis (1991, Nov). Absorption and scattering of light by polydisperse aggregates. *Appl. Opt. 30*(33), 4747–4754. *(p. 81, 82)*

Dobbins, R. A. and C. M. Megaridis (1987). Morphology of flame-generated soot as determined by thermophoretic sampling. *Langmuir 3*(2), 254–259. *(p. 8)*

Doyle, W. (1989, May). Optical properties of a suspension of metal spheres. *Phys. Rev. B 39*, 9852–9858. *(p. 93)*

Draine, B. (1988). The discrete-dipole approximation and its application

to interstellar graphite grains. *The Astrophysical Journal 333*, 848–872. *(p. 84, 85, 90, 91)*

Draine, B. and P. Flatau (1994, Apr). Discrete-dipole approximation for scattering calculations. *J. Opt. Soc. Am. A 11*(4), 1491–1499. *(p. 90, 93)*

Draine, B. and J. Goodman (1993, mar). Beyond Clausius-Mossotti - Wave propagation on a polarizable point lattice and the discrete dipole approximation. *The Astrophysical Journal 405*, 685–697. *(p. 84, 91, 93)*

Draine, B. T. and P. J. Flatau (2013, May). User Guide for the Discrete Dipole Approximation Code DDSCAT 7.3. *ArXiv e-prints*. *(p. 84)*

Enguehard, F. (2009). Mie theory and the discrete dipole approximation. calculating radiative properties of particulate media, with application to nanostructured materials. In S. Volz (Ed.), *Thermal Nanosystems and Nanomaterials*, Volume 118 of *Topics in Applied Physics*, pp. 151–212. Springer Berlin Heidelberg. *(p. 84, 88)*

Eymet, V., A. Brasil, M. El Hafi, T. Farias, and P. Coelho (2002). Numerical investigation of the effect of soot aggregation on the radiative properties in the infrared region and radiative heat transfer. *Journal of Quantitative Spectroscopy and Radiative Transfer 74*(6), 697 – 718. *(p. 82, 83, 143, 149)*

Farias, T., M. Carvalho, and U. Koylu (1998). Radiative heat transfer in soot-containing combustion systems with aggregation. *International Journal of Heat and Mass Transfer 41*(17), 2581–2587. *(p. 2)*

Farias, T., Ü. Ö. Köylü, and M. Carvalho (1996, Nov). Range of validity of the rayleigh–debye–gans theory for optics of fractal aggregates. *Appl. Opt. 35*(33), 6560–6567. *(p. 81)*

Fernandez-Alos, V., J. K. Watson, R. Vander Wal, and J. P. Mathews (2011). Soot and char molecular representations generated directly from {HRTEM} lattice fringe images using fringe3d. *Combustion and Flame 158*(9), 1807 – 1813. *(p. xvii, 39, 40)*

Filippov, A., M. Zurita, and D. Rosner (2000). Fractal-like aggregates: Relation between morphology and physical properties. *Journal of Colloid and Interface Science 229*(1), 261 – 273. *(p. 49)*

Fiveland, W. (1984). Discrete-ordinates solutions of the radiative transport equation for rectangular enclosures. *Journal of Heat Transfer, ASME 106*(4), 699–706. *(p. 142)*

Fiveland, W. (1991). The selection of discrete ordinate quadrature sets for anisotropic scattering. *Fundamentals of Radiation Heat Transfer 160*, 89–96. *(p. xviii, 97)*

Flagan, R. (2001). *Electrical techniques*, pp. 537–568. Wiley. New York. *(p. 45)*

Flatau, P. J., K. A. Fuller, and D. W. Mackowski (1993, Jun). Scattering by two spheres in contact: comparisons between discrete-dipole approximation and modal analysis. *Appl. Opt. 32*(18), 3302–3305. *(p. 112)*

Forrest, S. and T. Witten (1979). Long-range correlations in smoke-particle aggregates. *Journal of Physics A: Mathematical and General 12*(5), L109. *(p. 43, 51)*

Frenklach, M. (2002). Reaction mechanism of soot formation in flames. *Phys. Chem. Chem. Phys. 4*, 2028–2037. *(p. 2, 35, 36, 41)*

Frenklach, M., D. Clary, W. Gardiner, and S. Stein (1985). Detailed kinetic modeling of soot formation in shock-tube pyrolysis of acetylene. *Symp. Int. Combust. Proc. 20*, 887–901. *(p. xvi, 35, 36)*

Frenklach, M. and H. Wang (1991). Detailed modeling of soot particle nucleation and growth. *Symp. Int. Combust. Proc. 23*, 1559–1566. *(p. 35)*

Fry, D., A. Chakrabarti, W. Kim, and C. M. Sorensen (2004, Jun). Structural crossover in dense irreversibly aggregating particulate systems. *Phys. Rev. E 69*, 061401. *(p. 51)*

García Fernández, C., S. Picaud, and M. Devel (2015). Calculations of the mass absorption cross sections for carbonaceous nanoparticles modeling soot. *Journal of Quantitative Spectroscopy and Radiative Transfer 164*, 69 – 81. *(p. 40)*

Gérardy, J. and M. Ausloos (1980, Nov). Absorption spectrum of clusters of spheres from the general solution of maxwell's equations. the long-wavelength limit. *Phys. Rev. B 22*, 4950–4959. *(p. 94)*

Goedecke, G. and S. O'Brien (1988, Jun). Scattering by irregular inhomogeneous particles via the digitized green's function algorithm. *Appl. Opt. 27*(12), 2431–2438. *(p. 92)*

Grosshandler, W. L. (1980). Radiative heat transfer in nonhomogeneous gases: A simplified approach. *International Journal of Heat and Mass Transfer 23*(11), 1447 – 1459. *(p. 142)*

Gwaze, P., O. Schmid, H. J. Annegarn, M. O. Andreae, J. Huth, and G. Helas (2006). Comparison of three methods of fractal analysis applied to soot aggregates from wood combustion. *Journal of Aerosol Science 37*(7), 820 – 838. *(p. 10, 70, 71)*

Habib, Z. and P. Vervisch (1988). On the refractive index of soot at flame temperature. *Combustion Science and Technology 59*(4-6), 261–274. *(p. 111)*

Hage, J. and J. Greenberg (1990, sep). A model for the optical properties of porous grains. *The Astrophysical Journal 361*, 251–259. *(p. 92)*

Haynes, B. S. and H. G. Wagner (1982). The surface growth phenomenon in soot formation. *Zeitschrift für Physikalische Chemie 133*, 201–213. *(p. 37, 41)*

Henyey, L. and J. Greenstein (1941, jan). Diffuse radiation in the galaxy. *Astrophysical Journal 93*, 70–83. *(p. 95)*

Hoekstra, A., J. Rahola, and P. Sloot (1998, Dec). Accuracy of internal fields in volume integral equation simulations of light scattering. *Appl. Opt. 37*(36), 8482–8497. *(p. 93)*

Horvath, H. (1993). Atmospheric light absorption - a review. *Atmospheric Environment. Part A. General Topics 27*(3), 293 – 317. *(p. 19, 71)*

Hu, B. and U. Köylü (2004). Size and morphology of soot particulates sampled from a turbulent nonpremixed acetylene flame. *Aerosol Science and Technology 38*(10), 1009–1018. *(p. 58, 69)*

Hu, B., B. Yang, and U. Köylü (2003). Soot measurements at the axis of an ethylene air non-premixed turbulent jet flame. *Combustion and Flame 134*(1-2), 93–106. *(p. 70)*

Hunter, B. and Z. Guo (2013). Comparison of quadrature schemes in dom for anisotropic scattering radiative transfer analysis. *Numerical Heat Transfer, Part B: Fundamentals 63*(6), 485–507. *(p. 97)*

Jackson, J. (1975). *Classical Electrodynamics*. John Wiley, New York. *(p. 86)*

Jennings, S. (1988). The mean free path in air. *Journal of Aerosol Science 19*(2), 159 – 166. *(p. 37)*

Joy, D. C. (1995). *Monte Carlo Modeling for Electron Microscopy and Microanalysis (Oxford Series in Optical and Imaging Sciences)*. Oxford University Press, New York. *(p. 20)*

Jullien, R. and R. Botet (1987). Aggregation and fractal aggregates. Word Scientific, Singapore. *(p. 43)*

Jullien, R. and M. Kolb (1984). Hierarchical model for chemically limited cluster-cluster aggregation. *Journal of Physics A: Mathematical and General 17*(12), L639. *(p. 51)*

Kamp, C. J., A. Sappok, and V. Wong (2012). Soot and ash deposition characteristics at the catalyst-substrate interface and intra-layer interactions in aged diesel particulate filters illustrated using focused ion beam (fib) milling. Technical report, SAE Technical Paper. *(p. 1, 8)*

Katrinak, K., P. Rez, P. Perkes, and P. Buseck (1993). Fractal geometry of carbonaceous aggregates from an urban aerosol. *Environmental Science & Technology 27*(3), 539–547. *(p. 68)*

Khalizov, A. F., B. Hogan, C. Qiu, E. L. Petersen, and R. Zhang (2012). Characterization of soot aerosol produced from combustion of propane in a shock tube. *Aerosol Science and Technology 46*(8), 925–936. *(p. 1)*

Kim, T., J. Menart, and H. Lee (1991). Nongray radiative gas analyses using the s-n discrete ordinates method. *ASME. J. Heat Transfer 113*(4), 946–952. *(p. 146)*

Kim, T.-K. and H. Lee (1988). Effect of anisotropic scattering on radiative heat transfer in two-dimensional rectangular enclosures. *International Journal of Heat and Mass Transfer 31*(8), 1711 – 1721. *(p. 142)*

Kimura, H. (2001). Light-scattering properties of fractal aggregates: numerical calculations by a superposition technique and the discrete-dipole approximation. *Journal of Quantitative Spectroscopy and Radiative Transfer 70*(4-6), 581–594. Light Scattering by Non-Spherical Particles. *(p. 90)*

Koch, R. and R. Becker (2004). Evaluation of quadrature schemes for the discrete ordinates method. *Journal of Quantitative Spectroscopy and Radiative Transfer 84*(4), 423 – 435. Eurotherm Seminar 73 - Computational Thermal Radiation in Participating Media. *(p. 96, 97)*

Kolb, M., R. Botet, and R. Jullien (1983, Sep). Scaling of kinetically growing clusters. *Phys. Rev. Lett. 51*, 1123–1126. *(p. 44, 51)*

Köylü, Ü. and G. Faeth (1992). Structure of overfire soot in buoyant turbulent diffusion flames at long residence times. *Combustion and Flame 89*(2), 140 – 156. *(p. 42, 54)*

Köylü, Ü., G. Faeth, T. Farias, and M. Carvalho (1995). Fractal and projected structure properties of soot aggregates. *Combustion and Flame 100*(4), 621 – 633. *(p. xiii, 44, 47, 59, 68)*

Köylü, Ü., C. McEnally, D. Rosner, and L. Pfefferle (1997). Simultaneous measurements of soot volume fraction and particle size microstructure in flames using a thermophoretic sampling technique. *Combustion and Flame 110*(4), 494 – 507. *(p. 54)*

Kulkarni, P., P. A. Baron, C. Sorensen, and M. Harper (2011). *Nonspherical Particle Measurement: Shape Factor, Fractals, and Fibers*, pp. 507–547. John Wiley & Sons, Inc. *(p. 51)*

Lack, D. A., H. Moosmüller, G. R. McMeeking, R. K. Chakrabarty, and D. Baumgardner (2014). Characterizing elemental, equivalent black, and refractory black carbon aerosol particles: a review of techniques, their limitations and uncertainties. *Analytical and bioanalytical chemistry 406*(1), 99–122. *(p. 2, 8)*

Lallich, S. (2009). *Détermination expérimentale et modélisation des propriétés radiatives de matrices nanoporeuses de silice*. Ph. D. thesis, Thèse de doctorat, INSA, Lyon. *(p. xiii, 84, 93)*

Lebedev, V. and D. Laikov (1999). A quadrature formula for the sphere of the 131st algebraic order of accuracy. *Doklady Mathematics 59*(3), 477–481. *(p. xviii, 97, 98)*

Lee, C. and T. Kramer (2004). Prediction of three-dimensional fractal dimensions using the two-dimensional properties of fractal aggregates. *Advances in Colloid and Interface Science 112*(1-3), 49–57. *(p. 68)*

Lee, S. and C. Tien (1981). Optical constants of soot in hydrocarbon flames. *Symposium (International) on Combustion 18*(1), 1159–1166. Eighteenth Symposium (International) on Combustion. *(p. xix, 102, 111)*

Lee, S. and C. Tien (1983). Effect of soot shape on soot radiation. *Journal of Quantitative Spectroscopy and Radiative Transfer 29*(3), 259–265. *(p. 2)*

Lemonnier, D. (2007). *Microscale and Nanoscale Heat Transfer*, Chapter Solution of the Boltzmann Equationfor Phonon Transport, pp. 77–106. Berlin, Heidelberg: Springer Berlin Heidelberg. *(p. xviii, 97)*

Leopardi, P. (2006). A partition of the unit sphere into regions of equal area and small diameter. *Electronic Transactions on Numerical Analysis 25*(12), 309–327. *(p. 97)*

Liati, A. and P. D. Eggenschwiler (2010). Characterization of particulate matter deposited in diesel particulate filters: Visual and analytical approach in macro-, micro- and nano-scales. *Combustion and Flame 157*(9), 1658 – 1670. *(p. 2)*

Lieb, S. and H. Wang (2013). Height and phase mode images of soot using afm. In *8th US National Meeting on Combustion, Park City, Utah. (p. 8, 9)*

Lighty, J. S., J. M. Veranth, and A. F. Sarofim (2000). Combustion aerosols: factors governing their size and composition and implications to human health. *Journal of the Air & Waste Management Association 50*(9), 1565–1618. *(p. 1)*

lin Xu, Y. (1998). Electromagnetic scattering by an aggregate of spheres: asymmetry parameter. *Physics Letters A 249*(1-2), 30–36. *(p. 90)*

Liu, C., Y. Yin, F. Hu, H. Jin, and C. Sorensen (2015). The effects of monomer size distribution on the radiative properties of black carbon aggregates. *Aerosol Science and Technology 49*(10), 928–940. *(p. 56)*

Liu, F., O. Gulder, G. Smallwood, and Y. Ju (1998). Non-grey gas radiative transfer analyses using the statistical narrow-band model. *International Journal of Heat and Mass Transfer 41*(14), 2227 – 2236. *(p. xiv, xxi, 145, 146, 147)*

Liu, F., X. Mo, H. Gan, T. Guo, X. Wang, B. Chen, J. Chen, S. Deng, N. Xu, T. Sekiguchi, D. Golberg, and Y. Bando (2014). Cheap, gram-scale fabrication of bn nanosheets via substitution reaction of graphite powders and their use for mechanical reinforcement of polymers. *Sci. Rep. 4*. *(p. 19)*

Liu, F. and G. Smallwood (2010a). Radiative properties of numerically generated fractal soot aggregates: the importance of configuration averaging. *Journal of Heat Transfer 132*(2), 023308. *(p. 98, 100)*

Liu, F. and G. J. Smallwood (2010b). Effect of aggregation on the absorption cross-section of fractal soot aggregates and its impact on {LII} modelling. *Journal of Quantitative Spectroscopy and Radiative Transfer 111*(2), 302 – 308. Eurotherm Seminar No. 83: Computational Thermal Radiation in Participating Media {III}. *(p. 120, 121)*

Liu, F. and D. Snelling (2008). Evaluation of the accuracy of the rdg approximation for the absorption and scattering properties of fractal aggregates of flame-generated soot. In *Proceedings of the 40th Thermophysics Conference, 2008*. *(p. 83)*

Liu, F., B. Stagg, D. Snelling, and G. Smallwood (2006). Effects of primary soot particle size distribution on the temperature of soot particles heated by a nanosecond pulsed laser in an atmospheric laminar diffusion flame. *International Journal of Heat and Mass Transfer 49*(3), 777 – 788. *(p. 57)*

Liu, L., M. Mishchenko, and W. Arnott (2008). A study of radiative properties of fractal soot aggregates using the superposition t-matrix method. *Journal of Quantitative Spectroscopy and Radiative Transfer 109*(15), 2656 – 2663. *(p. xvii, xix, xx, 45, 83, 113, 114, 115, 116, 117, 122)*

Liu, L. and M. I. Mishchenko (2007). Scattering and radiative properties of complex soot and soot-containing aggregate particles. *Journal of Quanti-*

tative Spectroscopy and Radiative Transfer 106, 262 – 273. {IX} Conference on Electromagnetic and Light Scattering by Non-Spherical Particles. *(p. 2, 83)*

Liu, L., L. Ruan, and H. Tan (2002). On the discrete ordinates method for radiative heat transfer in anisotropically scattering media. *International Journal of Heat and Mass Transfer 45*(15), 3259 – 3262. *(p. xiv, 145, 148, 160)*

Lobert, J., D. Scharffe, H. Weimin, T. Kuhlbusch, R. Seuwen, P. Warneck, P. Crutzen, and J. Levine (1991). Experimental evaluation of biomass burning emissions: Nitrogen and carbon containing compounds. *(p. 10)*

Loke, V., M. Mengüç, and T. Nieminen (2011). Discrete-dipole approximation with surface interaction: Computational toolbox for matlab. *Journal of Quantitative Spectroscopy and Radiative Transfer 112*(11), 1711 – 1725. Electromagnetic and Light Scattering by Nonspherical Particles {XII}. *(p. 87)*

López-Yglesias, X., P. E. Schrader, and H. A. Michelsen (2014). Soot maturity and absorption cross sections. *Journal of Aerosol Science 75*(0), 43 – 64. *(p. 2)*

Lück, S., M. Sailer, V. Schmidt, and P. Walther (2010). Three-dimensional analysis of intermediate filament networks using sem tomography. *Journal of microscopy 239*(1), 1–16. *(p. 8, 13, 15)*

Ludwig, A. (1989, February). A new technique for numerical electromagnetics. *Antennas and Propagation Society Newsletter, IEEE 31*(1), 40–41. *(p. 80)*

Ludwig, C. B., W. Malkmus, J. E. Reardon, and G. Thomson, J. A. L. (1973). Handbook of infrared radiation from combustion gases. Technical report, NASA, United States. *(p. 142)*

Mackowski, D. (2006). A simplified model to predict the effects of aggregation on the absorption properties of soot particles. *Journal of Quantitative Spectroscopy and Radiative Transfer 100*(1-3), 237 – 249. {VIII} Conference on Electromagnetic and Light Scattering by Nonspherical Particles. *(p. 52, 110, 121)*

Mackowski, D. and M. Mishchenko (1996, Nov). Calculation of the t matrix and the scattering matrix for ensembles of spheres. *J. Opt. Soc. Am. A 13*(11), 2266–2278. *(p. 79)*

Mandelbrot, B. (1977). *Fractals, Form, Chance and Dimension*. Freeman, San Francisco. *(p. 41)*

Mandelbrot, B. (1982). *The Fractal Geometry of Nature*. Freeman, San Francisco. *(p. 41)*

Mansurov, Z. A. (2005). Soot formation in combustion processes (review). *Combustion, Explosion and Shock Waves 41*(6), 727–744. *(p. 1)*

Mätzler, C. (2002). Matlab functions for mie scattering and absorption. Technical report, Institute of Applied Physics, University of Bern. *(p. 79)*

Maugendre, M. (2009). *Etude des particules de suie dans les flammes de*

kerosene et de diester. Ph. D. thesis, Thèse de doctorat, INSA, Rouen. *(p. xiii, 47, 48)*

McEnally, C., L. Pfefferle, B. Atakan, and K. Kohse-Höinghaus (2006). Studies of aromatic hydrocarbon formation mechanisms in flames: Progress towards closing the fuel gap. *Progress in Energy and Combustion Science 32*(3), 247 – 294. *(p. 36)*

Meakin, P. (1983a, Mar). Diffusion-controlled cluster formation in 2—6-dimensional space. *Phys. Rev. A 27*, 1495–1507. *(p. 51)*

Meakin, P. (1983b, Sep). Formation of fractal clusters and networks by irreversible diffusion-limited aggregation. *Phys. Rev. Lett. 51*, 1119–1122. *(p. 51)*

Meakin, P. (1999). A historical introduction to computer models for fractal aggregates. *Journal of Sol-Gel Science and Technology 15*(2), 97–117. *(p. 52)*

Megaridis, C. and R. Dobbins (1989). Comparison of soot growth and oxidation in smoking and non-smoking ethylene diffusion flames. *Combustion Science and Technology 66*(1), 1–16. *(p. 54)*

Megaridis, C. M. and R. A. Dobbins (1990). Morphological description of flame-generated materials. *Combustion Science and Technology 71*(1-3), 95–109. *(p. 2)*

Melius, C. F., M. E. Colvin, N. M. Marinov, W. J. Pit, and S. M. Senkan (1996). Reaction mechanisms in aromatic hydrocarbon formation involving the {C5H5} cyclopentadienyl moiety. *Symposium (International) on Combustion 26*(1), 685 – 692. *(p. 36)*

Messaoudi, C., T. Boudier, C. O. Sorzano, and S. Marco (2007). Tomoj: tomography software for three-dimensional reconstruction in transmission electron microscopy. *BMC bioinformatics 8*(1), 288. *(p. 15)*

Miele, P., M. Bechelany, and S. Bernard (2014). *Hierarchically Nanostructured Porous Boron Nitride*, pp. 267–290. Wiley-VCH Verlag GmbH & Co. KGaA. *(p. 19)*

Miller, J., M. Pilling, and J. Troe (2005). Unravelling combustion mechanisms through a quantitative understanding of elementary reactions. *Proceedings of the Combustion Institute 30*(1), 43 – 88. *(p. 36)*

Mishchenko, M., L. Travis, and A. Lacis (2002). *Scattering, absorption, and emission of light by small particles*. Cambridge University Press, Cambridge, U.K. *(p. 80)*

Mishchenko, M. I., L. Liu, and D. W. Mackowski (2013). T-matrix modeling of linear depolarization by morphologically complex soot and soot-containing aerosols. *Journal of Quantitative Spectroscopy and Radiative Transfer 123*(0), 135 – 144. *(p. 83)*

Mitchell, P. and M. Frenklach (1998). Monte carlo simulation of soot aggregation with simultaneous surface growth - why primary particles appear spherical. *Symposium (International) on Combustion 27*(1), 1507 – 1514. Twenty-Seventh Sysposium (International) on Combustion Volume One.

(p. 41)

Mitchell, P. and M. Frenklach (2003, Jun). Particle aggregation with simultaneous surface growth. *Phys. Rev. E 67*, 061407. *(p. 52)*

Modest, M. (2013). Chapter 12 - radiative properties of particulate media. In M. Modest (Ed.), *Radiative Heat Transfer (Third Edition)* (Third Edition ed.)., pp. 387 – 439. Boston: Academic Press. *(p. xviii, 76, 88, 140, 141, 142, 143)*

Moosmüller, H., R. Chakrabarty, and W. Arnott (2009). Aerosol light absorption and its measurement: A review. *Journal of Quantitative Spectroscopy and Radiative Transfer 110*(11), 844–878. *(p. 10)*

Morgan, N., M. Kraft, M. Balthasar, D. Wong, M. Frenklach, and P. Mitchell (2007). Numerical simulations of soot aggregation in premixed laminar flames. *Proceedings of the Combustion Institute 31*(1), 693 – 700. *(p. 52)*

Mountain, R. and G. Mulholland (1988). Light scattering from simulated smoke agglomerates. *Langmuir 4*(6), 1321–1326. *(p. 44)*

Mulholland, G. W., R. J. Samson, R. D. Mountain, and M. H. Ernst (1988). Cluster size distribution for free molecular agglomeration. *Energy & Fuels 2*(4), 481–486. *(p. 70)*

Mullins, J. and A. Williams (1987). The optical properties of soot: a comparison between experimental and theoretical values. *Fuel 66*(2), 277 – 280. *(p. xix, 111)*

Nieminen, T., H. Rubinsztein-Dunlop, and N. Heckenberg (2003). Calculation of the t-matrix: general considerations and application of the point-matching method. *Journal of Quantitative Spectroscopy and Radiative Transfer 79-80*, 1019–1029. Electromagnetic and Light Scattering by Non-Spherical Particles. *(p. 80)*

Nyeki, S. and I. Colbeck (1995). Fractal dimension analysis of single, in-situ, restructured carbonaceous aggregates. *Aerosol Science and Technology 23*(2), 109–120. *(p. 51)*

Oh, C. and C. Sorensen (1997a). The effect of overlap between monomers on the determination of fractal cluster morphology. *Journal of Colloid and Interface Science 193*(1), 17 – 25. *(p. 68)*

Oh, C. and C. Sorensen (1997b). Light scattering study of fractal cluster aggregation near the free molecular regime. *Journal of Aerosol Science 28*(6), 937 – 957. *(p. 52, 57)*

Oh, C. and C. Sorensen (1999). Scaling approach for the structure factor of a generalized system of scatterers. *Journal of Nanoparticle Research 1*(3), 369–377. *(p. 67, 68)*

Oh, C. and C. M. Sorensen (1998, Jan). Structure factor of diffusion-limited aggregation clusters: Local structure and non-self-similarity. *Phys. Rev. E 57*, 784–790. *(p. 66)*

Okada, Y. (2008). Efficient numerical orientation averaging of light scattering properties with a quasi-monte-carlo method. *Journal of Quantitative Spectroscopy and Radiative Transfer 109*(9), 1719 – 1742. *(p. 99)*

Okada, Y., I. Mann, T. Mukai, and M. K"ohler (2008). Extended calculation of polarization and intensity of fractal aggregates based on rigorous method for light scattering simulations with numerical orientation averaging. *Journal of Quantitative Spectroscopy and Radiative Transfer 109*(15), 2613 – 2627. *(p. 99)*

Okamoto, H. (1995). Light scattering by clusters: the al-term method. *Optical Review 2*(6), 407–412. *(p. 93, 112)*

Okamoto, H. and Y. Xu (1998). Light scattering by irregular interplanetary dust particles. *Earth, Planets and Space 50*(6), 577–585. *(p. 90, 112)*

Oktem, B., M. Tolocka, B. Zhao, H. Wang, and M. Johnston (2005). Chemical species associated with the early stage of soot growth in a laminar premixed ethylene-oxygen-argon flame. *Combustion and Flame 142*(4), 364–373. *(p. xiii, 38)*

Okyay, G., E. Héripré, T. Reiss, P. Haghi-Ashtiani, T. Auger, and F. Enguehard (2016). Soot aggregate complex morphology: 3D geometry reconstruction by SEM tomography applied on soot issued from propane combustion. *Journal of Aerosol Science 93*, 63 – 79. *(p. 3)*

Onischuk, A., S. Di Stasio, V. Karasev, A. Baklanov, G. Makhov, A. Vlasenko, A. Sadykova, A. Shipovalov, and V. Panfilov (2003). Evolution of structure and charge of soot aggregates during and after formation in a propane/air diffusion flame. *Journal of aerosol science 34*(4), 383–403. *(p. 26, 69)*

Ouf, F. X., J. Yon, P. Ausset, A. Coppalle, and M. MaillÃ© (2010). Influence of sampling and storage protocol on fractal morphology of soot studied by transmission electron microscopy. *Aerosol Science and Technology 44*(11), 1005–1017. *(p. 9, 66)*

Pandey, A., R. K. Chakrabarty, L. Liu, and M. I. Mishchenko (2015, Nov). Empirical relationships between optical properties and equivalent diameters of fractal soot aggregates at 550 nm wavelength. *Opt. Express 23*(24), A1354–A1362. *(p. 121)*

Park, K., D. Kittelson, and P. McMurry (2004). Structural properties of diesel exhaust particles measured by transmission electron microscopy (tem): Relationships to particle mass and mobility. *Aerosol Science and Technology 38*(9), 881–889. *(p. xiii, 38)*

Penttilä, A. and K. Lumme (2011). Optimal cubature on the sphere and other orientation averaging schemes. *Journal of Quantitative Spectroscopy and Radiative Transfer 112*(11), 1741 – 1746. Electromagnetic and Light Scattering by Nonspherical Particles {XII}. *(p. 99)*

Penttilä, A., E. Zubko, K. Lumme, K. Muinonen, M. A. Yurkin, B. Draine, J. Rahola, A. G. Hoekstra, and Y. Shkuratov (2007). Comparison between discrete dipole implementations and exact techniques. *Journal of Quantitative Spectroscopy and Radiative Transfer 106*(1-3), 417–436. {IX} Conference on Electromagnetic and Light Scattering by Non-Spherical Particles. *(p. 107)*

Peterson, B. and S. Ström (1973, Nov). t matrix for electromagnetic scattering from an arbitrary number of scatterers and representations of e(3). *Phys. Rev. D 8*, 3661–3678. *(p. 79)*

Pettersen, E. F., T. D. Goddard, C. C. Huang, G. S. Couch, D. M. Greenblatt, E. C. Meng, and T. E. Ferrin (2004). Ucsf chimera-a visualization system for exploratory research and analysis. *Journal of Computational Chemistry 25*(13), 1605–1612. *(p. 15)*

Petzold, A., J. Ogren, M. Fiebig, P. Laj, S.-M. Li, U. Baltensperger, T. Holzer-Popp, S. Kinne, G. Pappalardo, N. Sugimoto, et al. (2013). Recommendations for reporting" black carbon" measurements. *Atmospheric Chemistry and Physics 13*(16), 8365–8379. *(p. 10)*

Potts, P. J. (1987). *A handbook of silicate rock analysis*, Volume 622. Blackie Glasgow; London. *(p. 19, 20)*

Prado, G., J. Jagoda, K. Neoh, and J. Lahaye (1981). Eighteenth symposium (international) on combustion a study of soot formation in premixed propane/oxygen flames by in-situ optical techniques and sampling probes. *Symposium (International) on Combustion 18*(1), 1127 – 1136. *(p. 40)*

Prado, G. and J. Lahaye (1981). Physical aspects of nucleation and growth of soot particles. In D. Siegla and G. Smith (Eds.), *Particulate Carbon*, pp. 143–175. Springer US. *(p. 40)*

Purcell, E. and C. Pennypacker (1973). Scattering and absorption of light by nonspherical dielectric grains. *Astrophysical Journal 186*, 705–714. *(p. 84, 87, 90)*

Rahmani, A., P. Chaumet, and G. Bryant (2002, Dec). Coupled dipole method with an exact long-wavelength limit and improved accuracy at finite frequencies. *Opt. Lett. 27*(23), 2118–2120. *(p. 92)*

Rahmani, A., P. Chaumet, and G. Bryant (2004). On the importance of local-field corrections for polarizable particles on a finite lattice: Application to the discrete dipole approximation. *The Astrophysical Journal 607*(2), 873. *(p. 92, 93, 94)*

Raithby, G. and E. Chu (1990). A finite-volume method for predicting a radiant heat transfer in enclosures with participating media. *Journal of Heat Transfer, ASME 112*, 415–423. *(p. 141, 142)*

Ramanathan, V. and G. Carmichael (2008). Global and regional climate changes due to black carbon. *Nature geoscience 1*(4), 221–227. *(p. 1)*

Reilly, P., R. Gieray, W. Whitten, and J. Ramsey (2000). Direct observation of the evolution of the soot carbonization process in an acetylene diffusion flame via real-time aerosol mass spectrometry. *Combustion and Flame 122*(1), 90–104. *(p. 54)*

Richter, H. and J. Howard (2000). Formation of polycyclic aromatic hydrocarbons and their growth to soot - a review of chemical reaction pathways. *Progress in Energy and Combustion Science 26*(4), 565 – 608. *(p. 36)*

Rogak, S. and R. Flagan (1990). Stokes drag on self-similar clusters of spheres. *Journal of Colloid and Interface Science 134*(1), 206 – 218.

(p. 45)

Rogak, S. N. and R. C. Flagan (1992). Characterization of the structure of agglomerate particles. *Particle & Particle Systems Characterization 9*(1-4), 19–27. *(p. 68)*

Rogak, S. N., R. C. Flagan, and H. V. Nguyen (1993). The mobility and structure of aerosol agglomerates. *Aerosol Science and Technology 18*(1), 25–47. *(p. 68)*

Rojanski, D., D. Huppert, H. D. Bale, X. Dacai, P. W. Schmidt, D. Farin, A. Seri-Levy, and D. Avnir (1986, Jun). Integrated fractal analysis of silica: Adsorption, electronic energy transfer, and small-angle x-ray scattering. *Phys. Rev. Lett. 56*, 2505–2508. *(p. 51)*

Samson, R. J., G. W. Mulholland, and J. W. Gentry (1987). Structural analysis of soot agglomerates. *Langmuir 3*(2), 272–281. *(p. 44, 57, 68, 70)*

Sansonetti, J. and J. Furdyna (1980, Sep). Depolarization effects in arrays of spheres. *Phys. Rev. B 22*, 2866–2874. *(p. 94)*

Schenk, M., S. Lieb, H. Vieker, A. Beyer, A. Gölzhäuser, H. Wang, and K. Kohse-Höinghaus (2015). Morphology of nascent soot in ethylene flames. *Proceedings of the Combustion Institute 35*(2), 1879 – 1886. *(p. 8, 9)*

Severin, K. (2004). Energy dispersive spectrometry of common rock forming minerals. Kluwer Academic. *(p. 19)*

Shaddix, C. R. and K. C. Smyth (1996). Laser-induced incandescence measurements of soot production in steady and flickering methane, propane, and ethylene diffusion flames. *Combustion and Flame 107*(4), 418 – 452. *(p. 1)*

Skorupski, K. and J. Mroczka (2014). Effect of the necking phenomenon on the optical properties of soot particles. *Journal of Quantitative Spectroscopy and Radiative Transfer 141*(0), 40 – 48. *(p. 2)*

Slowik, J., K. Stainken, P. Davidovits, L. Williams, J. Jayne, C. Kolb, D. Worsnop, Y. Rudich, P. DeCarlo, and J. Jimenez (2004). Particle morphology and density characterization by combined mobility and aerodynamic diameter measurements. part 2: Application to combustion-generated soot aerosols as a function of fuel equivalence ratio. *Aerosol Science and Technology 38*(12), 1206–1222. *(p. 19, 20, 69, 71)*

Smith, G. (1983). Kinetic aspects of diesel soot coagulation. In J. Lahaye and G. Prado (Eds.), *Soot in Combustion Systems and Its Toxic Properties*, Volume 7 of *NATO Conference Series*, pp. 163–170. Springer US. *(p. 41)*

Smith, O. (1981). Fundamentals of soot formation in flames with application to diesel engine particulate emissions. *Progress in Energy and Combustion Science 7*(4), 275 – 291. *(p. xvi, 35)*

Smunev, D., P. Chaumet, and M. Yurkin (2015). Rectangular dipoles in the discrete dipole approximation. *Journal of Quantitative Spectroscopy and Radiative Transfer 156*, 67–79. *(p. 87)*

Sorensen, C., N. Lu, and J. Cai (1995). Fractal cluster size distribution measurement using static light scattering. *Journal of Colloid and Interface Science 174*(2), 456 – 460. *(p. 44)*

Sorensen, C. M. (2001). Light scattering by fractal aggregates: a review. *Aerosol Science and Technology 35*(2), 648–687. *(p. xiii, 38, 46, 131)*

Sorensen, C. M. (2011). The mobility of fractal aggregates: a review. *Aerosol Science and Technology 45*(7), 765–779. *(p. 37, 46, 51, 83)*

Sorensen, C. M. and G. D. Feke (1996). The morphology of macroscopic soot. *Aerosol Science and Technology 25*(3), 328–337. *(p. xiii, 38)*

Sorensen, C. M., C. Oh, P. W. Schmidt, and T. P. Rieker (1998, Oct). Scaling description of the structure factor of fractal soot composites. *Phys. Rev. E 58*, 4666–4672. *(p. 51)*

Sun, W., G. Videen, Q. Fu, S. Tanev, B. Lin, Y. Hu, Z. Liu, and J. Huang (2012). Finite-difference time-domain solution of light scattering by arbitrarily shaped particles and surfaces. In A. Kokhanovsky (Ed.), *Light Scattering Reviews, Vol. 6*, pp. 75–113. Springer Berlin Heidelberg. *(p. 81)*

Teichmann, J. and K. van den Boogaart (2015). Cluster models for random particle aggregates-morphological statistics and collision distance. *Spatial Statistics 12*, 65 – 80. *(p. 52)*

Tence, M., J. Chevalier, and R. Jullien (1986). On the measurement of the fractal dimension of aggregated particles by electron microscopy : experimental method, corrections and comparison with numerical models. *J. Phys. France 47*(11), 1989–1998. *(p. 68)*

Tessé, L. (2001). *Modélisation des transferts radiatifs dans les flammes turbulentes par une méthode de Monte Carlo*. Ph. D. thesis. Thèse de doctorat dirigée par Taine, Jean Energétique Châtenay-Malabry, Ecole Centrale de Paris 2001. *(p. xxi, 144)*

Tian, K., F. Liu, K. Thomson, D. Snelling, G. Smallwood, and D. Wang (2004). Distribution of the number of primary particles of soot aggregates in a nonpremixed laminar flame. *Combustion and Flame 138*(1-2), 195 – 198. *(p. 57)*

Tian, K., F. Liu, M. Yang, K. A. Thomson, D. R. Snelling, and G. J. Smallwood (2007). Numerical simulation aided relative optical density analysis of {TEM} images for soot morphology determination. *Proceedings of the Combustion Institute 31*(1), 861 – 868. *(p. 8)*

Tien, C. and B. Drolen (1987). *Thermal Radiation in Particulate Media with Dependent and Indepentdent Scattering*, Volume 1, pp. 1 – 32. Hemisphere, New York. *(p. xviii, 76)*

Truelove, J. (1988). Three-dimensional radiation in absorbing-emitting-scattering media using the discrete-ordinates approximation. *Journal of Quantitative Spectroscopy and Radiative Transfer 39*(1), 27 – 31. *(p. 141)*

van de Hulst, H. (1957). *Light scattering by small particles*. John Wiley & Sons, New York. *(p. 78)*

Van Poppel, L. H., H. Friedrich, J. Spinsby, S. H. Chung, J. H. Seinfeld, and P. R. Buseck (2005). Electron tomography of nanoparticle clusters: implications for atmospheric lifetimes and radiative forcing of soot. *Geophysical research letters 32*(24). *(p. 28, 66)*

Vander Wal, R. and A. Tomasek (2003). Soot oxidation: dependence upon initial nanostructure. *Combustion and Flame 134*, 1–9. *(p. 39)*

Vander Wal, R. L. (2015). Carbon nanostructure: Characterization by hrtem and xps and alteration by plh. Presented at the CARBON 2015 spinoff workshop PyroMaN II, Dresden, Germany. *(p. 2)*

Vander Wal, R. L., V. M. Bryg, and M. D. Hays (2010). Fingerprinting soot (towards source identification): physical structure and chemical composition. *Journal of Aerosol Science 41*(1), 108 – 117. Special Issue for the 9th International Conference on Carbonaceous Particles in the Atmosphere. *(p. 1)*

Viskanta, R. and M. Mengüç (1987). Radiation heat transfer in combustion systems. *Progress in Energy and Combustion Science 13*(2), 97 – 160. *(p. 153)*

Volakis, J., A. Chatterjee, and L. Kempel (1994, Apr). Review of the finite-element method for three-dimensional electromagnetic scattering. *J. Opt. Soc. Am. A 11*(4), 1422–1433. *(p. 81)*

Walther, P., C. Schmid, M. Sailer, and K. Höhn (2012). Is the scanning mode the future of electron microscopy in cell biology? In H. Schatten (Ed.), *Scanning Electron Microscopy for the Life Sciences*, pp. 71–82. Cambridge University Press. Cambridge Books Online. *(p. 8)*

Wang, H. (2011). Formation of nascent soot and other condensed phase materials in flames. *Proceedings of the Combustion Institute 33*(1), 41 – 67. *(p. xvi, 36)*

Waterman, P. (1971, Feb). Symmetry, unitarity, and geometry in electromagnetic scattering. *Phys. Rev. D 3*, 825–839. *(p. 79)*

Waterman, P., M. Mishchenko, L. Travis, and D. Mackowski (2015, nov). T-Matrix: Codes for Computing Electromagnetic Scattering by Nonspherical and Aggregated Particles. Astrophysics Source Code Library. *(p. 79)*

Weitz, D. A. and M. Oliveria (1984, Apr). Fractal structures formed by kinetic aggregation of aqueous gold colloids. *Phys. Rev. Lett. 52*, 1433–1436. *(p. 51)*

Wentzel, M., H. Gorzawski, K.-H. Naumann, H. Saathoff, and S. Weinbruch (2003). Transmission electron microscopical and aerosol dynamical characterization of soot aerosols. *Journal of Aerosol Science 34*(10), 1347 – 1370. Intercomparison of Soot Measurement Techniques. *(p. 42, 57, 68)*

Wersborg, B., J. Howard, and G. Williams (1973). Physical mechanisms in carbon formation in flames. *Symposium (International) on Combustion 14*(1), 929 – 940. Fourteenth Symposium (International) on Combustion. *(p. 41)*

Wiscombe, W. (1980, May). Improved mie scattering algorithms. *Appl.*

Opt. 19(9), 1505–1509. *(p. 79)*

Witten, T. A. and L. M. Sander (1981, Nov). Diffusion-limited aggregation, a kinetic critical phenomenon. *Phys. Rev. Lett. 47*, 1400–1403. *(p. 43, 51)*

Woodward, J. and R. Wepf (2014). Macromolecular 3d sem reconstruction strategies: Signal to noise ratio and resolution. *Ultramicroscopy 144*, 43–49. *(p. 8)*

Wriedt, T. (2009). Light scattering theories and computer codes. *Journal of Quantitative Spectroscopy and Radiative Transfer 110*(11), 833 – 843. Light Scattering: Mie and More Commemorating 100 years of Mie's 1908 publication. *(p. 84)*

Wriedt, T. (2012). Mie theory: A review. In W. Hergert and T. Wriedt (Eds.), *The Mie Theory*, Volume 169 of *Springer Series in Optical Sciences*, pp. 53–71. Springer Berlin Heidelberg. *(p. 79)*

Wriedt, T. and U. Comberg (1998). Comparison of computational scattering methods. *Journal of Quantitative Spectroscopy and Radiative Transfer 60*(3), 411 – 423. *(p. 79, 80)*

Wu, Y., T. Cheng, L. Zheng, and H. Chen (2015). A study of optical properties of soot aggregates composed of poly-disperse monomers using the superposition t-matrix method. *Aerosol Science and Technology 49*(10), 941–949. *(p. 52)*

Xiong, C. and S. K. Friedlander (2001). Morphological properties of atmospheric aerosol aggregates. *Proceedings of the National Academy of Sciences 98*(21), 11851–11856. *(p. xvii, 59, 60, 61)*

Xu, Y. (1995, Jul). Electromagnetic scattering by an aggregate of spheres. *Appl. Opt. 34*(21), 4573–4588. *(p. 79, 90)*

Xu, Y. (1997, Dec). Electromagnetic scattering by an aggregate of spheres: far field. *Appl. Opt. 36*(36), 9496–9508. *(p. 90)*

Xu, Y. and B. Gustafson (1999). Comparison between multisphere light-scattering calculations: Rigorous solution and discrete-dipole approximation. *The Astrophysical Journal 513*(2), 894. *(p. 90)*

Xu, Y. and B. Gustafson (2001). A generalized multiparticle mie-solution: further experimental verification. *Journal of Quantitative Spectroscopy and Radiative Transfer 70*(4-6), 395 – 419. Light Scattering by Non-Spherical Particles. *(p. 81)*

Xue, Y., Q. Liu, G. He, K. Xu, L. Jiang, X. Hu, and J. Hu (2013). Excellent electrical conductivity of the exfoliated and fluorinated hexagonal boron nitride nanosheets. *Nanoscale Research Letters 8*(1). *(p. 19)*

Yaghjian, A. (1980, Feb). Electric dyadic green's functions in the source region. *Proceedings of the IEEE 68*(2), 248–263. *(p. 94)*

Yon, J., A. Bescond, and F. Liu (2015). On the radiative properties of soot aggregates part 1: Necking and overlapping. *Journal of Quantitative Spectroscopy and Radiative Transfer 162*, 197 – 206. Laser-light and Interactions with Particles 2014. *(p. 52, 121, 131)*

Yon, J., R. Lemaire, E. Therssen, P. Desgroux, A. Coppalle, and K. Ren (2011). Examination of wavelength dependent soot optical properties of diesel and diesel/rapeseed methyl ester mixture by extinction spectra analysis and lii measurements. *Applied Physics B 104*(2), 253–271. *(p. 57, 111)*

Yon, J., F. Liu, A. Bescond, C. Caumont-Prim, C. Rozé, F.-X. Ouf, and A. Coppalle (2014). Effects of multiple scattering on radiative properties of soot fractal aggregates. *Journal of Quantitative Spectroscopy and Radiative Transfer 133*(0), 374 – 381. *(p. 81, 83, 121)*

Yurkin, M., V. Maltsev, and A. Hoekstra (2007). The discrete dipole approximation for simulation of light scattering by particles much larger than the wavelength. *Journal of Quantitative Spectroscopy and Radiative Transfer 106*(1-3), 546–557. {IX} Conference on Electromagnetic and Light Scattering by Non-Spherical Particles. *(p. 88, 101)*

Yurkin, M. A. and A. G. Hoekstra (2011). The discrete-dipole-approximation code adda: Capabilities and known limitations. *Journal of Quantitative Spectroscopy and Radiative Transfer 112*(13), 2234 – 2247. Polarimetric Detection, Characterization, and Remote Sensing. *(p. 84, 94)*

ÉCOLE DOCTORALE
Sciences mécaniques et énergétiques, matériaux et géosciences (SMEMAG)

Titre: Impact de la morphologie des suies sur leurs propriétés radiatives et le transfert radiatif à travers des mélanges gazeux avec suies

Mots-clés: Suie, Rayonnement, Tomographie, Electromagnétisme, Transferts Thermiques

Résumé: Les suies et leur caractérisation constituent des sujets de recherche très actuels dans divers domaines tels que le diagnostic de la combustion, la combustion numérique, l'optique atmosphérique, l'environnement et les applications de santé. Notre étude se concentre sur les propriétés radiatives des agrégats de suie issus de flammes de combustion; notre objectif est de déterminer l'effet de la présence de suies sur le transfert de chaleur par rayonnement pour la simulation d'applications industrielles à haute température impliquant la combustion de gaz. Les études actuelles de modélisation du transfert de chaleur par rayonnement à travers les mélanges gazeux chargés de suies ne considèrent que l'absorption comme phénomène d'interaction rayonnement-matière. Des corrélations généralisées sont utilisées pour déterminer les propriétés radiatives des suies, soit sur la base de morphologies générées numériquement, soit plus simplement à partir de la taille moyenne des suies, de leur dimension fractale et de leur fraction volumique. Cependant, lorsque la taille de l'objet atteint l'ordre de grandeur des longueurs d'onde du rayonnement incident, l'interaction matière-rayonnement est susceptible d'être plus complexe du fait du phénomène de diffusion au niveau de l'agrégation qui ne peut plus être ignoré. Dans notre travail, nous établissons une méthodologie complète assortie d'une chaîne de calcul allant de la définition d'une morphologie de suie réaliste jusqu'au calcul du transfert de chaleur par rayonnement. A cette fin, des observations de suies émises par des flammes propane / air, méthane / air et méthane / oxygène sont effectuées par Microscopie Electronique à Balayage (MEB). La tomographie MEB est appliquée pour la première fois sur une suie issue d'une flamme propane / air, en combinaison avec la Microscopie Electronique en Transmission (MET) pour les observations. Des techniques d'analyse fractale 2D et 3D sont utilisées pour étudier les propriétés fractales d'agrégats de suie virtuels (générés numériquement) et de l'objet obtenu par la tomographie. Les propriétés radiatives des suies sont ensuite calculées en utilisant notre propre code d'Approximation Dipolaire Discrète (ADD - Discrete Dipole Approximation, ou DDA, en anglais). Une attention particulière est accordée à la modélisation ADD des suies en raison de l'indice optique complexe élevé de leur matériau constitutif, et aux méthodes numériques d'intégration directionnelle car les moyennes directionnelles des propriétés radiatives sont nécessaires pour les simulations ultérieures de transfert radiatif. La morphologie et les propriétés radiatives de l'agrégat de suie réaliste (tomographié) sont comparées à celles d'agrégats de suie numériques représentatifs, générés par un algorithme d'agrégation amas-amas limitée par la diffusion (DLCCA, en anglais). Les compatibilités et les écarts entre les propriétés radiatives sont examinés, et les différences entre agrégats numériques représentatifs d'une part et agrégat réaliste d'autre part en termes de propriétés radiatives sont soulignées. Enfin, l'effet de la présence et de la morphologie des suies sur le trans-

fert de chaleur par rayonnement est étudié par la résolution de l'équation du transfert radiatif en utilisant la méthode des ordonnées discrètes (DOM, en anglais) dans un mélange gazeux chargé de suies et dans une configuration académique 1D de plaques paralléles isothermes.

Title: Impact of the morphology of soot aggregates on their radiative properties and the subsequent radiative heat transfer through sooty gaseous mixtures
Keywords: Soot, Radiation, Tomography, Electromagnetism, Heat Transfer

Abstract: Soot and its characterization are of interest to researchers from various domains such as combustion diagnostics, numerical combustion, atmospheric optics, environmental and health applications. In this study, the main interest is on the radiative properties of soot aggregates issued directly from combustion flames in order to determine the effect of the presence of soot on the radiative heat transfer in the simulation of high temperature industrial applications involving gas combustion. Current studies modeling the radiative heat transfer through sooty gaseous media consider only the absorption as the main phenomenon of material-radiation interaction. Generalized correlations are used to determine the radiative properties of soot: these radiative properties are either computed over numerically generated aggregate morphologies or simply as a function of the soot average size, the fractal dimension and the volume fraction. However, the material-radiation interaction is susceptible to be more complex and morphology dependent at the aggregate level because of multiple scattering when the size of the object reaches the order of magnitude of the incident radiation wavelengths. In our work, we investigate the possibility to establish a computational methodology and workflow, starting from the definition of a realistic soot morphology up to the computation of the radiative heat transfer. To that end, observations of soot issued from propane/air, methane/air and methane/oxygen flames are performed using Scanning Electron Microscopy (SEM). SEM tomography is applied for the first time on soot issued from a propane/air flame, combined with Transmission Electron Microscopy (TEM) observations. 2D and 3D fractal analysis techniques are used to investigate the fractal properties of virtual (numerically generated) soot clusters and also of the tomography reconstructed objects. The radiative properties of soot are then computed using our in-house developed DDA (Discrete Dipole Approximation) code. Special attention is paid to the DDA modeling of soot because of the high complex extinction index of the material, and to the directional integration numerical methods because direction-averaged radiative properties are required for the subsequent radiative heat transfer simulations. The morphology and the radiative properties of the realistic morphology are compared to the ones of representative soot aggregates numerically generated by a DLCCA algorithm. The similarities and discrepancies on the radiative properties are investigated, and the differences between representative virtual aggregates on the one hand and the tomography reconstructed object on the other hand in terms of radiative properties are highlighted. Finally the effect of the presence and of the morphology of soot on the radiative heat transfer within a sooty gaseous mixture in a 1D isothermal parallel plate configuration is investigated by the resolution of the radiative transfer equation using DOM (Discrete Ordinates Method).
